SENSORLESS CONTROL OF THE SYNCHRONOUS RELUCTANCE MOTOR

A THESIS

SUBMITTED TO

THE DEPARTMENT OF ELECTRONICS & ELECTRICAL ENGINEERING

OF

THE UNIVERSITY OF GLASGOW

FOR THE DEGREE OF

DOCTOR OF PHILOSOPHY

By

Rolf Lagerquist

August 1993

ProQuest LLC.
789 East Eisenhower Parkway
P.O. Box 1346
Ann Arbor, MI 48106 – 1346

Abstract

This thesis presents sensorless closed-loop speed control for the synchronous reluctance motor. The sensorless control is based on torque vector control. This is believed to be the first implementation of torque vector control. It has been implemented using a high-speed digital signal processor DSP96002.

A constant current-angle controller (with rotor position sensor) for the synchronous reluctance motor was also developed on the same system. This controller was used as a benchmark for the sensorless torque vector control. It was also used to verify simulations and constant current-angle strategies. This is believed to be the first implementation of a number of original control strategies for the synchronous reluctance motor.

Experimental results for *sensorless* operation a 120W axially laminated synchronous reluctance motor are presented and compared with operation with a speed sensor and simulations. Under sensorless operation a (constant-torque) speed range of 400-1500rpm has been achieved. With constant-power flux-weakening operation to the top speed was extended from 1500rpm to 2750rpm. The drive can withstand a full-load step-change within this speed range without losing synchronism under sensorless control.

All the necessary equations for the various aspects of the performance of torque vector control have been developed. The effects of flux-linkage offset errors on the speed estimator and torque estimator have been analysed. Transient errors in the speed estimator due to sudden load changes have also been analysed.

Contents

List of Tables

List of Figures

Acknowledgement

Thanks to my supervisor Professor Tim J. E. Miller for help and advice.

Thanks to "The Committee of Vice-Chancellors and Principals of the Universities of the United Kingdom" and the "Scottish Power Electronics and Electrical Drives Consortium" for financial support.

The author also thanks: F. Flett & Analog Devices for contribution of linear and data-conversion devices, I. Duthie, A. Hutton & Motorola for the DSP96002 development system, S. E. Wood & Brook Crompton for the motor, D. Staton for designing the axially laminated synchronous reluctance motor rotor. W. Soong for theoretical and static data for the motor, J. Kelly for making the rotor, and P. Miller for building the power electronics.

Definitions

Sensorless	=	Operation without speed or shaft-position sensor
SYNCHREL	=	Synchronous reluctance motor (non-proprietary abbreviation)
CAC	=	Constant current angle controller
CCIAC	=	Constant current in the most inductive axis control
TVC	=	Torque Vector Control
PM	=	Permanent magnet
ADC	=	Analog to digital converter
DAC	=	Digital to analog converter
AFE	=	Analog front-end
α	=	Rotor angle (stator reference)
θ	=	Absolute flux-linkage angle (stator reference)
ε	=	Current angle (rotor reference)
δ	=	Voltage angle (rotor reference)
δ'	=	Flux-linkage angle (rotor reference, resistance corrected voltage angle
φ	=	Power factor angle
R	=	Phase resistance
L_d	=	Most inductive-axis inductance
L_q	=	Least inductive-axis inductance
X_d	=	Most inductive-axis reactance
X_q	=	Least inductive-axis reactance
λ_d	=	Most inductive-axis flux-linkage
λ_q	=	Least inductive-axis flux-linkage
ξ	=	Inductance ratio L_d/L_q

$\vec{V}$	=	Voltage space vector
v	=	Peak voltage vector magnitude ($v_{\max_{\sin}} = \frac{V_{DC-link}}{\sqrt{3}}$)
$\vec{I}$	=	Current space vector
$\vec{\lambda}$	=	Flux-linkage space vector
i_d	=	instantaneous d-axis current
i_q	=	instantaneous q-axis current
i	=	instantaneous current magnitude ($\sqrt{i_d^2 + i_q^2}$)
$\vec{I}_d$	=	d-axis current space vector
$\vec{I}_q$	=	q-axis current space vector
T	=	Torque
T_{max}	=	Maximum torque
$T_{max_{base}}$	=	Maximum torque at base speed
P_m	=	Mechanical power
ω, ω_e	=	Electrical rotor speed
ω_m	=	Mechanical rotor speed
p	=	Pole pairs
$T_{control}$	=	Control interval

SI units are used throughout.

Chapter 1

Introduction

Increasing interest has been shown in the synchronous reluctance motor in recent years, particularly in the axially-laminated designs. The interest in the synchronous reluctance motor can be justified by considering the advantages of the synchronous reluctance motor with respect to permanent-magnet and induction motors [1]:

1. It is likely to be more efficient than the induction motor since there are no rotor copper losses. This will be especially important for low speed operation.

2. It produces comparable torque to the induction motor. Under torque vector control or "constant-current-in-the-most-inductive-axis" control (CCIAC) the drive has a large overload torque capability.

3. The rotor is rugged and not subject to the temperature constraints of permanent magnet motors.

4. Since it is a synchronous machine, field oriented control is relatively simple to implement.

5. It can easily be operated under a flux-weakening regime, unlike permanent magnet motors.

6. As the induction motor, it produces smooth torque and is quiet in operation, unlike the *switched* reluctance motor.

The axially-laminated designs from the late 1980s onwards do not have a starting squirrel-cage; this improves the saliency-ratio ξ and hence the torque and efficiency. Without the starting cage the synchronous reluctance motor cannot be used for direct-on-line starts, but requires to be driven by an inverter to keep the rotor and flux in synchronism. Most inverter drives use a sensor to measure the rotor position to achieve this. However, the rotor position sensor has been a major complaint against variable speed inverter drives as it is expensive and fragile, and can prevent use in hostile environments.

Whereas sensorless control for *switched* reluctance motors has been heavily investigated [2, 3, 4] this has not been the case for the synchronous reluctance motor. A promising sensorless control method developed for the synchronous PM motor which should be applicable to the synchronous reluctance motor can be found in [5]. El-Antably proposes a method for sensorless control of the synchronous reluctance motor in [6]; this was further developed by Bolognani [7]. Bolognani implemented a current angle detection system; however he only observed the angle and did not drive an inverter.

This thesis presents an implementation of fully sensorless closed-loop speed control. The controller is based around the torque vector control theory originally developed by Boldea [8]. The torque vector control implements an inner torque loop. Closed-loop speed control has been implemented by estimating the rotor speed from the flux-linkage vectors angular velocity. A constant current-angle controller with a rotor position sensor has also been implemented to use as a benchmark for the sensorless control algorithms.

1.1 Project objectives

At the start of the project there were two main problems that needed to be addressed:

1. What control algorithms to use over a wide range of speed and torque?

2. Is it possible to operate without a shaft position sensor?

Question 1 was addressed rigorously for the first time by Betz [9]. Betz laid down the fundamental theory, but only for an ideal motor model without losses or saturation. Because the synchronous reluctance motor is known to be highly non-linear, a test programme was essential to verify the predictions.

To explain question 2 the original reasons for being interested in the synchronous reluctance motor have to be discussed. Brook Crompton (a motor manufacturer who supported the project in its initial stages) wanted a *low-cost* vector-controlled drive to compete with induction motor drives, but with simpler control. If sensorless control could be achieved it would be possible eliminate the 1000-line encoder (costing upwards of £70) normally required in AC drives.

Another reason is that a wide range of applications can not stand the cost of an encoder. Compressor drives is a very cost sensitive application that would not stand the cost of an encoder. This is especially true for the hermetic compressor.

Hostile operating environments is another reason for wanting sensorless control. Environmental factors that may preclude the use of encoders or resolvers are: extreme temperatures (aircraft), vibrations, dirt, etc.

The proposed sensorless system is based around a digital signal processor. The cost of a digital signal processor is at the present equal to or more than that of a resolver. However, in 5-20 years time the price of today's high-performance digital signal processors will have dropped dramatically. The price of encoders and resolvers, which are precision electro-mechanical devices, will probably remain at their present price level. Therefore it makes sense to investigate whetter the encoder could be replaced by a "sensorless control scheme".

1.2 What's new

This section gives an overview of what new developments are presented in this thesis.

- Experimental verification of the control strategies and simulations developed by Betz [10], for the constant current-angle controlled synchronous reluctance

motor.

- The torque vector control algorithm originally proposed by Boldea [8] for the synchronous reluctance motor has been implemented on a real drive system for the first time.
- A sensorless speed estimator for the the synchronous reluctance motor under torque vector control is proposed and implemented.
- The first operational implementation of a fully sensorless closed-loop speed controlled synchronous reluctance motor is presented. The control includes flux-weakening operation.
- An expression for selecting the appropriate flux-linkage magnitude based on desired (full-load) torque and current angle for operation under torque vector control has been derived.
- An expression for the motor currents as functions of load under torque vector control has been derived.
- An expression for the rate of change of torque for torque vector control has been derived.
- An approximate expression for expected flux-linkage ripple has been developed.
- Algorithms for flux-weakening operation of TVC have been developed and implemented.
- Advantages of flux-weakening operation under torque vector control relative to operation under current-angle control are shown.
- Analysis of the influence of flux-linkage offset on speed and torque estimates.
- Analysis of the effect of load change on speed estimate.
- Demonstration of speed reversals.
- Demonstration of load transients.

- Experimental investigation of the limits to low-speed operation with TVC.

1.3 Thesis overview

The thesis is divided into two parts. Part I is concerned with operation of the synchronous reluctance motor using constant-current angle control with a rotor position sensor. The constant current-angle controller is implemented on a high speed digital signal processor. The philosophy behind the use of the digital signal processor, the implementation, and results are presented. The results from Part I will be used as a benchmark for the controls used in Part II. Part I also covers the derivation of basic motor equations for readers unfamiliar with the synchronous reluctance motor.

Part II starts by reviewing previous works on sensorless control of the synchronous reluctance motor. The principles of the torque vector control algorithm theory originally developed by Boldea [8] are then explained. This is followed by further analysis of the torque vector control. The actual implementation of a closed-loop speed control system for the synchronous reluctance motor is then presented. The effect on speed estimation of flux-linkage offsets and torque changes are analysed. Results for both fully sensorless torque vector control and torque vector control with speed sensor are then presented.

For the reader interested in the controller hardware design a full account of the development of the digital controller and IGBT-inverter can be found in Appendix B. Appendix B can be useful for the reader contemplating building a digital controller.

The final two sections in the introduction presents a brief chronological account of the development of the synchronous reluctance motor and its control. The first section mainly describes the developments in the design of the the actual motor itself from 1923 to 1993. The section on control strategies for the synchronous reluctance motor is naturally shorter because field-oriented inverters only became available in the last half of the 1980s. Before field-oriented control the performance of the motor was mainly dictated by the rotor design. With field-oriented control the performance objectives can be more freely chosen.

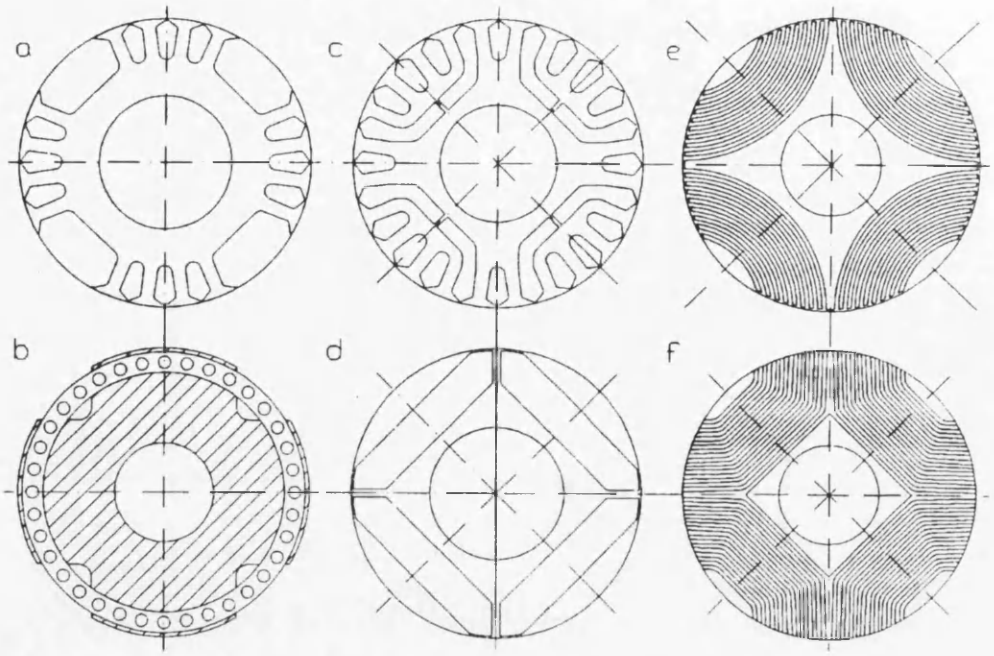

Figure 1: Main classes of synchronous reluctance motors (Source [12])

1.4 Chronological history of the development of synchronous reluctance motors

The salient pole synchronous reluctance motor (Fig. 1a-b) is one of the oldest types of motors, predating the induction motor by many years [11]. At first it was used only in instrumentation, but later it became more widely used due to its simplicity and constant speed. These early motors were usually limited to a few h.p. due to low efficiency and power/weight ratio [11].

One of the first papers to thoroughly analyse the synchronous reluctance motor was by Kostko [11] (1923). Previously the general opinion had been that the synchronous reluctance motor was inherently inferior to other types of a.c. motor. Kostko's paper shows that this inferiority was due to the use of poorly designed rotors. He claims that the synchronous reluctance motor can be designed with comparable performance to the a.c. induction motor. Kostko realised the importance of having a high saliency ratio (L_d/L_q), and that the way to achieve this is to divide the rotor into separate sections along the lines of the most inductive axis. Kostko developed the theory and proposed a segmented structure similar to Fig. 1c. Kostko

calculated that a motor with two sections should develop 80% of the torque of a similarly sized induction motor (1923 design), and that with 4 sections it could be further improved. Comparing the 4 segment motor to a salient-pole design it gives several times the torque. The saliency ratio of this design is predicted to be 25.6. Kostko also realised that the slot-leakage flux (which prevents low L_q) can be minimized by having a large number of segments.

Work on the synchronous reluctance motor was reviewed in the mid 1960s. The work at this time was generally split between the salient pole (Fig. 1a-b) and segmented rotor designs (Fig. 1c-d).

Lee [13] produced (1960) a low-speed salient-pole synchronous reluctance motor (Fig. 1b). The motor had a solid rotor and a hermetic-can design which limited the saliency ratio.

The salient-pole designs were further developed by Lawrenson in 1964-67 [14, 15, 16]. A saturated saliency ratio of 2.58 for the salient-pole design was obtained. A modified design using insulated pole-segments improved the saliency ratio to 4.5. The segmented design had a reported average efficiency of 75% and a power factor of 0.52.

In 1967 Fong [17] presented a synchronous reluctance motor design with a squirrel-cage induction motor rotor with part of the peripheral iron cut away (similar to Fig. 1a). The average efficiency was 50% and the power factor 0.45.

By 1970 Fong [18] had moved on to segmental rotor designs derived from Kostko's (1923) suggested designs. Fong's design had two flux-barriers punched out of a standard induction motor lamination. He achieved excellent an unsaturated saliency ratio of 10.7 which was reduced to 5.5 at full load. This design compares well against a similar induction motor. The efficiency and power-factor of the reluctance motor were 76% and 0.7 respectively. The values for the induction motor were 77.8% and 0.87 respectively. This shows that at least for small motors (3.25 h.p. in this case) the synchronous reluctance motor can compete with the induction motor.

In 1972 Honsinger [19, 20] published a paper on a new intrinsically stable segmented synchronous reluctance motor design. Honsinger states that there is a conflict between designing for high torque (high L_d/L_q) and for large stable operating area. His solution for obtaining a large stable operating area and high torque was to use saturable bridges. These bridges give an inductance ratio of 1.04 at light load and 4.15 at full load. The inductance ratios in his 1971 design [19], which did not use bridges, are 4.5 unsaturated and 4.49 saturated. This paper shows the classical compromises needed when the synchronous reluctance motor is designed for open-loop (and line-start) operation. Clearly the power-factor (and consequently the efficiency) suffers at light loads because of the low inductance ratio.

The 1970s saw an increased interest in the line-start axially laminated synchronous reluctance motor (Fig. 1f). Cruickshank [21] reported an inductance ratio of 5.2 using a design based on a (primitive) C-core design. This design was also used by Menzies (1972) [22, 23]. Menzies obtained inductance ratios of 4 (unsaturated) to 2.7 (saturated).

A paper on the dynamic performance of the axially laminated synchronous motor by Rao [24] (1976) shows that the axially laminated rotor is superior to the segmented rotor. The performance advantages are in the areas of power factor, efficiency, pull-out, and pull-in torque. An inductance ratio of 6.8 and efficiency of 86% are reported. The values for a segmental structure are 3.3 and 80% respectively. It must be noted that the motor used is rated at 15 h.p. whereas the motors described previously have been in the range 1–10 h.p.

In 1985 El-Antably [25] showed what is assumed to be the first axially laminated rotor designed not using C-cores (Fig. 1e). The motor was rated 15 h.p. and designed for line-start operation. The new structure has a much larger pole-arc to pole-pitch ratio (0.94) compared to the C-core design (0.5). The advantage of this is that the L_d axis inductance is increased. A very good efficiency of 94% is reported for this motor. The corresponding power factor is 0.89. This motor has become known as "the Westinghouse (synchronous reluctance) motor".

The rotors presented so far have all been designed for line-start applications.

It should be noted that the axially laminated structures presented for line-starting have not shown any great advantages over a well designed segmented structure.

In the late 1980s there was a revival of the synchronous reluctance motor. This was partly fuelled by disenchantment with the *switched* reluctance motor; but enabled by developments in power electronics and digital control. The use of inverter technology meant that the design of the synchronous reluctance motor could be changed considerably as there was no longer a need for a starting cage or damping bars.

There appear to be two main directions of design that followed the introduction of field oriented controls. The first design is a continuation of the axially laminated structure, but with much finer laminations. The second design is a very simple 2-pole dumbbell-shaped rotor used in very high speed applications.

An early analysis of a 2-pole axially laminated rotor was performed by Fratta and Vagati in [26].

The first finely axially laminated synchronous reluctance motor without a starting-cage or damper-bars was made by Platt [1] in 1990 (Fig. 1e). The motor had a lamination to barrier ratio of 1:1. The number of laminations appears to be 10. The measure inductance ratio was 10.5 unsaturated and 8.8 saturated. Only static test results were presented. One of the claims made in the analysis is that the rotor runs cool because there is no rotor current.

The claim made by Platt that the finely axially laminated motor operated with a cold rotor was refuted by Marongiu and Vagati in [27]. It was shown that the rotor losses are in the same class as the rotor losses in an induction machine. The losses are claimed to be due to the slotted nature of the stator. It was also claimed that this problem can be solved by reducing the number of laminations and properly relating the number to the number of stator teeth.

A study in optimization of the rotor geometry for highest inductance ratio was performed by Miller in [28] (1991) and further developed by Staton in [12] (1993). Staton showed that the maximum possible inductance ratio in a slotted stator (D132)

with an ideal 4-pole rotor is 30 unsaturated and 14 (heavily-)saturated. The corresponding ratios for an axially laminated rotor are 11 and 8. Staton's rotor (Fig. 1f) is different from Platt's (Fig. 1e) in that is uses a square shaft, making the construction slightly easier.

An axially laminated 2-pole synchronous reluctance generator was presented by Boldea in [29]. The inductance ratio for this motor was 16 saturated. As expected 2-pole designs give higher inductance ratio than 4-pole designs, mainly due to less stator slot leakage. One of the problems with the axially laminated 2-pole designs is that there is no shaft through the rotor. Boldea used kevlar pole holders to secure the rotor laminations onto the shaft ends. Efficiencies of up to 92% and power factors of 0.8 were reported.

A simple single-barrier design was presented by Miller in [28] (Fig. 1d). The design is simple, but has an inductance ratio of only 4.0. However the drive produced 50% more torque than a comparable induction motor based on equal losses. The low-speed torque is about 30% lower than a *switched* reluctance of similar frame size.

The salient-pole design has prevailed in super high-speed-motors. In 1989-91 Fukao and Chiba [30, 31, 32] reported on high-speed (48,000rpm) drives with 85% efficiency and power factors of 0.46. The inductance ratio of this motor was 2.86.

1.5 Developments in control strategies for the synchronous reluctance motor

The control developments of the synchronous reluctance motor are easily divided into two groups; line-start and inverter driven.

The first group is concerned with operating from a fixed-frequency, and fixed-amplitude voltage source. The maximum efficiency point of the motor is found in the stable region. However, the maximum efficiency is only obtained at one specific operating point. The efficiency of the motor is a function of the saliency ratio.

However, the saliency-ratio can not be maximized because of need for a starting cage. Another factor preventing optimizing for saliency ratio is that the motor becomes less stable as the inductance ratio increases. Optimization for saliency ratio may thus lead to less than optimum performance [33]. Most of the papers on control of the line-start synchronous reluctance motor are concerned with design to optimize pull-in torque, pull-out torque, efficiency, and power factor. Work in this field has been done by Honsinger [34], Lawrenson [14], and Finch [33, 35].

With the appearance of field-oriented inverters better control strategies for the synchronous reluctance motor became possible. The research in the control of the synchronous reluctance motor has been concerned with establishing the performance limitation of the system and also control strategies for optimizing various control objectives.

The first really thorough analysis of the synchronous reluctance motor was performed by Betz in 1991 [9, 10, 36]. The main limitation of this work was that it assumed no iron-losses and no saturation. However, he showed a range of interesting relationships between different control objectives for the synchronous reluctance motor. Control objectives considered were: maximum torque per ampere control, maximum power factor control, maximum rate of change of torque control, constant current in the most inductive axis control, and flux-weakening operation. The condition for maximum rate of change of torque had earlier (1987) been presented by Chiba in [37].

Fratta [38] and Xu [39] looked at more special forms (spindle drive applications) of high-speed control of the synchronous reluctance motor.

In [39] (1991) Xu also considered the influence of iron loss and saturation on the maximum torque per ampere and maximum efficiency modes of operation. It was found that the current angles were significantly different from what was found when assuming an ideal motor [10]. In [40] Xu considered a method for observing the currents actually flowing in the magnetizing branch of the circuit. He did not consider how to control the magnetizing currents.

In 1992 Betz [41, 42] include saturation and iron-losses in his analysis. Betz

concludes that taking variations in ironloss resistance and L_d into account does not change the results much from when they are assumed to be constant as in [39]. Another interesting result also observed in [39] is that the current angle for maximum efficiency is much larger than that for the ideal motor. Using a non-saturated model (but including iron-loss) produced results very close to the ideal model.

Betz also observed that the synchronous reluctance motor model including iron loss and saturation could be flux-weakened much the same as the ideal motor. However, the flux-weakening angle was quite different from the one for the ideal model. An approximate solution for the flux-weakening angle which did not take into account variation in iron loss resistance or saturation was developed. However, the approximate angle was erroneous enough to be of little real value.

In [8] Boldea shows simulations of a new control method, torque vector control, for the synchronous reluctance motor. This method keeps constant flux-linkage magnitude and almost all change in current occurs in the least inductive axis. This ensures fast torque response. Boldea also shows that his synchronous reluctance motor can produce 5 times the rated torque of the induction motor at up to 2/3 the rated speed. However, it must be mentioned that these results were simulations and that the q-axis current was 10 times the rated current. Of course 10 times rated current in a real motor is not realistic.

Sensorless operation methods for the synchronous reluctance motor have been proposed by El-Antably [6], Bolognani [7], and Boldea [8]. Works that involve sensorless control are reviewed in Part II, Chapter 4.

Part I

Current Angle Control using Rotor Position Sensor

Chapter 2

Fully Digital Constant Current-angle Controller

2.1 Introduction

This chapter describes the development and implementation of a fully digital controller for the synchronous reluctance machine. The controller uses a fast digital signal processor, the Motorola DSP 96002. A shaft position sensor is used in the control described in this chapter.

Basic motor equations and current angle control of the synchronous reluctance motor will be introduced. The philosophy behind the development of the controller will then be covered, followed by implementation and control structure details. Experimental results will be presented and compared with simulations in chapter 3.

Current angle control is one of the most obvious methods for vector control of synchronous reluctance motors. It is particularly important to investigate this mode of operation to have a benchmark with which the sensorless and semi-sensorless methods used in Part II can be compared.

Another important reason for developing this control software was so that the current angle control algorithms for the synchronous reluctance motor developed by Betz [9] could be verified. As only a simulation program had been used to test and

develop the algorithms, it was vital to back the simulations up with experimental data. If simulations and experimental results agreed it implied that the simulations are correct and that simulations can be used to develop further control methods.

2.2 The ideal synchronous reluctance machine

This section is concerned with the derivation of various motor quantities and *dq*-equations used elsewhere in this thesis. This section is intended as an introduction for readers who are not familiar with the basic equations or operation of the synchronous reluctance motor.

The stator of a normal three phase AC motor consists of three phases a, b, and c each of which is sinusoidally distributed in the stator. The rotor of a synchronous reluctance motor has an position dependent permeance. This is illustrated in Fig. 2. The rotor has a set of steel-laminations spaced by a non-magnetic material. It is clear that the permeance of the rotor is greater if flux enters the rotor in the direction of the steel laminations (d-axis) because it will travel most of the distance through the rotor in a high permeance material (steel). If the flux entered perpendicular to the laminations (q-axis) it would have to travel most of the distance through a low permeance material (air). It is this difference in reluctance that produces the torque in the synchronous reluctance motor.

To simplify the analysis it is assumed that the motor is a synchronous reluctance motor without any saturation effects. It is also assumed that the windings and the space mmf are sinusoidally distributed. The notation used by Fitzgerald and Kingsley in [43] will be used.

The relationship between applied voltage and current for each of the phases can be written as:

$$v = Ri + \frac{d\lambda}{dt} \tag{1}$$

where v is the phase-voltage, i is the phase-current, R is the phase resistance, and λ is the flux-linkage.

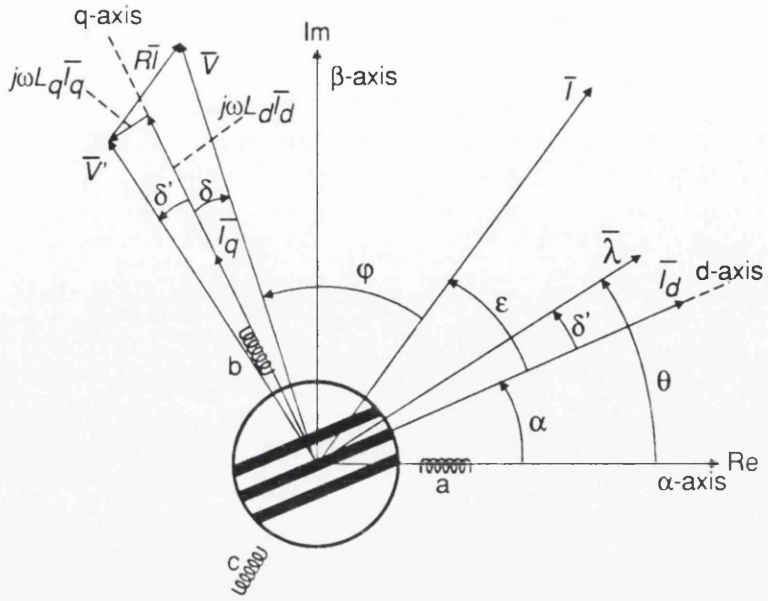

Figure 2: Synchronous reluctance motor phasor diagram

The circuits a, b, and c all have their own resistance and self-inductance. Between the circuits there are also mutual inductances. The mutual inductance and self-inductances also vary with the rotor position α. The letter $\mathcal{L}$ denotes position dependent self- or mutual-inductance. The flux-linkage can be written in matrix form as a function of inductances as [43]:

$$\begin{bmatrix} \lambda_a \\ \lambda_b \\ \lambda_c \end{bmatrix} = \begin{bmatrix} \mathcal{L}_{aa} & \mathcal{L}_{ab} & \mathcal{L}_{ac} \\ \mathcal{L}_{ba} & \mathcal{L}_{bb} & \mathcal{L}_{bc} \\ \mathcal{L}_{ca} & \mathcal{L}_{cb} & \mathcal{L}_{cc} \end{bmatrix} \begin{bmatrix} i_a \\ i_b \\ i_c \end{bmatrix} \tag{2}$$

All the inductances in the above equations are functions of α and are thus time varying.

2.2.1 Stator self-inductances

The self-inductance in a phase will always have a positive value but it will be modulated by a second harmonic function due to the difference in d- and q-axis permeance. From the diagram in Fig. 2 it can be seen that the self inductance of phase a ($\mathcal{L}_{aa}$) will have a maximum when the rotor is aligned with the phase at $\alpha = 0°$ and $\alpha = 180°$. Similarly it will have minimum at $\alpha = 90°$ and $\alpha = 270°$.

The mmf of phase a is a cosine wave centered on the phase a axis. The peak mmf is given by the equation $F_a = N_a i_a$ where N_a is the effective turns number of phase a. The mmf of phase a can then be decomposed into the rotor d-q frame by the following equations:

$$F_{da} = F_a \cos\alpha \tag{3}$$

$$F_{qa} = F_a \cos(\alpha + 90°) = -F_a \sin\alpha \tag{4}$$

where α is the angle between phase a and the d-axis.

Having decomposed the mmf wave in d and q components, the air-gap flux in each axis can be calculated as [43]:

$$\Psi_{gda} = F_{da}\mathcal{P}_{gd} = F_a\mathcal{P}_{gd}\cos\alpha \tag{5}$$

$$\Psi_{gqa} = F_{qa}\mathcal{P}_{gq} = -F_a\mathcal{P}_{gq}\sin\alpha \tag{6}$$

where $\mathcal{P}_{gd}$ and $\mathcal{P}_{gq}$ denote the permeance coefficient in the d- and q-axis respectively. The permeance will be here be regarded as known quantities. However, they actually depend on machine geometry and saturation.

The air-gap flux linking phase a can now be found as:

$$\Psi_{gaa} = \Psi_{gda}\cos\alpha - \Psi_{gqa}\sin\alpha \tag{7}$$

$$\Psi_{gaa} = F_a(\mathcal{P}_{gd}\cos^2\alpha + \mathcal{P}_{gq}\sin^2\alpha) \tag{8}$$

$$\Psi_{gaa} = N_a i_a \left(\frac{\mathcal{P}_{gd}+\mathcal{P}_{gq}}{2} + \frac{\mathcal{P}_{gd}-\mathcal{P}_{gq}}{2}\cos 2\alpha\right) \tag{9}$$

Since inductance is the proportionality factor that relates flux-linkage to current, the self-inductance $\mathcal{L}_{gaa}$ of phase a due to the air-gap flux can be found as:

$$\mathcal{L}_{gaa} = \frac{N_a\Psi_{gda}}{i_a} = N_a^2\left(\frac{\mathcal{P}_{gd}+\mathcal{P}_{gq}}{2} + \frac{\mathcal{P}_{gd}-\mathcal{P}_{gq}}{2}\cos 2\alpha\right) \tag{10}$$

$$\mathcal{L}_{gaa} = L_{g0} + L_{g2}\cos 2\alpha \tag{11}$$

where L_{g0} is a constant term and L_{g2} is the amplitude of the second harmonic [43].

To get the total self inductance of the phase, the leakage inductance, L_{al}, of the phase must be included [43].

$$\mathcal{L}_{aa} = L_{al} + \mathcal{L}_{gaa} \tag{12}$$

$$\mathcal{L}_{aa} = L_{aa0} + L_{g2}\cos 2\alpha \tag{13}$$

where $L_{aa0} = L_{al} + L_{g0}$

The self-inductance equations for all the phases are thus:

$$\begin{aligned} \mathcal{L}_{aa} &= L_{aa0} + L_{g2}\cos 2\alpha \\ \mathcal{L}_{bb} &= L_{aa0} + L_{g2}\cos(2\alpha + 120°) \\ \mathcal{L}_{cc} &= L_{aa0} + L_{g2}\cos(2\alpha - 120°) \end{aligned} \tag{14}$$

2.2.2 Mutual inductances

The mutual inductances also have a second order harmonic because of the rotor shape. The mutual inductance between phase a and b can be found by evaluating the air-gap flux linking phase b when only phase a is excited. Using (7) and replacing α by $\alpha - 120°$.

$$\Psi_{gba} = \Psi_{gda}\cos(\alpha - 120°) - \Psi_{gqa}\sin(\alpha - 120°) \tag{15}$$

Substituting in from (5) and (6):

$$\Psi_{gba} = F_a\left[\mathcal{P}_{gd}\cos\alpha\cos(\alpha - 120°) + \mathcal{P}_{gq}\sin\alpha\sin(\alpha - 120°)\right] \tag{16}$$

$$\Psi_{gba} = N_a i_a\left[-\frac{\mathcal{P}_{gd} + \mathcal{P}_{gq}}{4} + \frac{\mathcal{P}_{gd} - \mathcal{P}_{gq}}{2}\cos(2\alpha - 120°)\right] \tag{17}$$

The mutual inductance between phases a and b then becomes [43] (neglecting small amount of flux not crossing air-gap):

$$\mathcal{L}_{gba} = \frac{N_a\Psi_{gba}}{i_a} = -0.5L_{g0} + L_{g2}\cos(2\alpha - 120°) \tag{18}$$

The stator mutual-inductances for all phases are thus:

$$\begin{aligned} \mathcal{L}_{gab} &= \mathcal{L}_{gba} = -0.5L_{g0} + L_{g2}\cos(2\alpha - 120°) \\ \mathcal{L}_{gbc} &= \mathcal{L}_{gcb} = -0.5L_{g0} + L_{g2}\cos 2\alpha \\ \mathcal{L}_{gac} &= \mathcal{L}_{gca} = -0.5L_{g0} + L_{g2}\cos(2\alpha + 120°) \end{aligned} \tag{19}$$

2.2.3 DQ-axis transformations

The motor equations in section 2.2 can be considerably simplified for synchronous machines by transforming them into a synchronous rotor reference frame. The rotor

reference frame is often call the d-q frame where the d or direct axis is aligned with the rotor. The q or quadrature axis is perpendicular to the d-axis.

Taking the general case when all three phases are excited, the mmf can then be decomposed into a d and a q-axis component [43].

$$F_d = N_a [i_a \cos\alpha + i_b \cos(\alpha - 120°) + i_c \cos(\alpha + 120°)] \quad (20)$$

$$F_q = N_a [-i_a \sin\alpha - i_b \sin(\alpha - 120°) - i_c \sin(\alpha + 120°)] \quad (21)$$

The currents i_d and i_q can be defined in a similar fashion. Arbitrary constants k_d and k_q are included.

$$i_d = k_d [i_a \cos\alpha + i_b \cos(\alpha - 120°) + i_c \cos(\alpha + 120°)] \quad (22)$$

$$i_q = k_q [-i_a \sin\alpha - i_b \sin(\alpha - 120°) - i_c \sin(\alpha + 120°)] \quad (23)$$

This can be used to simplify (20) and (21). Thus

$$F_d = \frac{N_a}{k_d} i_d \quad (24)$$

$$F_q = \frac{N_a}{k_q} i_q \quad (25)$$

Notice the simplicity of (24), (25) compared to (20), (21).

The constants are chosen to simplify the performance equations described in the next section. It is common to take k_d and k_q as being 2/3. Thus

$$i_d = 2/3 [i_a \cos\alpha + i_b \cos(\alpha - 120°) + i_c \cos(\alpha + 120°)] \quad (26)$$

$$i_q = 2/3 [-i_a \sin\alpha + i_b \sin(\alpha - 120°) + i_c \sin(\alpha + 120°)] \quad (27)$$

These transformations are often referred to as the Blondel or Park transformations.

If the motor is assumed to connected in a Y, which is usually the case for inverter driven motors, the transforms from stator to d-q form can be written in matrix notation as:

$$\begin{bmatrix} i_d \\ i_q \end{bmatrix} = \frac{2}{3} \begin{bmatrix} \cos\alpha & \cos(\alpha - 120°) & \cos(\alpha + 120°) \\ -\sin\alpha & \sin(\alpha - 120°) & \sin(\alpha + 120°) \end{bmatrix} \begin{bmatrix} i_a \\ i_b \\ i_c \end{bmatrix} \quad (28)$$

The reverse transform going from dq quantities to stator quantities can similarly be written as:

$$\begin{bmatrix} i_a \\ i_b \\ i_c \end{bmatrix} = \begin{bmatrix} \cos\alpha & -\sin\alpha \\ \cos(\alpha - 120°) & -\sin(\alpha - 120°) \\ \cos(\alpha + 120°) & -\sin(\alpha + 120°) \end{bmatrix} \begin{bmatrix} i_d \\ i_q \end{bmatrix} \tag{29}$$

The relationships for voltage and flux-linkage are exactly the same and can be written by replacing the current by voltage or flux-linkage respectively.

2.2.4 Basic motor equations

Using the dq-transformations on the flux-linkages and currents the results are:

$$\lambda_d = L_d i_d \tag{30}$$

$$\lambda_q = L_q i_q \tag{31}$$

These new inductances are related to those used in the previous section as follows:

$$L_d = L_{al} + 3/2(L_{g0} + L_{g2}) \tag{32}$$

$$L_q = L_{al} + 3/2(L_{g0} - L_{g2}) \tag{33}$$

L_d and L_q are known as the direct and quadrature synchronous inductances [43].

By using dq-transformations on the voltage equations they can be written as:

$$v_d = Ri_d + \frac{d}{dt}\lambda_d - \lambda_q\omega \tag{34}$$

$$v_q = Ri_q + \frac{d}{dt}\lambda_q + \lambda_d\omega \tag{35}$$

where $\omega = d\alpha/dt$ the electrical angular velocity. The dq currents and voltages are shown in the phasor diagram Fig. 2 on page 37. Note that the phasor diagram shows the steady-state case where the di/dt components are zero.

The above equations are the basic equations needed to analyse the synchronous reluctance motor.

The sign convention adopted is that applied voltage and current into the stator windings are positive, and that positive currents produce positive flux-linkages.

To complete the motor equations the expressions for power and torque are needed. The instantaneous power in the motor is given by:

$$P = v_a i_a + v_b i_b + v_c i_c \tag{36}$$

The power can be written in terms of dq quantities using (36) and (29) as:

$$P = 3/2(v_d i_d + v_q i_q) \tag{37}$$

The torque developed can be found by using the power equation (37) and substituting the voltages using (34) and (35). Also ω is the *electrical* rotor speed in radians related to the *mechanical* rotor speed as $\omega = p \cdot \omega_m$, where p is the number of pole-pairs. The electromagnetic torque is thus [43]:

$$T = \frac{3}{2} \cdot p \cdot (\lambda_d i_q - \lambda_q i_d) \tag{38}$$

where the torque is positive for motoring action.

Alternatively the torque can be written in terms of inductances, current magnitude ($i = \sqrt{i_d^2 + i_q^2}$) and the angle between the d-axis and the current as:

$$T = \frac{3}{2} \cdot p \cdot (L_d - L_q) \cdot i^2 \cdot \frac{\sin 2\varepsilon}{2} \tag{39}$$

It should be noted that the inductance L_d is a non-linear function of the current i_d.

The above equations fully specify the ideal Y-connected synchronous reluctance motor in terms of currents, voltages, power, and mechanical torque.

2.2.5 Current vector control for the synchronous reluctance motor

Vector control for electrical motors is in general described as control through application of current or voltage vectors. Under vector control the current or voltage vector is controlled in both magnitude and phase. Vector control of electrical motors is generally accepted as a method for extracting better performance, both dynamic and static.

In this section the special case of vector control where the current vector magnitude and phase are controlled is considered. The applicable torque equation for this mode of operation is (39). From (39) it is clear that the torque depends on the current angle ε (see Fig. 2), and that the maximum torque occurs with a current angle of 45° for a fixed current magnitude.

The choice of current angle will affect the motor performance in different ways. The current angles corresponding to different performance objectives were identified by Betz in [9, 10] as:

1. Maximum Torque Control (MTC). This refers to the well-known maximum torque per ampere control strategy. This is obtained with a current angle $\varepsilon = \frac{\pi}{4}$ radians. The speed at which the inverter runs out of volts using this control method is known as the rated speed, ω_0.

2. Maximum Rate of Change of Torque Control (MRCTC). This refers to the control strategy proposed in [37] where the rate of change of torque is optimised. The required current angle for this is: $\varepsilon = \tan^{-1} \xi$, where ξ is the ratio L_d/L_q.

3. Maximum Power Factor Control (MPFC). This control operates the machine at the highest power factor obtainable. This gives the lowest ratio of inverter kVA rating to output power. The required current angle is [10]:

$$\varepsilon = \tan^{-1} \sqrt{\xi} \tag{40}$$

4. Constant Current in the Inductive Axis Control (CCIAC). This control method keeps the current in the most inductive axis constant and varies the current in the least inductive (q-axis) to control the torque. Of all the strategies this strategy gives the highest rate of change of torque at low speeds [10]. However, at rated speed and torque the MRCTC has the highest rate of change of torque of all the methods.

5. Field Weakening Control (FWC). When the inverter runs out of volts at high speeds, the current angle is increased to maintain constant power. The current

angle required for operation above rated speed is [10]:

$$\varepsilon = \tan^{-1}\left[\frac{(\xi^2+1) - \sqrt{(\xi^2+1) - 4\omega_n^2\xi^2}}{2\omega_n}\right] \tag{41}$$

It should be noted that the current angle in all cases (except certain CCIAC conditions) is 45° or larger. This means that the operating point is intrinsically unstable. Most controllers therefore use a rotor position sensor so that the current vector can be placed at the desired position relative to the rotor. The motor can thus be operated stably even at an intrinsically unstable current angle.

The control of the motor usually takes place in the dq-frame since under steady-state all the variables are represented by DC-values. This simplifies the control considerably, even if measured values must be transformed into dq-frame before the control action and then transformed back into stator reference frame before controlling the real system.

2.3 Philosophy behind DSP based synchronous reluctance motor controller

The philosophy behind the development of this control system was to minimise the time from when an idea is conceived until it can be tested out on an actual system. As explained in appendix B the most flexible way to develop new control algorithms is to use a digital processor to execute the control algorithms. It is usual to first test out new ideas using a simulation. It is obvious that time can be saved if the simulation code and the real-time control code could be developed in parallel. The most efficient way of achieving this parallelism is to share the same code between the simulation and the control program.

To implement this sharing of code it would be ideal if the two programmes were merged into one unit in which one could select either a hardware interface to a real motor or a simulation of a motor. In most cases a simulation and the controller system will not use the same processor and hence not the same instruction set. By

writing the code in a high-level language the peculiarities of a processor's instruction set can be hidden from the programmer, and a compiler will translate the high-level instructions into processor-specific instructions. In most cases the use of a high-level language will result in larger and slower code than if a program was written in assembler for a specific processor. This loss of performance must be accepted if the development time is critical. The only way of compensating the performance is to ensure that the real-time control system uses a processor that is sufficiently fast so that the control does not suffer. Another advantage of high-level languages is that the code is structured, more readable, and maintainable.

Another issue which is important for a quick development cycle is how variables are stored. The most convenient way of performing calculations is to use floating-point variables. When performing operations with floating-point variables one does not have to consider factors such as scaling and variable range. Floating-point variable operations however tend to be slow on most processors. The other type of variables are fixed-point or integers. This type of variable demands that the programmer pays close attention to the scaling and range limitations of the variables used. The use of fixed-point variables will generally result in the fastest program. However, to ensure that variables are kept in range and have enough accuracy (scaling) at all times can take a huge amount of time. Clearly it is desirable to use floating-point variables to minimize development time, and fortunately there exist processors with floating-point hardware built in. The speed of floating-point hardware can also vary considerably between processors. Floating-point digital signal processors are generally fastest and can often execute a floating-point multiply in one instruction cycle. To summarise the requirements for a short idea to implementation time is to:

1. Use a high-level language.

2. Use floating-point variables.

3. Use a fast digital signal processor with built in floating-point operations in hardware.

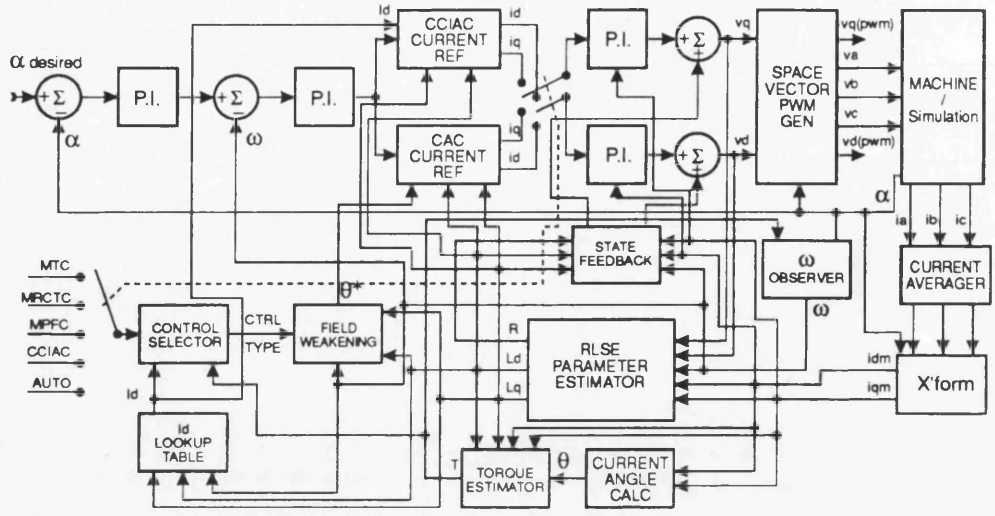

Figure 3: Original synchronous reluctance motor control structure

2.4 Adapting simulation to real-time operation

As stated in 2.3 there are great advantages in combining the operations of the simulation and real-time control programs, as long as the processor that is going to execute them is fast enough. The processor chosen to implement this system is a digital signal processor (Motorola DSP96002-33) capable of executing floating-point instructions in one instruction cycle [44]. It was thus decided to use a combined simulation / real-time control program. The DSP96002 was also one of the fastest floating-point digital signal processor available at the time. The DSP96002-33 has an instruction cycle time of 60ns. However, the DSP96002-33 was found not to be powerful enough to execute certain parts of the original simulation program in real-time.

To speed the development of the real-time control software a simulation programme written by Dr. R.E. Betz [42] was used as a base from which to develop a combined simulation/real-time control version. The control structure of the original combined control program is shown in Fig. 3. The first thing to realise from this figure is that the program was not written with real-time operation in mind, and would take far too long to execute if used as it is shown in Fig. 3. Consequently the program had to be simplified even if this was contrary to the philosophy behind the controller.

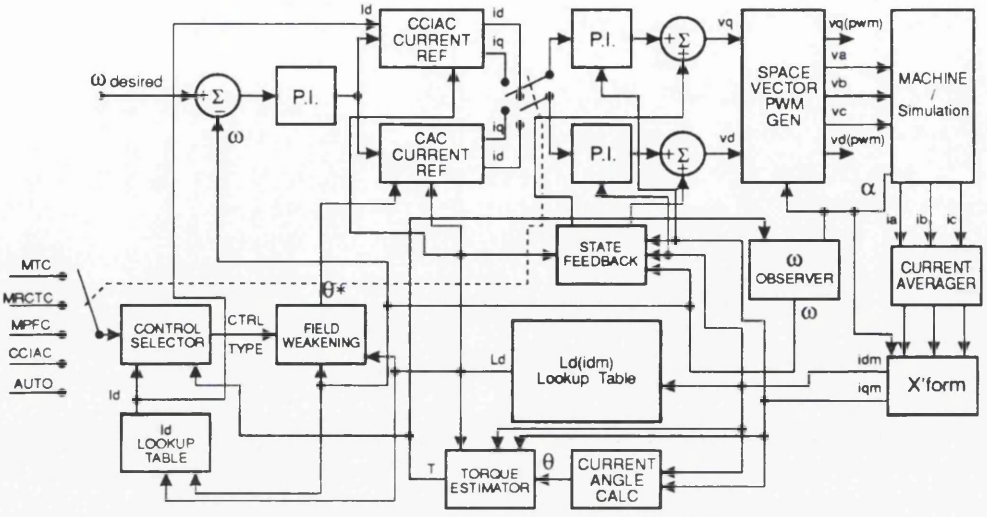

Figure 4: Simplified synchronous reluctance motor control structure

Fig. 4 shows the new simplified version. The main component that has been modified is the machine parameter estimator. In the simulation the machine parameter estimator used a recursive least square estimator (RLSE), this is a particularly computational intensive process. The operation of the RLSE machine parameter estimator is fully described in [42]. In the simulation the main motor parameters R, L_d, and L_q were estimated. However, this can be simplified since L_q is known to be fairly constant regardless of i_q. R varies with temperature but is not critical for the control. This leaves L_d, which is dependent on i_d. It is important to know L_d since it is an important part of the control equations. L_d is a strong function of i_d and it can thus be estimated quite well by using a lookup-table of L_d as a function of i_d. The RLSE machine parameter estimator was thus replaced by a simple lookup-table, which does not use much execution time.

The main purpose of building this controller was to provide a benchmark for sensorless control methods. Since it was not likely that any sensorless *position* control would be made, the outer position controller was also removed to increase the execution speed. Position control was not needed to verify the constant current control algorithms or simulations.

It should also be noted that *constant speed* operation is probably the mode of operation most used.

2.5 Control Overview

As can be seen from Fig. 4 the controller supports speed control. The speed controller is a conventional PI controller which produces a current magnitude demand signal. The current demand signal from the speed controller is limited to the maximum allowable motor current. The integral part of the controller is under current limit constraint conditions prevented from saturating unnecessarily (anti-windup).

The current magnitude demand signal is then passed on to an i_d, i_q current reference generator. The current references generated will obviously depend on the control selected with the control selector.

For constant current angle control methods the i_d current is given by $i_d = I\cos\varepsilon$, and the i_q current is given by $i_q = I\sin\varepsilon$. For CCIAC the i_d current is fixed and set at a predetermined level. The i_q current for CCIAC is related to the demanded current magnitude as $i_q = \sqrt{I^2 - i_d^2}$

The i_d and i_q desired currents are then passed on to separate PI controllers. The outputs from the i_d and i_q PI regulators are desired v_d and v_q respectively. To prevent the rotational (ω) terms in (34) and (35) from causing state disturbance the rotational voltage components in each axis are calculated in the state-feedback block and added to the voltage demand from the PI controllers. This in effect decouples the two dq voltage equations from each other.

The demanded v_d and v_q voltages are then transformed back into stator reference frame and used to generate a voltage space vector using the algorithm given in [45]. Fig. 5 shows the possible voltage vectors. In addition to the vectors shown there are two zero voltage vectors. The desired voltage space vector V_{ref} is then decomposed into three parts. This is illustrated in Fig. 6. Over the control interval Δ the inverter voltage vector V_1 is applied for a time σ_1 and voltage vector V_2 is applied for time σ_2. If there is any time left after the two voltage vectors have been applied a zero voltage vector is applied during the remaining time $(\Delta - \sigma_1 - \sigma_2)$. On average over the control interval Δ these voltage vectors will form the desired voltage vector

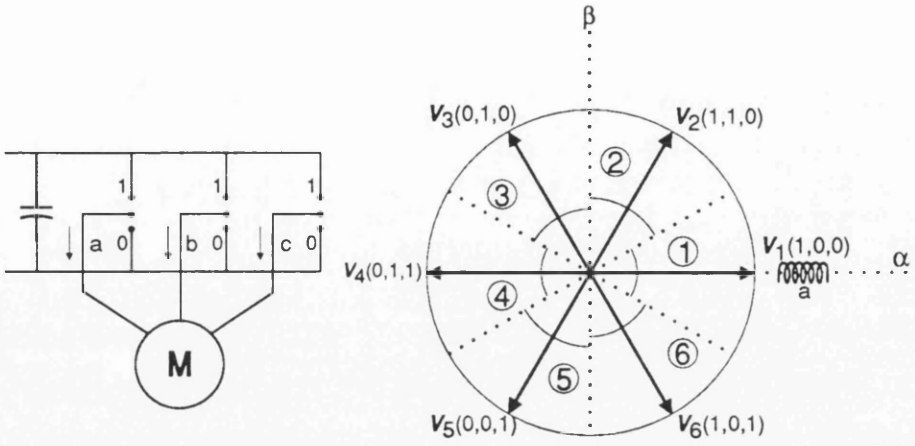

Figure 5: PWM inverter voltage vector positions

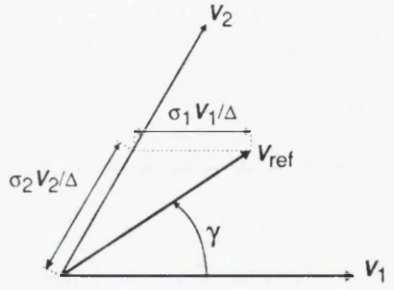

Figure 6: Voltage space vector PWM principle

V_{ref}. The duration of σ_1 and σ_2 can be calculated by:

$$\sigma_1 = \frac{2}{\sqrt{3}} \cdot \frac{|V_{ref}|}{\frac{2}{3}V_{DC-link}} \Delta \sin(60° - \gamma) \tag{42}$$

$$\sigma_2 = \frac{2}{\sqrt{3}} \cdot \frac{|V_{ref}|}{\frac{2}{3}V_{DC-link}} \Delta \sin(\gamma). \tag{43}$$

The voltage vector is then applied to the machine (or simulation). The absolute rotor position and stator phase currents (averaged over one control cycle) are measured. Using the measured rotor position the phase currents are transformed into the dq frame.

Based on the i_d current L_d is estimated using a lookup table. Electromagnetic torque is also estimated based on the estimated L_d and the measured i_d and i_q. However, it is not used in the control algorithms.

The rotor speed, ω, is calculated by taking the difference between the rotor position α in the current control interval and the previous control interval and then dividing by the control interval. To eliminate quantisation noise the output is

filtered using a digital first order "RC-filter" with a cutoff-frequency of 280 Hz. (In the original simulation the speed was estimated using an algorithm found in [46]. The algorithm in [46] relies on knowledge of the load parameters such as inertia and friction. However since the RLSE parameter estimator was too computational intensive for real time implementation this could obviously not be used.)

If the rotor speed exceeds the base speed then flux-weakening operation is used. Under flux-weakening the desired current angle is continuously updated according to equation (41).

The auto setting on the control type selects an automatic bump-free transfer between the CCIAC and MTC methods. CCIAC is selected for low speeds and low torques while MTC is used for higher speeds and torques. This maximises the rate of change of torque according to the load conditions [42]. The selection is done using a 3-dimensional lookup table of current magnitude, speed, and inductance ratio.

2.6 Implementation of a DSP based constant current angle controller

This section describes the hardware and software of the synchronous reluctance motor controller.

2.6.1 Hardware

The system consists of a power-electronics unit and a DSP-control unit. The power-electronics is designed for operation from a 415V 3-phase supply, and can handle an output power of 7.5kW. The power-electronics unit is capable of handling small amount of regeneration (100W continuously) into the inverter. This can be extended with an external resistive load.

The DSP-controller unit consists of a powerful Motorola DSP96002 operating at 33.33 MHz, advanced 12bit analog to digital converters (ADC), 12bit digital to analog converters (DAC) and a resolver to digital converter (RDC). The absolute

rotor position is measured using a resolver. Motor currents are measured using high-bandwidth flux-nulling current sensors. The DACs are used to output internal control variables for real-time monitoring.

The philosophy behind this controller was to create a general test facility that would enable tests of almost any sinusoidally excited machine without having to build machine specific hardware for each type of machine. To achieve this full digital control implemented in software is used, and has been taken to the extreme by having the processor directly control the phase leg switching times using voltage space vector PWM.

Full details of the power-electronics and the DSP-controller unit can be found in Appendix B.

The control and user interface is entirely done over an RS-232 serial link. The user can issue simple commands to control the operation of the motor and receive status information using a simple terminal. Several of the control parameters can be changed on-line through the terminal interface. If a computer is connected to the controller the computer can be used to automate complex command sequences.

2.6.2 Program Structure and Operation

The control program running on the DSP was written mainly in C, with a small part ($< 1\%$) in assembler. The program flow is shown in Fig. 7, this follows the conceptual control flow outlined in section 2.5 closely. Thus only particular points of interest will be covered in this section.

The program consists of an interrupt driven main control loop and a background processing loop, both written in C. The main control loop is executed every $576\mu s$ (the control interval). This gives a maximum switching frequency of 1.8 kHz.

Upon entering the main routine the first task is to setup the voltage PWM sequence. From section 2.5 it is known that the desired voltage vector is created by applying two of the 6 possible vectors for times σ_1 and σ_2. The PWM over one control interval is implemented in hardware. First the starting vector is applied to

the inverter, the times at which the second vector is to be applied and when the zero voltage vector is to applied is programmed into a hardware timer. The hardware timer will then perform the necessary switch of phaseleg states during the control interval without the DSP having to be involved (see also B.2.7).

The phase currents are then read from the ADCs and averaged. This uses a specific feature of the AD1332 ADC which allows it to store 32 or 16 samples before interrupting the processor. This interrupt was used to enter the main control interrupt routine. In this implementation the ADCs are set to interrupt when 16 samples have been acquired. The ADC sample rate is controlled by a programmable 16bit timer, and thus the control interval can be controlled by programming the timer. The sample frequency used is 27.7kHz, this gives a good estimate of the average current over the control interval. The phase currents are then transformed into dq-frame.

The transformation into dq-frame and back into stator-frame are done using Parks equations. These equations make extensive use of cos and sin functions. The C-library cos and sin functions had to be replaced with lookup tables as they were far too slow. The tables used are 1024 entry 180° ones and thus have a resolution of 0.18°. This is sufficient as the resolver is set to produce 10bit results i.e. a resolution of 0.35°.

The i_d and i_q currents are predicted forward so that an estimate for their value at the end of the current control interval is obtained. This is done so that the state feedback circuit which decouples the two current PI controllers by adding the rotational voltage terms to the desired v_d and v_q voltages experiences a minimum control delay. The prediction is done purely by looking at the rate of change of current in each axis and projecting this forward by one control interval.

The serial communication and command processing is split between the interrupt driven main control loop and the background processing loop. To ensure that loss of characters will not occur, the serial input register is polled for characters at each control interval. As the control interval is operating at 1.8kHz and the maximum character rate is about 960 characters per second it is obvious that the DSP will not

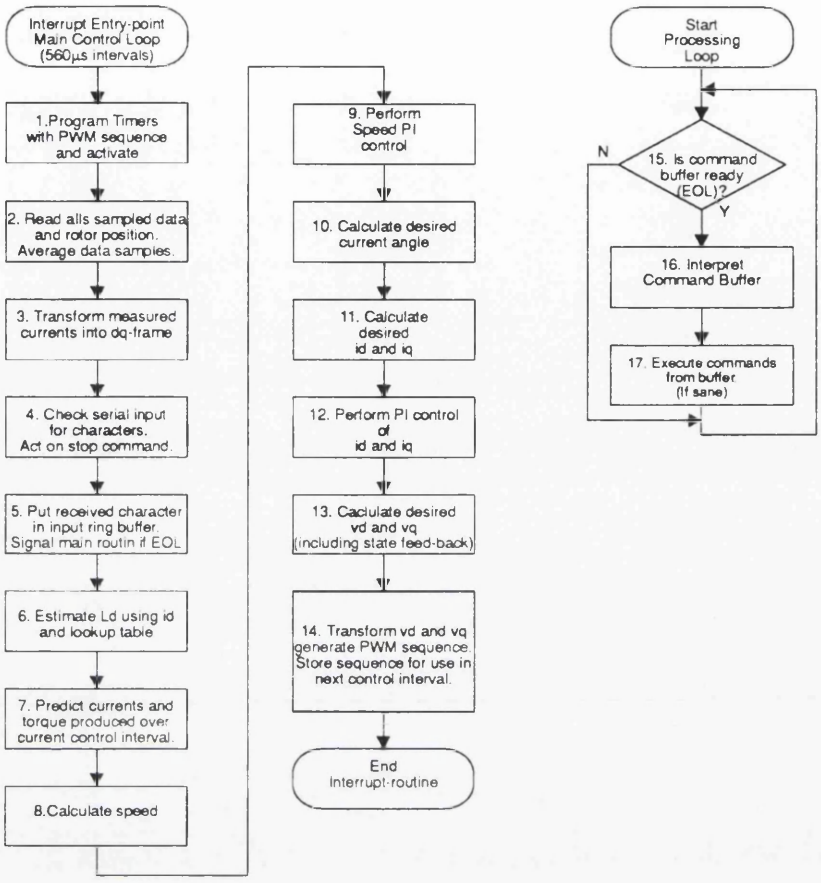

Figure 7: Constant current angle controller flow chart

lose any characters.

The interrupt routine will continuously look for a stop command character "S" in the input stream. This is the only command that is processed by the interrupt routine and can appear in the middle of any command stream. The action taken is to stop the motor. Other commands are line buffered and only processed by the background processing loop once a carriage return character is entered. The communication between the interrupt routine and the background routine is setup with a double buffer and a set of semaphores.

The main reason for not processing everything in the interrupt routine is that some of the commands are requests to print out information over the serial link. If this was done in the interrupt routine the process would halt while characters were printed over the serial link. This is obviously not desirable. When printing is done in the background processing routine it will not affect the control operation as it

only uses spare time in the control intervals to process the printing.

However, as both the interrupt and the background processing loops were written in C, and the compiler had a rather liberal use of registers which is insufficiently documented, all the registers had to be restored and saved when entering and leaving the interrupt procedure. This context switching takes about 45 instruction cycles (2.7μs).

2.6.3 Improvements

The main improvement needed in this controller is to increase the control frequency. Currently it is running at 1.8kHz which is too low for high speed flux-weakening operation. It is believed that the slow control frequency can be attributed to two main factors.

The first factor is the quality of the code produced by the Intermetrics C compiler. It is generally acknowledged that the C compiler can only realise about 10% of the DSP's potential. This can be compared to the C compiler for the AT&T DSP32C which realises about 50% of its potential. However, this might also be due to suitability of the different instruction sets and architectures of the two processors with respect to generating efficient C code.

The other factor is that as the program was written in a modular and software engineering sense correct fashion it contains a large amount of function calls. It appears that function calls are a particularly weak point of the compiler/processor. It should be possible to increase the speed of the program by simply removing all function calls and replacing them with in-line code.

Chapter 3

Constant Current Angle Control – Results

A simulation program was used to test the control algorithms developed by Betz [9, 10, 41, 42]. To verify the validity of these simulations they must be compared with experimental data. In this chapter experimental and simulation data are presented and compared.

Equally important, the experimental data creates an important set of benchmark results. The benchmarks are used to compare sensorless control implementations with controls operating with a position sensor.

3.1 Steady-state performance tests

The steady-state tests given in Figs. 8, 9, and 10 are used to illustrate the motor performance with respect to current angle.

In Fig. 8 it can be seen that instead of being sinusoidally shaped, the measured torque versus current angle is skewed towards the right. This skewing is caused by saturation of the most inductive axis inductance L_d. When the current angle, ε, is small more current is in the d-axis causing L_d to saturate. The saturation reduces the inductance. Thus the torque produced for a specific current magnitude becomes

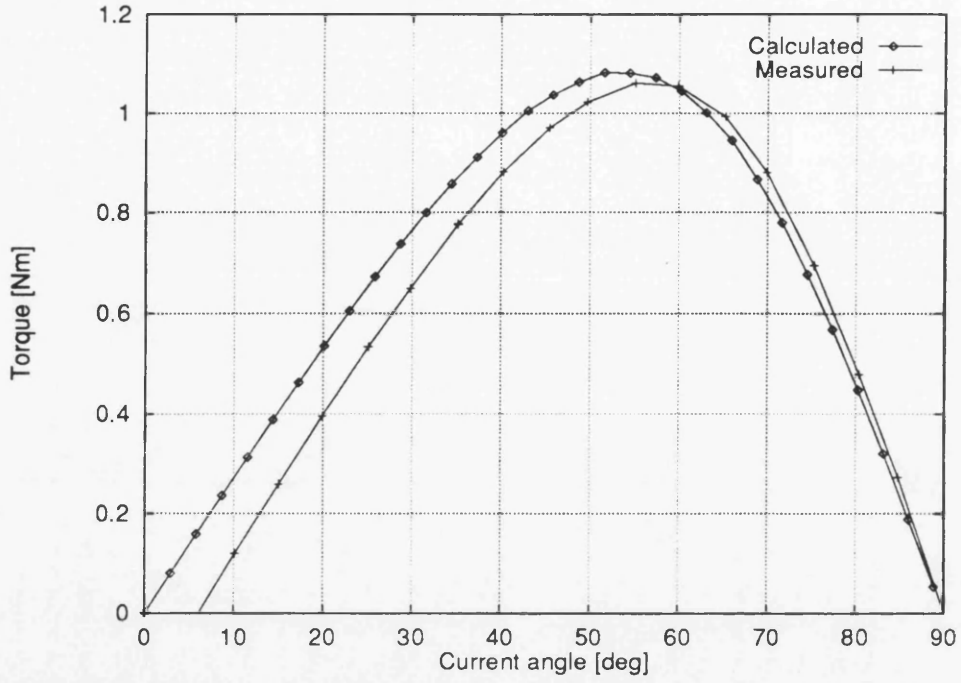

Figure 8: Torque vs. current angle ($I_{phase} = 1.7A_{rms}$) in 120W synchronous reluctance motor

lower. At high current angles the d-axis current becomes small and the inductance approaches its unsaturated value.

This means that maximum torque is not produced at 45° as expected for an ideal motor, but is achieved at a slightly higher current angle due to the saturation effects.

Notice that the torque curve goes to zero before the current angle reaches zero degrees. This is because the curve shows the load torque. The load torque is measured after the motor friction and windage losses has occurred.

Fig. 9 shows the fundamental power factor ($\cos\varphi$) of the motor. The apparent power factor (W/VA) is not very useful for comparisons with theory because the voltage is essentially a square-wave when the motor is operated from an inverter. The steady-state theory does not account for square-wave voltages. Theory predicts that the maximum fundamental power factor will occur when the current angle is $\varepsilon = \tan^{-1}\sqrt{\frac{L_d}{L_q}}$. Using unsaturated inductance values ε becomes 70°. From the graph the maximum fundamental power factor occurs at 75°. It can thus be said to be good correlation between the theory and the experimental data. The calculated

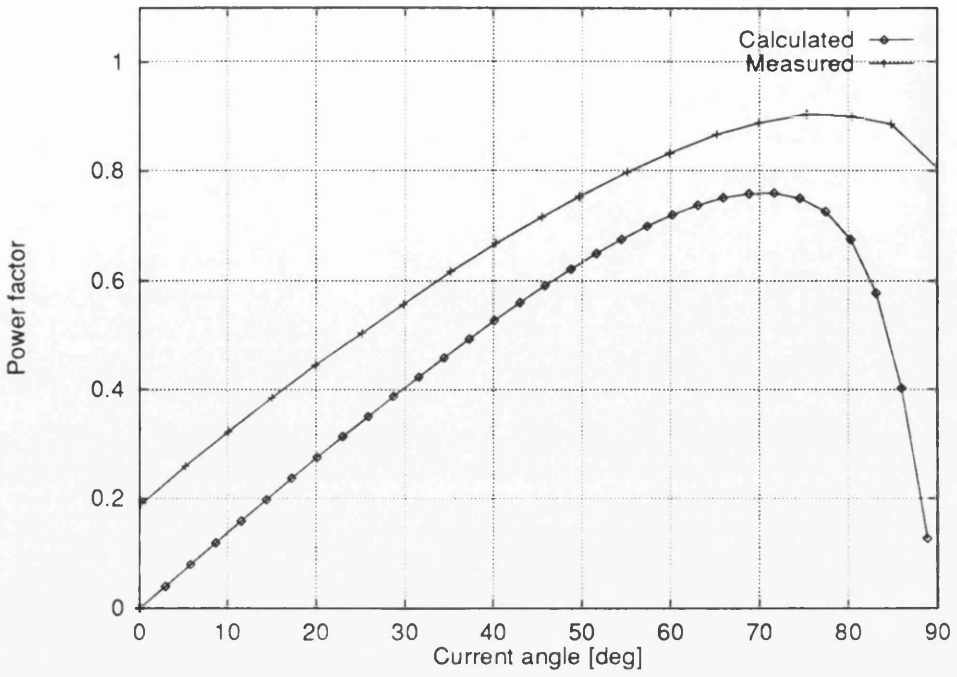

Figure 9: Fundamental power-factor ($\cos\varphi$) vs. current angle ($I_{phase} = 1.7$ A_{rms}) in 120W synchronous reluctance motor

power factor is lower than the measured power factor because resistance is not taken into account when calculating the power factor.

The efficiency curve in Fig. 10 shows that the maximum efficiency of the motor occurs at about the same point as the maximum torque. This is as expected since the 120W motor has a relative large per unit resistance. The per unit resistance goes down for larger drives (eg. above 5kW), and in that case the shape of the efficiency curve will change. The calculated efficiency is higher than the measured because it only takes resistive losses into account. It is also important to note that the efficiency curve is quite flat around its maximum efficiency point and could be varied $\pm 15°$ without much variation in the efficiency. For comparison the maximum efficiency of the synchronous reluctance motor was measured to be 68%. This compares well with the induction motor (using the same stator) which has an efficiency of 61%. This may again be particular to the small motor size used.

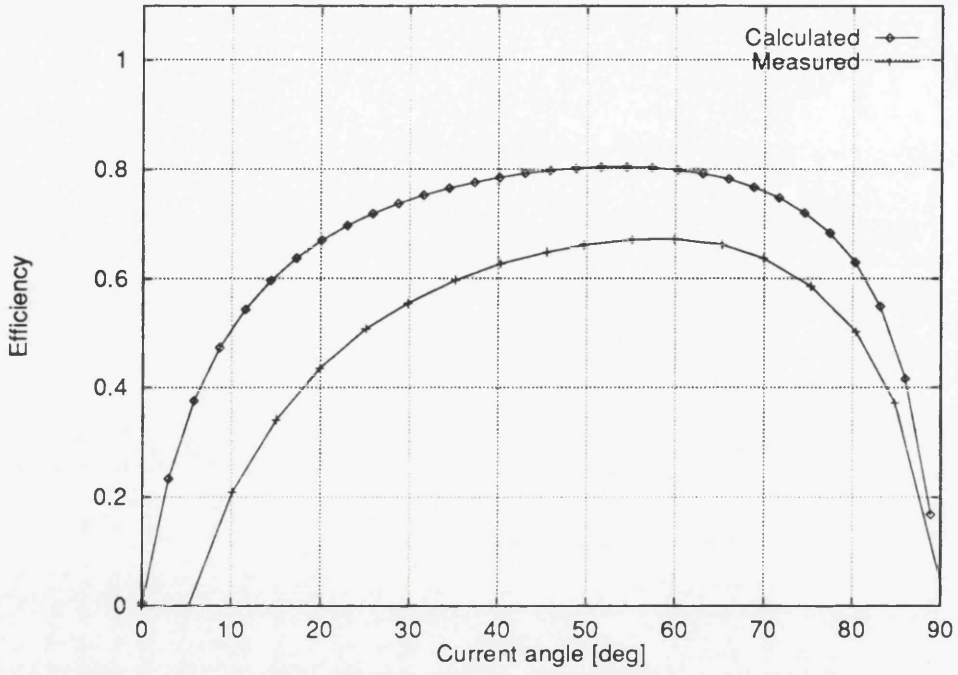

Figure 10: Efficiency vs. current angle (I_{phase} = 1.7 A_{rms}) in 120W synchronous reluctance motor

3.2 Dynamic performance test

The dynamic tests which consist of speed reversals and step-load changes are used to verify that the simulations are valid. The experimental data also sets a benchmark for the sensorless control method used in Part II.

The motor used in these tests is essentially the same as the one used in the other tests except that it has a 415V stator whereas the other tests use a motor with a 115V stator. A conversion factor of 3.6 is thus needed to convert between the two (for current and voltage). The system parameters used were:

Motor:

L_d	=	2.6H(unsat)
		1.7H(sat)
L_q	=	390mH
R_{phase}, R	=	98Ω
Pole-pairs, p	=	2
$V_{\text{phase}_{\text{rated}}}$	=	240Vrms(Y)

$I_{\text{phase}_{\text{rated}}}$ = 0.47Arms

$\omega_{m_{base}}$ = 1500rpm

T_{rated} = 0.95 Nm

Load data (motor and load):

Inertia = 0.00044 kgm^2

Friction coefficient = 0.00015 Nm-s/rad

Inverter & control data:

$V_{DC-link}$ = 600V

T_{control} = 576μs

Maximum inverter switching frequency = 1.8kHz

3.2.1 Simulation results

Figures 11, 12, 13, and 14 shows the motor's response to a change of speed reference between ±1400rpm. The operating mode being used is maximum torque per ampere control (MTC). The machine moves between these two speeds in about 150ms with very little overshoot, and accurately follows the demanded speed in steady-state. Notice also the the close correlation between demanded and actual torque.

Figures 15 and 16 shows the response to a step-load change in torque from 0% to 90% of rated torque applied at 0.5s and removed at 1.25s. The control method used here is CCIAC, whose main difference from the other control methods is that the current in the d-axis is kept constant. As can be seen the speed dips by a small amount when the load is applied. Figure 16 shows the increase in shaft torque as the load is being applied. Notice also the fast rise time of the torque.

3.2.2 Experimental results

These results was obtained using the control system described in 2.6. The load machine was a permanent magnet servo motor controlled by an Electrocraft BRU

controller. The data was sampled at 1MHz using a 12bit Nicolet data acquisition system. The sampled data set was reduced before plotting by averaging 100 sample points for each point plotted. This reduces the sample frequency to 10kHz which is more than sufficient when considering that the control frequency is 1.8kHz.

Figures 17, 18, 19, and 20 show the experimental results using a maximum torque per ampere control (MTC) strategy doing speed reversal from -1400rpm to +1400rpm. The speed reversal is done in about 100-150ms, and there is negligible overshoot. As can be seen these results agree well with the simulation results in Figs. 11-14.

The ripple in the d-axis and q-axis currents is caused by the current demand from the speed controller. The magnitude of the ripple is inversely proportional to the inverter switching frequency. It is also worth noticing that the q-axis current has a larger amount of current ripple around the nominal desired value compared to the d-axis current. This is because the q-axis inductance is considerably lower than the d-axis inductance.

Other control methods such as MPFC and MRCTC did little to influence the operation except that the speed reversal times were increased due to less available torque. It was difficult to notice any difference in the rate of change of torque of the different methods. To be able to take advantage of the higher torque bandwidth of MRCTC it would obviously be necessary to increase the bandwidth of speed control loop.

Figures 21 and 22 show the performance of the system using constant current in the most inductive axis control (CCIAC) when applying a step-load from 0% to 90% of the rated torque of the motor. The dip in speed is due to the limited bandwidth and delays in the speed control loop. To really take advantage of the synchronous reluctance machine a much higher speed control bandwidth must be used. In the current system the speed control loop bandwidth is limited by the 1.8kHz switching frequency. The experimental data obtained agreed with the simulations.

3.3 Summary

- A DSP based drive system for the synchronous reluctance motor (SYNCHREL) has been built. It has been shown that this system can be used to facilitate rapid testing of new control methods. The increased development speed is obtained by the use of source code (with minimal modifications) from simulations in the real-time control system.

- Control strategies [9] for the SYNCHREL have been verified and shown to agree well with the experiments.

- The system has shown good dynamic performance without any stability problems.

- The field weakening capability has not been tested fully as the d-q frame movement with the present control interval gets too large at high speeds. If this was to be tested the control code would have to undergo considerable modification: in particular, function calls must be removed. A more powerful DSP may also be used for this.

In conclusion the main goals of Part I have been achieved: a test facility for new control algorithms has been made, simulations and control algorithms have been verified, and benchmark data for operation with a rotor position sensor has been obtained.

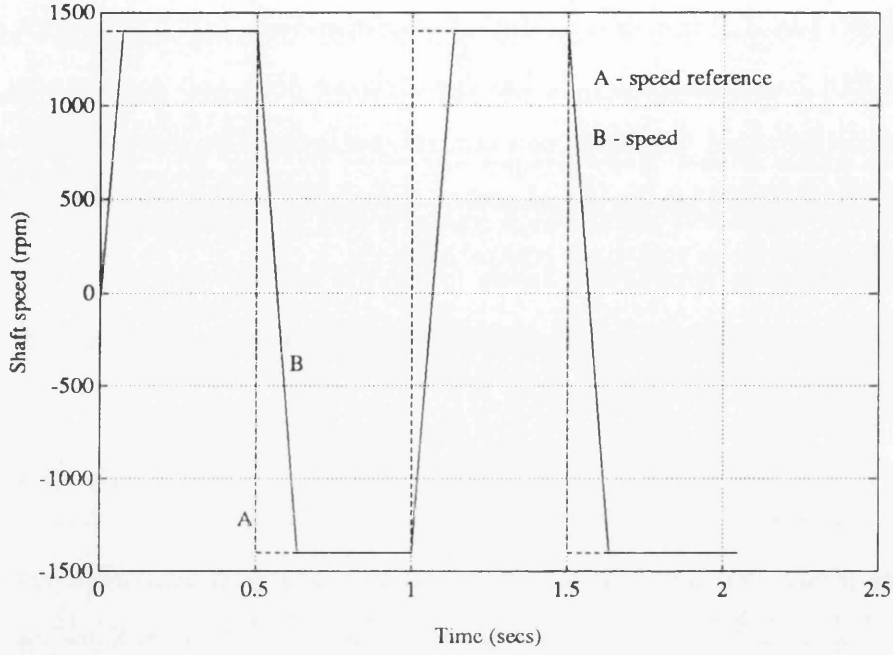

Figure 11: Simulated speed reversal ±1400rpm, speed.

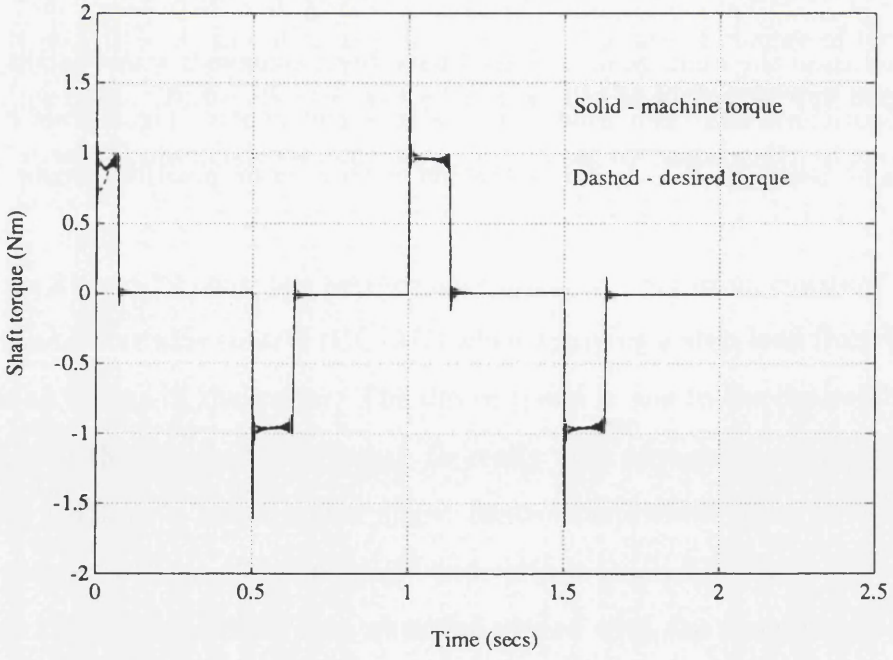

Figure 12: Simulated speed reversal ±1400rpm, torque.

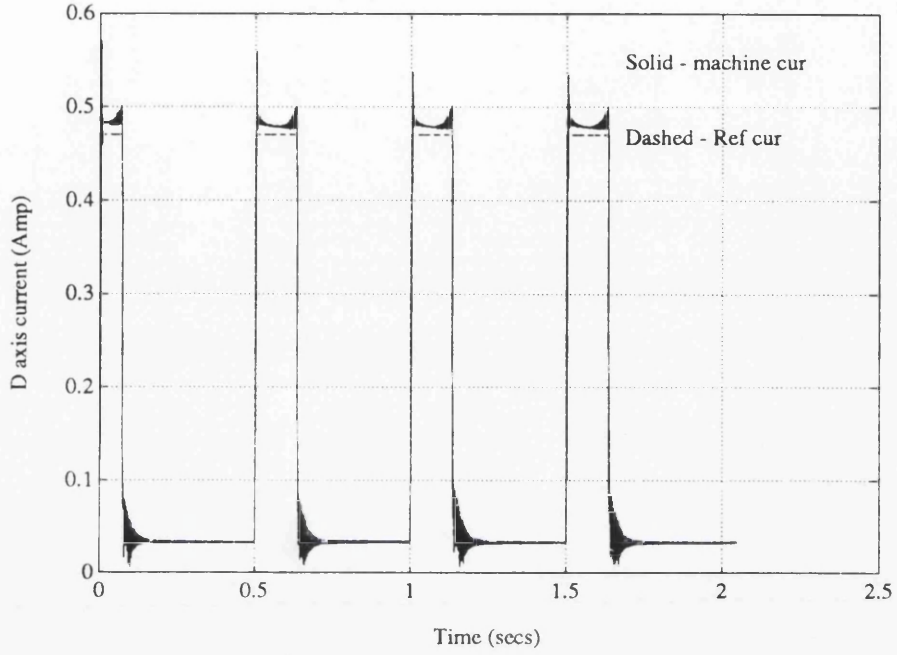

Figure 13: Simulated speed reversal ±1400rpm, d-axis current.

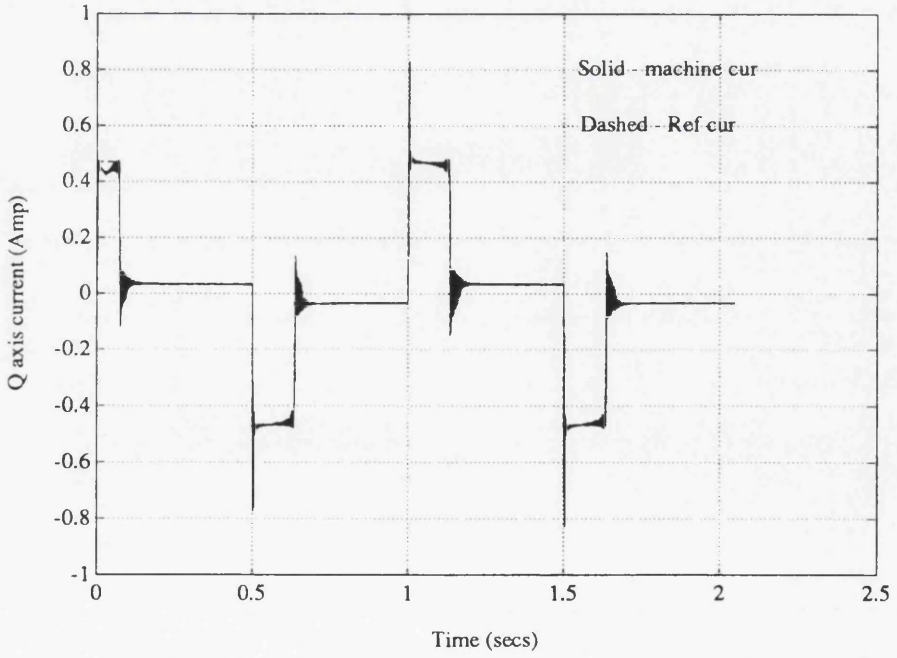

Figure 14: Simulated speed reversal ±1400rpm, q-axis current.

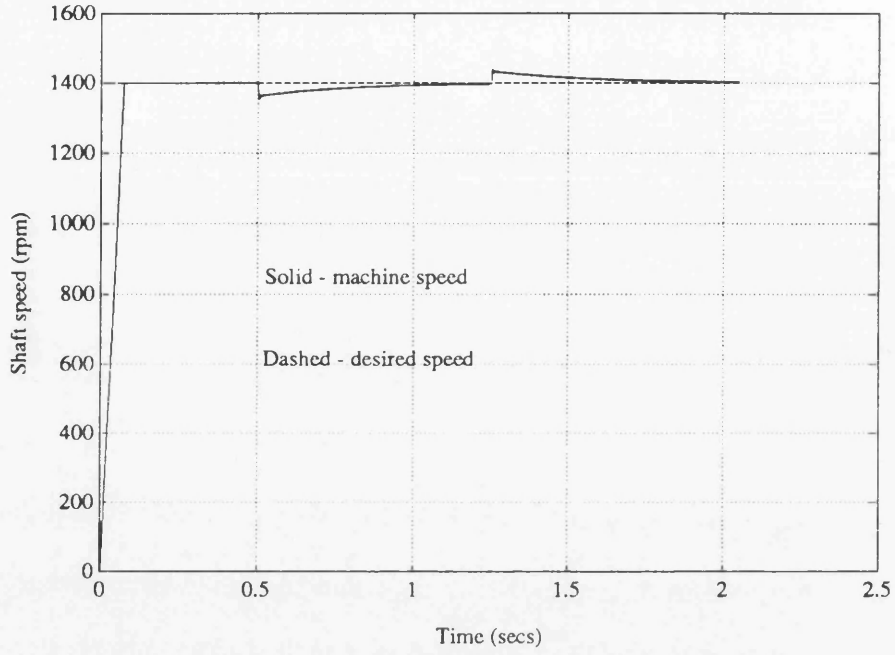

Figure 15: Simulated step-load change (0 - 0.84Nm), speed.

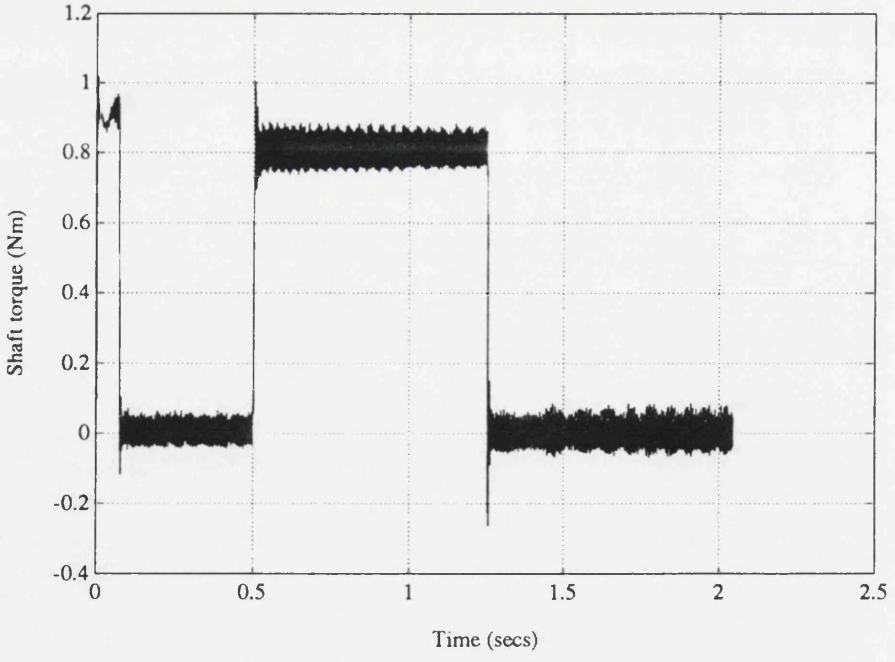

Figure 16: Simulated step-load change (0 - 0.84Nm), torque.

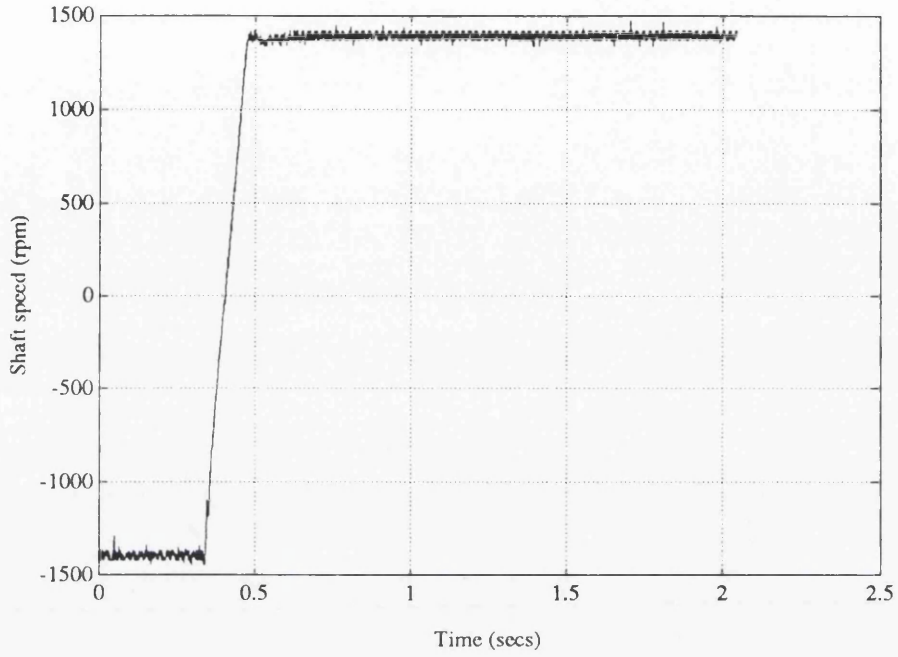

Figure 17: Experimental speed reversal $\mp$1400rpm, speed.

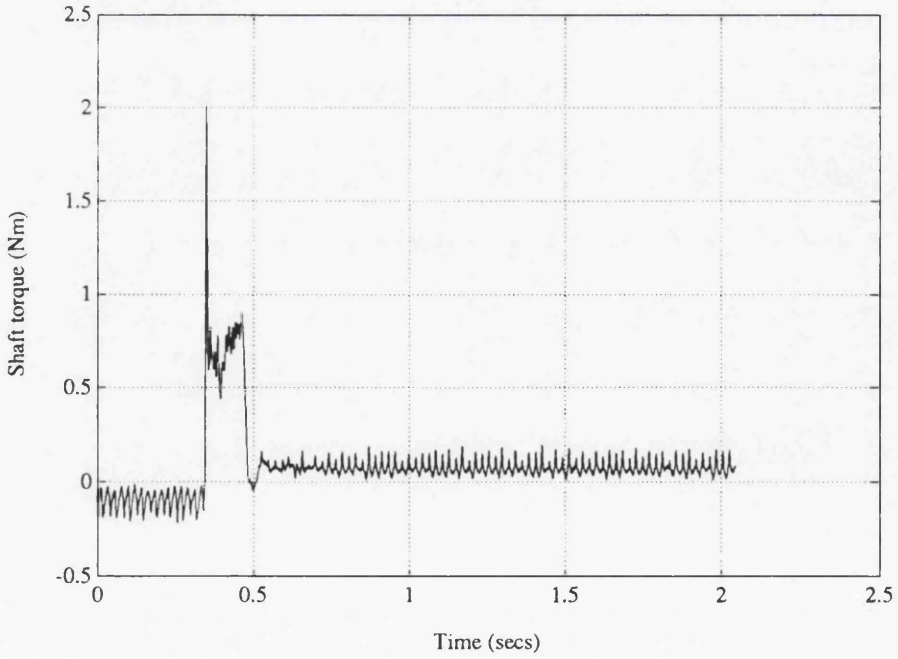

Figure 18: Experimental speed reversal $\mp$1400rpm, torque.

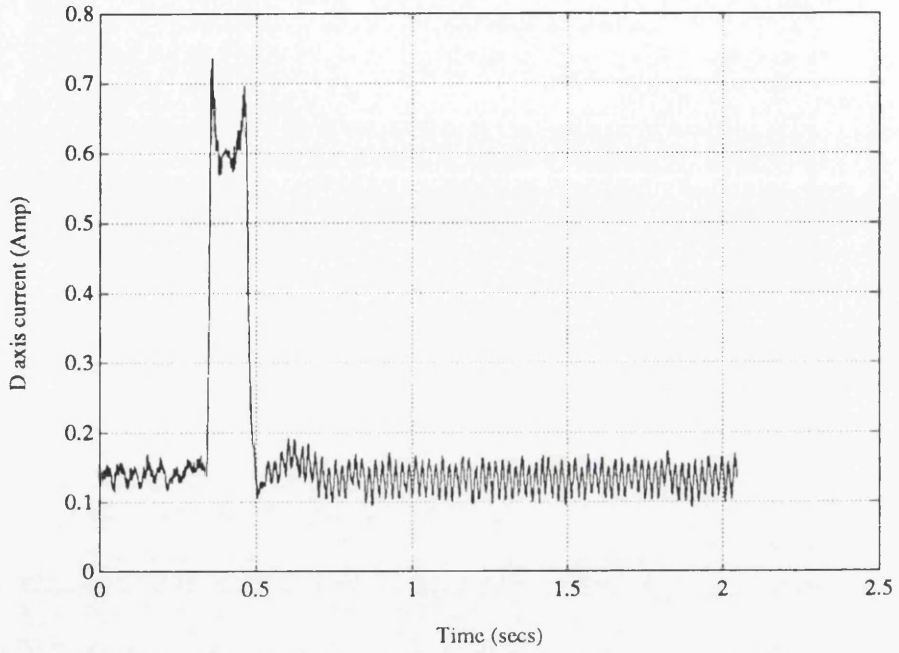

Figure 19: Experimental speed reversal $\mp$1400rpm, d-axis current.

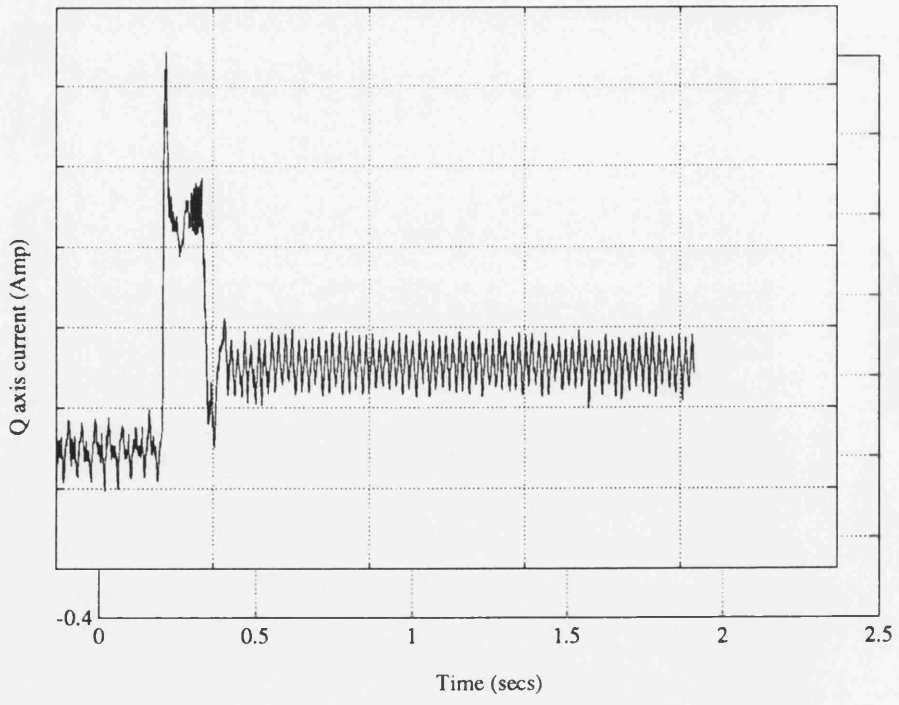

Figure 20: Experimental speed reversal $\mp$1400rpm, q-axis current.

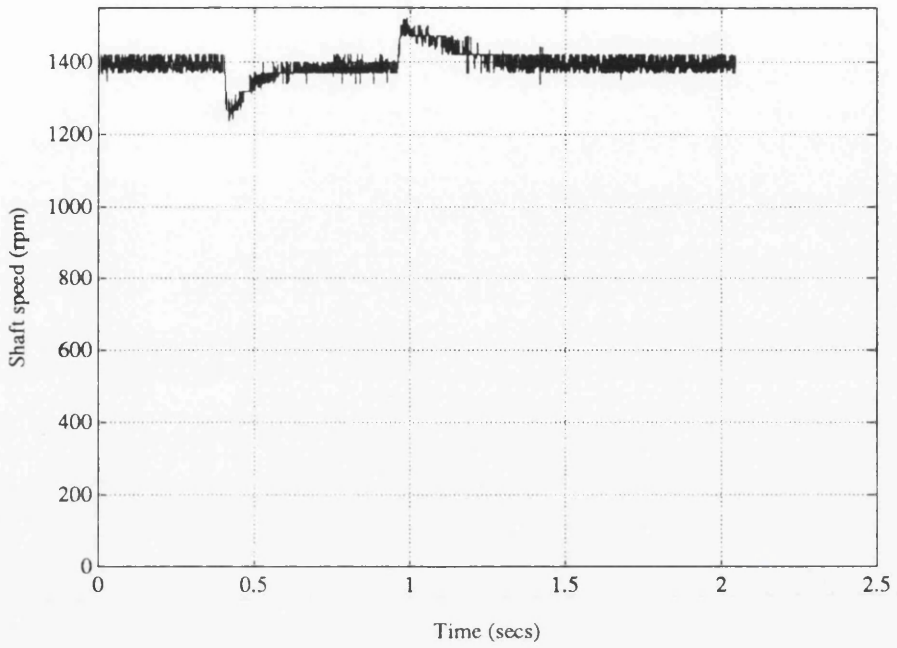

Figure 21: Experimental step-load change (0 - 0.84Nm), speed.

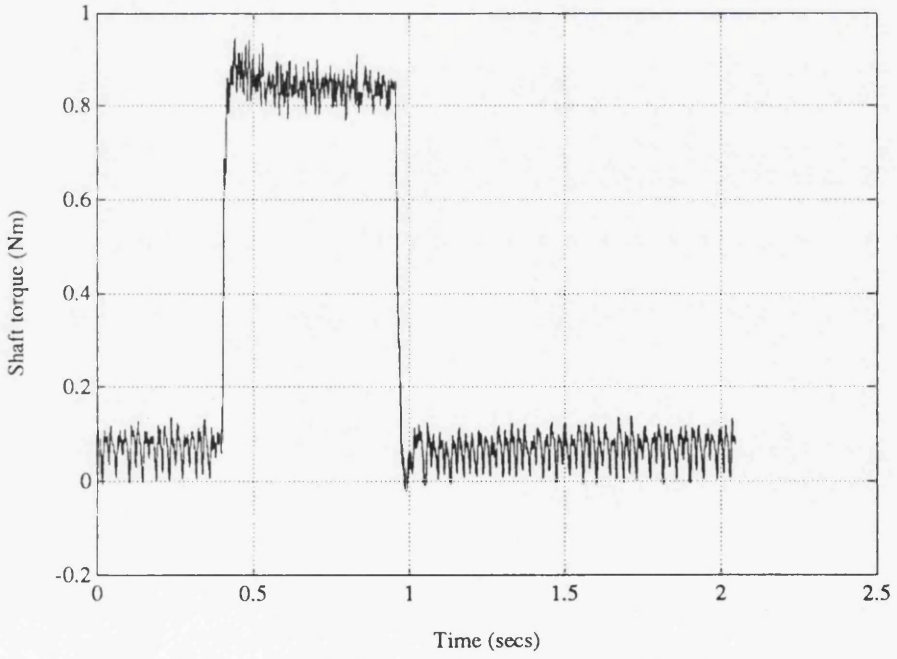

Figure 22: Experimental step-load change (0 - 0.84Nm), torque.

Part II

Sensorless Control of the Synchronous Reluctance Motor

Chapter 4

Survey of sensorless operation for reluctance and PM drives

This chapter reviews possible methods for sensorless operation of the synchronous reluctance motor. There has been a definite lack of articles on this specific subject. Only three articles [6, 7, 8] proposing sensorless control methods specifically for the sensorless control of the synchronous reluctance motor have been identified.

On the general subject of sensorless control there has been quite a lot of activity, particularly in the areas of *switched* reluctance, stepping motors, brushless-DC and synchronous PM.

4.1 Sensorless operation in *stepping* and *switched* reluctance motors

The *switched* reluctance motor differs from the *synchronous* reluctance motor in that it has saliency on both rotor and stator. The *switched* reluctance motor also uses pulsed currents instead of sinusoidal currents. The detection methods used are thus only intended to detect the positions when to commutate. There is therefore no need for a continuous position estimate in the *switched* reluctance motor. The majority of methods used for sensorless control of the *switched* reluctance motor

rely on the pulsed nature of the drive current. As the *synchronous* reluctance motor uses sinusoidal currents these methods are not applicable or would become very complicated.

Frus and Kuo [47] presented a method for operating step motors without position feedback in 1976. It is indicated that the the detection method uses some feature of the current waveform and may be specific to the motor used. However, no details of the detection method used are given. Kuo and Cassat [48] presented a further development on this in 1977. Kuo concludes that only features in the current that occur after the phase is switched off can be used. Two points in the waveform are identified that can be used for commutation. A similar scheme was also proposed by Bakhuizen in 1979 [49].

In a 1985 patent a scheme for sensorless commutation of stepping motors was proposed by Hill and Acarnley [3]. The commutation is based on driving circuits with a hysteresis controlled current. The switching frequency of the hysteresis controller depends on the inductance of the phase. As the phase inductance is position dependent the switching frequency will also vary with rotor position. As a certain frequency is reached the motor is commutated. The main problem with this method is that the current level in the phase causes saturation and this changes the inductance. Another problem is that at high speeds the motional emf will become significant and this introduces a further change in the switching frequency. At very high speeds there may even not be enough voltage to cause the necessary chopping.

Panda and Amaratunga [4] also proposed a similar scheme to Hill's. However, the motional emf effects are also compensated for, to allow operation at higher speeds.

In [50] MacMinn proposes a scheme for commutating the *switched* reluctance motor. The scheme uses impedance sensing by probing un-excited phases of the motor. The un-excited phase is applied a short voltage pulse of fixed duration. As the current in the phase when applying the voltage is zero the current level at the end of the interval will depend on the inductance in the phase. The inductance in the phase varies with position hence the position can be determined. The phase

inductance variation is however not completely sinusoidal, but exhibits a flattening at the unaligned position. However, the area where detection is needed is outside the flat area. The commutation is simply done by comparing the current at the end of the probe pulse with a set level and if the measurement is largest then the motor would be commutated.

The method of probing un-excited phases in the *switched* reluctance motor was explored more rigorously by Harris and Lang in [51]. Secondary effects that can affect position sensing are examined. The examined effects include: eddy currents in motor laminations, inverter switching noise, magnetic coupling between motor phases, and quantization introduced by digital implementations. Solutions to the secondary effects included limiting the probing to times when there was minimum coupling between excited and probing phases. Eddy currents were addressed by allowing them to decay and then take a two point measurement to get the current rise time. Harris reports a commutation accuracy of $\pm 1\%$ of an electrical cycle throughout the speed range.

A method for commutating the *switched* reluctance motor based on flux-linkage measurements was proposed by Hedlund and Lundberg [52]. The proposed scheme is based on flux-linkage measurements in the excited phases. Using the fact that the flux-linkage can be obtained as $Li = \int (v - Ri)dt$, the time at which a predetermined level of flux-linkage is reached in the motor is measured. The time delay from the sensed time point to when the commutation should occur is then calculated. A problem with this method is both the current level in the phase and the motor speed must be taken into account when calculating the time delay.

A simple option to improve stability and efficiency of the *switched* reluctance motor was proposed by Bass, Ehsani, and Miller [53]. The efficiency of the *switched* reluctance motor generally improves with smaller dwell angles. However, if the dwell angle is too small the motor can not produce enough torque and will lose synchronism. The method proposed by Bass is essentially an open-loop system that modulates the dwell angle so that good efficiency is achieved at the same time as the motor remains in synchronism for variable loads. The dwell angle is modulated as a

function of the DC-link current. Increasing DC-link current indicates a larger load and the dwell angle is increased to ensure that the motor does not pull-out. The actual commutation in this scheme is done open-loop without any position feedback.

4.2 Sensorless operation of permanent magnet motors

The permanent magnet motor shares many features with the synchronous *reluctance* motor. In particular the sinusoidally excited synchronous PM motor is very similar to the synchronous *reluctance* motor. Because of the similarity, sensorless methods for the PM motor will be reviewed in light of their suitability for application to the synchronous reluctance motor. The main difference between a synchronous PM and a synchronous reluctance motor is the production of the main torque producing flux. In the PM motor this flux is produced by the permanent magnets and is not much influenced by the stator currents. In a synchronous reluctance motor there are no magnets to produce the flux and hence it must be produced by passing current through the stator windings.

Wu and Slemon [5] used the flux produced by the magnets in the PM motor to achieve sensorless control. The flux-linkage in a brushless PM motor is mainly produced by the magnets on the rotor and is thus fixed in position to relative to the rotor. The flux-linkage was obtained by analog integration of $(v - Ri)$. Having obtained the position of the flux-linkage vector the current vector is applied at 90° using a hysteresis current controller. There are two problems with this scheme. The first problem is that at low speeds the voltage across the phase resistance becomes dominant and thus limits low speed operation. The lowest operating frequency obtained by Wu was 1.0Hz. The other problem is offsets in the flux-linkage measurements. However, the offset can easily be corrected in the PM motor by monitoring the circle describing the estimated flux-linkage. If there is an offset the centre of the circle will be offset and the offsets can thus be easily compensated for. This offset compensation is only feasible since the flux-linkage is only marginally affected by current

flowing in the stator. This method of sensorless control is not applicable to the synchronous reluctance motor because the flux-linkage vector position in the synchronous reluctance motor is not fixed in relation to the rotor. In the synchronous reluctance motor the flux-linkage vector position depends on the applied current.

A method based on the back-emf and/or third-harmonic voltage was proposed by Jufer and Ossani [54] for the square wave drive PM synchronous motor (brushless-DC and stepping motor). This method again depends on having a strong field produced by permanent magnets. Jufer shows various ways of determining the back-emf. The best method to determine the back-emf appears to be to use a micro transformer to obtain the current derivative. Alternatively the integral of the back-emf can be used instead. The reason for using these methods is that the estimated back-emf signal is much cleaner, in particular when used with a chopper type supply. Using the zero crossings of the back-emf the motor can be commutated at 180° intervals. Using the third harmonic voltage in the neutral point of the motor in conjunction with the back-emf, the motor can be commutated using 120° pulses. Again there is a lower speed limit to this type of drive. This method is not really applicable to the synchronous reluctance motor as it uses the fixed flux-linkage field created by the permanent magnets to effect the commutation. This method also assumes that the phase inductance does not vary with position. In the synchronous reluctance motor there are large inductance variations with rotor position.

In [55, 56] Acarnley and Ertugrul propose a method for sensorless control of the permanent magnet motor that is based on flux-linkage and line-current estimation. The control using 120° conduction and sinusoidal currents is demonstrated. The algorithm has a two current-loop structure, with an outer loop used to correct position and an inner loop used to correct the estimated flux-linkage. The position is estimated forward using polynomial curve fitting. At the next control interval the position is corrected based on the difference between the estimated phase currents (from flux-linkage estimate) and the measured phase currents. The inner loop uses the predicted rotor position to transform the estimated flux-linkage into current that is compared with measured currents. This is used to correct the flux-linkage

estimate. Position independent phase inductance is assumed. The system has only been verified using off-line calculations. The off-line data appear to give good position estimates. However, there appears to be a delay between the estimated and actual rotor position; this could cause problems when the estimated position is used to control the inverter. It is claimed that the method should also work for reluctance motors. It is possible that it may work, but the position varying inductance introduces a further unknown variable. Further the flux-linkage vector is no longer fixed with respect to the rotor position.

A method for sensorless control of a direct drive servo motor (low speed PM) was proposed by Katsushima [57]. This method uses uses the fact that a PM synchronous motor has a salient pole characteristic whether it is of the salient pole or cylindrical type. This characterisation is caused by permeance variation in the stator due to saturation caused by the permanent magnet field. As this method is based on the position dependent variation in phase inductance it is immediately clear that it might be suitable for application to the synchronous *reluctance* motor. The method determines the position of the rotor by using two coordinate systems located at 90° to each other. Assuming that the rotor is aligned two each coordinate systems the expected voltages are calculated based on the current measured (using the normal dq-frame equations). The ratio of the difference obtained with measured and calculated voltages for the two coordinate systems gives the absolute rotor position. The experimentally obtained rotor position shows good correspondence with the actual rotor position. A method for determining the direction of the rotor (magnet) at standstill is also presented. The obvious flaw in this detection method, if applied to a synchronous reluctance motor, is that it relies on the motor parameters. In a synchronous *reluctance* motor the most inductive axis inductance depends strongly on the current in the axis. This dependency might cause problems unless a control strategy such as CCIAC is used. CCIAC keeps the current in the d-axis constant. However, instabilities might still occur.

4.3 Sensorless operation of synchronous reluctance motors

The first method for sensorless control of the synchronous reluctance motor was proposed by El-Antably and Zubeck in 1985 [6]. They also proposed to operate with current angles outside the ±45° static stability region. This would give the highest efficiency as it is obtained with current angles larger than 45°. A shaft position sensor (resolver) was used to dynamically stabilize the operation. An equivalent circuit of the reluctance motor [16] that includes stator resistance, leakage reactance, iron, friction and windage losses, and position varying resistance and reactance was used. The power being dissipated in the position varying resistance can be obtained by subtracting the power being dissipated in the stator resistance and the equivalent phase resistance from the average power going into the motor. If the rotor speed and a motor constant K_2 [16] are known then the current angle can be calculated. The problems with method are that it uses an equivalent steady-state model and the average power. This means that the currents and voltages must be filtered to obtain the fundamental currents and voltages. This filtering causes a considerable delay, and can cause stability problems. Further the estimation of the various losses in the motor and the motor constant K_2 can be difficult. It appears that this method of sensorless operation was never implemented.

Bolognani [7] proposed a similar sensorless control scheme which also detects and controls the current angle. Bolognani's method would appear to be easier to implement than El-Antably's. Bolognani's method relies on the measurement of $v\cos\varphi$ and $v\sin\varphi$. Claiming slow motor dynamics Bolognani simplifies his equations by ignoring all terms containing di_d/dt or di_q/dt. In the steady-state this is of course valid. However, any change in torque, error in position estimate, or switching ripple may cause an inaccurate estimate, and eventually this may lead to instability. The equations also require knowledge of the rotor speed. Again this depends on the accuracy of previous estimates. Saturation effects on L_d will probably not be a problem as Bolognani operates using constant current in the most inductive axis

control (CCIAC). Bolognani shows some experimental results that use open-loop off-line data processing. The method appears to give a reasonable estimate. However, as it is not used in the control of the motor any instability due to feedback would not be shown in these results. A further problem is that to obtain the fundamental $v\cos\varphi$ and $v\sin\varphi$ filtering must be used. The filtering will introduce a phase lag which also may cause instability in the system. Further work on the actual implementation of this method appears not to have been published, if indeed any has been done.

Boldea, Fu, and Nasar [8] proposed a method for fast closed-loop torque control in 1991 of the synchronous reluctance motor. The mode of operation has been termed Torque Vector Control (TVC). A sensorless implementation of torque vector control was also proposed at the same time. The method is based on operation with constant flux-linkage magnitude. To achieve synchronism, the torque and flux-magnitude are controlled such that the flux-linkage angle never exceeds the stable $\pm 45°$ operating area. It should be noted that the maximum efficiency flux-linkage angle is around 12° for a motor with a saliency ratio of 6. Hence maximum efficiency is obtained at an intrinsically stable operating point. This is in contrast to current angle control methods where the maximum efficiency is at an intrinsically unstable operating point. The flux-linkage is proposed to be estimated by integrating $(v - Ri)$. The flux-linkage and torque are calculated instantaneously. The current position of the flux-linkage vector is determined to be in one of 6 sectors. Depending on which sector the flux-linkage vector is in, there exist 4 voltage vectors that can be applied to change current or flux-linkage magnitude. It is important to note that this method does not make any assumptions of steady-state operation. It does not make use of any motor equations either. The only machine parameter that needs to be known is the stator resistance. The limitation of this method is that at low speeds the voltage across the resistance becomes dominant. If the resistance is not known accurately (it varies with temperature) it may cause the flux-linkage estimate to be incorrect. If an incorrect flux-linkage position is used synchronism could be lost. Boldea presented some simulation results for operation of Torque Vector Control with a position sensor. These simulations showed fast dynamic response. However,

the simulation results presented had currents more than 10 times the rated motor current in them (in q-axis). No experimental results were published by Boldea.

4.4 Selection of method for implementation of sensorless control

The methods that have been presented in this chapter were considered for implementation of sensorless control for the synchronous reluctance motor.

The methods has been evaluated using the following criteria:

- Suitability for operation with synchronous reluctance motor.
- Minimum risk of loss of synchronism.
- Minimum phase-lag in control loop responsible for synchronism.
- Allow motor to operate efficiently.
- Intrinsic stability.
- Depend on as few motor parameters as possible.
- Method should require as little computing power as possible.

The methods obviously unsuitable for implementation of sensorless control for a synchronous reluctance motor include: all methods described for stepping motors, *switched* reluctance motor, and methods relying on back-emf.

The method proposed by Acarnley and Ertugrul [55, 56] is not suitable as it assumes a non-salient rotor. It is claimed that method can be extended to cover salient-pole machines. The extensions would probably make the method very complex and time consuming.

The method proposed by Katsushima for a PM motor is not suitable for the synchronous reluctance motor due to its strong dependence on motor parameters.

The problem with the method proposed by El-Antably [6] and the method proposed by Bolognani [7] is that they both rely on measurement of fundamental quantities. The fundamental quantities combined with most of the motor parameters are used to calculate the current-angle. The problem is that low-pass filtering is used to obtain the fundamental quantities. The filtering will introduce a delay which may cause instabilities a closed-loop system. Furthermore, the maximum efficiency occurs with current-angles larger than 45°. Thus the system must operate in an intrinsically unstable region to obtain maximum efficiency. The effects of operating in an unstable region may further amplify the possibility of instability due to delays in the control. Bolognani's proposed method is further compromised by ignoring di_d/dt and di_q/dt.

The torque vector control method proposed by Boldea [8] provides closed loop torque control without knowledge of any motor parameter except for the phase resistance. Accurate knowledge of the phase resistance is only important when operating at low speeds. The method operates with flux-linkages and so it is not sensitive to saturation effects. The phase-lag is kept to a minimum since torque vector control operates with instantaneous quantities and hence no filtering is needed. The maximum efficiency occurs with flux-linkage angles smaller than 45°. Hence torque vector control can operates in an intrinsically stable operating area with maximum efficiency. The method can be implemented without the need of microprocessors. Torque vector control provides quick torque response because all the change of current occurs in the least inductive axis.

The limitation of torque vector control is that it does not operate well at very low speeds (without accurate knowledge of phase resistance), and that the maximum efficiency is only obtained at rated torque. However, maximum efficiency can be obtained for any operating point by adjusting the flux-linkage magnitude. Some dynamic response is lost when optimizing for efficiency.

Even with these limitations, torque vector control appears to be the control method that satisfies the most of the criteria listed above. It was thus decided to use torque vector control as the basis for implementing sensorless control for the

synchronous reluctance motor.

Chapter 5

Theory of Torque Vector Control of the Synchronous Reluctance Motor

5.1 Introduction

This chapter presents the torque vector control theory originally developed by Boldea [8]. The most attractive feature of torque vector control is that it can be used for *sensorless* closed-loop torque control. The theoretical analysis of torque vector control has been extended in this thesis with respect to rate of change of torque, currents, efficiency, flux-linkage ripple, and flux-weakening control.

5.2 Torque Vector Control Principle & Motor Equations

The theory of torque vector control (TVC) was first described by Boldea in [58]. Torque vector control uses closed-loop control of torque, flux-linkage magnitude and position to achieve synchronism of the rotor and the flux-linkage vector. Neglecting iron losses the equations for torque vector control can be written, in stator reference

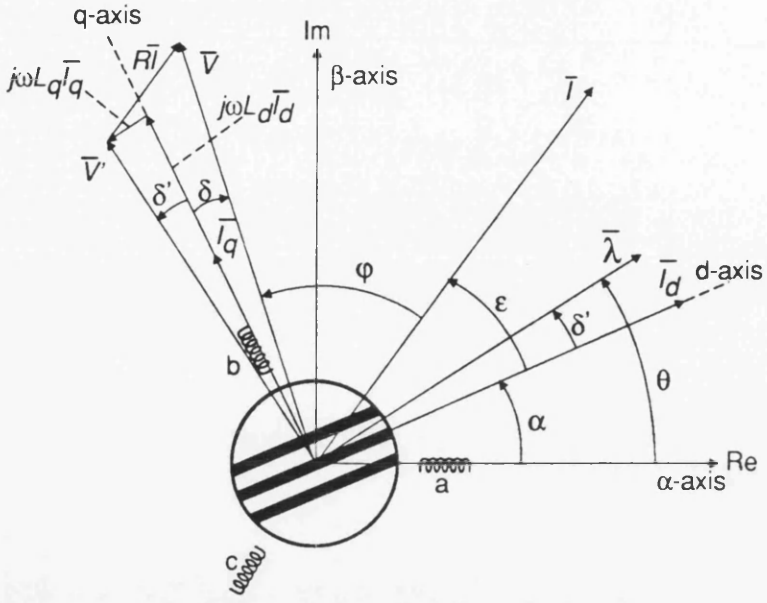

Figure 23: Synchronous Reluctance Motor Phasor Diagram

frame, as (44) and (45). Fig. 23 shows a phasor representation of the equations. The angle ε is referred to as the current angle, angle δ' is the flux-linkage angle. The symbols used follow the convention used by Lipo in [59].

$$\bar{v} = R\,\bar{i} + \frac{d\,\bar{\lambda}}{dt} \tag{44}$$

$$T = \tfrac{3}{2}\mathrm{Re}\left(\bar{\lambda}\,\bar{i}\right) \tag{45}$$

Rearranging (44) gives the flux-linkage

$$\bar{\lambda} = \int (\bar{v} - R\,\bar{i})dt \tag{46}$$

where

$$\bar{v} = \tfrac{2}{3}\left(v_a + v_b e^{j2\pi/3} + v_c e^{-j2\pi/3}\right) = v_\alpha + jv_\beta \tag{47}$$

$$\bar{i} = \tfrac{2}{3}\left(i_a + i_b e^{j2\pi/3} + i_c e^{-j2\pi/3}\right) = i_\alpha + ji_\beta \tag{48}$$

Variables subscripted α and β are the three-phase values transformed into a two-phase coordinate system α,β with the α-axis oriented in line with the motor phase-a winding and denoted as the real axis. The β-axis is at 90°, and is denoted as the imaginary axis.

In this scheme the rotor position is not used, or detected. It relies purely on orientation of stator flux-linkage and torque control. The flux-linkage angle, δ', is indirectly controlled through the control of torque and flux-magnitude.

In an ideal motor with $R = 0$ the voltage angle, δ, and the flux linkage angle, δ', are identical.

Torque is related to the current and voltage angle as [59]:

$$T = \tfrac{3}{2}p\,(L_d - L_q)\,i^2 \frac{\sin 2\varepsilon}{2} \tag{49}$$

$$T = \tfrac{3}{2}p\left[\frac{1}{L_q} - \frac{1}{L_d}\right]\left(\frac{v^2}{\omega^2}\right)\frac{\sin 2\delta'}{2} = \tfrac{3}{2}p\left[\frac{1}{L_q} - \frac{1}{L_d}\right]\lambda^2 \frac{\sin 2\delta'}{2} \tag{50}$$

Under constant current angle control, the maximum efficiency for the test motor at rated speed (1500rpm), torque (0.95Nm) and current (1.7A) was found using a current angle, ε, of 55°. The angle is larger than 45° because of saturation effects.

Under the same conditions as stated above the corresponding flux-linkage angle is given by

$$\delta' = \tan^{-1}\left[\frac{L_q}{L_d}\tan\varepsilon\right] \tag{51}$$

As L_d is strongly dependent on the flux-linkage magnitude equations (50) and (51) must be solved numerically to determine the flux-linkage magnitude that satisfies the required full-load torque and current angle requirements.

For the test motor the flux-linkage angle corresponding to a current angle of 55° was 12° (0.2 rad). Thus under flux-linkage control the motor has an inherent torque margin of 33° before it becomes unstable by moving beyond 45°. This means that the motor is inherently stable under flux-linkage angle control whereas it is inherently unstable under constant current angle control since $\varepsilon > 45°$.

Fig. 24 shows the behaviour of the current and torque for different flux-linkage magnitudes. It can easily be appreciated that for best possible inherent stability the flux-magnitude should be chosen as large as possible under current and voltage limit constraints. However as efficiency is also an aim, the flux-magnitude must be reduced so that the full-load operating point coincides with the maximum efficiency point. It must also be noted that the current increases considerably when exceeding the rated

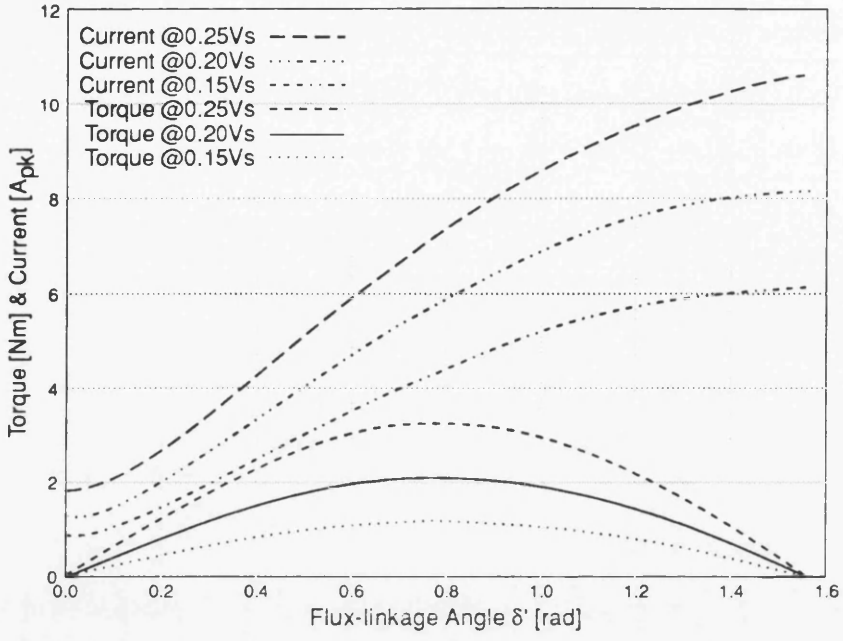

Figure 24: Torque and current magnitude vs. flux-linkage angle with flux-linkage magnitude as a parameter

flux-linkage angle. TVC normally operates with voltage angles that ensure operation within the current limit, but after a load change is applied it may transiently slip back to a larger voltage angle due to delays in the control loop.

To achieve synchronism with the rotor TVC controls the applied voltage so that the flux-linkage magnitude is constant and the maximum torque, calculated by (45), is limited so that the flux-linkage angle is kept less than 45°. The flux-linkage magnitude is controlled by applying voltage vectors that are directed towards the centre of the rotor to decrease the magnitude or outwards to increase the magnitude. The torque is controlled by applying voltage vectors that either advance the flux-linkage vector in the direction of rotation to increase the torque, or oppose the direction of rotation to reduce the torque.

As the flux-linkage vector is the integral of the applied voltage vector (46), it will move in the direction of the applied voltage vector for as long as the voltage vector is applied. The voltage angle is thus indirectly controlled by the torque and flux-linkage magnitude. An increasing torque causes an increasing flux-linkage angle.

Flux-Sector		1	2	3	4	5	6
λ +ve	T −ve	V_2	V_3	V_4	V_5	V_6	V_1
λ +ve	T −ve	V_6	V_1	V_2	V_3	V_4	V_5
λ −ve	T +ve	V_3	V_4	V_5	V_6	V_1	V_2
λ −ve	T −ve	V_5	V_6	V_1	V_2	V_3	V_4

Table 1: Optimal Torque Vector Control Voltage Vectors

TVC is designed to provide a simple and fast control algorithm that can be implemented in hardware without the use of a microprocessor. Torque vector control uses a six-pulse voltage source inverter (Fig. 25). By using a hardware implementation it can be assumed that it will control the inverter switching at a rate which is fast enough to make it unnecessary to modulate the applied voltage vectors. Hence the only available voltage vectors are the six in Fig. 25. Since there are only six voltage vectors available it is sufficient to determine the flux-linkage vector position to be in one of the six sectors defined in Fig. 25. As TVC operates at the inverter maximum switching frequency the torque demand is reduced to a simple choice of increase or decrease (+/−). The flux-linkage magnitude is likewise limited to a choice of increase or decrease (+/−).

For the case when the flux-linkage vector is in sector 1 (Fig. 26) one of four voltage vectors can be applied. If the flux magnitude should be increased and the torque should be positive then V_2 should be applied to advance the flux vector. If the flux is too large and a positive torque is demanded then V_3 should be applied. If negative torque is demanded then V_6 would be applied to increase the flux and V_5 to decrease the flux. A compact table of optimal voltage vectors for all the different cases of flux-linkage position and desired control inputs [8] is listed in Table. 1.

A high-speed low-tech implementation of torque vector control could be achieved using op-amps, comparators, a small ROM look-up table and 4 analog multipliers, ideally suited for implementation as an ASIC (Fig. 27).

At no point in the TVC algorithm is there a need to know anything but the desired flux-linkage magnitude and the associated maximum torque. In particular the absence of any reliance on knowledge of L_d and L_q should be noted; this can be contrasted to the conventional constant current angle control that needs to know L_d

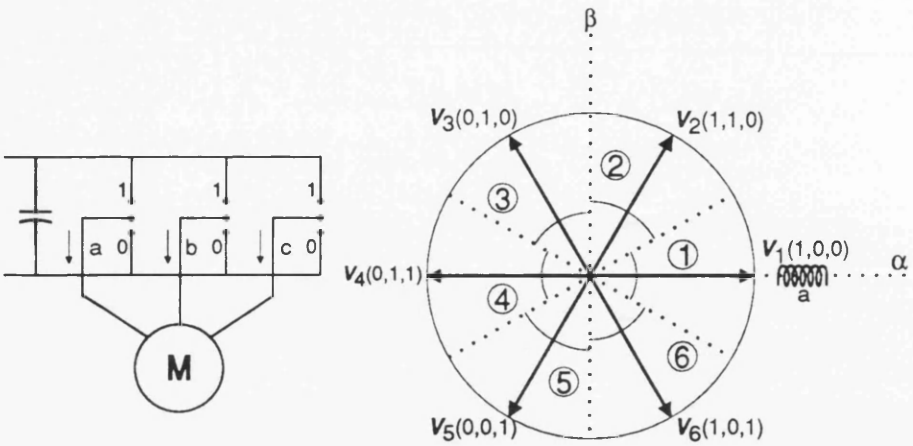

Figure 25: PWM inverter voltage vector positions

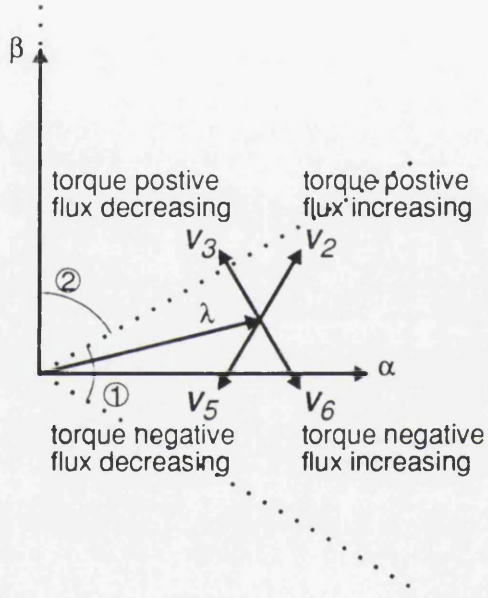

Figure 26: TVC Voltage Vectors for stator flux-linkage vector in region 1

and L_q to compensate for the speed-term cross coupling between the d and q axis current equations.

To summarise, the advantages of TVC are:

1. Self synchronised torque control.
2. Inherently stable ($\delta' < 45°$) at maximum efficiency operating point.
3. Simple hardware implementation possible, no microprocessor necessary.
4. Does not need to know L_q, L_d or saturation characteristic.

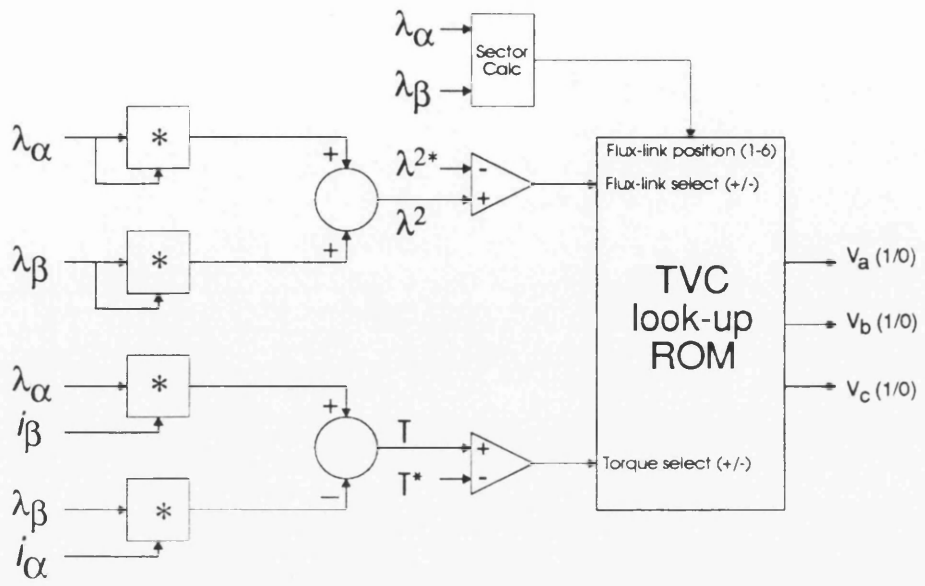

Figure 27: Hardware implementation of TVC

5.3 Torque Vector Control - Further Analysis

This section expands on certain aspects of torque vector control described in the previous section that differentiate it from constant current angle control schemes.

5.3.1 Current and d-q Inductances

The current under torque vector control is expected to be higher than for constant current angle control at light loads as a certain amount of current is needed to maintain the constant flux magnitude. For a constant angle controller the current magnitude can be directly derived from the torque equation as:

$$T = \tfrac{3}{2}p(L_d - L_q)i_d i_q \tag{52}$$

$$T = \tfrac{3}{2}p(L_d - L_q)\left|\vec{i}\right|^2 \frac{\sin 2\varepsilon}{2} \tag{53}$$

$$\left|\vec{i}\right| = \sqrt{\frac{T}{\frac{3}{2}p(L_d - L_q)\frac{\sin 2\varepsilon}{2}}} \tag{54}$$

For torque vector control the current can be expressed as a function of flux magnitude and torque:

$$\bar{\lambda} = L_d i_d + jL_q i_q \tag{55}$$

$$\left|\vec{\lambda}\right| = \sqrt{L_d^2 i_d^2 + L_q^2 i_q^2} \tag{56}$$

$$\left|\vec{\lambda}\right|^2 = L_d^2 i_d^2 + L_q^2 i_q^2 \tag{57}$$

Substituting (57) into (53) gives the following to equations for i_d and i_q:

$$i_d^2 = \frac{\left|\vec{\lambda}\right|^2 \pm \sqrt{\left|\vec{\lambda}\right|^4 - \frac{4L_d^2 L_q^2 T^2}{\frac{3}{2}p(L_d - L_q)}}}{2L_d^2} \tag{58}$$

$$i_q^2 = \frac{\left|\vec{\lambda}\right|^2 \mp \sqrt{\left|\vec{\lambda}\right|^4 - \frac{4L_d^2 L_q^2 T^2}{\frac{3}{2}p(L_d - L_q)}}}{2L_q^2} \tag{59}$$

Combining (58) and (59) we can obtain an expression for the current magnitude:

$$|i| = \sqrt{\left(\frac{\left|\vec{\lambda}\right|^2 \pm \sqrt{\left|\vec{\lambda}\right|^4 - \frac{4L_d^2 L_q^2 T^2}{\frac{3}{2}p(L_d - L_q)}}}{2L_d^2}\right)^2 + \left(\frac{\left|\vec{\lambda}\right|^2 \mp \sqrt{\left|\vec{\lambda}\right|^4 - \frac{4L_d^2 L_q^2 T^2}{\frac{3}{2}p(L_d - L_q)}}}{2L_q^2}\right)^2} \tag{60}$$

From (58, 59, 60) it clear that there exist two solutions for the i_d and i_q currents, one on either side of the peak of the torque versus voltage angle curve (Fig. 24). The operating point located on the left-hand side of the peak is stable as torque increases with increasing voltage angle, but the operating point on the right-hand side is only stable if operated with a shaft position sensor. However, a motor would never be operated on the right-hand side of the torque peak as the current levels here are very large, and the operating point is unstable.

The flux magnitude as a function of desired current angle and torque can be derived by substituting equation (57) into (52) and as $\frac{i_q}{i_d} = \tan\varepsilon$ the flux magnitude becomes:

$$\left|\vec{\lambda}\right| = \sqrt{\frac{T(L_d^2 + L_q^2 \tan^2\varepsilon)}{\frac{3}{2}p(L_d - L_q)\tan\varepsilon}} \tag{61}$$

Equation (61) is useful when determining what flux level to use when the current angle and desired torque are known. For the 120W synchronous reluctance motor the flux-linkage magnitude giving maximum efficiency (ε=55°) at full load (T=0.95Nm)

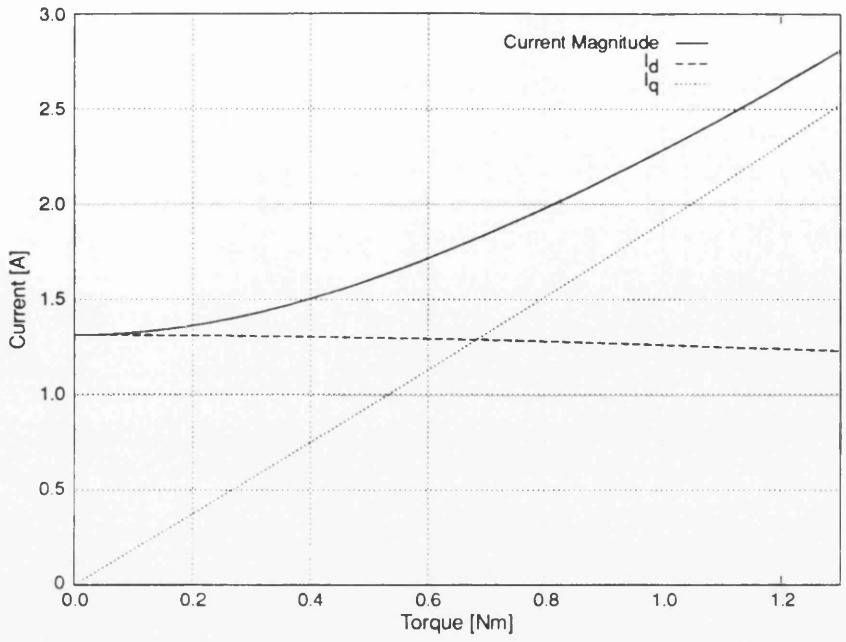

Figure 28: Current Magnitude, I_d and I_q as function of torque under Torque Vector Control, $\lambda = 0.2$Vs. (120W Synchronous reluctance motor)

was 0.2Vs. The current angle that gives maximum efficiency is best determined from measured efficiency curves.

Figs. 28 and 29 show the currents in the 120W synchronous reluctance motor as function of torque. From Fig. 28 it can be seen that under torque vector control the d-axis current remains almost constant and the q-axis current increases almost linearly with torque. Higher inductance ratios lead to a flatter d-axis current curve. For the constant angle controller case (Fig. 29) the i_d and i_q currents both increase in the same proportion with increasing torque. Normally when considering equations for the synchronous reluctance motor they have to be solved numerically as inductance in the most inductive axis, L_d, decreases non-linearly with increasing current due to saturation. In the case of torque vector control a simplification may be possible since the d-axis current remains fairly constant irrespective of torque. Fig. 30 shows the variation in L_d as a function of torque for torque vector and constant angle control. For torque vector control the variation in L_d is 2.6%. For constant angle control the variation in L_d is 17.4%. Hence L_d may be taken as constant for torque vector control, but not for constant angle controllers.

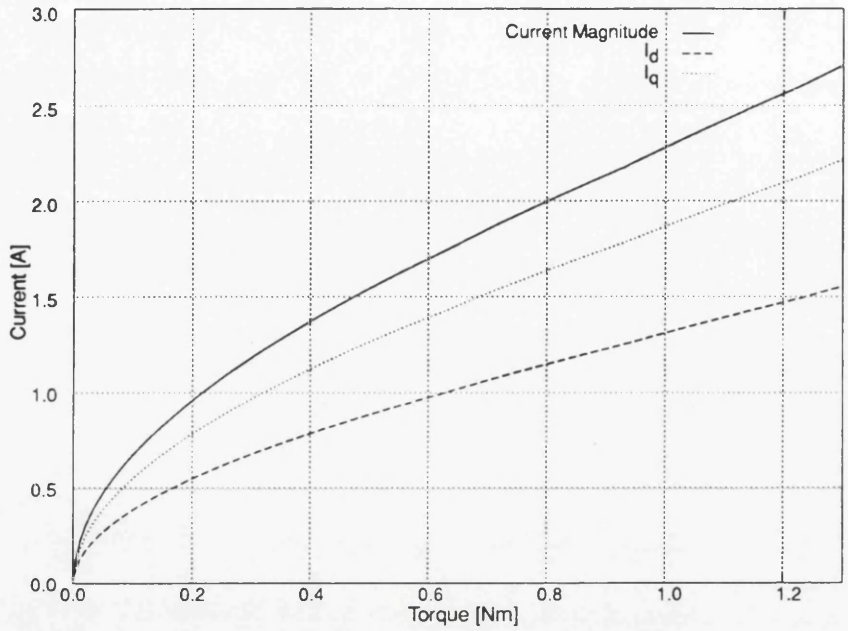

Figure 29: Current Magnitude, I_d and I_q as function of Torque under Constant Angle Control, $\varepsilon = 55°$. (120W Synchronous reluctance motor)

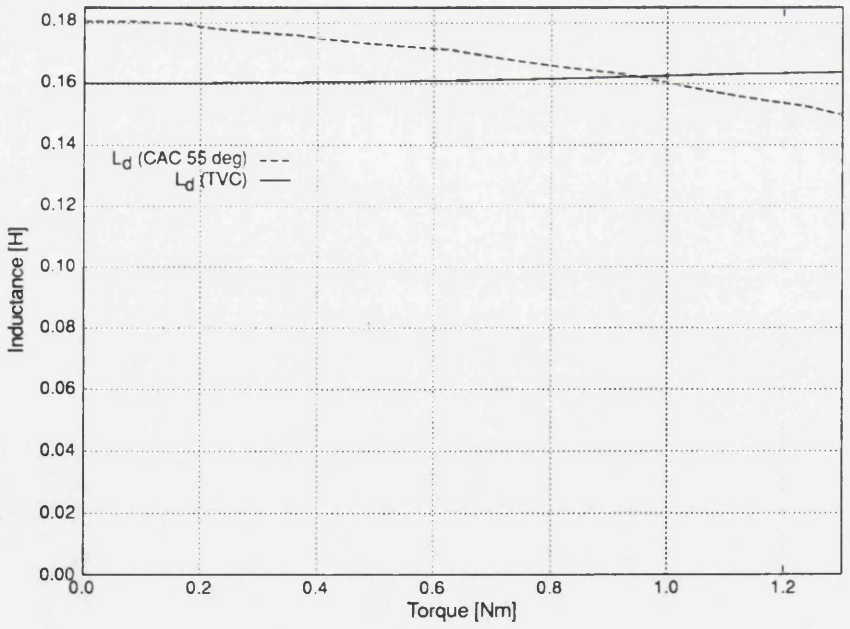

Figure 30: Saturated L_d vs. Torque. Torque Vector Control ($\lambda = 0.2$Vs)and Constant Angle Control (ε=55°)

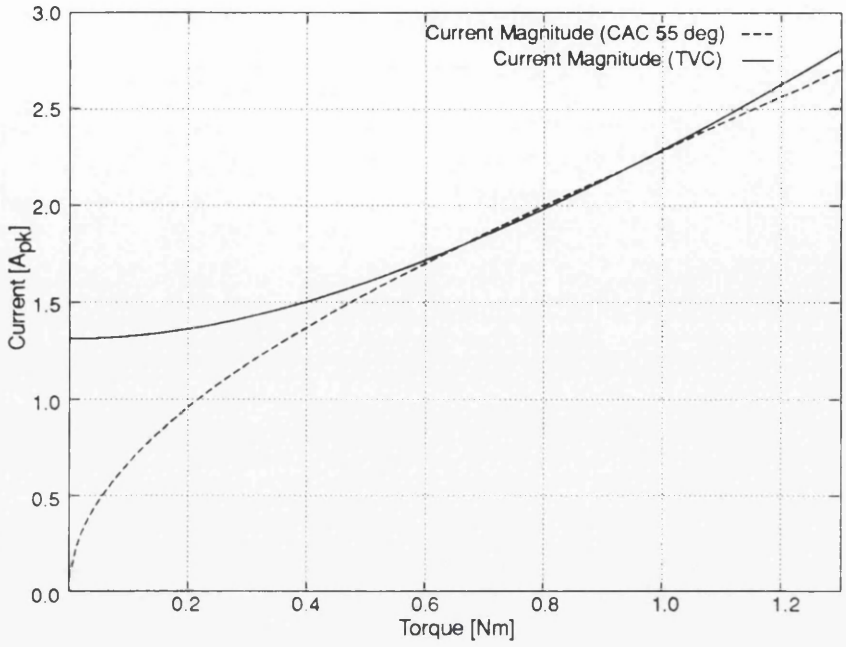

Figure 31: Theoretical current magnitude as function of torque in TVC and CAC controllers. Rated torque = 0.95Nm.

5.3.2 Efficiency

Torque vector control operates with a constant flux-linkage magnitude at all loads. The use of constant flux-linkage means that there will be always current flowing in the motor to maintain the flux, even in no-load situations. The effect this has on the performance will depend on loss mechanisms in the motor. In the 120W test motor the iron-losses were found to be relatively independent of the load, and mostly a function of the flux-linkage ripple (see section 5.3.4). However the major part of the loss was found to be due to copper loss.

To compare the difference in losses of torque vector control and constant angle control it should thus be sufficient to compare the copper losses. Fig. 31 shows the current magnitude for a constant angle control (CAC) of 55° compared with torque vector control. The flux-linkage magnitude is set to achieve the maximum efficiency current angle at a load of 0.95Nm (100% of rated torque). As can be seen the copper losses of the two control methods will be almost the same for loads ranging from 60% to 110% of rated torque. Outside this range TVC has larger copper losses than constant angle controllers, especially at low loads.

Torque vector control has fast dynamic torque response compared to constant current angle controllers since the currents in the motor can be changed faster. The torque change is faster under TVC as almost all the current change occurs in the least inductive axis whereas for constant current angle control the change in current is equal in both axis.

The efficiency of torque vector control could be increased at low loads by including an efficiency optimising loop that would lower the flux-linkage magnitude when the motor is operating at light loads. However, some of the dynamic response of TVC would have to be sacrificed if efficiency optimising is used because the flux-linkage magnitude would have to be rebuilt before full torque could be produced. This would make TVC dynamic performance on a par with constant current angle controllers.

5.3.3 Rate of change of Torque

To evaluate the dynamic performance of torque vector control compared to constant current angle control, the rate of change of torque must be derived. Throughout the derivation it is *assumed that stator resistance can be ignored.*

The rate of change of torque for *torque vector control operation (i.e. constant flux-linkage magnitude)* can be derived as follows. The torque equation (50) can be written in dq coordinates as:

$$T = \tfrac{3}{2}p\left[\frac{1}{L_q} - \frac{1}{L_d}\right]\lambda_d\lambda_q \tag{62}$$

The dq-voltage equations can be written as:

$$v_d = \frac{\partial\lambda_d}{\partial t} - \omega\lambda_q \tag{63}$$

$$v_q = \frac{\partial\lambda_q}{\partial t} + \omega\lambda_d \tag{64}$$

Taking the derivative of (62) and substituting (63) and (64) into the result:

$$\frac{\partial T}{\partial t} = \tfrac{3}{2}p\left[\frac{1}{L_q} - \frac{1}{L_d}\right]\left\{\lambda_d\frac{\partial\lambda_q}{\partial t} + \lambda_q\frac{\partial\lambda_d}{\partial t}\right\}$$

$$= \tfrac{3}{2}p\left[\frac{1}{L_q} - \frac{1}{L_d}\right]\{\lambda_d(v_q - \omega\lambda_d) + \lambda_q(v_d + \omega\lambda_q)\} \tag{65}$$

The following identities can be found from the space vector diagram (Fig. 23):

$$\sin\delta = \frac{\lambda_q}{\lambda} = \frac{-v_d}{v} \tag{66}$$

$$\cos\delta = \frac{\lambda_d}{\lambda} = \frac{v_q}{v} \tag{67}$$

Using the above identities the rate of change of torque for *torque vector control* can be written in terms of flux-linkage angle as:

$$\frac{\partial T}{\partial t} = \tfrac{3}{2}p\left[\frac{1}{L_q} - \frac{1}{L_d}\right]\lambda\{v - \omega\lambda\}\cos 2\delta \tag{68}$$

Substituting (50) back into (68) to gives the rate of change of torque for *torque vector control* in terms of torque:

$$\frac{\partial T}{\partial t} = \tfrac{3}{2}p\left[\frac{1}{L_q} - \frac{1}{L_d}\right]\lambda\{v - \omega\lambda\}\cos\left(\sin^{-1}\left\{2T/\left(\tfrac{3}{2}p\left[\frac{1}{L_q} - \frac{1}{L_d}\right]\lambda^2\right)\right\}\right) \tag{69}$$

The rate of change of torque for *constant current angle control* will now be derived, again *assuming that stator resistance can be ignored.* The current form of the torque equation (70) will be used to derive the rate of change of torque.

$$T = \tfrac{3}{2}p[L_d - L_q]i^2\frac{\sin 2\varepsilon}{2} = \tfrac{3}{2}p[L_d - L_q]i_d i_q \tag{70}$$

From the space vector diagram (Fig. 23):

$$i^2 = i_d^2 + i_q^2 \tag{71}$$

$$v^2 = v_d^2 + v_q^2 \tag{72}$$

$$\sin\varepsilon = \frac{i_q}{i} \tag{73}$$

$$\cos\varepsilon = \frac{i_d}{i} \tag{74}$$

The dq currents can be expressed in terms of torque and current angle by combining (70), (71) and either (73) or (74).

$$i_d = \sqrt{i^2 - i_q^2} = \sqrt{i^2(1 - \sin^2\varepsilon)} = \sqrt{\frac{T}{\tfrac{3}{2}p[L_d - L_q]}\cot\varepsilon} \tag{75}$$

$$i_q = \sqrt{i^2 - i_d^2} = \sqrt{i^2(1 - \cos^2\varepsilon)} = \sqrt{\frac{T}{\tfrac{3}{2}p[L_d - L_q]}\tan\varepsilon} \tag{76}$$

The voltage dq-equations (63, 64) in current form are (assuming that L_q and L_d are not functions of time, i.e. ignoring saturation effects):

$$v_d = L_d \frac{\partial i_d}{\partial t} - \omega L_q i_q \tag{77}$$

$$v_q = L_q \frac{\partial i_q}{\partial t} + \omega L_d i_d \tag{78}$$

Substituting (75) into (77) and (76) into (78):

$$v_d = L_d \sqrt{\cot \varepsilon}\, \frac{\partial}{\partial t} \sqrt{T} - \omega L_q \sqrt{T \tan \varepsilon} \tag{79}$$

$$v_q = L_q \sqrt{\tan \varepsilon}\, \frac{\partial}{\partial t} \sqrt{T} - \omega L_d \sqrt{T \cot \varepsilon} \tag{80}$$

Substituting (79) and (80) into (72):

$$\begin{aligned} v^2 &= \frac{L_d^2 \cot \varepsilon}{4T} \left(\frac{\partial}{\partial t} T \right)^2 + \frac{L_q^2 \omega^2 T \tan \varepsilon}{\frac{3}{2} p \left[L_d - L_q \right]} + \frac{L_q^2 \tan \varepsilon}{4T} \left(\frac{\partial}{\partial t} T \right)^2 + \frac{L_d^2 \omega^2 T \cot \varepsilon}{\frac{3}{2} p \left[L_d - L_q \right]} \\ &= \left(\frac{1}{4T} \left(\frac{\partial}{\partial t} T \right)^2 + \frac{\omega^2 T}{\frac{3}{2} p \left[L_d - L_q \right]} \right) \left(L_d^2 \cot \varepsilon + L_q^2 \tan \varepsilon \right) \end{aligned} \tag{81}$$

Rearranging (81) gives the rate of change of torque for *constant current angle* operation:

$$\frac{\partial T}{\partial t} = 2 \sqrt{T \left(\frac{v^2}{L_d^2 \cot \varepsilon + L_q^2 \tan \varepsilon} - \frac{\omega^2 T}{\frac{3}{2} p \left[L_d - L_q \right]} \right)} \tag{82}$$

As can be seen from (69) and (82) the rate of change of torque for the controllers are complex functions of T, ω, L_d and L_q. To help understanding the relationship of the rate of change of torque between the torque vector controller and the constant current angle controller consider Fig. 32 to Fig. 34. There are a number of remarks that can be made:

- TVC rate of change of torque is always superior to constant current angle control at light loads and low speeds.
- Rate of change of torque for torque vector control depends mainly on speed, and is inversely proportional to it.

- Rate of change of torque for torque vector control is almost constant regardless of torque.

- Rate of change of torque for constant current angle control is a strong function of torque.

- The torque level at which constant current angle control rate of change of torque exceeds torque vector control is approximately inversely proportional to speed.

It should also be noted that in the worst case the rate of change of torque for torque vector control is only about a factor of 2 lower than constant current angle control. Whereas constant angle control is significantly worse at low speeds and light loads. Also note that the results presented here are specific to the 120W synchronous reluctance motor used throughout this thesis. Further note that the inverter is capable of delivering a sinusoidal voltage 25% larger than the required base-speed voltage, this is to ensure that the motor has sufficient dynamic response at speeds at and above the base speed. From (68), if the voltages are exactly equal the rate of change of torque for torque vector control goes to zero at and above base-speed. This is also the case for operation with 45° constant current angle at rated speed and torque. Another important result of using a slightly high DC-link voltage is that under torque vector control there is always a high rate of change of torque available regardless of operating point. The minimum rate of change of torque for the 120W motor under torque vector control was 0.4Nm/ms (0.42p.u./ms) which should be more than sufficient for most applications.

5.3.4 Flux-linkage ripple

Flux-linkage ripple affects the motor performance as a secondary ironloss effect, but more importantly it controls the amount of filtering necessary in the speed estimator (section 6.4). It is therefore important to quantify the flux-linkage ripple in terms of operational parameters.

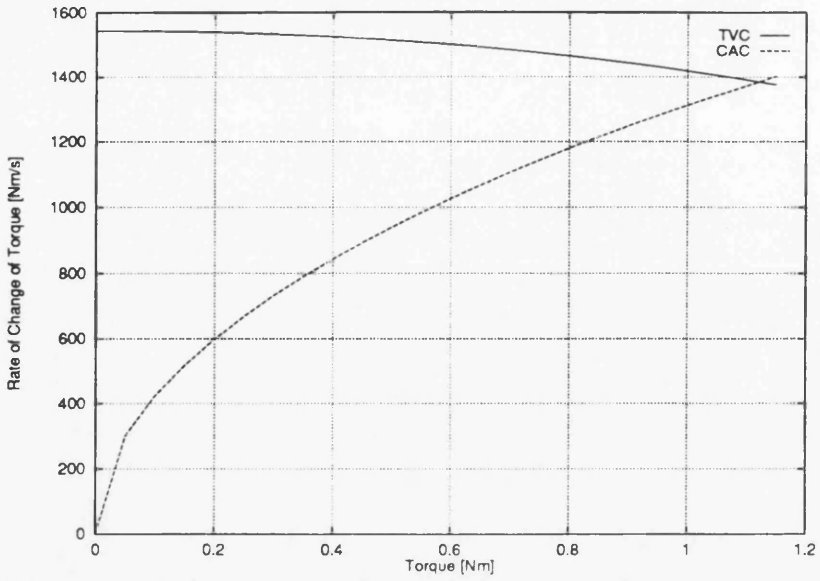

Figure 32: Rate of Change of Torque @400rpm for torque vector control (TVC) and constant current angle control (CAC). (CAC set for maximum efficiency, ε=55°)

First assume that the current vector is aligned with an inductance given by:

$$L_i = L_q + (L_d - L_q)\cos\varepsilon. \tag{83}$$

Further assume that the voltage available to change the flux-linkage is:

$$V_{\Delta\lambda} = \left(\tfrac{2}{3}V_{DC-link} - \omega\lambda\right). \tag{84}$$

Then the change in flux-linkage over one control interval is given by:

$$\Delta\lambda = \mathrm{T_{control}}\frac{\frac{2}{3}V_{DC-link} - \omega\lambda}{L_q + (L_d - L_q)\cos\varepsilon} \tag{85}$$

In the case for the controller in use where the DC-link voltage is 150V and the control interval, $\mathrm{T_{control}}$, is 96μs the average flux-linkage ripple is ±17mVs, or ±8% at the rated speed of 1500rpm. At zero speed the flux-linkage ripple is ±23%, and at the top speed of 2750rpm (using flux-weakening) the flux-linkage ripple is ±12%. All figures quoted are full load figures with ε=55°.

Fig. 35 shows a trace of the flux-linkage as the motor accelerates from 1500rpm to 2750rpm under flux-weakening. The operational parameters for Fig. 35 are: λ=0.25Vs, $\mathrm{V_{DC-link}}$=200V and $\mathrm{T_{control}}$=104μs. The expected flux-linkage ripple

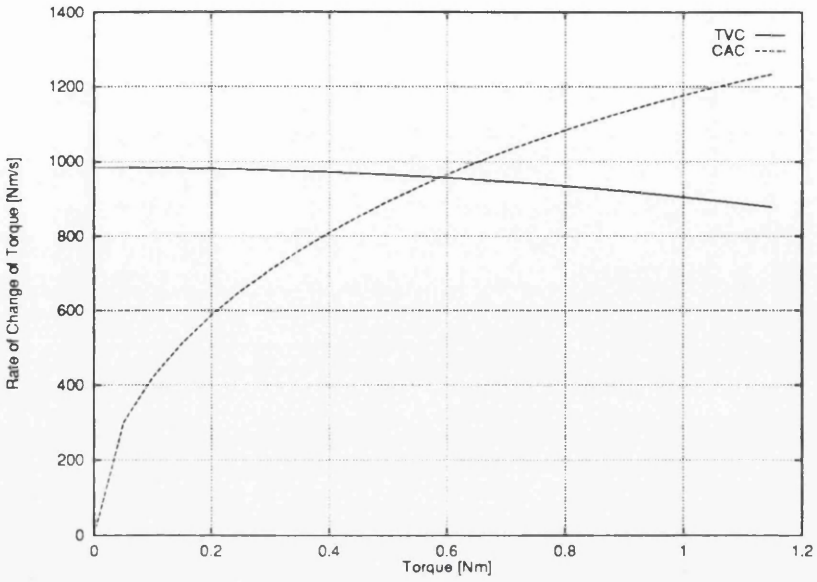

Figure 33: Rate of Change of Torque @1000rpm for torque vector control (TVC) and constant current angle control (CAC). (CAC set for maximum efficiency, $\varepsilon = 55°$)

using (85) is $\pm 12\%$ full load, $\pm 7\%$ no load @1500rpm. At 2750rpm the corresponding figures are $\pm 17\%$ and $\pm 13\%$ respectively. This agrees with the flux-linkage ripple values from Fig. 35 which are $\pm 8\%$ @ 1500rpm and $\pm 14\%$ @2750rpm. This means equation (85) can be used to predict the flux-linkage ripple. If the flux-linkage ripple can be predicted it is also possible to predict the amount of filtering needed in the speed estimator for a particular control interval, motor type and DC-link voltage.

5.4 Flux-Weakening and Torque Vector Control

Flux-weakening is used to operate above the rated speed of a motor. The term flux-weakening is derived from the term field-weakening which was used for separately excited DC-motors. When the separately excited motor reaches its base speed the motor voltage is equal to the supply voltage. To further increase the speed the field-current would be decreased. The decrease in field current naturally also resulted in a decrease in torque per ampere.

As there is no separately excited field winding in a synchronous reluctance motor the term flux-weakening is used to signify that the total flux in the motor is reduced

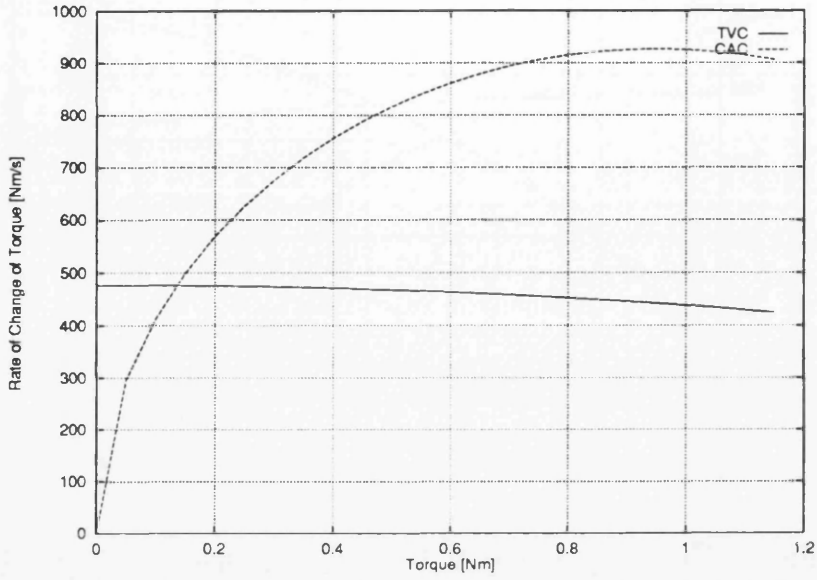

Figure 34: Rate of Change of Torque @1500rpm for torque vector control (TVC) and constant current angle control (CAC). (CAC set for maximum efficiency, ε=55°)

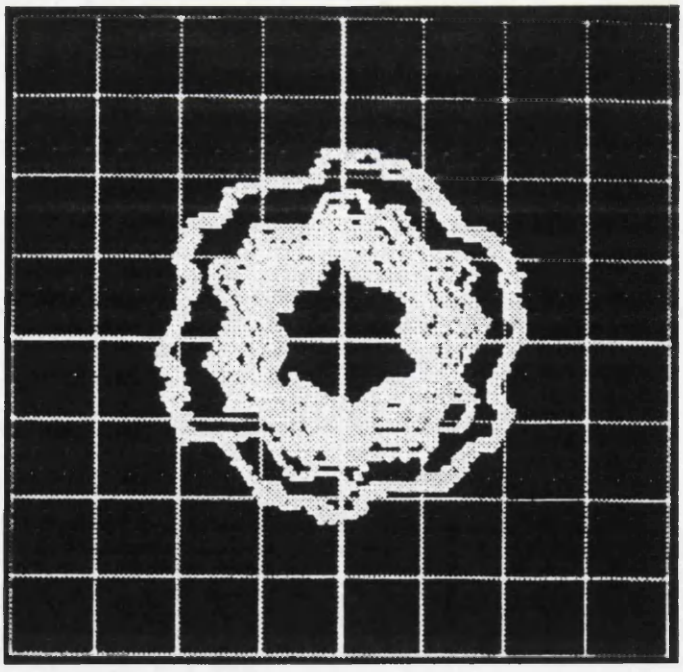

Figure 35: Space vector of flux-linkage when accelerating form from 1500rpm to 2750rpm using flux-weakening. (0.116Vs/div.)

when operating above base speed. The maximum torque is usually kept inversely proportional to the speed when operated above base speed. This gives constant power in the flux-weakening range. The flux-weakening range is often referred to as the constant power speed range (CPSR) [36, 10, 60].

Constant power operation above the base speed is easily implemented for torque vector control. When the motor reaches base speed the inverter has reached its voltage limit and can not increase the voltage further. To go above the base speed the voltage must thus be kept constant at the base speed level. As the voltage magnitude is given by:

$$|V| = \omega\,|\lambda| \tag{86}$$

It is clear that to go above the base speed the flux-linkage magnitude must be reduced as:

$$|\lambda| = \frac{\omega_{base}}{\omega}\,|\lambda_{base}| \tag{87}$$

As flux-linkage magnitude is one of the directly controlled parameters in torque vector control this is easily achieved. Similarly the maximum torque for constant power operation above base speed is given by:

$$P_m = T\omega_m = \text{constant} \tag{88}$$

$$T_{max} = \frac{\omega_{base}}{\omega} T_{max_{base}} \tag{89}$$

The maximum torque of the torque/flux-linkage angle curve is reduced when the flux-linkage magnitude is reduced. It is vital to limit the maximum torque demand because excess torque demand would push the flux-linkage angle beyond the 45° point and the motor would lose synchronism. Since torque is directly controlled by torque vector control this is easily implemented.

The behaviour of the flux-linkage angle and the i_d, i_q and current magnitude is shown in Fig. 36 and 37. It has been shown in [60] that the theoretical flux-weakening range with estimated ironloss, for the motor used, is 2.52:1 and the measured range is 2.13:1. It should be noted that the flux-linkage angle is significantly

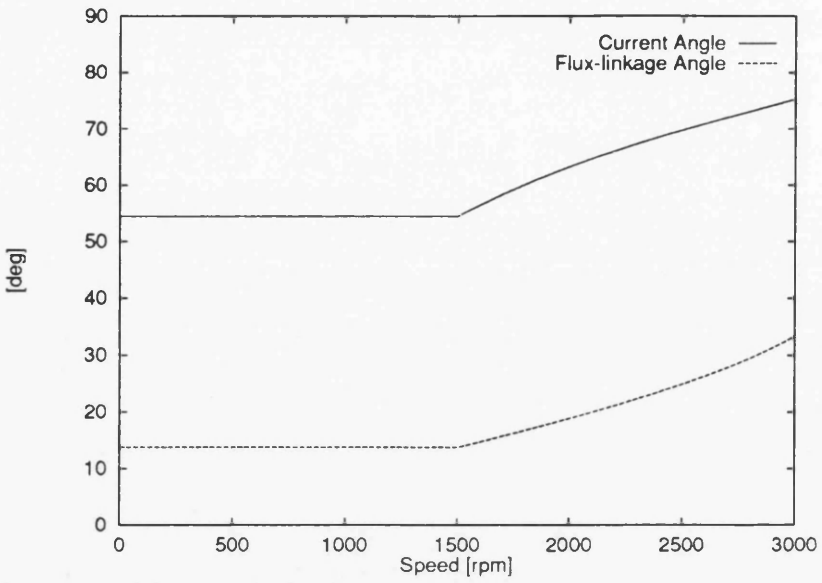

Figure 36: Full-load flux-linkage and current angle vs. speed. (Constant power operation above base speed.) (Base speed = 1500rpm.)

less than 45° when operating within this speed range, ensuring that the torque vector control remains stable.

It is important to note that as torque vector control operates on the measured flux-linkage and torque, the control is not affected by variations in the machine inductances. The great simplicity in achieving flux-weakening operation for torque vector control can be contrasted by the complex operations that must be performed by a current angle controller.

The required current angle for flux-weakening operation for a current angle controller for an ideal motor is given in [42] as:

$$\varepsilon = \tan^{-1} \frac{\left(\frac{L_d}{L_q}+1\right)^2 - \sqrt{\left(\frac{L_d}{L_q}+1\right)^2 - 4\left(\frac{\omega}{\omega_{rated}}\right)^2\left(\frac{L_d}{L_q}\right)^2}}{2\frac{\omega}{\omega_{rated}}} \tag{90}$$

which is clearly more complex than (87) and (89). Also note the dependency on L_d, a parameter that varies strongly with i_d and hence torque. The correct determination of L_d is essential to proper flux-weakening operation and must be estimated on-line [9]. Further, to control a real motor the iron loss resistance must also be estimated and an even more complex equation for the current angle must be used if flux-weakening is to be performed under current angle control [41]. All this makes

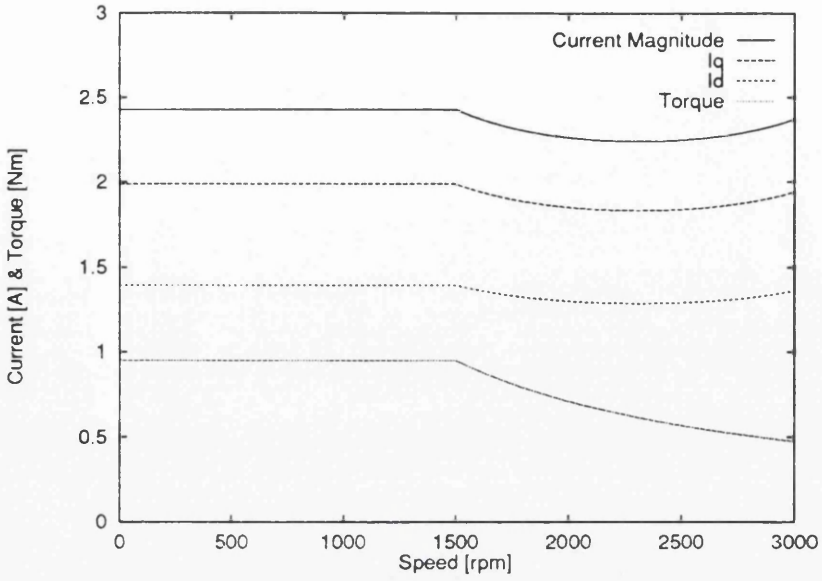

Figure 37: Full-load motor currents and torque vs. speed. (Constant power operation above base speed.) (Base speed = 1500rpm.)

flux-weakening control under current-angle control more complex than for torque vector control.

Chapter 6

Implementation of Sensorless Torque Vector Control

6.1 Control Overview

A sensorless speed control system has been implemented around the torque vector control algorithm described in section 5.2. The complete system results in a fully sensorless closed-loop speed control drive system for the synchronous reluctance motor. The control structure for the system is shown in Fig. 38. The system consists two control loops: an outer speed loop and an inner torque loop. The outer speed control loop uses a standard PI-controller to provide a torque demand signal to the torque vector control algorithm. The input to the PI-controller is a speed error signal which is derived from the difference between the desired and estimated speed. The speed estimator uses the speed of the flux-linkage vector to estimate the rotor speed. The flux-linkage vector is estimated from the motor terminal voltages and currents.

The inner torque loop is implemented using the torque vector control algorithm (see section 5.2). The torque vector control algorithm requires the torque and flux-linkage magnitude to be obtained. The electromagnetic torque and flux-linkage magnitude are estimated from the motor terminal voltages and currents.

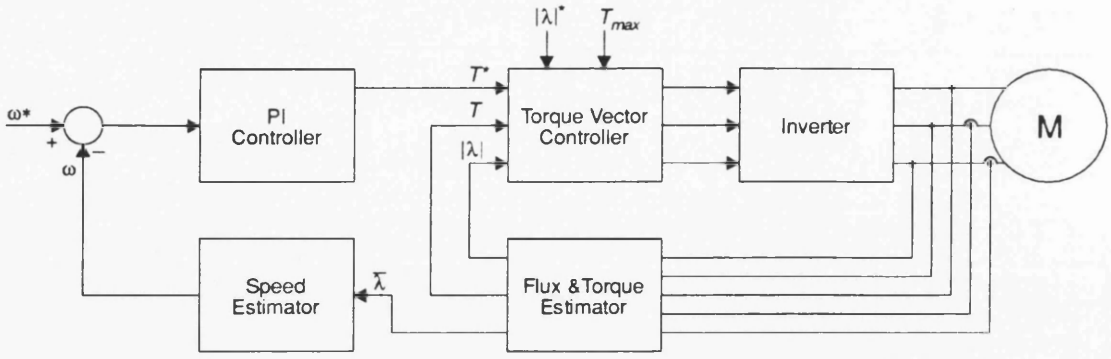

Figure 38: Controller overview

6.2 Hardware Overview

A digital signal processor (DSP), the DSP96002 from Motorola, has been used to implement most of the control algorithms. An analog circuit has been used to transform 3-phase quantities into two phase-quantities and to integrate ($\overline{v} - R\,\overline{i}$) to obtain flux-linkage to obtain the flux-linkage vector. Analog components were used to reduce the execution time of the algorithms and provide a quality flux-linkage estimate. The sensorless torque control algorithm does not require the use of a DSP. It could have been implemented entirely in analog and digital hardware. However, the development time was greatly reduced using a DSP for the entire system.

The control algorithms are executed every 96μs, giving a maximum switching frequency of 5.2kHz. The sensorless speed estimate and the speed measured using a resolver is output on digital to analog converters for real-time monitoring and comparison.

The system units are shown in Fig. 39. The other main unit in addition to the DSP unit is the inverter. The inverter is a three-phase hard-switched IGBT system. The inverter has built-in dead-band generators and other protection features such as over current and voltage protection circuits. The inverter unit also contains flux-nulling high band-width current transducers. The inverter is rated for a DC-link voltage of 600V and a peak phase current of 50A. The inverter is however used with a DC-link voltage of 150V and current transducers set for a maximum current of 12.5A as this is more suitable for the test motor.

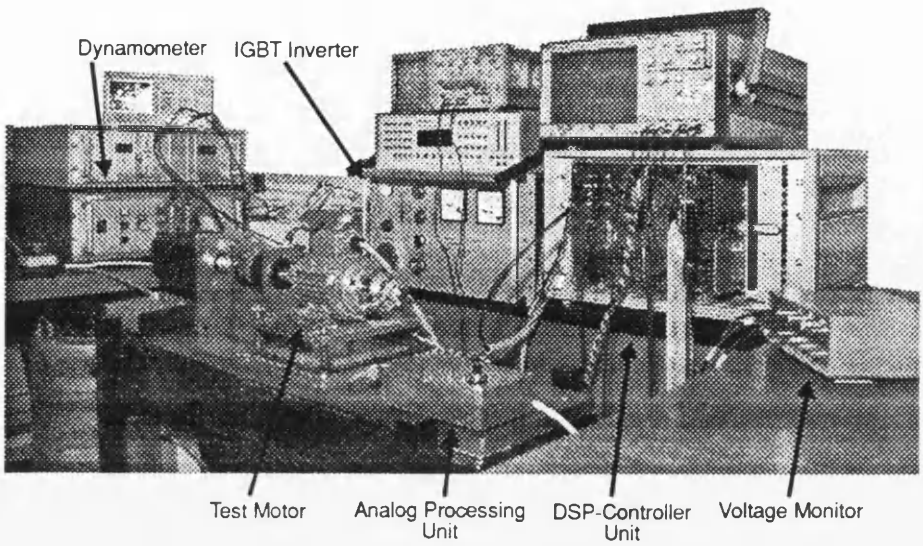

Figure 39: Hardware overview

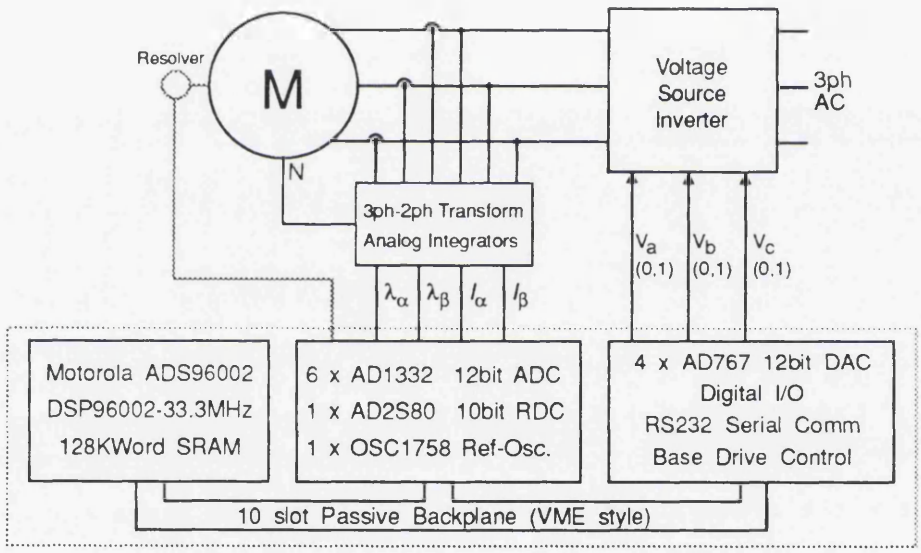

Figure 40: Diagrammatic hardware overview

For further details of the DSP system see B.2, and inverter see section B.3.

A voltage-monitor is used to measure the motor phase-voltages using a high-impedance resistor network. It interfaces with the analog-processing unit which estimates the flux-linkage and does 3-phase to 2-phase transform. The voltage-monitor is kept separate from the rest of the control electronics for safety reasons.

For TVC control software details see Appendix C.

6.3 Stator Flux-linkage and Torque Estimator

Torque vector control requires the flux-linkage vector and torque to be estimated. Using a rotor position sensor the stator currents could be transformed into the rotor d-q frame and calculated as $\bar{\lambda}_{dq} = L_d i_d + jL_q i_q$. However, as the aim is to produce a sensorless scheme the stator flux-linkage must be estimated using (47). The implementation of the flux-linkage estimator is shown in Fig. 41 [8]. The currents and voltages are transformed into a 2ph stator coordinate system using op-amps. The flux-linkage is found by analog integration of the voltage.

As expected there was some drift in the DC output level from the analog integrators. However, most of the drift was caused by DC-drift in the current and voltage transducers and hence there would be no great advantage to perform the integration digitally in the DSP. Analog integration also gives a more accurate result than digital integration due to the discrete nature of digital integration. To compensate for the integrator input drift the DC-gain of the integrators was limited to 10x by paralleling the integrator capacitor with a resistor (Fig. 42). A fair amount of the offset problems can probably be contributed to the distributed configuration of the system; current transducers in the inverter unit, voltage transducers in the voltage monitor unit, and integrators in the analog-processing unit. In a distributed system like this there are possibilities for ground loops that might affect operation. It can be expected that a single unit solution would provide much better performance with respect to the offset problem.

The drift compensation introduces a gain error when operating at low speeds. The gain error causes the estimated flux-linkage magnitude to be 25% too low @400rpm, resulting in an increased flux-linkage magnitude in the motor at low speeds. This increase in flux at low speeds does not in fact influence the control much. The current magnitude stays virtually constant. The voltage angle is decreased giving a slightly lower fundamental power factor and efficiency. A positive side effect of the increased flux magnitude is increased torque reserve. The increase in flux occurs at low speeds so there is no risk of running out of volts.

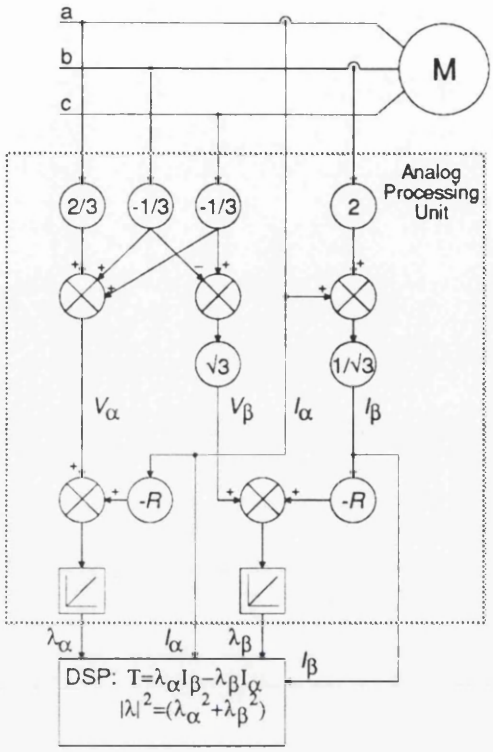

Figure 41: Stator flux-linkage and torque estimator

The conventional method used to compensate for integrator offset measures the distance the centre of the flux-linkage circle has moved from the origin and compensate for this [5]. This method is fine for PM motors as the flux is constant and mainly produced by magnets and there is a relatively small contribution due to the currents in the machine. However, torque vector control can not use this approach because the flux-linkage is being produced by the currents, and is controlled so that the measured flux-linkage describes a "perfect" circle. The actual flux-linkage magnitude will thus under offset conditions vary as it rotating. Compensation for DC-offset under TVC is done by recording the offset values whenever the motor is stopped and subtracting the offset values from the measured values when the motor is running. The influence of flux-linkage offset on the sensorless control scheme will be discussed further in section 6.4.

Since the calculation of torque and flux-linkage magnitude (squared) are much simpler to perform digitally than analogly, and since they are not computational intensive they were computed by the DSP. The square of the flux magnitude was

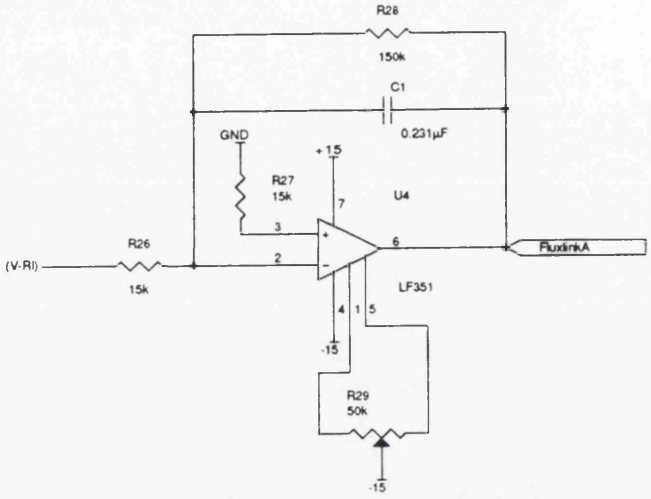

Figure 42: Integrator circuit for flux-linkage calculator

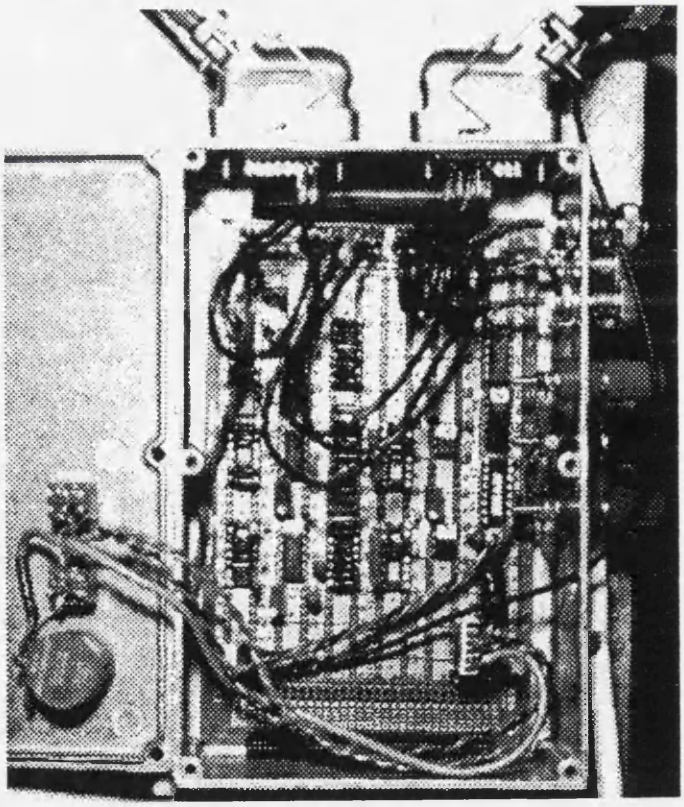

Figure 43: Analog Processing Unit

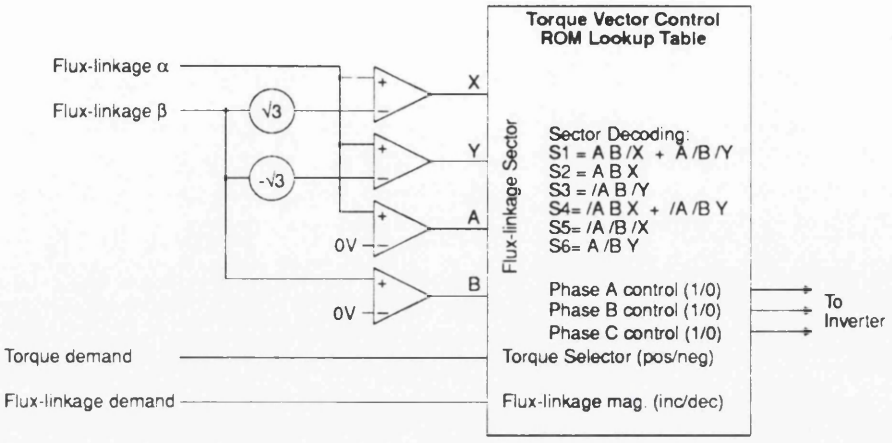

Figure 44: Hardware implementation of TVC sector decoding

used since finding the square-root would be very time consuming.

As TVC only requires the flux-linkage vector position to be determined to be in one of the six sectors in Fig. 25 the position can be uniquely identified by testing for the sign of λ_α, the sign of λ_β and a magnitude comparison $\sqrt{3}\,|\lambda_\beta|$ and $|\lambda_\alpha|$. These tests are performed by the DSP on the raw flux-linkage values from the analog integrator. Use of the arctan function to determine the position of the flux-linkage vector is thus not necessary for the torque loop and this saves valuable CPU time. The position test could also have been implemented in hardware by use of a few comparators and op-amps. Fig. 44 shows an example of how this can be done. The torque vector control voltage-vector-selector from Table 1 and sector decoding can be incorporated into a single ROM.

At low speeds the motional voltage component becomes less than or equal to the voltage across the stator resistance. It thus becomes important that the correct value of stator resistance is used in the flux-linkage estimator. A wrong stator resistance value causes an offset in the flux-linkage angle. The offset can cause the torque vector control algorithm to detect and use the wrong flux-linkage sector. This may be a limiting factor when considering low speed operation because an incorrect sector estimate will most likely cause loss of synchronism.

6.4 Speed Estimator

To achieve sensorless closed loop speed control the rotor speed must be estimated from the terminal current and voltages. The rotor speed can be estimated by calculating the speed of the estimated flux-linkage vector using (91). The speed of the flux-linkage vector can be used to estimate the rotor speed since in the steady-state the flux-linkage vector and the rotor are synchronised and hence rotate with the same speed. The flux-linkage was used rather than the current or voltage vectors to estimate the rotor speed because it has a much cleaner waveform than the others.

$$\omega = \frac{d\theta}{dt} \tag{91}$$

There are three potential problems with this approach:

1. The raw flux-linkage vector is not uniform and constant, but contains large amounts of switching noise.
2. During torque changes the flux-linkage vector is temporarily no longer synchronised to the rotor.
3. Offset in the flux-linkage estimate causes a speed variation at the electrical rotor frequency

6.4.1 Flux-linkage switching noise

Even though the flux-linkage waveforms may look quite sinusoidal (Fig. 57, page 126) they contain huge amounts of switching noise (Fig. 45) due the fact that the flux-linkage vector can move backwards during any particular control interval. However, on average the flux-linkage vector moves in the direction of rotation. This switching noise would inject huge amount of noise in the speed estimate if it was not filtered before the differential of the flux-linkage vector position was taken.

Simulations and test proved that quite hard filtering was required to get a usable speed estimate. To save time and for simplicity a simple digital RC type filter was

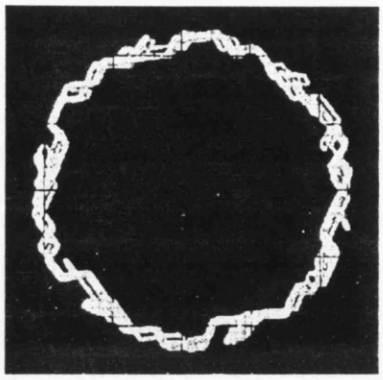

Figure 45: TVC flux-linkage. ($0.25Vs_{pk}$)

used. The flux-linkage waveform was filtered using a first order (RC) filter with f_c=16Hz. The filter introduces a delay of 2-5ms, which naturally affects the bandwidth of the controller. This delay would not be acceptable if this flux-linkage vector position estimate was used in the torque control loop. However, as the position is only used in the speed estimator this may be acceptable.

6.4.2 Change in speed-estimate due to torque change

This problem is due to the fact that the angle δ' changes when the motor torque changes. When δ' changes the position of the flux-linkage vector relative to the rotor changes. This means that transiently the rotor and flux-linkage vector are no longer synchronised, but move relative to each other. The filters will tend to suppress this, but the effect gets magnified by the differentiation taking place to obtain the speed.

When rotating in a positive direction an increase in torque demand will lead to an increase in the flux-linkage angle, this means that the flux-linkage vector will have to advance relative to the rotor. This makes the speed estimator think that the speed has increased more than it in actual fact has. This also has to be seen in the light that the increase in demand was a result of the rotor speed decreasing in the first place. This might result in a somewhat sluggish behaviour.

To quantify this effect one can use the torque (50) and the rate of change of torque equation (68) as a starting point. Assuming small variations around an operating point the rate of change of torque can be assumed to constant. The torque equation

can then be used to extract an estimate of the change in δ' w.r.t. a torque change.

To get an idea about what the effect might be on the speed estimate a case study is useful. Take the case where the motor is rotating at 750rpm and the torque changes from 0.1 to 0.95Nm. The rate of change of torque at 0.1Nm is 1600Nm/s decreasing to 1500Nm/s @ 0.95Nm (assuming constant speed of 750rpm). The change in δ' over one control interval is then 0.006rad. The corresponding error in speed is 600rpm, this error will last until the torque reaches the desired value after 500μs. Note that these estimations assume that no filtering is used.

$$\text{Speed\_error} = \frac{\delta'_t - \delta'_{t-1}}{\text{T}_{\text{control}}} = \frac{0.006\text{rad}}{96\mu s} = 62.5\text{rad/s} \approx 600\text{rpm} \tag{92}$$

Simulations and experiments have shown that because of the filtering used to remove the effects of switching noise the effects of torque changes are largely removed. The only place they manifest themselves is by a small kink in the speed estimate during speed reversal. When applying step load changes this effect can not be seen. Hence it was not deemed necessary to further compensate for this effect. It may be possible to use the torque equation to estimate the change in δ' and use this to compensate the speed estimator. This effect can be minimised by limiting the rate of change of torque.

6.4.3 Flux-linkage offset influence on speed estimate

The offsets that occur in the flux-linkage while the motor is running can not be compensated for since the torque vector control algorithm forces the measured values to appear as a circle centered at what in reality is an offset origin. The variation in speed estimate and actual speed due to offsets in the flux-linkage measurements manifests itself in two distinct ways:

1. At low speeds the rotor speed is modulated by a signal with a frequency equal to the electrical rotor frequency. The speed estimate in this situation would indicate constant rotor speed.

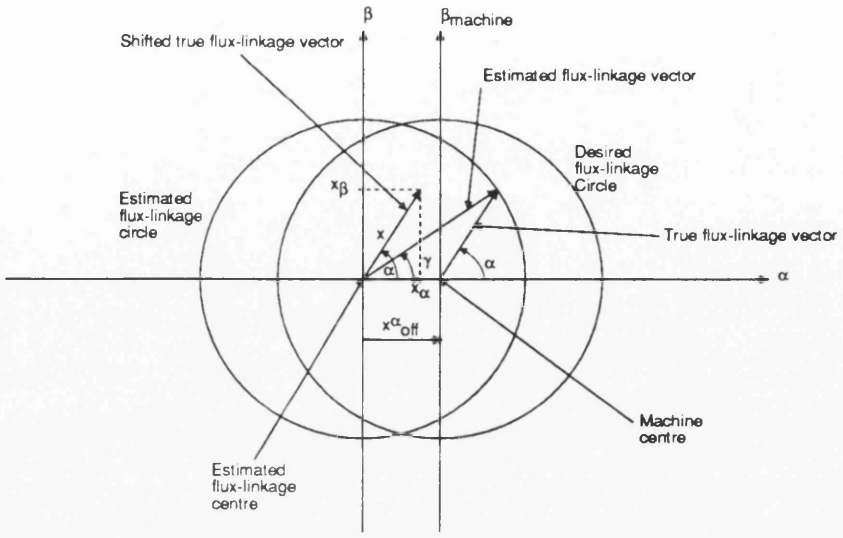

Figure 46: Offset flux-linkage circles

2. At high speed the the speed-controller bandwidth is reached and the load acts as a filter and produces a stable rotor speed. Under this condition the speed variation is evident in the speed estimate, but not in the rotor speed. (This ripple in the estimate may make the speed controller unstable under certain conditions.)

Offsets in the flux-linkage estimate that occur during the operation are not compensated for and cause the real flux-linkage vector to be moved off-centre. The measured flux linkage appears centred, but the speed of the estimated flux-linkage vector is modulated by a sinusoidally shaped function with a frequency equal to the electrical rotor frequency.

Intuitively it is easy to appreciate that this will cause a speed variation. The visualisation is done as follows:

Start off by assuming that the controller can actually control the *estimated* speed to be constant and also that the *estimated* flux-linkage magnitude is constant, this is a valid assumption as long as the controller bandwidth is large enough.

Further assume that the rotor is aligned in the direction of the point at which the *estimated* flux-linkage vector touches the *estimated* flux-linkage circle. (This is true in the limit where the speed goes to zero.) It can then easily be seen that the

angle to that point from the center of the rotor is different from the angle from the center of the *estimated* flux-linkage.

Now consider moving this point along the *estimated* flux-linkage circle at a fixed speed, in this case the angle of the *estimated* flux-linkage changes at a *constant* rate, but the rate at which the the angle centred at the rotor-centre does not change at the same rate. This can easily be proved by moving the *estimated* flux-linkage angle by 90°, in this case the angle from the centre of the rotor is less than 90°. As the time taken for this movement is the same, but the angular distance is different the two vectors must have moved at a different speed. (There will also be an error due to the modulation of the actual torque, and consequently the angle between the rotor and the flux-linkage vector. However, this is believed to be a secondary effect.)

An equation for the speed variation can be derived as follows, assuming that the offset error occurs in the α axis. From Fig. 46:

$$\tan\alpha = \frac{x_\beta}{x_\alpha} \tag{93}$$

$$x_\beta = x_\alpha \tan\alpha \tag{94}$$

$$\tan\gamma = \frac{x_\beta}{x_\alpha + x_{off}^\alpha} \tag{95}$$

$$\tan\gamma = \frac{x_\alpha \tan\alpha}{x_\alpha + x_{off}^\alpha} \tag{96}$$

$$\cos\alpha = \frac{x_\alpha}{x} \Rightarrow x_\alpha = x\cos\alpha \tag{97}$$

$$\tan\gamma = \frac{x\cos\alpha\tan\alpha}{x\cos\alpha + x_{off}^\alpha} \tag{98}$$

$$\tan\gamma = \frac{\cos\alpha\tan\alpha}{\cos\alpha + \frac{x_{off}^\alpha}{x}} \tag{99}$$

$$\gamma = \tan^{-1}\left[\frac{\sin\alpha}{\cos\alpha + \frac{x_{off}^\alpha}{x}}\right] \tag{100}$$

$$\frac{d}{d\alpha}\left(\frac{\sin\alpha}{\cos\alpha + k}\right) = \frac{k+1}{(\cos\alpha + k)^2} \tag{101}$$

where $k = \frac{x_{off}^{a}}{x}$, the relative magnitude error in the flux-linkage measurement. Therefore:

$$\frac{d\gamma}{d\alpha} = \frac{1}{1 + \left[\frac{\sin\alpha}{\cos\alpha + k}\right]^2} \cdot \frac{k+1}{(\cos\alpha + k)^2} \tag{102}$$

$$\frac{d\gamma}{d\alpha} = \frac{k+1}{(\cos\alpha + k)^2 + \sin^2\alpha} \tag{103}$$

Hence

$$\Delta\gamma = \frac{d\gamma}{d\alpha} \cdot \Delta\alpha \tag{104}$$

$$\frac{\Delta\gamma}{\Delta t} = \frac{d\gamma}{d\alpha} \cdot \frac{\Delta\alpha}{\Delta t} \tag{105}$$

$$\tag{106}$$

where $\frac{\Delta\gamma}{\Delta t}$ is measured speed and $\frac{\Delta\alpha}{\Delta t}$ is actual speed. The speed error is thus:

$$\begin{aligned} \omega_{err} &= \omega_{true} - \omega_{meas} \\ &= \omega_{true} - \frac{\delta\gamma}{\delta\alpha} \cdot \omega_{true} \\ &= \omega_{true}\left(1 - \frac{\delta\gamma}{\delta\alpha}\right) \end{aligned} \tag{107}$$

The speed variation can be plotted as seen in Figs. 47, 48 and 49. The offset of these wave forms depends on the individual offset in each axis. The relative speed error appears to be a non-linear function of the flux-linkage offset. Also note that when the flux-linkage offset is less than 10% the speed-error waveform is almost sinusoidal, but becomes increasingly distorted with larger offsets.

The flux-linkage offset also affects the torque controller. The flux-linkage offset causes a modulation of the torque. This occurs because the estimated flux-linkage magnitude and in effect the actual motor flux-linkage magnitude varies with the rotor position. This variation also occurs at the electrical rotor frequency. This torque modulation will cause a variation in the actual rotor speed. If the speed controller has high enough bandwidth this effect can be suppressed. The relative torque modulation magnitude will be proportional to twice the relative flux-linkage variation since torque is proportional to flux-linkage squared.

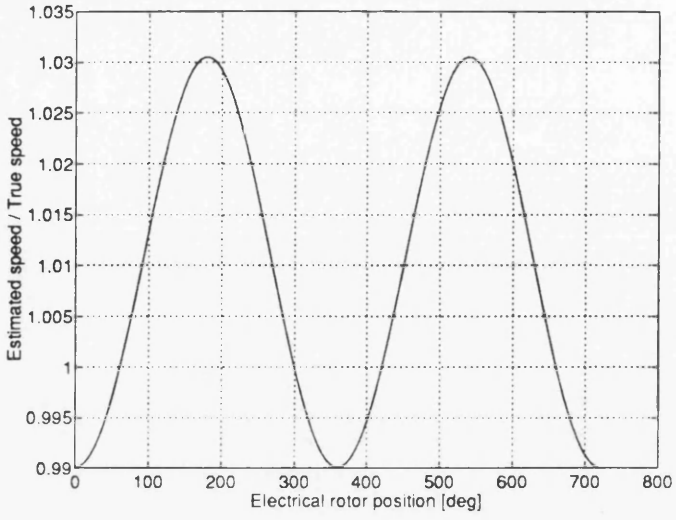

Figure 47: Relative speed-estimate with @1% flux-linkage offset

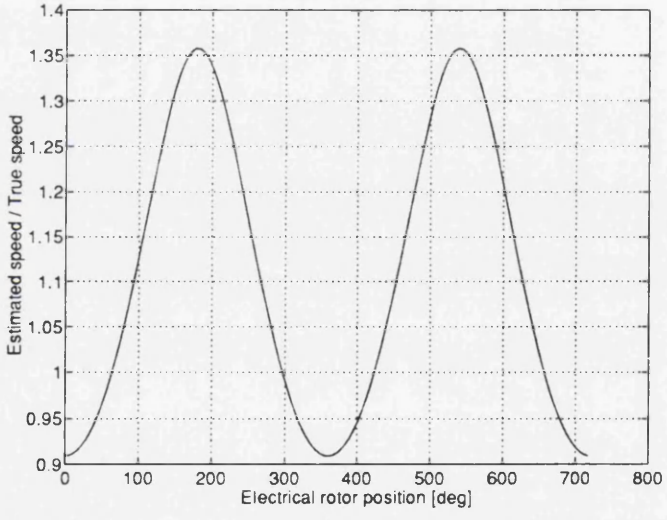

Figure 48: Relative speed-estimate with @10% flux-linkage offset

As the system forms a closed loop it is difficult to visualise the way flux-linkage offset will interact with the torque and speed controllers (it is also load dependent). A good way to obtain an appreciation of the effects is to simulate the system. Fig. 50 is a benchmark test @750rpm where there are no flux-linkage offsets. (A 0-0.5Nm step load is applied at t=0.5s.) Fig. 51 shows the results of injecting a 5% flux-linkage offset in the speed estimator α axis only. In Fig. 52 the effect of flux-linkage offset in just the torque estimate is shown. Fig. 53 shows the real-life situation where

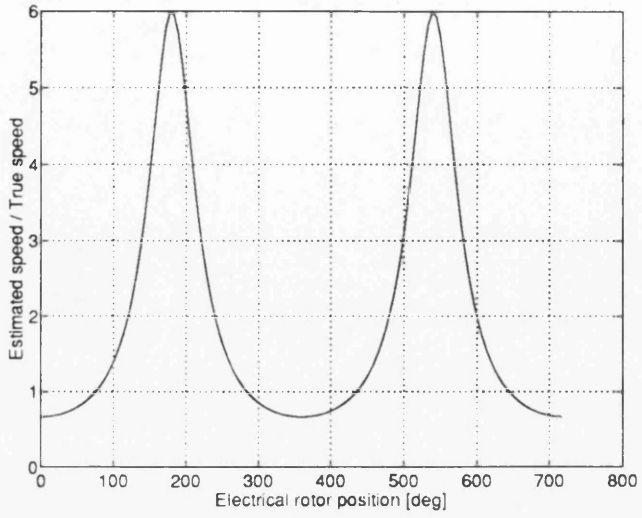

Figure 49: Relative speed-estimate with @50% flux-linkage offset

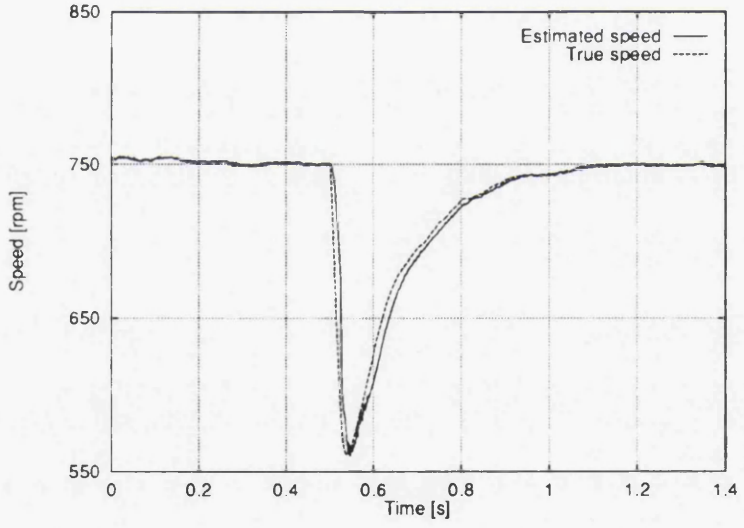

Figure 50: Speed regulation with no flux-linkage offset

the flux-linkage offset affects both the speed and torque estimate simultaneously.

Notice that the effect of offset on the torque controller is considerably less than the effect of offset on the speed estimator. Further observe that the speed-ripple is actually less in the case where the flux-linkage offset affects both torque and speed controllers than when only one is affected. Surprisingly, but fortunately, these two effects seems to cancel each other rather than to accumulate.

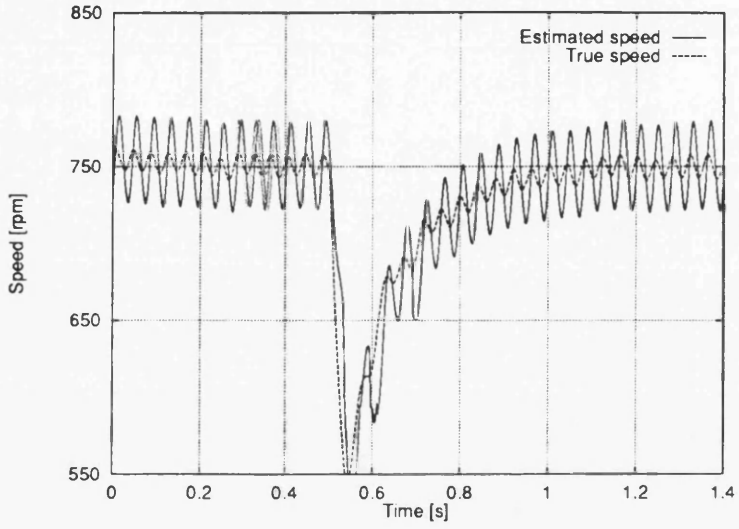

Figure 51: Speed regulation with 5% flux-linkage offset in speed estimator only

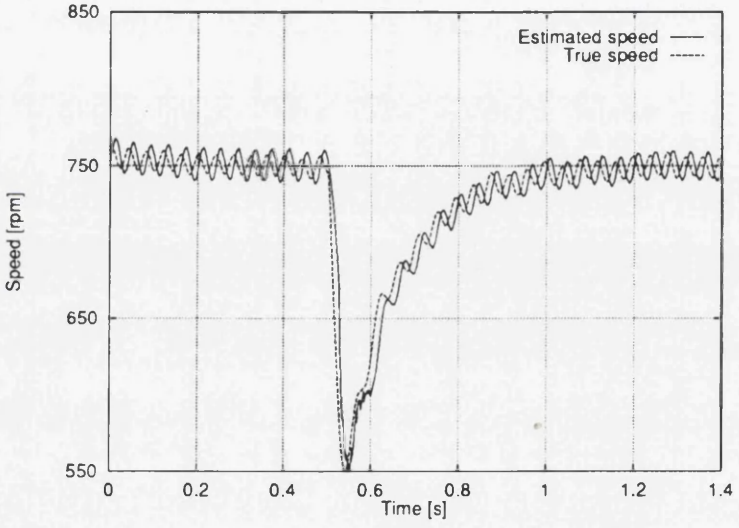

Figure 52: Speed regulation with 5% flux-linkage offset in torque estimator only

Considering ways to improve the speed estimate it would should apparently be possible to filter out the speed variation using a band-stop filter centered on the electrical rotor frequency. Doing this would result in the case where only the torque controller is affected by flux-linkage offset (Fig. 52) and not give any improvement. It might seem logical to notch filter the torque controller as well, but this can not be done as the torque controller need a high bandwidth with minimal delay.

Another method might be to estimate the speed only once per revolution. This would result in the correct speed estimate, but the bandwidth is so low that any

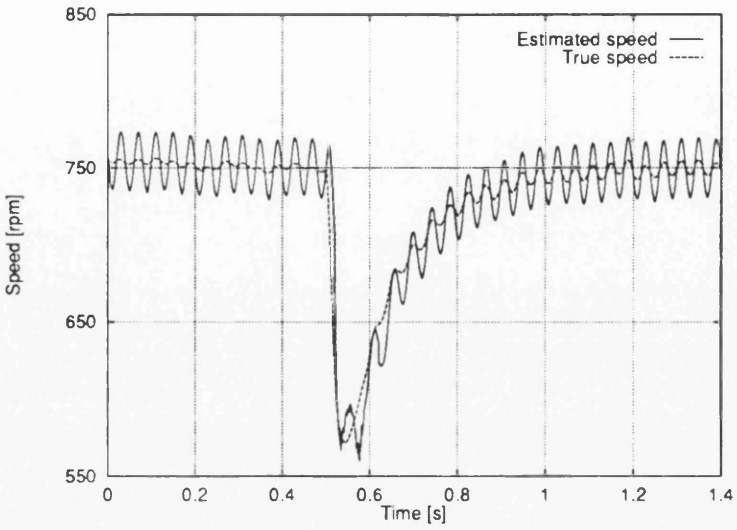

Figure 53: Speed regulation with 5% flux-linkage offset in speed & torque estimators

speed variation due to the offset effect in the torque controller would not be correctable. Then net effect would be as shown in Fig. 52.

Whereas both these suggestions would provide a clean speed estimate with the effects of the flux-linkage offset suppressed, it will not work in practice because the torque is also affected.

A state observer based approach was also attempted in simulation. The observer provided an extremely smooth speed estimate. The steady-state error was also very low. However, the biggest failing of the observer based approached is that it tries to model the whole system. This is fine as long as the system does not change. When there is a change in the system such as a change in inertia or torque then the observer will take a long time to respond. This is because the observer and the real system are forced together using integral action only. To improve the response of an observer based system all the system parameters must be identified on-line with minimal delay. The on-line identification of system parameters would be too costly in computational time to implement on the current system.

The best (and maybe only) way to ensure that one can get a quality speed estimate is to ensure by design that the flux-linkage measurements are offset free. The estimate when there is no flux-linkage offsets are quite good as can be seen in

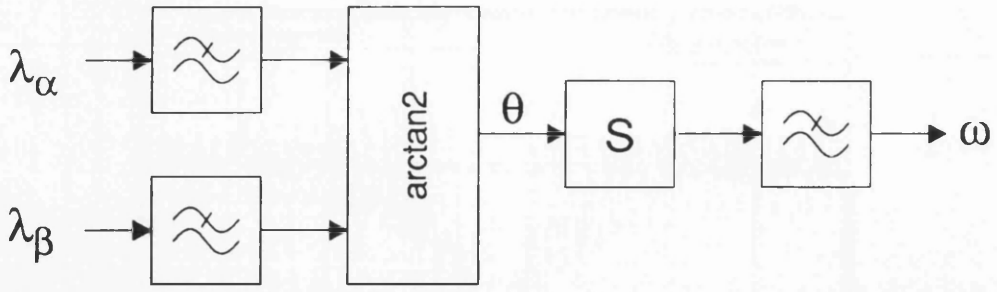

Figure 54: Speed estimator

Fig. 50.

6.4.4 Speed estimator implementation

The speed estimator has been implemented digitally in the DSP. The speed estimator calculates the speed of the flux-linkage vector to obtain a rotor speed estimate.

The block diagram of the speed estimator is shown in Fig. 54. First the α, β flux-linkage signals are filtered using low-pass filters with 16Hz cut-off frequency to remove the switching noise.

The position is then determined using a four quadrant arctan2 function on the α, β flux-linkages. The standard arctan function in the DSP C-library was found to be too slow for real-time operation. It was replaced by a 1024 (90°) entry look-up table with a bisection search algorithm, which yielded significantly faster operation at the cost of decreased accuracy in the arctan2 function. The resolution of the new arctan2 function is 0.09°, which gives an equivalent resolution of almost 1 in 4000. This is more than good enough considering that most drives are operated with 1000 line encoders.

The differential of the flux-linkage vector is calculated by taking the difference in flux-linkage vector position over a control interval of 96μs. The differentiation process naturally tends to amplify any noise in the position estimate. A further low-pass filter with cut-off frequency of 25Hz was applied to the output of the differentiator to remove this noise.

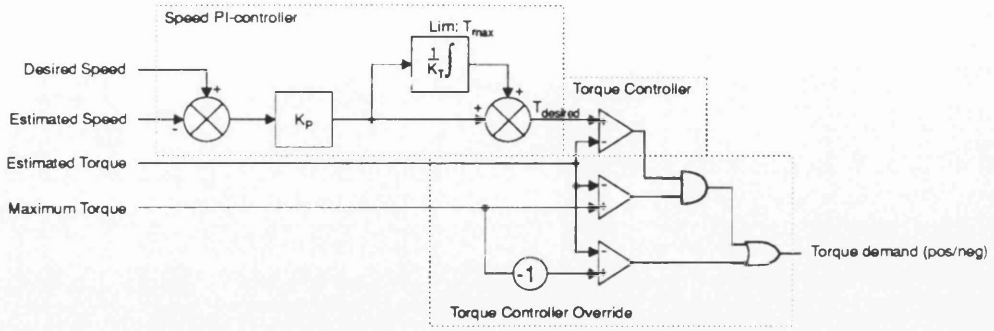

Figure 55: Speed & Torque controller

6.5 Speed and Torque Controller

An overall view of the speed and torque controller was given in Fig. 38 on page 106, Fig. 55 gives an expanded view of this.

The speed controller is a standard proportional-integral (PI) controller. The speed controller accepts as inputs the desired and the estimated speed. The difference is a error signal which is then amplified by a fixed gain (K_p) to produce the a torque demand signal proportional to the speed error. The proportional torque demand is also integrated in an integrator with gain $\frac{1}{K_T}$. The output of the integrator is limited to the motor's rated torque to prevent integrator windup. The integral and proportional torque demand signals are then added to produce an overall torque demand signal which is fed into the torque controller.

The torque controller used is quite simple as the torque vector control algorithm only accepts request for positive or negative torque. The desired torque from the speed controller is compared with the estimated motor torque. If the motor torque is less than the desired torque a request for positive torque is passed to the TVC control algorithm, otherwise a request for negative torque is passed.

The torque vector control algorithm may override any torque request passed to it if the motor torque is larger than the rated torque. If the motor torque is positive and larger than the rated torque then a negative torque demand overrides any previous selection. Likewise if a negative motor torque of magnitude greater than the rated torque is measured then a positive torque request overrides and is

applied.

Fixed settings going into the torque vector controller are flux-linkage vector magnitude and maximum torque. These two settings are continuously adjusted when the motor is operating above base speed, i.e. using flux-weakening. Below base speed these two settings could be used to form part of an efficiency optimizing outer loop.

The most problematic aspect of the speed controller was the ripple in estimated speed due to offsets in the flux-linkage. The effects of this were most noticeable at higher speeds as the ripple frequency approached the speed controller bandwidth and could have caused instability. The proportional gain of the PI speed controller must be set relatively low so that the torque demand signal does not get unduly disturbed by the speed estimate ripple caused by the flux-linkage offset. Careful tuning of the PI gains and the filter settings resulted in a stable system with a speed variation of an approximately fixed magnitude (25rpm), which is clearly visible at low speeds. At high speeds the load tends to filter out the ripple from the actual speed.

Chapter 7

Sensorless control – Results

To explore the performance and limitations of the sensorless closed-loop speed controller an experimental set-up with a 120W axially laminated synchronous reluctance motor was used. The motor has a standard induction motor stator with a low-voltage winding. The test motor and the load machine were coupled with a Vibrometer torque transducer using flexible rubber couplings.. The load machine was a brushless permanent magnet motor powered by an Electrocraft BRU controller.

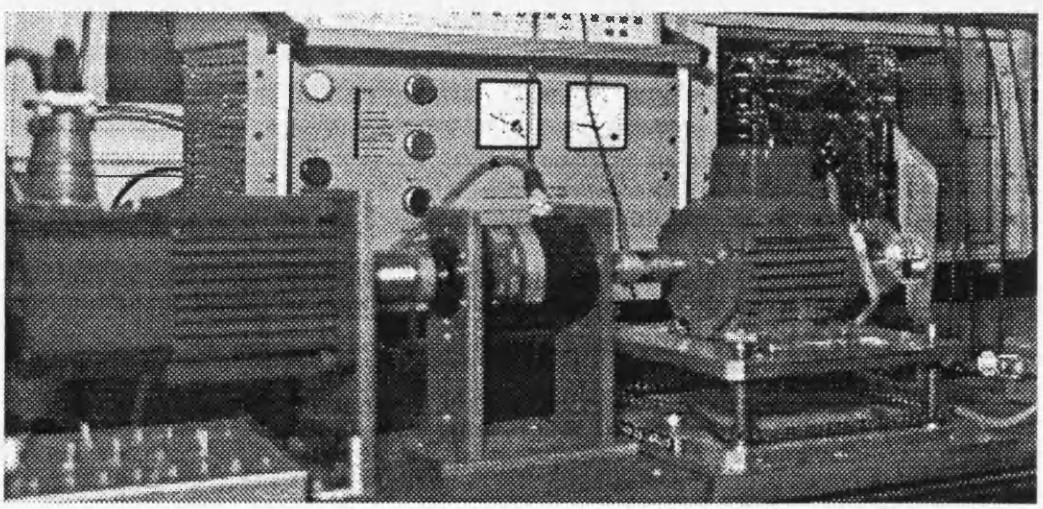

Figure 56: Electrocraft PM load motor (left), Vibrometer torque transducer, and axially laminated synchronous reluctance motor.

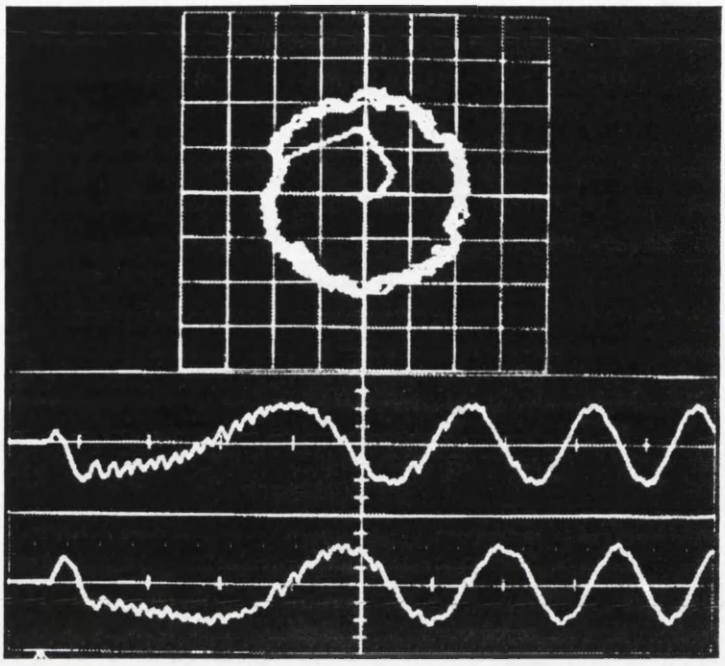

Figure 57: Flux-linkage (α,β) during startup. (0.1Vs/div. 10ms/div.)

7.1 Startup

When starting the motor any voltage vector may be applied. As can be seen in Fig. 57 the correct flux-linkage position is achieved in less than 4ms, during this time the motor may develop torque in the wrong direction. Fig. 57 illustrates the worst case where the initial applied voltage vector is located 180° from the desired position. Also notice the relatively smooth flux-linkage waveform compared to the current (Fig. 58), making it preferable to use in the speed estimator.

7.2 Speed Estimator & Simulation

Simulations of the dynamic behaviour and the actual system have been shown to agree well. Fig. 59 shows a simulation of a speed reversal from -1500rpm to +1500.

In the simulation the flux-linkage was offset by 2.5% in both axes, notice the characteristic ripple on the speed estimate introduced by the offset. This ripple is also present in the experimental waveform Fig. 60. The characteristic kink in the speed estimate occurs due to the rapid change of flux-linkage angle, causing the

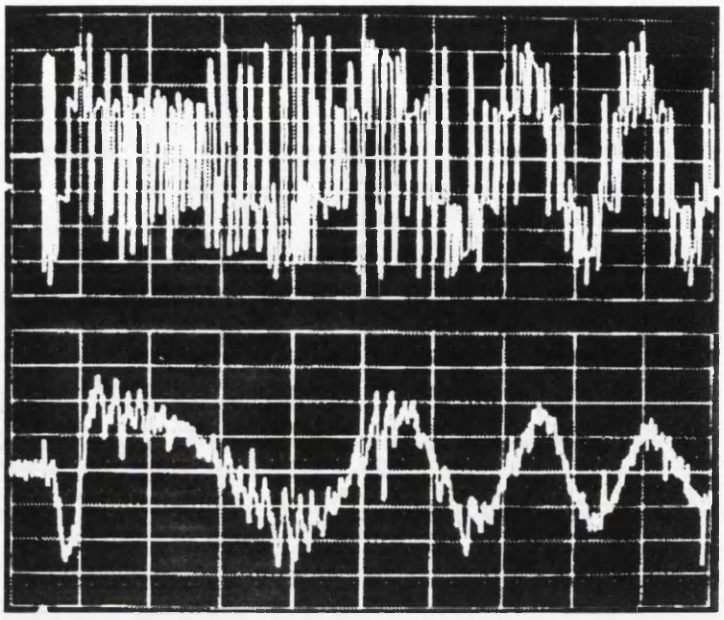

Figure 58: Phase-Voltage (top) and Current (btm) during startup. (50V/div, 2A/div, 10ms/div.)

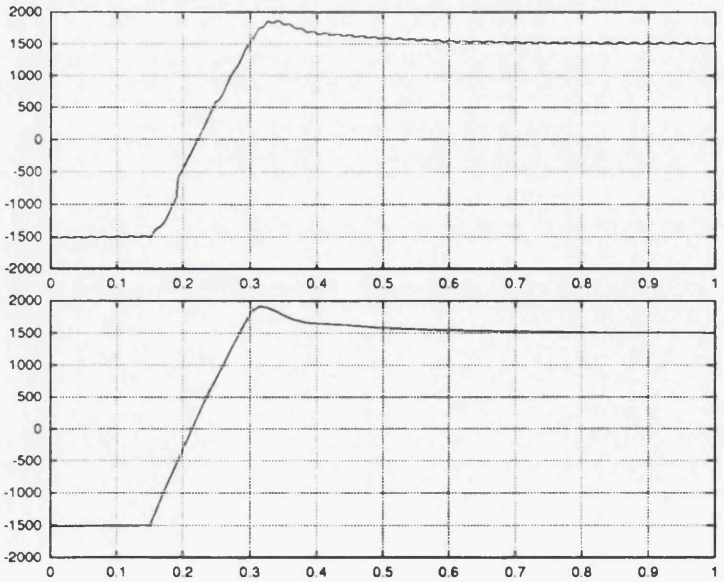

Figure 59: Sensorless: Simulated Speed Reversal $\mp$1500rpm. Estimated Speed (top) & True Speed (btm). (500rpm/div, 0.1s/div.)

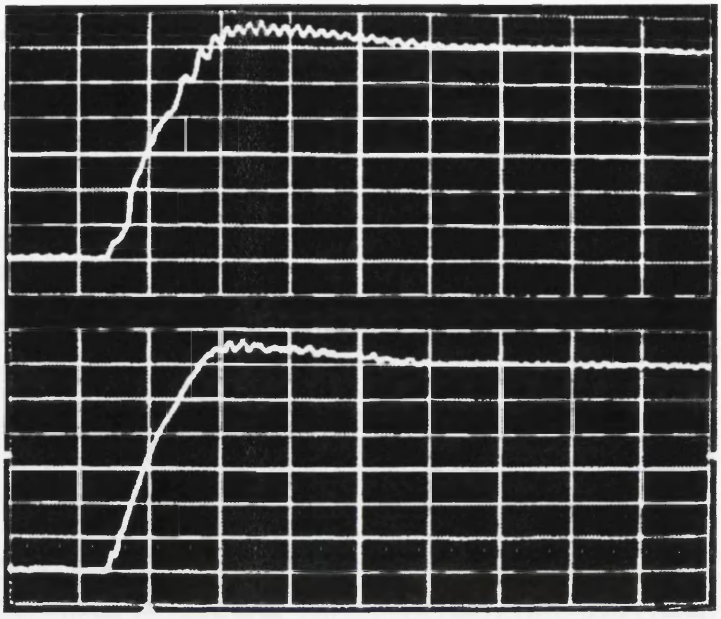

Figure 60: Sensorless: Speed Reversal $\mp$1500rpm. Estimated Speed (top) & True Speed (btm). (500rpm/div, 0.1s/div.)

speed temporarily to be estimated to be much smaller than it actually is (or even of opposite sign). This kink can be found in both the simulation and the experimental waveform and is the response of the digital filter to the impulse speed change present while the flux-linkage angle changes.

7.3 Dynamic Performance

The speed range of the drive has been defined to be the range in which the motor could be applied a step-load from no-load to 90% of rated torque without losing synchronism. The minimum speed achieved that satisfied the above criterion was 400rpm. If the step-load change is limited to 53% of full load the lower speed limit becomes 150rpm.

Fig. 61 shows the $\pm$400rpm speed reversal, steady-state speed ripple due to the flux-linkage offset can be seen. A $\pm$1500rpm speed reversal is shown in Fig. 62, the speed reversal takes 150ms which is comparable with the constant current angle controller in chapter 2 (see also [42, 61]). The settling-time is 325ms compared to a constant current angle control which does not have any noticeable settling time.

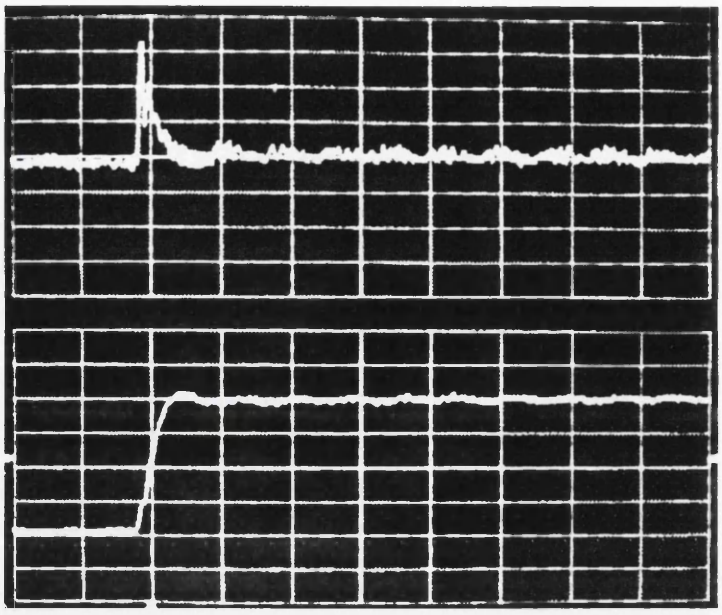

Figure 61: Sensorless: Speed Reversal ∓ 400rpm. Torque (top) & Speed (btm). (0.5Nm/div, 200rpm/div, 0.1s/div.)

This is not a fault of TVC itself, which has excellent response when used with a speed sensor (Fig. 63), but a function of the speed estimator.

The response of the drive to a 90% step-load change is shown in Figs. 64 & 65, notice that the speed dip is constant in magnitude and the recovery time is the same at 400rpm and 1500rpm. The magnitude of the speed dip is a function of the delay in the speed estimator and the recovery time a function of the available acceleration torque. The recovery time for TVC is 400ms compared to a constant current angle controller recovery time of 200ms. If operated with a speed sensor (Fig. 66) the initial dip is much less due to the shorter delay before the change in speed is sensed. Hence the recovery time is also reduced.

The lowest operating speed of torque vector control when used with a speed sensor was found to be 50rpm. Below this speed the resistance term in the voltage becomes too dominant to achieve proper synchronism, inclusion of a stator resistance estimator should improve this.

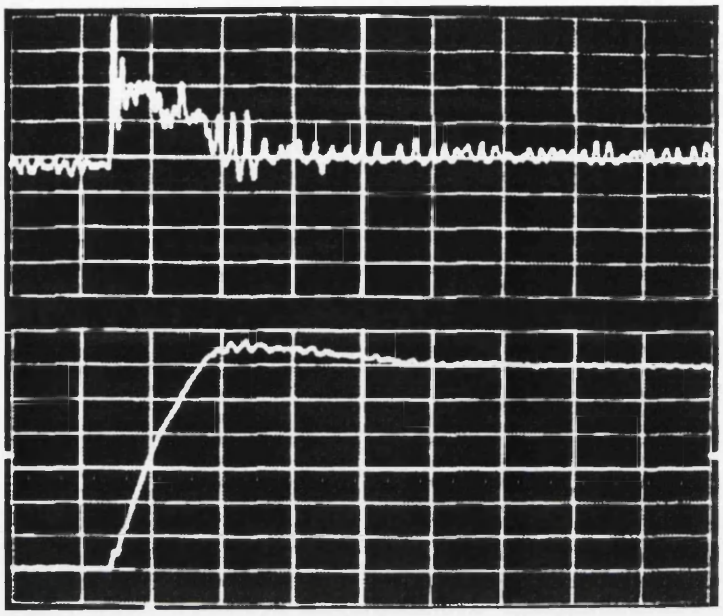

Figure 62: Sensorless: Speed Reversal $\mp$1500rpm. Torque (top) & Speed (btm). (0.5Nm/div, 500rpm/div, 0.1s/div.)

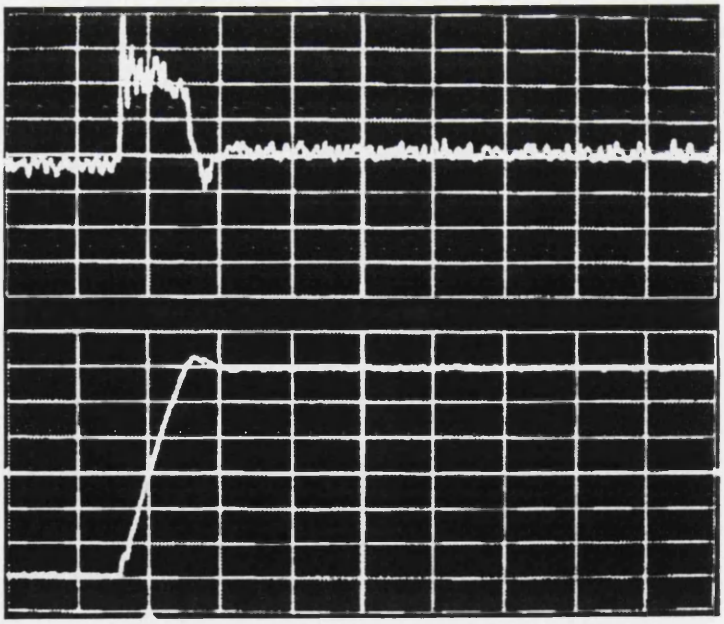

Figure 63: Using Speed-Sensor: Speed Reversal $\mp$1500rpm. Torque (top) & Speed (btm). (0.5Nm/div, 500rpm/div, 0.1s/div.)

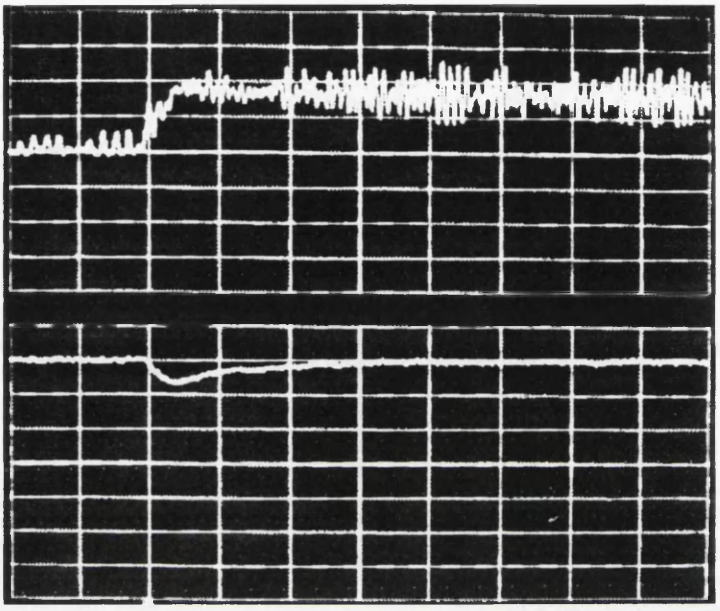

Figure 64: Sensorless: Step-load change 0-0.86Nm @1500rpm. Torque (top) & Speed (btm). (0.5Nm/div, 200rpm/div, 0.1s/div.)

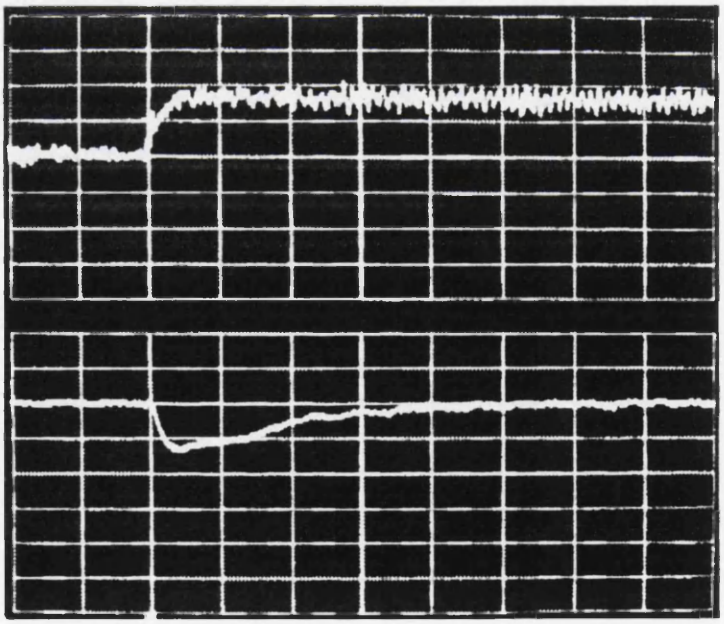

Figure 65: Sensorless: Step-load change 0-0.86Nm @400rpm. Torque (top) & Speed (btm). (0.5Nm/div, 200rpm/div, 0.1s/div.)

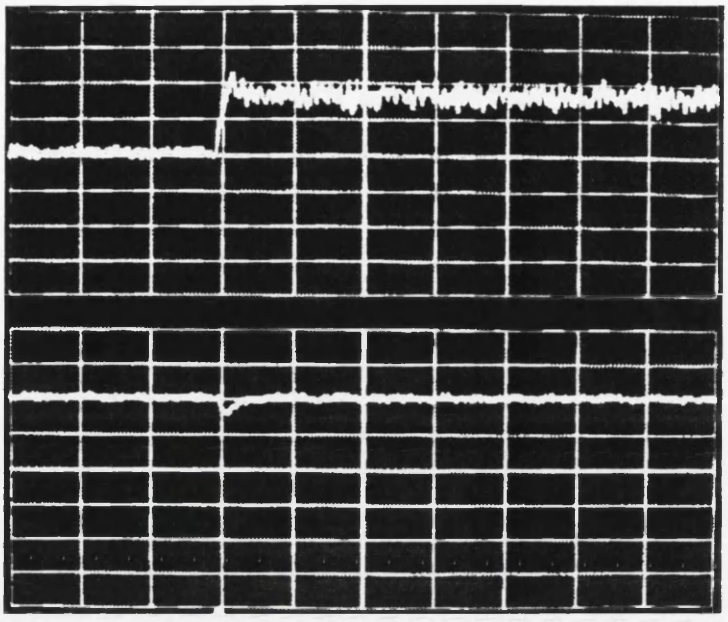

Figure 66: Using Speed-Sensor: Step-load change 0-0.86Nm @400rpm. Torque (top) & Speed (btm). (0.5Nm/div, 200rpm/div, 0.1s/div.)

7.4 Flux-weakening Operation

The speed range was extended beyond the base speed (1500rpm) using flux-weakening. Above the base speed the motor is operating with constant power. The maximum speed at which the drive could be applied a 90% step-load was 2750rpm, giving a constant-power-speed range of 1.83:1. The maximum constant power-speed range for the motor used is 2.13:1 [60]. The limiting factor at this speed is probably a combination of low switching frequency, and small flux-linkage magnitude. Fig. 67 shows the motor accelerating from 0rpm to 2750rpm. Notice the characteristic slowdown in acceleration when the flux-weakening region is entered (1500rpm).

7.5 Steady-State Performance

The phase current vs. torque is plotted in Fig. 68. This agrees well with the theoretical current (Fig. 31). The measured currents are slightly larger than the theoretical, but this is to be expected as the theoretical results do not include iron losses.

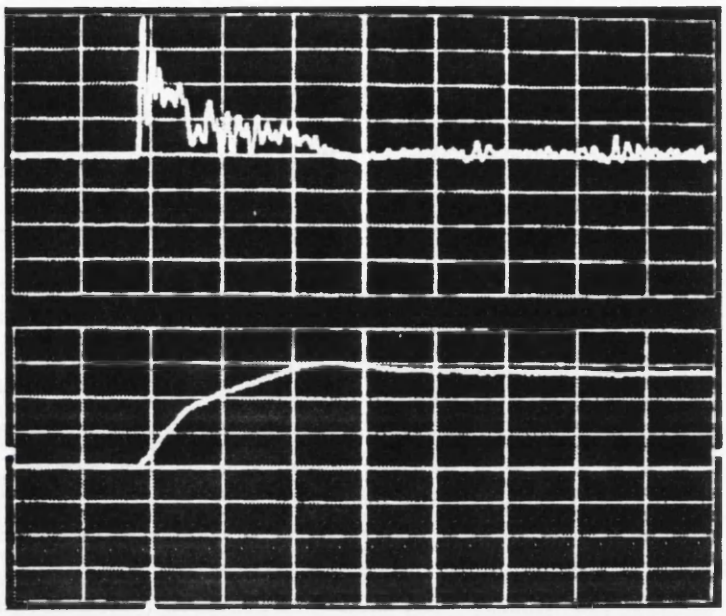

Figure 67: Sensorless: Start 0-2750rpm. Torque (top) & Speed (btm). (0.5Nm/div, 1000rpm/div, 0.1s/div.)

The efficiency is shown in Fig. 69. As expected the efficiency of torque vector control is lower than constant current angle control, except at rated torque. The major part of the losses in the motor was due to copper losses (relatively high per unit resistance). The iron losses were found to be an almost constant 13W regardless of speed and torque. The efficiency could easily be improved by applying an efficiency optimising outer loop to adjust the flux-linkage magnitude. However this would affect the dynamic response.

A comparison of power factor for torque vector control and maximum power factor constant current angle control (MPFC) is shown in Fig. 70. As can be seen the power factors of the two control methods converge when the torque is increased. The two curves are shifted 0.07Nm with respect to each other because the torque vector control is set for maximum efficiency at rated torque while MPFC is set for maximum power factor.

The steady-state speed regulation (table 2) of the drive is generally better than $\pm 5\%$ for speeds in the range 400-2750rpm. The absolute speed regulation is almost constant at speeds below base speed, and most likely due to offsets in the flux-linkage measurements. Using a speed sensor (resolver) improved the speed regulation by a

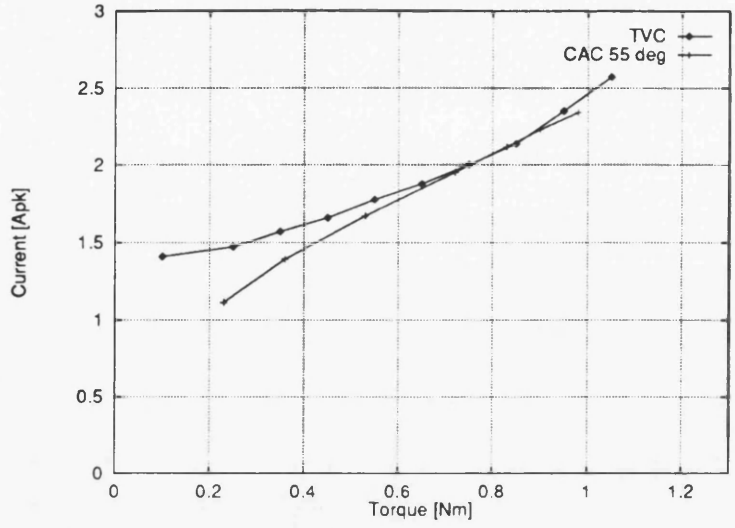

Figure 68: Phase Current @1500rpm for torque vector control (TVC) and constant current angle control (CAC)

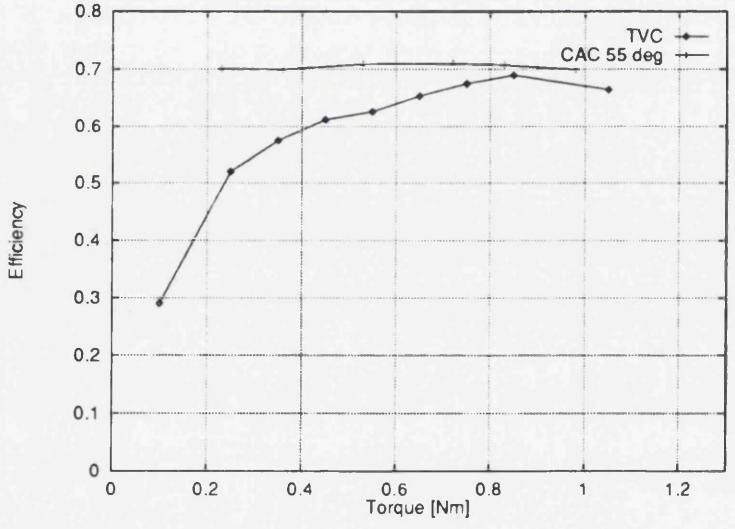

Figure 69: Efficiency @1500rpm for torque vector control (TVC) and constant current angle control (CAC)

factor of 2.

It should be remarked that the resolution of the output speed signal is at most 1.5rpm. Further the speed sensor has a resolution of only 10 bits. The noise may further have been amplified by a short sampling time. These factors probably contributes to the high frequency noise of about $\pm$8rpm on top of a slower signal. A higher resolution speed sensor and longer sample intervals should perhaps have been used to improve the signal to noise ratio in the reference signal. The speed regulation

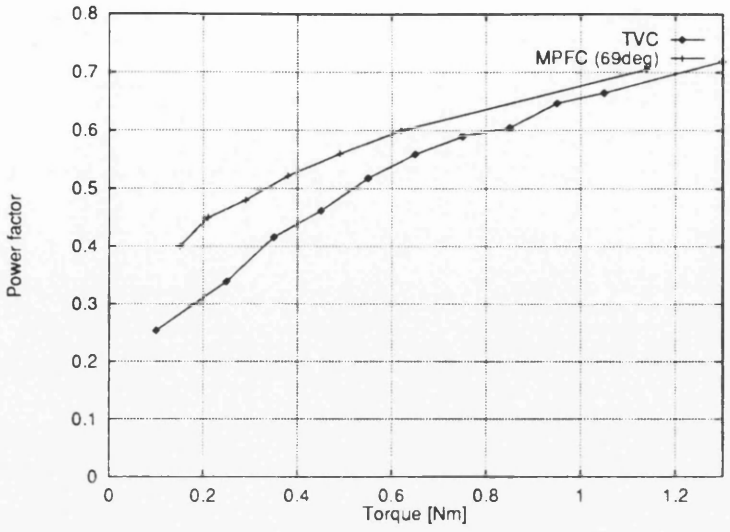

Figure 70: Power factor @1500rpm for torque vector control (TVC) and maximum power factor constant current angle control (MPFC)

Speed [rpm]	No-load [rpm]	Full-load [rpm]
150	±25	±25
400	±20	±30
1000	±20	±20
1500	±40	±40
2750	±50	±50

Table 2: Steady-State Speed Regulation

results may thus be a bit pessimistic.

Chapter 8

Conclusions

A constant current-angle controller for synchronous reluctance motors has been implemented using a Motorola DSP96002-33 signal processor. The control program was a modified version of a simulation program. A control and switching frequency of 1.8kHz was obtained. The low switching frequency was attributed to too frequent use of subroutine calls, DSP96002 not being very efficient on C-style subroutine calls, and less than optimal C-compiler. To improve the speed the control program should be re-written without any subroutine calls. Re-writing in assembler would of course give the fastest execution.

The constant current-angle control algorithms developed and simulated by by Betz [9] were implemented. Good correlation between the simulated and the experimental data was obtained. The constant current-angle controller results are used as a benchmark for the sensorless torque vector controller developed.

Sensorless closed-loop speed control has been successfully implemented for the synchronous reluctance motor. The control consists of an inner self-synchronising torque loop, and an outer speed control loop. The torque vector control theory proposed by Boldea [8] has been used for the inner torque loop. The speed control was implemented using a normal PI-controller. The speed was estimated from the angular velocity of the flux-linkage vector.

Analog integration of $(v - Ri)$ is used to measure the the flux-linkage vector. The

rest of the control was implemented using the same DSP96002 system as used in the constant current-angle controller. The control frequency for the sensorless controller was 10.4kHz. The inverter switching frequency was 5.2kHz, half the control frequency.

Fully sensorless operation has been achieved with a base speed range of 400rpm-1500rpm in which a step-load change of 90% full-load torque can be applied. For a step-load of 50% full-load torque the speed range can be extended downwards to 150rpm.

The factor that limits the low speed operation of torque vector control is the uncertain knowledge of the phase resistance. At very low speeds any error in the resistance may cause the position of the flux-linkage vector to be determined incorrectly. This may result in a loss of synchronism. When performing speed reversals the drive will pass through the low speed region fast enough not to lose synchronism. When operating with a speed sensor the lower range may be extended because a step load change will not cause the speed to dip as low.

Flux-weakening operation has been implemented to extend the top speed using constant power operation above 1500rpm. The constant-power speed-range achieved was 1.81:1, this compares well with the 2.13:1 speed range obtained under current-angle control by Soong [60]. Overall speed range is thus 6.9:1 for 90% step-load change, and 18:1 if step-load changes of less than 50% are used. Flux-weakening under torque vector control is significantly easier to implement than under current-angle control because determination of the correct current-angle is dependent on both saturation and the iron-loss resistance. Torque vector control however, operates using direct flux-linkage and torque control and hence is not much affected.

The steady-state speed regulation for sensorless torque vector control in the speed range 400–1500rpm was ±5%–±2%. The speed regulation obtained when using a speed sensor was ±3%–±1%. This is comparable to operation under constant current-angle control. The speed-regulation under torque vector control is adversely affected by flux-linkage offsets. Flux-linkage offsets will cause a pulsating torque that affects the operation of both sensorless and resolver operation. The flux-linkage

offsets cause a further problem with sensorless operation by injecting a disturbance, pulsating at the rotor frequency, into the speed estimate itself.

The dynamic performance has been evaluated by performing speed reversals and applying step-load changes. To go from -1500rpm to +1500rpm under torque vector control takes about 150ms regardless of whether a speed sensor is used or not. This is almost exactly the same as was obtained for the constant current-angle controller. The speed reversal time is mainly governed by the amount of torque the drive produces, which is the same in all cases. The main difference between the sensorless operation and operation with a speed sensor is the settling time. With a speed sensor (torque vector control or current-angle control) the drive does not overshoot. However, when operating under sensorless control it over-shoots and takes about 325ms to settle. This is mainly due to the delay caused by filtering and the abrupt change in torque which makes the speed estimator think the speed is lower than what it actually is.

The response of the sensorless torque vector control to a step increase in torque from 0% to 90% of rated torque was a 130rpm dip in speed with a recovery time of 400ms. The dip in speed and recovery time was largely constant regardless of speed. The dip is mainly a function of the delay in the speed estimator. The corresponding data for a constant current-angle control was 120rpm and 200ms. For torque vector control with speed sensor the dip was 70rpm with a recovery time of 50ms.

The theoretical rate of change of torque for torque vector control is higher at low speeds and light loads than what it is for a efficiency optimized current angle controller. This implies that the torque vector controller should have a faster torque response. With varying loads torque vector control has a much more constant rate of change of torque than constant current-angle controllers. How much this has to say in practice is difficult to assess. It seems that the rate of change of torque is high enough for both torque vector control and constant current-angle control to have little influence on the speed reversal. Torque vector control with a speed sensor seems to have a slight edge with regard to step-load changes. However, the differences are so small that it may be due to different tuning of the PI-controllers.

The efficiency of the basic torque vector control matches that of the maximum efficiency constant current-angle controller only at rated speed and torque. The efficiency of torque vector control becomes worse at lighter loads. However, an efficiency optimizing loop can be put around the speed and torque loops. The efficiency optimizing loop would be used to regulate the flux-linkage magnitude to obtain maximum efficiency at all operating points. Some dynamic response would have to be sacrificed. The dynamic response of torque vector control would then become comparable with that of the constant current-angle control. The maximum efficiency for the test motor was 70%. This might seem low, but the motor is only rated 120W and has a relatively high resistance compared to larger motors. The efficiency is greater than that of the original induction motor (61.2%).

The power factor of an efficiency optimized constant current-angle control and a torque vector controller coincides at the rated torque and speed. At lower speeds the constant current-angle controller is better. The power factor at rated speed and torque for torque vector control was 0.62 compared with 0.66 for a maximum power factor constant current-angle control. The maximum *fundamental* power factor for the motor is 0.9 (partly due to its resistive characteristic). The *fundamental* power factor for the original induction motor was 0.7.

8.1 Summary and further work

A fully-sensorless closed-loop-speed-control synchronous reluctance motor speed drive has been produced. It has a wide base-speed range of 3.75:1 and can be extended to 6.8:1 using constant-power flux-weakening. The transient performance is not as good as for a drive with a speed sensor. However, torque vector control can be used with a cheap speed sensor (eg. tacho generator) and can then provide comparable or better performance than constant current angle controllers without the need for an expensive rotor position sensor (encoder/resolver).

The efficiency at light loads is not as good as for a constant current-angle controller, but can easily be improved.

Typical applications that can accept the performance of a fully sensorless implementation are: Heating and air-conditioning systems, pump drives and electrical vehicles. For hostile environment applications sensorless operation may be so desirable that some compromise on performance is acceptable.

The totally sensorless operation requires at the moment the computing power of a DSP. However, it should be possible to implement a integer version to run on a 80196 or possibly even a 8051.

The basic torque vector control is simple and ideally suited for implementation as an ASIC providing closed loop torque control. If the drive was operated with an inexpensive speed sensor such as a tacho-generator a system with good dynamic performance and low cost could be made. In both cases use of torque vector control will save the coset of a £70–£200 resolver/optical encoder while retaining closed-loop speed control. Torque vector control is ideal for applications that only require torque control eg. electric power drills.

Future work includes: implementation of torque vector control in ASIC, improving speed estimator, implementing efficiency optimization, and enhanced or alternative scheme for sensorless low speed operation.

By implementing the TVC in an ASIC higher switching frequencies can be used without concern about processing power. An increased switching frequency would naturally improve the torque quality and reduce flux-linkage ripple.

Reduced flux-linkage ripple would also mean that less filtering is needed in the speed estimator thus reducing the delay and improve performance. Since the speed-loop only needs a relatively slow update frequency a low-cost processor could be used to implement fully sensorless torque vector control.

The fully sensorless torque vector control system could possibly even integrated into a single smart-power module including power devices, mixed-mode ASIC and microprocessor (eg. 8051).

Appendix A

Motor and System Data

Motor:

L_d	=	180mH(unsat)
		152mH(sat)
L_q	=	24.5mH
R_{phase}, R	=	8.1Ω
Pole-pairs, p	=	2
$V_{\text{phase}_{\text{rated}}}$	=	66Vrms(Y)
$I_{\text{phase}_{\text{rated}}}$	=	1.7Arms
$\omega_{m_{base}}$	=	1500rpm
T_{rated}	=	0.95 Nm

Load data (motor and load):

Inertia	=	0.00044 kgm^2
Friction coefficient	=	0.00015 Nm/rad/s

Inverter & control data:

$V_{DC-link}$	=	150V
λ_{peak}	=	0.2Vs

TVC control:

$T_{control} = 96\mu s$

Maximum Inverter switching frequency = 5.2kHz

Appendix B

Design of DSP Controller and IGBT inverter

B.1 Introduction

B.1.1 Controller Implementation

The philosophy behind this controller was to make a controller capable of implementing any control algorithm that might be devised for the synchronous reluctance motor. This chapter describes the hardware design choices, implementation, problems encounter ed during development, and solutions. One of the earliest design decisions to be taken is the decision of how to implement the controller:

1. Hardware-only implementation using discrete devices and ICs: This design would result in a controller that might be overly complex or have limited flexibility. It might require major modifications to implement new algorithms, and would be suitable only for small-scale production.

2. Hardware-only implementation using application-specific ICs (ASIC): Using ASICs the hardware complexity could be reduced and extra flexibility added to the system. However the development of ASICs is expensive and if an algorithm needs revising new ASICs might have to be made. This design

would be suitable for large scale production.

3. Microprocessor executing control algorithms: Using a microprocessor the result is a clean hardware design that would require no or minor hardware modifications for implementation of new control algorithms. New control algorithms can be implemented by software upgrades. This method requires a powerful microprocessor and this might at present make the design suitable only suited for research and development or for special cost-insensitive applications.

Of the above designs the software-based design (3) was chosen as it is an ideal platform on which to develop new control strategies. It offers a fast test cycle where algorithms can be tested within minutes after they are developed.

B.1.2 Power electronics and interface implementation

The power rating of the inverter is also a decision that had to be made at an early stage in the development. It was decided to design the inverter for a continuous output power of 7.5kW. This choice was made because motors of this power rating start to exhibit characteristics similar to those of larger machines; several motors and frames of this size were available; and there is a large body of design and performance data on induction motors at this power-level. It is also a very widely used rating in the industry.

As can be seen from Fig. 71 there is a natural division between the low-voltage control electronics and the power inverter. It thus makes sense to make a two-unit system. By having the control electronics in a separate box it is protected from most of the electrical noise emitted by the power electronics. By also creating an interface specification for the interface between the two units a mix-and-match approach of controllers and inverters can be adopted in the future as more controllers and inverters are being built using this interface. The advantages of this modular approach have already been proven as a simple hardware-only three-phase current controller has been built using the inverter described in this thesis. The simple hardware-only

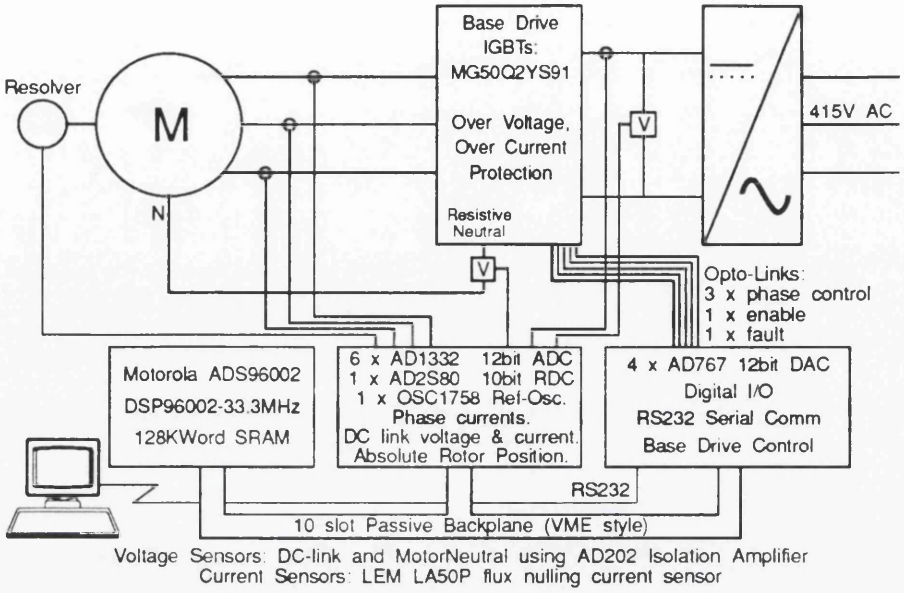

Figure 71: Block diagram of synchronous reluctance motor controller

controller is used for steady-state motor characterisation tests, a description of this controller can be found in section D.

B.2 Design of DSP based Control Hardware

B.2.1 Selection of Processor

The selection of processor was based on the idea of having a system where a simulation program could be converted into a real-time control program with the minimum number of modifications. To do this the processor had to:

1. Support floating-point operations in hardware.
2. Support high-level languages.
3. Execute code fast.

The main competitors were the Texas Instruments TMS320C50 and the Motorola DSP96002-33. Both processors are digital signal processors (DSP) and support floating-point operations. C-compilers were available for both processors.

There would appear not to be much difference between the two processors. The TMS320C50 has a long pedigree in real-time control applications, but it is backwards compatible with earlier versions of the TMS320 series which had a rather peculiar instruction-set. The DSP96002 however is a new design where the instruction-set has been constructed with high-level languages in mind.

The DSP96002 was chosen over the TMS320 on the merit of an enhanced instruction set, which should result in faster code. The DSP96002's performance when clocked at 33.3MHz is 16.5 MIPS and 49.5M FLOPS peak throughput. This is slightly faster then the TMS320C50. Another attractive feature of the Motorola DSP96002 is that it uses a "super scalar" design allowing more than one instruction per cycle. The bus interface of the DSP96002 is also particularly well suited for interfacing to both fast and slow peripheral-devices as the number of wait states is individually programmable for different parts of the memory. This ensures optimum performance of both memory and peripheral devices.

B.2.2 Selection of Processor Board

Having selected the DSP96002 it was decided to get a ready-made processor board as the 96002 operates at 33.3MHz which makes design of the PCB critical, and requires a multi-layer PCB. DSP96002-based processor boards were available from Loughborough Sound Images and from Motorola.

The Loughborough Sound Images board is a PC expansion board. To interface hardware to this system is by a proprietary expansion bus called a "DSP-link". External devices such as AD-converters would have to be external as it is difficult to work on development boards inside a PC, and because the power supply in a PC is not intended to drive analog circuitry. The DSP-link would have to be brought out from the PC on a ribbon cable to interface with the external devices. As the system is going to be used in an electrically noisy environment where high voltages and currents are being switched, it seems foolish to have high-speed TTL signal running over a long ribbon-cable. The delivery date was also uncertain for this board.

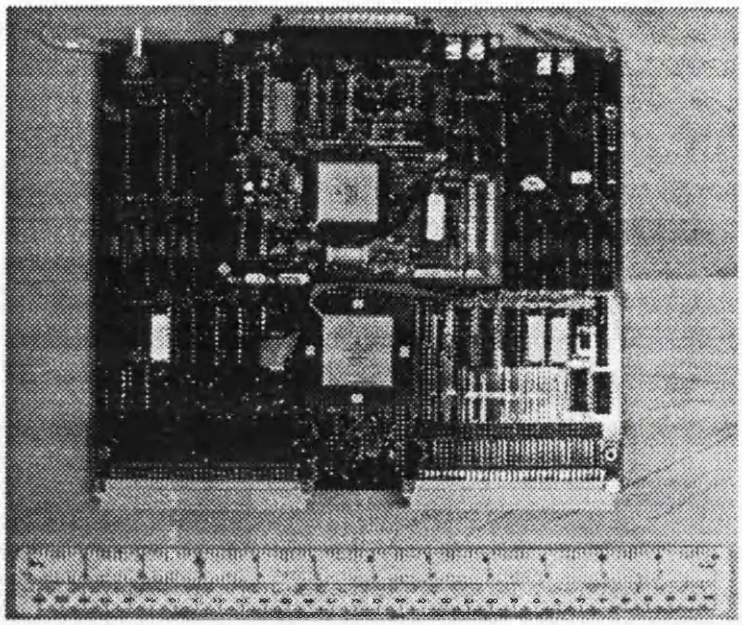

Figure 72: Motorola DSP96002ADS Development Board

The Motorola DSP96002 board is a stand-alone double-size Euro-card. The processor bus was available on two 96-pin connectors. The processor board and the necessary expansion boards could be housed in a 19" rack-system with the processor bus being distributed to the expansion cards over a passive backplane. The Motorola DSP96002ADS board was chosen because the entire control system could be housed within a single unit which is desirable in electrically noisy environments. The Motorola development system includes 128k words (32 bits) of zero wait state static RAM and 2k word of EPROM. Having 512kB of RAM might at first seem excessive; however, replacing complex equations with large multi-dimensional look-up tables saves time. The larger the look-up tables the better the accuracy. Another important reason for choosing the Motorola board was that it was available immediately.

B.2.3 DSP Controller Architecture

One of the aims of this controller system was to make it flexible, this has partly been achieved by executing the control algorithms in software. However, to make the system truly flexible the hardware must also be made equally easy to upgrade.

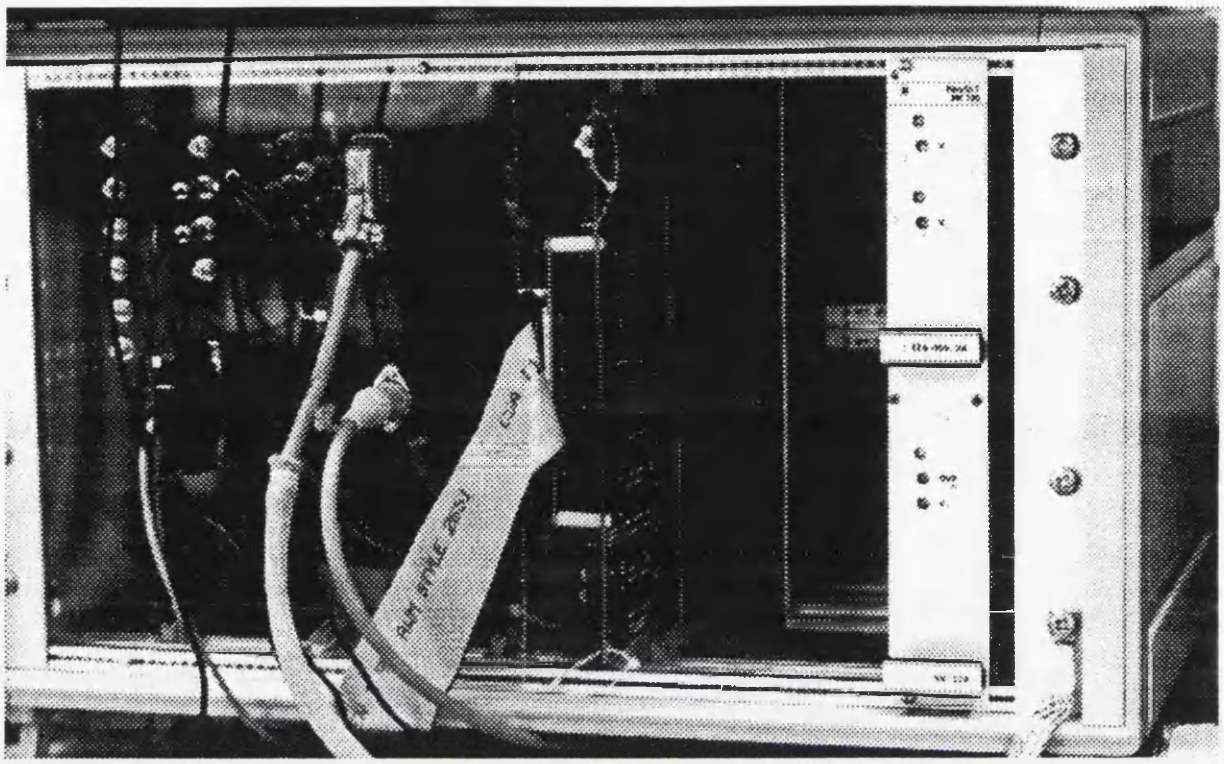

Figure 73: DSP96002 Control Unit

The best method for achieving flexibility is to use a system where all the system components that are likely to change reside on separate plug-in boards.

The DSP96002ADS board is of a double Euro-card size type, with the processor buses brought out on two IEC 603-2 (DIN 41612) 96/96 VMEbus style connectors. The controller is thus well suited for building into a 19" rack system which is fundamentally based around the idea of plug-in modules. It was decided to use a standard 19" rack of double Euro-card height to house the DSP board and have a passive backplane distributing the DSP's data and address bus to the expansion modules (Fig. 73). Fig. 71 shows a block diagram of the complete controller/inverter system. The DSP control system is located at the lower left of the diagram, where the DSP96002 can be seen connected to the expansion cards through the passive backplane (capable of housing 10 expansion cards depending on component height). To the right of the DSP board are the two expansion boards that at present make up the control hardware. The functions of the expansion boards are described in full in sections B.2.6 and B.2.7.

B.2.4 DSP96002 Memory Architecture

Before describing the implementation of the controller using the DSP96002ADS development board, the memory architecture and bus interfaces of the DSP96002 chip [44] must be examined.

From the programmer's point of view there are three separate memory spaces in the DSP96002. Each memory space is 32 bits wide and is addressed using 32-bit linear addressing. The first is the P memory, where all program code is stored. The others are X and Y memory, used to store constants and variables. X and Y memory can each hold a single-precision floating-point number in each location. Together X and Y form L memory. L memory is used to store double-precision floating-point numbers or other data types that can be conveniently accessed using a single pointer for two data items, such as complex numbers.

Moving to a hardware designer's point of view, the advantages of forming L memory is that the processor has two identical 32-bit address and data buses known as port A and port B. By placing X memory on port A and Y memory on port B one can fetch two data items, using parallel data moves, in just one bus cycle. All memory must be mapped either to port A or to port B, except a small amount that is internal RAM/ROM and processor control registers. The 4 giga-word of memory for each memory space P, X, Y is individually mapped to ports A and B on a 512 mega-word segment basis. This means that for each space there are 8 segments that can be mapped to either port A or port B. The mapping is controlled through a processor control register located internally in the processor at the top of the X memory.

The DSP96002 has the facility to control the number of wait states used for memory access, to allow slow memory or devices to be used. The number of wait states is controlled separately for each port A/B and the memory spaces X/Y/P. The number of wait states can be individually selected in the range 0-15.

B.2.5 Memory Configuration & Backplane Bus Design

On a typical microprocessor system one expects to find a large range of devices connected to the processor bus. Some processors such as the Intel x86 series have special instructions to access an I/O memory space. The DSP96002 does not have a special memory space for I/O devices, so memory and I/O devices must share the same memory space.

When decoding the address lines to select a specific device it may be done fully, in which case the device appears in only one location of the memory map. To fully decode an address gives the highest utilisation of the memory space, but might require a large number of devices to implement the decoding circuit which in turn might slow the system down.

A partial decoding scheme will result in the same device appearing in multiple places in the memory map. However the partial decoding is fast and makes the decoding circuit simpler. Not all devices have the same response time, so the insertion of wait states is required for slow devices. On most processors the insertion of wait states is done by having a hardware wait-state generator which will use the chip-select lines from the address decoder to activate the insertion of wait states when accessing slow devices.

As not many I/O devices use more than 16-bit wide data buses, it is only necessary to buffer and bring the lower 16 bits of the data bus onto the backplane.

Memory Mapping and Decoding

As the DSP96002 does not have a special I/O access mode all I/O devices are mapped to memory addresses together with ROM and RAM. The DSP96002ADS development board has been configured as follows:

2k word EPROM	:	Port A, P-memory, Address FF000000h-FFFFFFFFh.
32k word RAM	:	Port B, X-memory, Address 00000000h-1FFFFFFFh.
32k word RAM	:	Port B, Y-memory, Address 00000000h-1FFFFFFFh.

The memory on the DSP96002ADS has been only partly decoded, so the content of the EPROM and RAM repeats itself through the assigned memory range.

The I/O devices on the expansion bus have been assigned the following memory space

I/O Devices : Port A, X-memory, Address 10000000h-FEFFFFFFh.
I/O Devices : Port A, Y-memory, Address 10000000h-FEFFFFFFh.

Partial decoding is used throughout the system and the decoding scheme does not differentiate between X- and Y-memory access. The devices will be accessed as X- or Y-memory depending on the speed of the device as explained in section B.2.5.

The address decoding used is as follows:

A31-A28 : Full decoding for board select.
A27-A16 : Not Present on Backplane.
A15-A4 : Partial decoding for selection of device in board.
A3-A0 : Internal register select in device.

The decoding system requires each expansion board to fully decode the 4 most significant address lines as a board select address. Board address #0 is not used because this address range is assigned to RAM on port B. Board address #15 is not used either since it is partly reserved for DSP internal control registers. The maximum number of expansion boards is thus 14.

The boards are not required to follow any special decoding scheme for the lower 15 address lines. The following scheme has been used for the boards made so far and it is an advantage to keep as much as possible of the bus interface on the expansion cards similar so development time is not wasted.

The decoding circuit used is shown in principle in Fig. 74, and functions as follows:

A3-A0 is buffered and fed to any device requiring internal register select.

A15-A4 is used to select the individual devices in the following way: Each address line controls a separate device and is ORed with the active low board select line giving an active low output when the device is selected. Using this scheme the maximum number of devices per board is 12. This is quite economical as each additional device only requires an OR gate to be added to the decoding logic. It is not envisaged that the maximum number of 12 devices per expansion board will be a limitation.

A31-A26 is compared with the DIP-switch setting and generates a board select signal.

I/O Device Access Timing

The DSP96002 does not support a hardware wait-state generator, but allow software to set the number of wait states on a per-port and memory-space basis. One could get away with accessing all devices at the speed required by the slowest device, however this wastes time if large amounts of data are to be read from fast devices. To ensure maximum performance this system has a fast and a slow access mode for I/O devices.

To achieve this all X and Y memory RAM on the DSP96002ADS is configured to be on port B. All P memory is mapped to port A. All I/O devices are accessed through port A as X or Y memory.

To ensure maximum program performance the 25ns static-RAM port A P-memory, and port B X- and Y-memory are accessed using zero wait states. To get the maximum performance from fast devices port A Y-memory is set programmed to 2 wait states. This gives an access time of 90ns which is equivalent to a bus speed of 10MHz. To access a device using this speed it should be read from or written to as Y-memory.

The slow devices which would not be able to respond to the fast 2-wait-state access of Y-memory can be accessed as port A X-memory. The port A X-memory has been programmed to use 5 wait states. This gives an access time of 180ns which

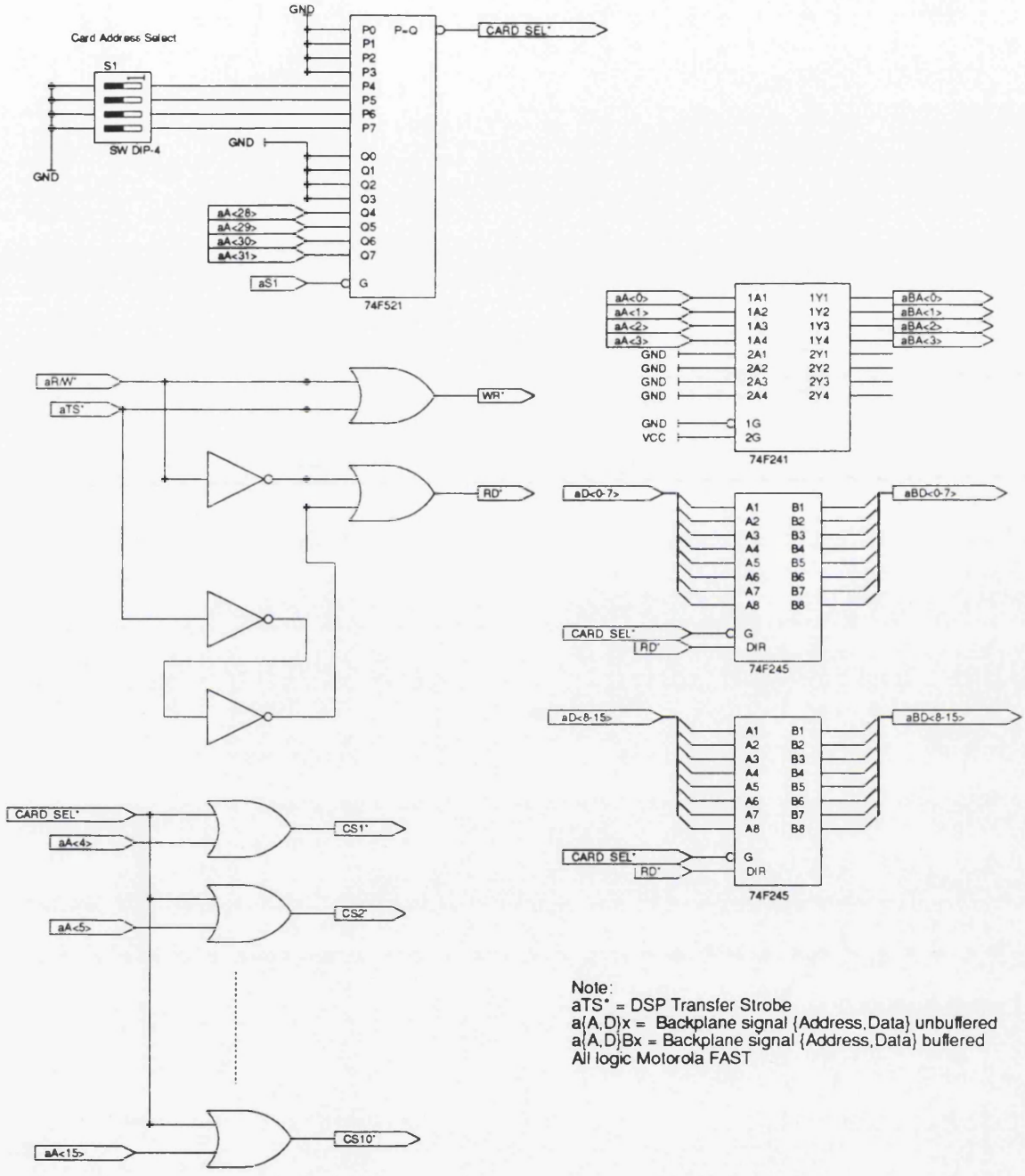

Figure 74: Partial-Decoding and Buffer Circuit used on Expansion Boards (extract)

is equivalent to a bus speed of 5.56MHz. An access speed of 5.56MHz is almost universally acceptable to any I/O devices, except for very old devices.

This configuration of memory and assigning of wait states is intended to give good I/O performance and near optimum program execution. The only compromise on program performance is that X- and Y-memory reside on the same port. This means that any L memory access and parallel data moves will take two memory access cycles instead of one. How many L memory accesses or parallel data moves that are used in a program depends on how the program was generated. Hand written highly optimised assembly code tends to use more parallel data moves than compiler generated code. The controller is intended to be programmed in a high level language and so the performance impact, due to X- and Y-memory being on the same port, might not be noticeable. If the DSP96002 had allowed wait states to be assigned on the same basis as memory is mapped to specific ports the system could have been designed without any performance compromises.

DSP96002ADS Development System Implementation Issues

The Motorola DSP96002ADS application development system board is connected to a PC using a Motorola proprietary interface board in the PC. Using the supplied debug/monitor program 96002 code can be downloaded from the PC to the DSP. The monitor program can also be used to enter programs straight into the DSP for test purposes.

The DSP is configured to boot (start after reset) from P memory address FFFFFFFEh on port A, which is mapped to the EPROM memory. As supplied the EPROMs are blank and will most likely generate an illegal instruction interrupt. The interrupt vectors are located at the beginning of the RAM starting at 00000000h. At power-up these locations will contain random data causing random code to be executed.

Normally the DSP will be halted from the PC using the debug interface, at this point and code is downloaded an executed. This might be sufficient if the

board is used only for evaluating code; however, we cannot have a system that controls power electronics start executing random instructions. The consequence of executing random code can have quite dangerous effects if connected to an energised drive system.

Clearly the EPROMs must be programmed to avoid executing random code. The EPROMs that came with the development system where 35ns ultra fast EPROMs so that code could be executed from the EPROMs with zero wait states. The facility for programming special devices like these were not available so the special 35ns EPROMs were replaced with standard 150ns EPROMs. This can be done since after a reset the DSP is running as default with 15 wait states and the memory cycle time of the processor becomes 480ns. The 150ns EPROMs are thus fast enough for executing the code at startup. However, when running with zero wait states the EPROMs are no longer readable as they would be accessed using a cycle time of 30ns which is well beyond their capability.

To achieve the maximum performance programs should be executed from memory with zero wait states, hence the EPROMs cannot be used to store the main program. Instead the program is downloaded after each power-up from the PC. This method of working gives a short development cycle since there is no need to burn new EPROMs for each revision of the control program. Clearly this is not suitable for a product that is to be put in production, but it works well in a research environment.

The boot ROMs are written so that they contain only enough code to take the development board into a known state at power-up without affecting the subsequent execution of the control program; hence they need not be reprogrammed with each new revision of the control program. The expansion boards should be designed such that they enter a "safe" state after reset or power-up. Once board-initialisation code in the EPROMs has executed the DSP goes into an endless do-nothing loop and stays in the loop until the processor is halted by the PC and a program is downloaded into RAM and set to execute. The initialisation code is shown in Fig. 75, and its operation is explained below.

```
1   ; BOOTROM.ASM
2   ; Programs DSP96002ADS to map memory to correct ports
3   ; Version 1.0
4                   org pa:$fffffffe      ;Reset Vector Address
5                   jmp boot-start        ;Jump to Boot Routine
6                   org pa:$ffffe000      ;Start of EPROM
7   boot-start      reset                 ;Reset all on chip Peripherals
8                                         ;and Interrupt Mask Registers
9                   move #$00010100,d0.l  ;Map Addresses to Physical Memory Port
10                  move d0.l,x:$fffffffc ;Write to Port Select Register
11  lo1             jmp lo1               ;Wait here until Host takes Control
```

Figure 75: DSP96002ADS Boot EPROM Assembly Listing

Lines 4 and 5 set the reset vector to point to the start of the EPROM.

Line 7 resets all the internal peripheral devices and interrupt mask registers in the DSP96002.

The most important lines are 9 and 10; here the DSP is programmed to map X and Y memory in the range 00000000h-1FFFFFFFh to port B. If this was not done, data downloaded from the host to X or Y memory would be written to non-existent memory on port A.

Line 11 is an infinite loop where the processor waits for the host computer (PC) start downloading the control program. The processor is halted through the ONCE (on-chip-emulator) debugging interface by the host computer. The ONCE can completely control the operation of the processor. The control program is downloaded through the ONCE interface. Once the control program is downloaded the processors instruction pointer register is set to the start of the control program, and the processor released.

Backplane Implementation Issues

The DSP96002ADS makes the address- and data-bus available on two IEC 603-2 (DIN 41612) 96/96 connectors. The connector signal layout partly follows the VMEbus layout; however it differs in a few important places. In particular some of the data- and address-bus signals use VMEbus signal lines not intended to carry

high-frequency signals. This makes it impossible to connect the DSP96002ADS directly to an "off the shelf" VMEbus backplane.

Since a standard VMEbus backplane was not suitable, two uncommitted BICC-Vero backplanes were purchased. The backplanes had room for 10 IEC 603-2 (DIN 41612) 96/96 connectors each giving a maximum number of expansion cards of 9; however, the actual number of expansion boards will depend on the height of the individual boards.

To test the DSP and backplane a small test program was executed; however when the DSP was connected to the backplane the DSP would no longer execute the program correctly. The program would execute correctly when singled-stepped, and by trial-and-error it was found that the DSP would only run when all memory access was slowed down with 4 wait states.

It was clearly unacceptable to run the control program with 4 wait states. By examining the data-bus with an oscilloscope it was found that the backplane capacitively loaded the signal lines too much giving long rise- and fall-times. After looking at the DSP96002ADS circuit diagrams it became clear that the address- and data-bus were connected straight from the DSP96002 to the backplane connectors. There were buffers on the DSP96002ADS but unfortunately these only buffered the on-board memory. It seems a bit odd that Motorola would make a system that is so obviously suited to be plugged straight into a backplane but not buffering the bus going to the connectors when the DSP96002 itself can only drive two TTL loads.

Having identified why the DSP would not run when connected to the backplane the solution was clearly to insert some form of bus buffers. Ideally the best solution would be to make a new CPU board with buffers on board. However this was not a practical solution in this case as suitable multilayer PCB making facilities were not available. Another solution would be to make an active backplane with built-in buffers. This still involves making a multi-layer PCB and is not an acceptable solution. The solution that was decided on was to make and insert a small bus-buffer board between the DSP96002 connector and the backplane connector. An unfortunate consequence of inserting the board is that the DSP board now protrudes

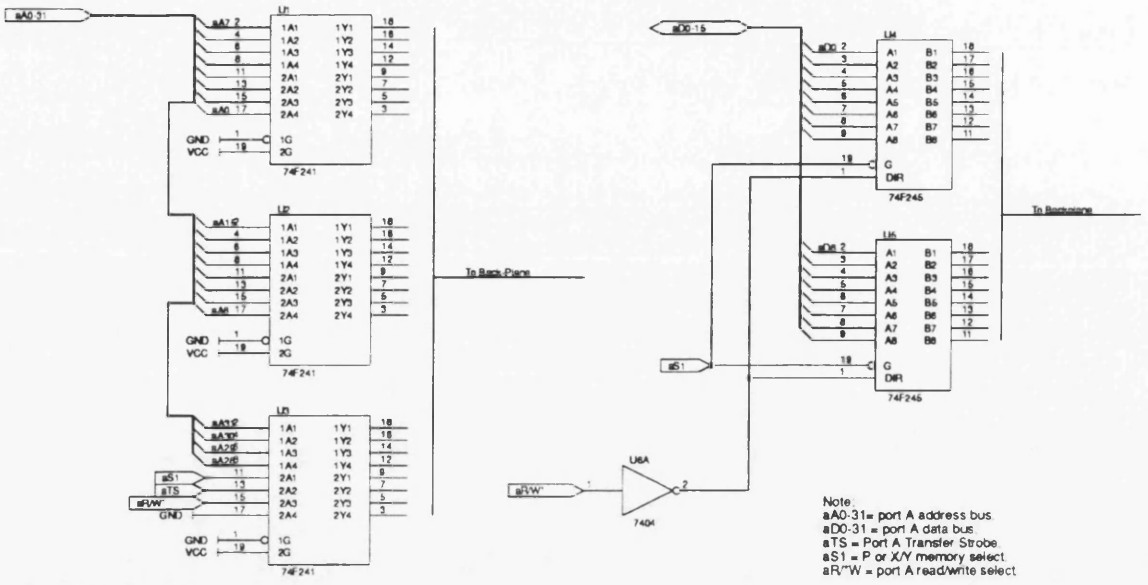

Figure 76: Port A Bus-Buffer Circuit

about 1cm outside the sub-rack making it impossible to fit a flush front-panel. The DSP board fortunately does not protrude outside the main-rack.

Since only DSP port A is used to communicate with the I/O devices it was only necessary to buffer this port. On port B only four signals needed to be brought through to the backplane: the three interrupt lines and the reset line. The interrupt lines are inputs and the reset line is well buffered already. The board between port B and the backplane only serves as a connection board for 4 signal lines (irqa, irqb, irqc and reset). The buffers on port A use Motorola 74F241 and 74F245 FAST bus-driver ICs, capable of sinking 48mA and sourcing 15mA, making them suitable for driving capacitive loads such as backplanes. The delay in these buffers is in the order of 3-5ns. The data-bus buffers only transmit X and Y memory accesses to the backplane, since this is what is needed for access to the I/O devices, reducing the backplane activity. This helps to reduce radiated electro-magnetic noise which might affect ana log circuitry.

Having inserted the bus-buffer board (Fig. 76) the DSP could now execute the test program successfully with zero wait states, showing that the buffer board does not introduce excessive load, crosstalk or ringing on the DSP board.

The bus buffer board did not solve all problems. Wrong values would sometimes

be read from or written to I/O devices. Spurious accesses to devices would also intermittently be generated.

Examining the data- and address-bus on the backplane it was found that there was severe ringing on the signal lines, the signal could go as high as 8V and as low as -2V. The ringing was found to last for more than 40ns. This ringing would cause the address decoders to glitch the chip-select signals to random devices. The "Transfer Strobe (TS)" signal from the DSP signals that data and address lines are stable, and goes active 15ns after the data- and address-buses are applied. Ringing will thus still be going on when the bus is signalled as stable. This problem might not affect slower devices, but fast devices might easily be triggered by the ringing. The digital output (on board #2) consists of 74F174 D-flip-flops and is a prime example of a fast device. The 74F174 can react to a pulse of 4ns width or less. The 74F174 would latch random data through during the time when the address- and data-bus was still ringing. This problem was first noticed because serial communications would stop working when the digital output was accessed. The cause was found to be that random data on the digital outputs would reset the serial-chip because the serial-chip reset is controlled by one of digital outputs.

At first it was attempted to terminate the bus with standard 220R/330R resistor networks. This reduced the spikes but did not solve all the problems. It was noticed that the boards would behave differently if the select address was mostly '1's or '0's fro m when it was mostly a mix. This indicated that there were also problems with transitions from one line affecting adjacent signal lines, known as crosstalk between the lines. An experiment was carried out on the backplane. Rows a and c on the backplane was connected to 0V giving ground tracks between each of the row b signal lines. A standard TTL square wave was applied to one of the row b signal line and a oscilloscope was connected to an adjacent row b signal line which was pulled-up to 5V through a 1.5kΩ resistor. On the adjacent track positive and negative spikes of almost 1V were recorded at the edge of each square wave. This is a a cross coupling of about 20%, far in excess of what is tolerable when considering that the noise margin of TTL logic is only 0.4V. The problem will be worse on the lines driven by

the 74F241 and 74F245 buffer circuits since the crosstalk is dependent on the rise and fall time of the signals. FAST TTL has a rise time of 2ns versus normal TTL's 6ns, thus using FAST TTL increases the crosstalk.

There is not much that can be done with crosstalk except for slowing down the edges, not really an option in a 33.3MHz system. The only practical solution was to go for a better designed backplane. An uncommitted backplane of the desired quality was not obtainable, so the 5 layer BICC-Vero VMEbus backplane originally considered was obtained. This backplane is terminated 330R/470R and has a patented system of micro strip signal guard tracks between the signal tracks. These guard tracks form 0V loops around each signal line. The original choice of the uncommitted backplane was made before it was realised that a bus-buffer board had to be inserted between the DSP and the backplane. With the bus-buffer board in place the re-assignments of the signal lines to avoid VMEbus signal lines not intended for high speed signals could easily be implemented. If a bus-buffer board was not needed this re-assignment would have resulted in an extra patch board, which at the time was undesirable. The cost (£250) of the VMEbus backplane was also thought excessive at the time compared to the uncommitted backplane (£48). The new backplane solved the problems of ringing and crosstalk. It was found that the maximum bus-speed for the fast devices was an acceptable 10MHz. This speed compares well with the 8MHz bus speed used in PCs. To save cost only one of the backplanes were changed to the VMEbus type. The other backplane, which only carries the interrupt and reset lines, still uses the old type backplane. There is however a limitation in that only one of the three interrupts may be in use, otherwise false interrupts may be produced due to crosstalk.

B.2.6 Expansion Board #1

The function performed on this board is to acquire the analog input signals using analog to digital converters. The board has 6 analog inputs at 12 bits resolution. The rotor position is measured using a resolver to digital converter.

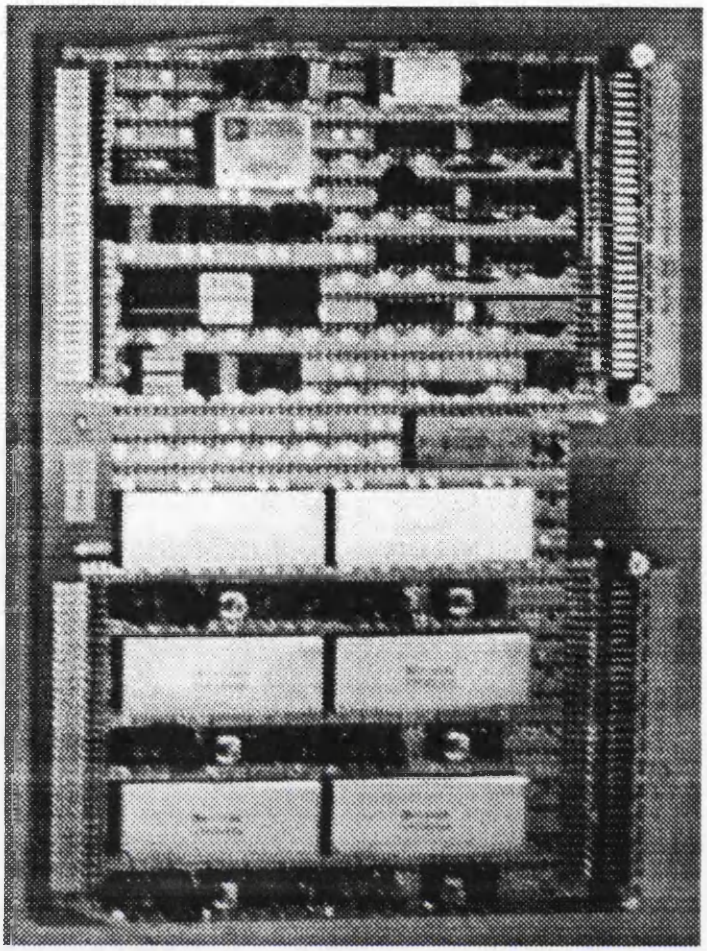

Figure 77: Interface Board#1: ADCs,Timer, Resolver Interface.

The card can be mapped into memory at any of the 14 available address ranges. The devices on this board interface to the backplane through a set of bi-directional data buffers (Fig. 74). The buffers are placed close to the backplane connector to minimise capacitive loading on the backplane and reduce the possibilities for crosstalk.

The expansion board has been made using the speedwire system. Speedwire is significantly faster and more compact than wire-wrap. Speedwire boards feature a ground plane which reduces "ground bounce" by reducing the ground return path impedance. The signal wires run close to the ground-plane giving a more controlled impedance on the signal lines than for wire-wrap or simple double-layer PCBs. When using speedwire attention must be paid not to use long parallel runs of wires in close proximity, otherwise there is a strong possibility of crosstalk.

Analog to Digital Converters

To chose a suitable analog to digital converter (ADC) the application requirements had to be considered. This application requires accurate measurement of the analog values of the respective currents and voltages. To define "accurate" is not easy, but generally it is considered sufficient to have a resolution of 10 bits or more.

The sampling speed of the ADCs is also important. The maximum sampling speed of most ADCs is around 100kHz. Flash converters have much greater speed, but most are limited to 8 bits resolution. For typical motor applications the control frequency is around 5kHz; however, if more than one sample can be obtained during a control interval these can be averaged or digitally filtered to obtain a cleaner signal.

Special features must also be taken into account, for example, three-state microprocessor interface, fast microprocessor interface for DSP applications, or other special features. When looking for a suitable ADC the Analog Devices AD1332 was found to have some very interesting features. The AD1332 has a resolution of 12 bit, meaning that a signal can be resolved into 1 part in 4096 ($\pm 1/2$ LSB). This satisfies the need for accuracy. The maximum sampling rate of the AD1332 is 125kHz, satisfying the sampling rate requirement.

What really distinguished this ADC from the rest was definitely the special features:

1. The AD1332 has on-board anti-aliasing filters which can easily be tuned with external capacitors, making external anti-aliasing filters unnecessary.

2. The chip has a 12-bit wide fast DSP/microprocessor interface, making retrieval of sampled values quick.

3. The AD1332 is capable of a master/slave configuration in which one master controls the sampling of other AD1332s. This ensures synchronous sampling on all channels.

4. The best feature of the AD1332 is the buffering of sampled values. The AD1332 is capable of storing 32 samples in a First-In-First-Out buffer on the chip before

it has to be read by the DSP. The AD1332 can create an interrupt on either full or half-full buffer. This means that the associated interrupt overhead in the DSP can be reduced by a factor of 32 or 16 respectively. The half-full interrupt has its advantages as the interrupt latency (time taken from an interrupt is generated until it is serviced) can be greater since there is no danger of buffer overflow or data overrun. The AD1332 can also be used in a standard one-interrupt per sample mode.

The AD1332 was chosen on the merit of its special features listed above. In particular since on a DSP96002 the interrupt overhead can be as much as $5\mu s$ if a full context switch has to be performed. (A full context switch being defined as preserving all registers and switching stacks.) The time saved per control interval by using the buffered mode can thus be as much as $160\mu s$ or $80\mu s$ depending on whether full or half-full interrupt is used. It was chosen to have 6 ADCs in the system. Having 6 ADCs should cover most configurations typical for AC motor applications. With 6 ADCs all voltages and currents of a three-phase motor could be monitored. Another possibility is to use 2 to monitor the current vector and 2 for the flux-linkage vector leaving two spare for other control inputs, for example speed from tacho-generator and desired speed.

The input range of the AD1332 was set to ± 5V, which produces an offset natural binary output. The AD1332s are all connected together with one as master. This ensure that all samples are taken at the same instant. The sample rate is controlled by an i8254 16-bit programmable timer. The AD1332 has an internal divide-by-20 circuit and the i8254 is clocked by a 10MHz crystal oscillator. The sample rate is thus adjustable in the range 7.7Hz to the maximum sample rate of 125kHz in steps of 7.7Hz. There is however a limit on the lower sampling rate set by how much the internal sample and hold amplifier can be allowed to droop during the conversion. The manufacturer's recommended minimum is 20kHz.

The master AD1332 is connected to the DSP96002 interrupt C. this interrupt can be triggered either at the completion of each conversion or at full or half-full buffer. The AD1332 is accessed using the backplanes fast mode which means that

each data point can be read in just 90ns. If the ADCs are used in half-full buffer mode and all the 6 ADCs are in use it will take only 23μs to retrieve the 96 data points. No problems were encountered during development using the AD1332.

Rotor Position Measurement

The position of the rotor is important if vector based control is to be used. The accuracy of the measured rotor position can influence the performance of the control. Generally a resolution of 1000 per revolution is considered sufficient.

To measure the rotor position there is a choice between optical incremental encoders, optical absolute encoders and resolvers. The incremental optical encoder was not used because on power-up the rotor position can not be determined. The absolute optical encoder has its disadvantage in the number of signal lines used if it is a parallel device. Optical encoders in general are fragile using either glass or thin metal disks. Optical encoders also tend to use TTL level signals making them susceptible to electrical noise.

A resolver was chosen as these devices are more rugged than an optical encoder, and give absolute position with only 6 wires. Resolvers also use balanced signals giving them increased noise immunity. The operation of a resolver is quite simple: a sine wave is applied to a wound rotor through a rotating transformer. There are two coils placed perpendicular to each other on the stator. These coils produce voltages proportional to cosα and sinα respectively, where α is the angle relative to the position of the first coil. The cosα and sinα signals are converted into a digital position signal using a resolver to digital converter (RDC).

The RDC used in this design is the tried and proven AD2S80A RDC from Analog Devices. The AD2S80A can be programmed to produce an accuracy of 10, 12, 14 or 16 bits. The maximum speed is a function of the accuracy selected. The AD2S80A was set to 10-bits as this is accurate enough for most applications, giving a maximum speed of 1020rps according to the manufacturer's data for a 5.6kHz sine wave source. The AD2S80A uses a ratio-metric method for determining the position; however the

overall accuracy depends on the magnitude of the signals being as close to 2Vrms as possible. The accuracy is also best if a harmonic-free sinusoidal oscillator is used, such as the Analog Devices OSC1758. The OSC1758 is capable of driving a resolver, and was set to produce a 5.6kHz sine wave. The frequency was chosen such that the frequency is still within the operating range of the resolver and at the same time high enough to operate the AD2S80A at the maximum operating speed. The AD2S80A is a tracking device and can produce a result 2μs after it is requested. Even if this position is locked until a new conversion is started, the device will continue to track the rotor position in the background. This device is accessed using the slow bus mode, and no problems were encountered using it.

B.2.7 Expansion Board #2

This board provides analog real-time output, serial communication, general digital I/O and a specialised power inverter drive interface. The general description of the expansion board is the same as for expansion board #1, as they both use the same bus interface circuit design (section B.2.6). Following below is a description of how the functions have been implemented.

Digital to Analog Converters

The controller has four digital to analog converters. These converters are used to monitor internal program variables in real time. Variables that are commonly output through these devices are: i_d, i_q, speed, torque and program status. The program status can be used as a simple profiler to determine "hot spots" in the program.

The DACs can also be used to control external analog devices; for example, an external analog current controller could be implemented. The DSP would output desired current magnitude and angle. The external analog circuit would do the actual current control and control the switching of the transistors.

Analog Devices AD767 analog to digital converters were chosen. These devices can produce an output of $\pm$5V with an accuracy of 12 bits from a offset natural

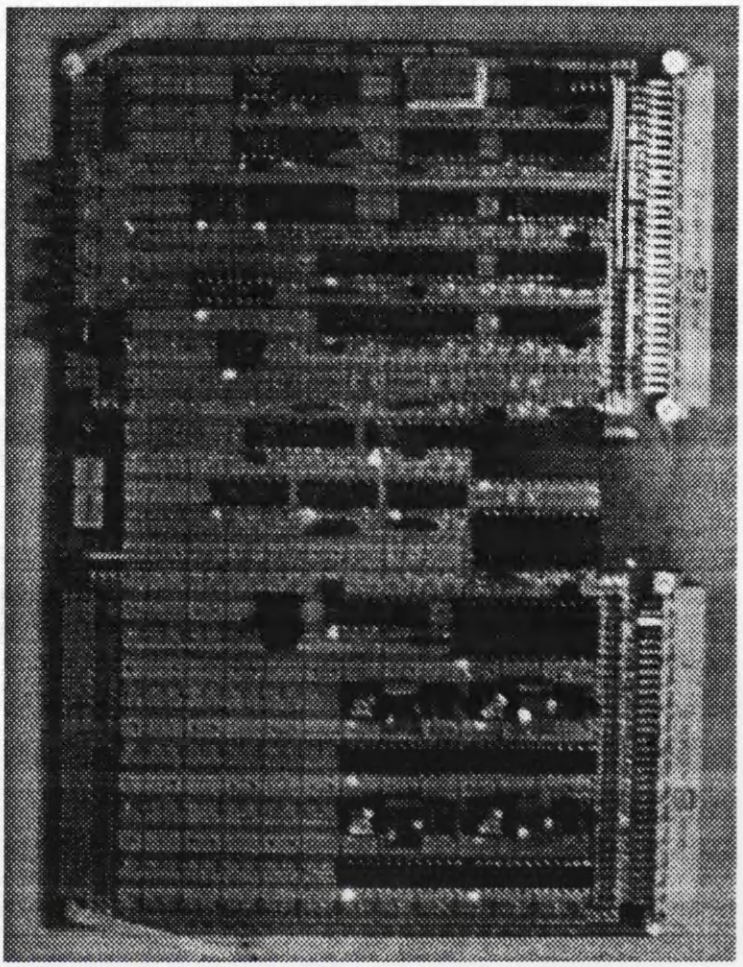

Figure 78: Interface board#2: DACs,Timers, Serial I/O, Digital I/O and Inverter optical I/O.

binary input. This matches the characteristic of the DACs. A problem was encountered using these devices, because the chip acts as a transparent latch. When the chip is selected slight ringing on the data bus during the first ns after the devices were selected sometimes caused the devices to produce a very short output glitch before settling at the desired value. To solve this problem the falling edge of the select pulse to the devices were delayed to ensure that the data bus was stable before the digital data was gated through to the analog output.

Serial Interface

A serial interface is incorporated into the design. The serial interface is used during development for debugging, and can be used to send commands during operation and

to retrieve status information from the controller. The serial interface is implemented using an Intel i8251 universal asynchronous receiver and transmitter (UART).

The i8251 requires two clock signals: the first is the baud rate clock and the second is the system clock. The CPUs that were around when the i8251 was designed used clock frequencies around 5MHz and the system clock was the same as the CPU clock. The i8251 is an old device and cannot handle the fast bus mode, but works fine with the slow bus mode. An artificial 5MHz system clock is provided by one of the 16-bit timers in an i8254. The baud rate is controlled by another of the three 16-bit timers in the i8254. This system can produce most standard baud rates from a 10MHz crystal, and is typically used at 9600bps.

To convert between the i8251's TTL level and RS232-C level signals a Maxim MAX233 chip is used. This chip only requires a 5V supply as it has on-board charge-pumps and capacitors to generate ± 9V exceeding the ± 7 volts called for in the RS232-C standard by 2 volts.

Digital I/O

The system has one 16-bit digital input and one 16-bit digital output. The digital input is implemented using two 74F244 gated latches. The digital output is implemented using three 74F174 D-type flip-flops. These devices are accessed using the fast bus access mode.

This simple implementation was chosen in preference to more advanced solutions using programmable I/O devices because it was desirable to have the I/O as fast as possible. The digital I/O was also only intended for controlling internal controller I/O devices, not as a general interface port. The I/O is distributed between the expansion boards using a ribbon-cable. At present 3 (2 free) input and 3 (2 free) output bits are distributed over the cable with the option of adding two more signals.

The output status cannot be retrieved from the digital output as can be done from programmable I/O devices. This means that it is necessary to keep a copy of the digital output status in memory. To keep the integrity of this system the

copy of the digital output should be read, modified, written back into memory and to the digital output without interruption. This must be taken care of in software, making it slightly more difficult compared to using a programmable I/O devices and a processor that supports read-modify-write. The DSP96002 does not support general read-modify-write so using programmable I/O would not have given any advantages.

Inverter Drive Interface

This circuit normally interfaces directly to the power inverter and directly controls the switching of the inverter phaselegs. The interface has four fibre-optic outputs that connect the controller to the power electronics. Optical fibre have been used as these signals has to be sent a considerable distance in an electrically noisy environment. If electrical signals were used there would be a real risk of them picking up electro-magnetic noise, which could cause undesired switching of the inverter transistors. Optical fibres are totally immune to electro-magnetic fields and so any possibility of the inverter switching due to noise pick-up has been removed.

Three of the outputs are used to control the state of the individual phaselegs. If the output is transmitting light the upper transistor in a phaseleg will be turned on, if not the lower will be turned on. The last output is used to disable or enable all of the transistors in all of the phaselegs: this is done so that the DC-link voltage can be removed from the motor (by the high impedance state of the transistors).

On power-up and after a reset all the outputs are reset, disabling the phaselegs to ensure that the motor is not energised before the control software has been loaded.

The circuit which drives the three phaseleg control optical outputs can operate in three modes, depending on what type of control is being executed. Fig. 79 shows a discrete-logic version of one phase of the phaseleg control circuit which is implemented in a PAL. The function of the modes will be described, but the actual programming sequence will not. The possible modes are:

1. Direct drive: The state of each of the optical outputs is directly controlled

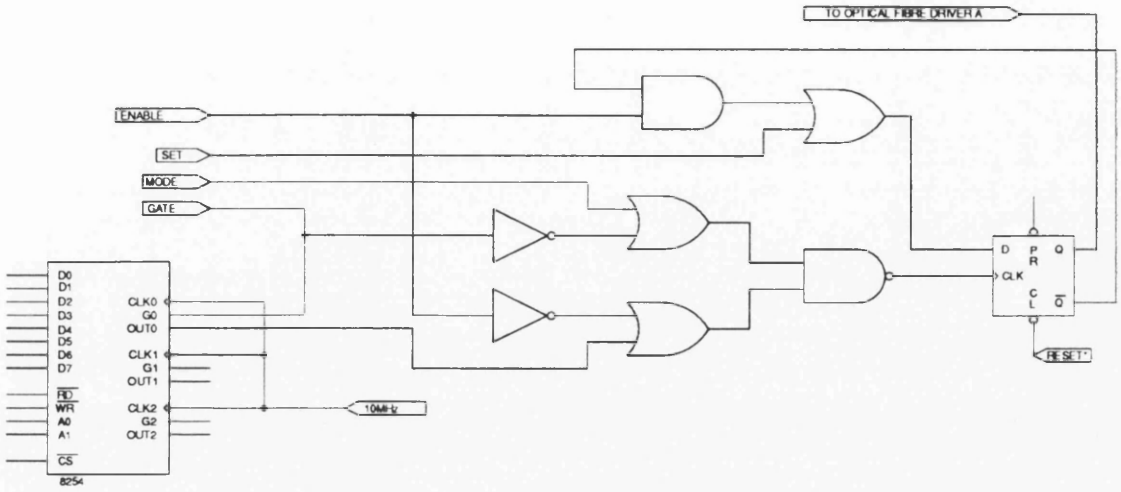

Figure 79: Phaseleg Timing Control Circuit

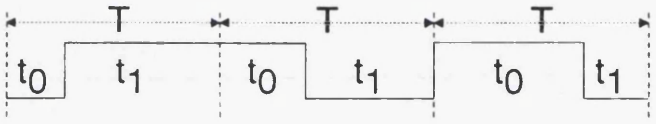

Figure 80: Switching Pattern In Programmable Timer Mode.

from the DSP. This is similar to using a normal digital latch.

2. Programmable Frequency: Each output can be programmed to output a fixed frequency pulse. This mode can be used to clock external control circuits. In this mode the interface is not connected directly to the power inverter, but might be used to drive a sine wave generator.

3. Programmable Timer Switching: In this mode the circuit is programmed once per control interval T. The initial states of the phaselegs are set when programming the circuit. The phaselegs can also be programmed to change state at time $\{t_{0a}, t_{0b}, t_{0c}\}$ respectively after the start of the interval, as illustrated in Fig. 80.

When the three outputs are combined, this circuit can generate a maximum of 4 different states during the control interval T. Normally there is only need for three different states during a control interval. The practical use of this circuit by control software is covered in chapter 2.6 Without this circuit the processor would either have to poll a timer at regular intervals or use an interrupt to update the phaseleg

states during the control interval, wasting valuable processor time. At the start of a control interval the initial states of the phaselegs will be set. Each phaseleg can then change its state once during the control interval using a i8254 timer. The i8254 contains 3 individual timers which can be programmed to change the state of an optical output to within 200ns of the desired switching time.

B.3 Operation of Power Inverter

This section describes the operation of the power inverter. Peter Miller designed and built the power inverter, and although it was not designed by myself this section has been included for completeness as the power electronics forms an significant part of the system.

The inverter is the part of the system that converts the control signals into actual voltage or current applied to the motor. The inverter shown in Fig. 81 is a voltage source inverter, in which the constant source voltage is approximated by a large capacitor supplied from rectified 3-ph 415V mains. The motor phases are applied either a constant positive or negative voltage through the inverter switches. Modern inverters in the kW range often switch between the two voltages at rates of 2-50kHz, the higher the frequency the less current and torque ripple. Ultrasonic switching frequency also reduces audible noise. The applied voltage is averaged over time, and if the correct firing pulses are applied to the 6 transistors a sinusoidal current can be achieved.

The inverter specifications are:

Continuous output power	:	10kVA
AC input power (max)	:	Three-phase 415V 50Hz
Output voltage	:	Depends on Control Algorithm
Output Current	:	10Arms, $50A_{peak}$
Max switching frequency	:	10kHz
Power devices	:	3 IGBT modules

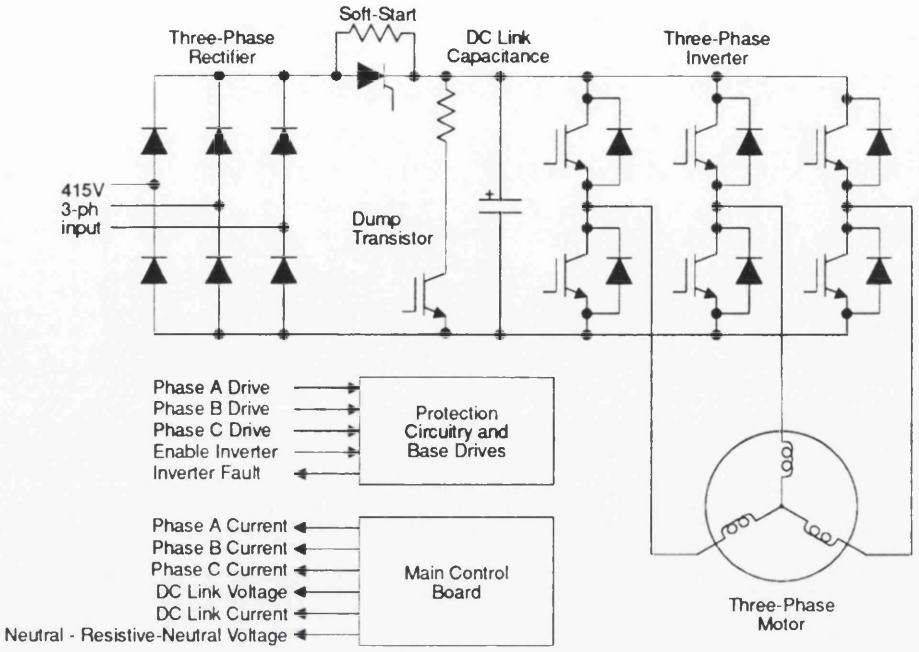

Figure 81: Power Inverter Overview

		(1200V, 50A)
Regenerative Power	:	$25A_{peak}$ @ DC-link voltage
		(continuous, with external load)
Protection	:	Over Current (phase & link)
	:	Over Voltage (DC-link)

B.3.1 Controller Interface

The inverter has been designed to allow the control algorithm designer maximum flexibility by allowing direct control of the switching of the transistors. To minimise the risk to the inverter from being destroyed by controller errors, a set of safety features has been incorporated. To protect the motor and inverter from overcurrents the peak current in the motor phases and the DC-link are monitored. If any of the currents exceeds the set limits the controller trips out. A heat sink temperature sensor protects the inverter from long time overload conditions. To protect the phaselegs from being blown-up by shoot-through the controller is not allowed control over individual transistors, but must treat each phaseleg as a unit being either at the

positive rail or the negative rail of the DC-link. The inverter has an internal lockout circuit that prevents simultaneous ON conditions when a phaseleg is changing state.

The inverter provides the controller with 4 optical fibre inputs to control the three phaselegs. Three of these control the individual phaseleg states and the fourth is used to disable all 6 transistors, in effect making the motor terminals "safe" by putting a high impedance load between the motor terminals and the DC-link voltage. An optical fibre fault indicator is also provided.

The inverter presents the controller with instantaneous current measurements taken using high bandwidth (100kHz) flux-nulling current sensors. The currents measured are the 3 phase currents and the DC-link current. The inverter also provides measurements of the DC-link voltage and the voltage between the motor neutral point and a resistive neutral point (of possible use in sensorless control). The voltage measurements have quite a low bandwidth (2kHz) due to the use of AD202JN isolation amplifiers; however, the isolation is excellent at ±2000V. The full interface specification is given below.

B.3.2 Interface Specification

Phase Controls :

4 x Optical Inputs :

Input Device : HP Versatile Link HFBR-2521. [1]

Use Connector : HP Versatile Link HFBR-4511.

Fault Indicator :

1 x Optical Output :

Output Device : HP Versatile Link HFBR-2522. [2]

Use Connector : HP Versatile Link HFBR-4501.

Analog Outputs :

Connector : DB-15 (Female)

Pin-out : 1) Phase 1 Current

2) Phase 2 Current

3) Phase 3 Current

4) DC-link Current

5) DC-link Voltage

6) Neutral - Resistive-Neutral Voltage

8) Screen

7,9-15) Signal Ground (Connect All)

Scale	:	Phase Currents	= 20A/V [3]
		DC-link Current	= 20A/V
		DC-link Voltage	= 200V/V
		Neutral Voltage	= 100V/V
Termination	:	Currents	= 50Ω [4]
		Voltages	> 100kΩ

B.3.3 Power Electronics Circuit

The main power circuit is clearly shown in Fig. 81. The input power (3-ph 415V) is rectified by 6 diodes. The rectified output from the diodes is applied to a bank of capacitor (total 4500μF, 770V) giving a DC-link voltage level of approximately 600V. A thyristor is placed between the diodes and the capacitors to limit the inrush current through the diodes into the capacitor when power is applied. When power is applied the thyristor is off and the capacitors are charged slowly through the resistor that is in parallel with the thyristor. After the capacitor has been charged to near

[1]Light on input marked "Enable" on inverter back panel enables the phaselegs for operation, no light disables all transistors. Light on inputs marked "Phase 1", "Phase 2", and "Phase 3" on the back panel of the inverter turns the upper transistor of the individual phase on and the lower off. No light turns the lower transistor on and the upper off.

[2]Light on output indicates inverter ready. No light indicates inverter not-ready or a fault has occurred.

[3]For more than one turns on current transducers reduce by number of turns.

[4]Special cable contains 50Ω terminators in connector on controller end.

its working voltage the thyristor is gated and current is allowed to flow freely from the rectifier to the capacitor and onto the transistors. The thyristor is continuously gated to prevent it switching off if the current goes below the holding current. The connection between the capacitors and the transistors is often referred to as the "DC-link". The DC-link is usually made of solid copper-bars with de-coupling capacitors placed close to the transistors to reduce the stray impedance further. It is important to keep the stray impedance of the DC-link low to reduce voltage spikes caused by stray inductance when the transistors are switching. When regenerating the DC-link voltage kept down by dumping excess energy into a resistive load, this dumping starts when the DC-link voltages increases above 713V (118%) and stops when the voltage has been reduced to 662V (110%). An overvoltage trip occurs if the voltage rises to 739V (123%).

The 6 transistors and associated freewheeling diodes are divided into three phaselegs with an upper and a lower transistor. The phaselegs used are Toshiba MG50QYS91 IGBTs rated 50A-1200V, packaged in modules containing 2 transistors and 2 diodes.

The IGBT's advantage is that it is a voltage controlled device like a MOSFET while still retaining the power handling capability of the bipolar transistor. The switching time of these devices is less than 2μs and the on-state collector-emitter voltage is 2.7V. To turn on an IGBT a positive gate voltage must be applied with respect to the IGBT's emitter terminal. The voltage potential of the upper transistor's emitter will vary from 0 to the full DC-link voltage, as the phase leg is switched. To maintain a constant gate voltage on the upper transistors each upper transistor must have a separate floating gate drive. Isolation was achieved using high isolation rating power supplies and opto-couplers. Although the lower transistors all could have used a common drive circuit 6 identical gate drive modules were used, each with an integral power supply.

By using identical modules shorter design time was achieved. The gate drive modules use a single rail 15V power supply. To ensure rapid switching of the transistors each gate should be driven positive and negative; however if the switching

speed is not too critical it is possible to just drive the gate positive and have a resistor between gate and emitter to discharge the gate on turn off. In this inverter a compromise is reached in that the gate is driven between +12.3V in the on state and -2.7V in the off state. This is achieved by generating a low impedance voltage source at +2.7V and connecting this to the emitter. The supply zero voltage is thus -2.7 relative to the emitter. Having a negative gate voltage also gives better margin against induced voltages turning the device on.

As can be seen from Fig. 81 there is a danger of destroying the transistors if both an upper and a lower transistor was turned on at the same time, as this would effectively short circuit the DC-link. To prevent this from happening the IGBT gate drive circuit interlocks the upper and lower drive signals, with a delay of 5μs between one transistor turning off and until the other is turned on. The lockout-time selected is a compromise between having an acceptable safety margin against shoot-through and limiting the inverter switching frequency.

Appendix C

TVC Software Overview

The control program for the sensorless torque vector controller was written in 99% ANSI C. The C-language is highly standardised and available on a large range of systems, making the program portable.

The control program was written so that it includes both a real-time version and a simulation within the same source code. The selection of simulation or real-time version is done at compile time by means of a compiler definition. This makes the program smaller and marginally faster than if an if-statement was used during execution.

Compiling for simulation includes the 4th order Runge-Kutta (RK4) solver which solves the non-linear motor equations. Compiling for real-time execution replaces the RK4 solver by a hardware interface routine that controls the inverter and reads in measured results. The inputs and outputs from both the RK4 solver and the real-time hardware interface are identical and the rest of the code thus remains unchanged regardless of simulation or real-time operation.

The extra code required for the real-time implementation of the control program is minimal. The real-time version has a single very tight interrupt routine which is called every $8\mu s$ when new data is available from the analog to digital converters. Only every 12th value is stored in RAM, and a flag is set to inform the main routine that new data is available and a new control interval can begin. 11 of the data points

are discarded so that the time between the control interval start and the time when the 12th data point was sampled is minimized. The data read are α-β flux-linkages and currents. The control interval is determined by the counter in the interrupt routine. The minimum control interval possible is determined by first running with a long control interval while monitoring the time necessary to execute the main control code.

The structure of the main program is optimized for speed. This means that re-usability of code has been sacrificed to increase speed. In particular the control loop of the program contains no function calls. The hardware interface functions are actually in-line assembly code. It is important to remove any function calls as the DSP96002 / Intermetrics C has a particularly large overhead for function calls.

The program structure of the main control loop in the program is shown in the flow-chart in Fig. 82. The program flow is as follows:

1. Wait at this point until the interrupt routine has set the flag, i.e. when 96μs has passed.

2. Take the current and flux-linkage values that the interrupt routine stored in RAM in raw format and convert them into floating point values.

3. Apply the voltage vector that was calculated in the last control interval.

4. Determine in which of the 6 sectors the flux-linkage vector is, this is used when selecting the voltage vector for the next interval in 15.

5. Calculate torque and flux-linkage magnitude squared. The square of the flux-magnitude is used to avoid the time consuming square-root function.

6. Filter the flux-linkage values through a 16Hz low-pass filter before using them in the speed estimator.

7. Estimate speed by first determining the flux-linkage vector position using the arctan2 function, and then taking the difference in position from the last control interval.

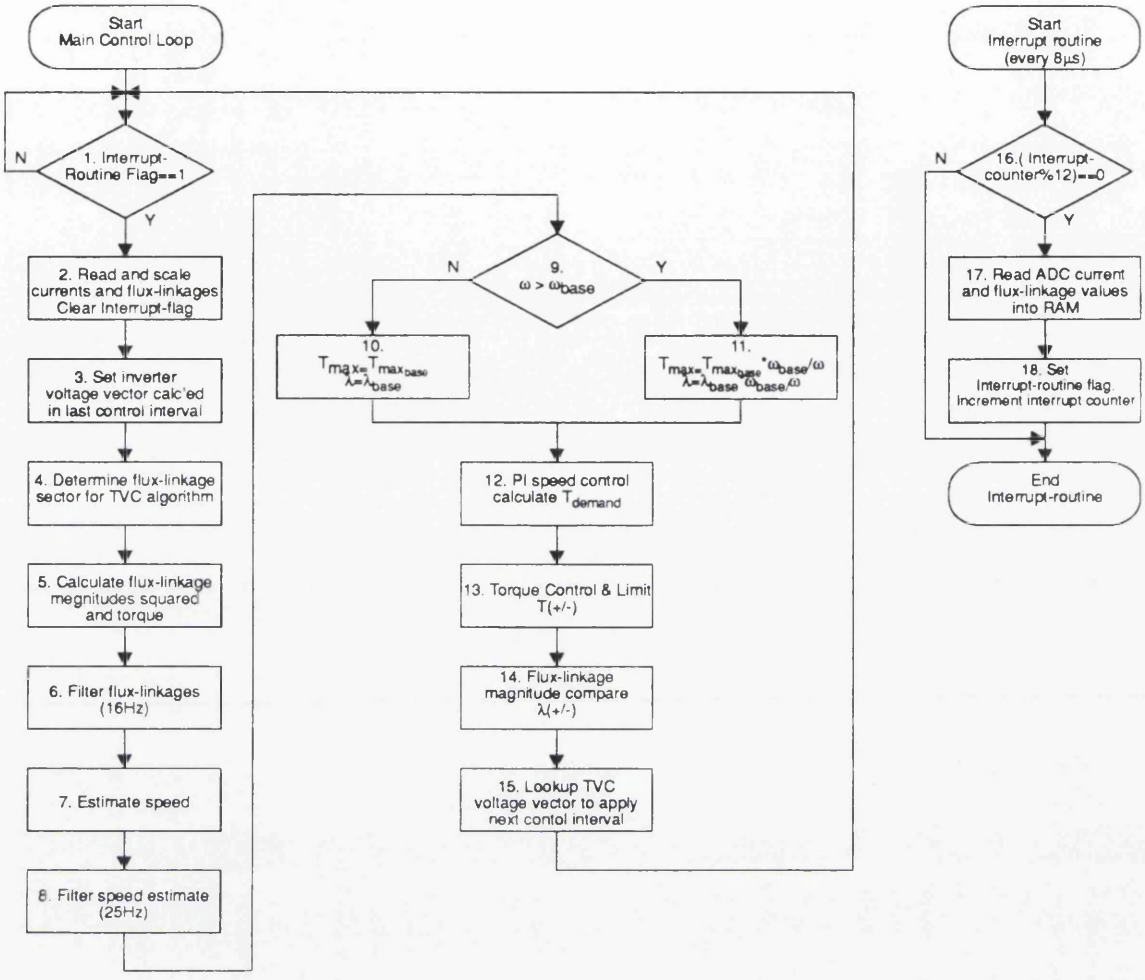

Figure 82: Flow-diagram, sensorless TVC program

8. Filter the estimated speed with a 25Hz low-pass filter.

9. If speed is less than 1500rpm goto 10 else goto 11.

10. Set desired flux-linkage magnitude and maximum torque to their base speed levels.

11. Flux-weakening operation. Reduce flux-linkage magnitude and maximum torque as $\frac{1}{\omega}$ from their base speed values.

12. Do PI speed control to produce a torque demand signal.

13. Calculate bi-level TVC torque signal. Also perform any necessary torque (indirect current) limiting.

14. Calculate bi-level flux-linkage demand signal.

15. Using flux-linkage sector and the bi-level torque and flux-linkage magnitude signals use lookup table to find desired voltage vector to be applied in next control interval.

16. Interrupt routine: Is this time a multiple of 12? If not exit, else continue. ($12 * 8\mu s = 96\mu s$).

17. Interrupt routine: Read the current and flux-linkage values from the analog to digital converter and store them in RAM for use by the main control routine.

18. Interrupt routine: Set the flag to indicate that new current and flux-linkage values are available and the control routine can continue.

For full hardware details see Appendix B .

Appendix D

Stand-alone analog front-end for inverter

The analog-front-end (AFE) was built to provide an easy to operate facility for characterising 3-phase synchronous motors. This controller is radically different from the controllers presented in the main body of this thesis in that it only control the current being fed into the motor and does not control torque or speed as the DSP based controllers do. Torque is however manually controlled by the operator.

The AFE is intended to be used with a dynamometer which provides constant speed operation. The operator can control the current angle/current magnitude or the d-axis and q-axis currents individually, thus making it easy to fully characterise

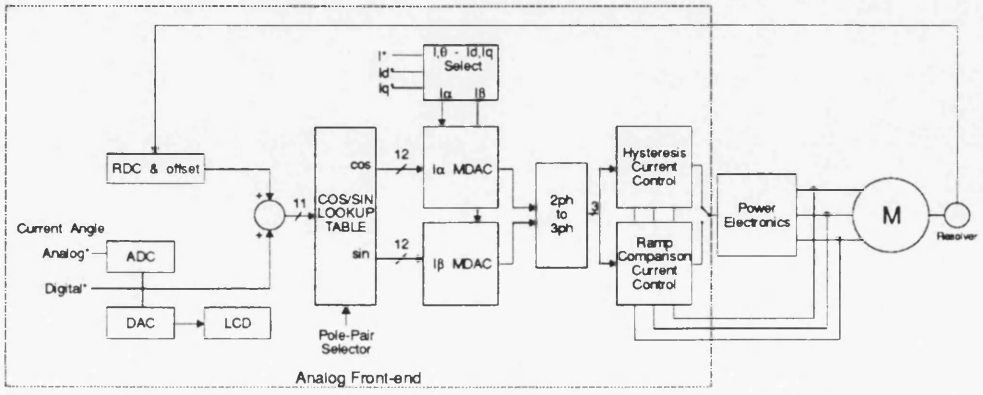

Figure 83: Stand-alone analog controller

the steady-state performance.

The AFE measures the rotor d-axis position using a resolver, this is converted into a 11-bit digital signal. The current angle can be input using either an analog or digital signal. A potentiometer is provided on the front panel for inputing the analog current angle. The analog current angle signal is converted into an 11-bit binary offset value, this is added to the digital rotor position. The digital current angle signal is displayed on a LCD for monitoring.

The digital position of the current vector is then fed into a ROM sin/cos lookup table. The ROM contains tables for motors with 1 to 4 pole pairs, configurable with dip-switches. The ROM produces a 12-bit binary offset α,β-current reference. The 2-phase α,β reference is transformed into an equivalent 3-phase representation corresponding to the motor phases.

The 3-phase reference currents are then used to control the motor currents using either hysteresis control or ramp-comparison control. Hysteresis control changes the state of an inverter leg when the current error exceeds a set hysteresis band. The output from the hysteresis control is gate at 50μs intervals limiting the maximum switching frequency to 10kHz. Ramp-comparison compares the current error with a reference ramp, with no error a 50% duty cycle is produced.

The AFE conforms to the inverter interface specifications in section B.3.2. This is the standard inverter interface which uses fiber-optic control signals and analog current-loops for analog signals.

Appendix E

Publications

E.1 Sensorless Control of the Synchronous Reluctance Motor

Annual Meeting IEEE–Industry Applications Society
Toronto, Canada, October 3-8, 1993

Sensorless Control of the Synchronous Reluctance Motor

R. Lagerquist[1], I. Boldea[2], T.J.E. Miller[1]

[1]University of Glasgow
SPEED Laboratory
Dept. of Electronics & Electrical Eng.
Glasgow G12 8LT, Scotland

[2]Polytechnic Institute of Timisoara
1900 Timisoara
Romania

Abstract – In this paper a sensorless closed-loop speed control for the synchronous reluctance motor is presented. The sensorless control is based on the Torque Vector Control. It has been implemented using a high-speed digital processor DSP96002. Experimental results for a 120W axially laminated synchronous reluctance motor are presented and compared with operation with a speed sensor and simulations. A base speed range of 400-1500rpm has been achieved. The top speed was extended to 2750rpm using flux-weakening. The drive can be applied a full-load step-change within this speed range without losing synchronisation.

I. Introduction

Increasing interest has been shown in the synchronous reluctance motor in recent years particularly in the axially-laminated design first introduced by Cruickshank [4] in 1966 and further developed by [5]. The later axially-laminated designs do not have a starting squirrel-cage; this improves the saliency-ratio and hence torque and efficiency. Without the starting cage the synchronous reluctance motor can not be used for direct-on-line starts, but requires to driven by an inverter to keep the rotor and flux in synchronism. Most inverter drives use a sensor to measure the rotor position to achieve this. However, the rotor position sensor has been a major complaint in variable speed inverter drives as it is expensive, fragile and can prevent use in hostile environments.

Whereas sensorless control for *switched reluctance motors* has been heavily investigated [6,7,10] this has not been the case for the synchronous reluctance motor. Promising sensorless control methods developed for the synchronous PM motor, which should be applicable to the synchronous reluctance motor can be found in [12]. El-Antably proposes a method for sensorless control of the synchronous reluctance motors in [5]; this was further developed by Bolognani [3]. Bolognani implemented a current angle detection system, however he only observed the angle and did not drive an inverter.

This paper presents the implementation of a closed loop torque controller based on theory developed by Boldea [2]. Closed-loop speed control has been implemented by estimating the rotor speed from the flux-linkage vector velocity.

II. Torque Vector Control Principle & Motor Equations

The principle of torque vector control (TVC) as described by Boldea in [2] has been used to implement an inner torque loop. Torque vector control is based on the control of torque, flux-linkage magnitude and position to achieve synchronisation of the rotor and the flux-linkage vector.

Neglecting iron losses the equations for torque vector control can be written, in stator reference frame as (1) and (2). Fig. 1 shows a phasor representation of the equations. The angle ε is referred to as the current angle, angle δ' is the voltage or flux-linkage angle: this follows the convention used by Lipo in [9].

$$\bar{V} = R\bar{I} + \frac{d\bar{\lambda}}{dt} \tag{1}$$

$$T = \tfrac{3}{2} p \mathrm{Re}\left(\bar{\lambda}\, \bar{I}^{*}\right) = \tfrac{3}{2} p\left(\lambda_{\alpha} I_{\beta} - \lambda_{\beta} I_{\alpha}\right) \tag{2}$$

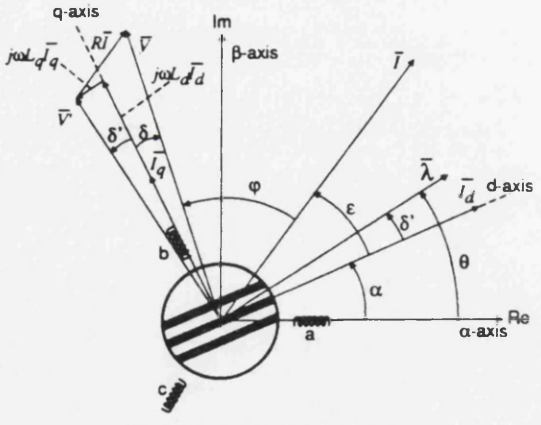

Fig. 1. Synchronous Reluctance Motor Phasor Diagram.

Rearranging (1) gives the flux-linkage

$$\bar{\lambda} = \int (\bar{V} - R\bar{I})dt \tag{3}$$

where

$$\bar{V} = \tfrac{2}{3}\left(V_a + V_b\, e^{j2\pi/3} + V_c\, e^{-j2\pi/3}\right) = V_\alpha + jV_\beta \tag{4}$$

$$\bar{I} = \tfrac{2}{3}\left(I_a + I_b\, e^{j2\pi/3} + I_c\, e^{-j2\pi/3}\right) = I_\alpha + jI_\beta \tag{5}$$

p = pole pairs.

Variables subscripted α and β are the three-phase values transformed into a two-phase co-ordinate system α,β with the α-axis oriented in line with the motor phase-*a* winding and denoted as the real axis. The β-axis is at 90°, and is denoted as the imaginary axis.

In this scheme the rotor position is not used, or detected, it relies purly on orientation of stator flux-linkage and torque control. The flux-linkage angle, δ', is indirectly controlled through the control of torque and flux-magnitude.

In an ideal motor with R=0 the voltage angle, δ, and the flux linkage angle, δ', are identical.

Torque is related to the current and voltage angle as

$$T = \tfrac{3}{2} p(L_d - L_q) I^2 \frac{\sin 2\varepsilon}{2} \tag{6}$$

$$T = \tfrac{3}{2} p\left[\frac{1}{L_q} - \frac{1}{L_d}\right]\left(\frac{V}{\omega_e}\right)^2 \frac{\sin 2\delta'}{2} = \tfrac{3}{2} p\left[\frac{1}{L_q} - \frac{1}{L_d}\right]\lambda^2 \frac{\sin 2\delta'}{2} \tag{7}$$

Under constant current angle control, the maximum efficiency for the test motor at rated speed (1500rpm), torque (0.95Nm) and current (1.7A) was found using a current angle, ε, of 55°. The angle is larger than 45° because of saturation effects.

Under the same conditions as stated above the corresponding flux-linkage angle is given by

$$\delta' = \tan^{-1}\left[\frac{L_q}{L_d}\tan\varepsilon\right]. \tag{8}$$

As L_d is strongly dependent on the flux-linkage magnitude equations (7) and (8) must be solved numerically to determine the flux-linkage magnitude that satisfies the required full-load torque and current angle requirements.

For the test motor the flux-linkage angle corresponding to a current angle of 55° was 12° (0.2 rad). Thus under flux-linkage control the motor has an inherent torque margin of 33° degrees before it becomes unstable by moving beyond 45°. This means that the motor is inherently stable under flux-linkage angle control whereas it is inherently unstable under constant current angle control since ε>45°.

Fig. 2 show the behaviour of the current and torque for different flux-linkage magnitudes. It can easily be appreciated that for best possible inherent stability the flux-magnitude should be chosen as large as possible under current and voltage limit constraints. However as efficiency is also an aim, the flux-magnitude must be reduced so that the full-load operating point coincides with the maximum efficiency point. It must also be noted that the current increases considerably when exceeding the rated torque. TVC normally operates with voltage angles that ensures operation within the current limit, but after a load change is applied it may transiently slip back to a larger voltage angle due to delays in the control loop.

To achieve synchronisation with the rotor TVC controls the applied voltage so that the flux-linkage magnitude is constant and the maximum torque, calculated by (2), is limited so that the flux-linkage angle kept less than 45°.

The flux-linkage magnitude is controlled by applying voltage vector that are directed towards the center of the rotor to decrease the magnitude and outwards to increase the magnitude. The torque is controlled by applying voltage vectors that either advances the flux-linkage vector in the direction of rotation to increase the torque or oppose the direction of rotation to reduce the torque.

As the flux-linkage vector is the integral of the applied voltage vector (3), it will move in the direction of the applied voltage vector for as long as the voltage vector is applied. The voltage angle is thus indirectly controlled by the torque and flux-linkage magnitude, an increasing torque causing an increased angle.

TVC is designed to provide a simple fast control algorithm that can be implemented in hardware without the use of a microprocessor.

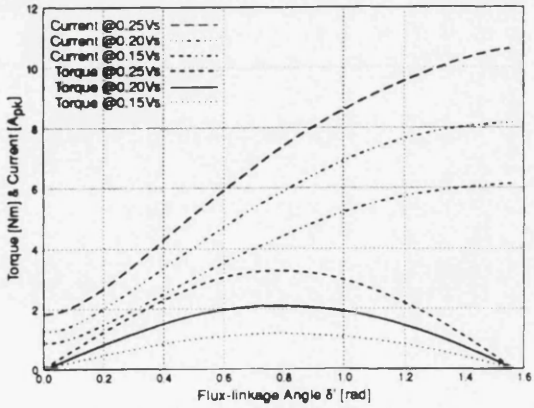

Fig. 2 Torque and Current Magnitude vs. flux angle. Flux-linkage peak-magnitude as parameter.

Torque vector control uses a six-pulse voltage source inverter (Fig. 3) and by being able to be a hardware implementation it can be assumed that it will control the inverter switching at a rate which makes it unnecessary to modulate the applied voltage vectors. Hence the only available voltage vectors are the six in Fig.3.

Since there are only six voltage vectors available it is sufficient to determine the position flux-linkage vector position to be in one of the six sectors defined in Fig.3. As TVC operate the inverter maximum switching the torque demand is reduced to a simple choice of increase or decrease (+/-). The flux-linkage magnitude is likewise limited to a choice of increase or decrease (+/-).

For the case when the flux-linkage vector is in sector ① (Fig. 4) one of four voltage vectors can be applied. If the flux magnitude should be increased and the torque should be positive then V_2 should be applied to advance the flux vector. If the flux is too large, but the torque should still be positive then V_3 should be applied. If the torque should be negative then V_6 would be applied to increase the flux and V_5 to decrease the flux. A compact table of optimal voltage vectors for all the different cases of flux-linkage position and desired control inputs is listed in Table I.

A high-speed low-tech implementation of torque vector control could be achieved using op-amps, comparators, a small ROM look-up table and 4 analog multipliers, ideally suited for implementation as an ASIC.

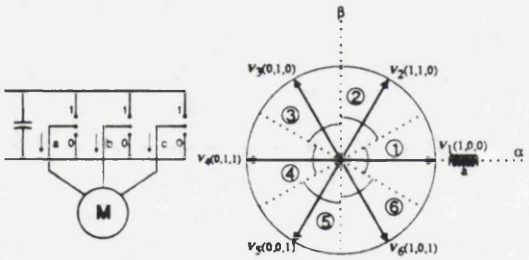

Fig. 3. Six Pulse PWM Inverter

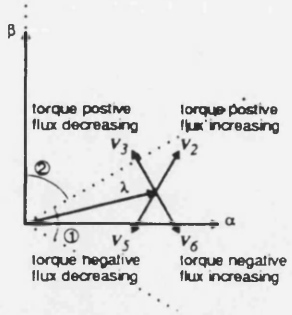

Fig. 4. TVC Voltage Vectors for stator flux-linkage vector in region 1.

TABLE I
OPTIMAL TORQUE VECTOR CONTROL VOLTAGE VECTORS.

Flux-Sector		1	2	3	4	5	6
λ +ve	T +ve	V_2	V_3	V_4	V_5	V_6	V_1
λ +ve	T -ve	V_6	V_1	V_2	V_3	V_4	V_5
λ -ve	T +ve	V_3	V_4	V_5	V_6	V_1	V_2
λ -ve	T -ve	V_5	V_6	V_1	V_2	V_3	V_4

At no point in the TVC algorithm is there a need to know anything but the desired flux-linkage magnitude and the associated maximum torque. In particular the absence of the any reliance on knowledge of L_d and L_q should be noted, this is can be contrasted to the conventional constant current angle control that needs to know L_d and L_q to compensate for the speed term cross coupling between the d and q axis current equations.

To summarise the advantage of TVC are:

1) Self synchronised torque control.

2) Inherently stable (δ'<45°) at maximum efficiency operating point.

3) Simple hardware implementation possible, no microprocessor necessary.

4) Does not need to know L_q, L_d or saturation characteristic.

III. FLUX WEAKENING AND TORQUE VECTOR CONTROL

Constant power operation above the base speed is easily implemented for torque vector control. When the motor reaches the base speed the inverter has reached its voltage limit. To go above the base speed the voltage must be kept constant. As the voltage magnitude is given by

$$|V| = \omega_e |\lambda|. \tag{9}$$

It is clear that to go above the base speed the flux-linkage magnitude must be reduced as

$$|\lambda| = \frac{\omega_{base}}{\omega_e} |\lambda_{base}|. \tag{10}$$

As TVC directly controls the flux-linkage magnitude this is easily achieved.

Similarly for the maximum torque for constant power operation above base speed is:

$$P_m = T\omega_m \tag{11}$$

$$T_{\max} = \frac{\omega_{base}}{\omega_e} T_{\max_{base}}. \tag{12}$$

The maximum torque of the torque/flux-linkage angle curve is reduced when the flux-linkage magnitude is reduced. It is vital to limit the maximum torque demand because excess torque demand would push the flux-linkage

angle beyond the 45° and the motor would lose synchronisation. Since torque is directly controlled this is easily implemented with TVC.

IV. Implementation of Sensorless Closed-Loop Speed Control

Controller Overview

Sensorless closed-loop speed control system for the synchronous reluctance motor has been implemented using a versatile digital control system based around a 32-bit floating point digital signal processor (DSP). The sensorless control algorithm does not require the use of a DSP, but could have been implemented entirely in analog and digital hardware. However, the development time greatly reduced using a DSP.

A digital signal processor, DSP96002, from Motorola has been used to implement most of the control algorithms. An analog circuit has been used to transform 3-phase quantities into two phase quantities and to integrate $\left(\bar{V} - R\bar{I}\right)$ to obtain the flux-linkage vector. Analog components were used to reduce the execution time of the algorithms and provide a quality flux-linkage estimate.

The DSP96002 has a theoretical performance of 50MFLOPS @33MHz. This performance is however only possible with hand-optimised assembly code. The realisable performance when using C is only about 10%. The reason for using a high-level language is that development time is greatly reduced. The control program for this controller is written in 99% ANSI C. The use of C makes the program portable. The control program includes both a real-time version and a simulation within the C-code. If the program is compiled for execution on a PC the simulation code is compiled in. If the target is the DSP the simulation code is simply replaced by an equivalent hardware interface section. The control algorithm code remains the same regardless. The control algorithms are executed every 96μs, giving a maximum switching frequency of 5.2kHz.

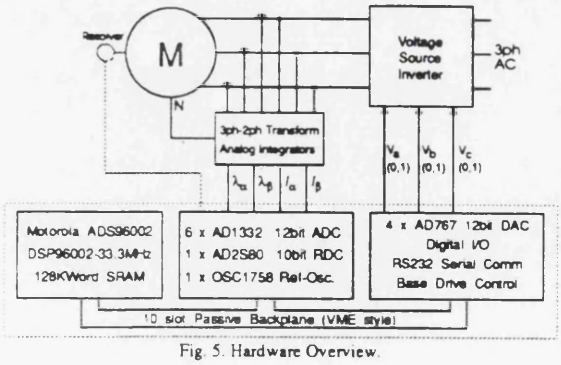

Fig. 5. Hardware Overview.

The analog to digital converters are run with a conversion rate of 125kHz. The sensorless speed estimate and the speed measured using a resolver is output on digital to analog converters for real-time monitoring.

Stator Flux-linkage and Torque Estimator

Torque vector control requires the flux-linkage vector and torque to be estimated. Using a rotor position sensor the stator currents could be transformed into the rotor d-q frame and calculated as $\bar{\lambda}_{dq} = L_d I_d + jL_q I_q$. As the aim is to produce a sensorless scheme the stator flux-linkage must be estimated using (4). The implementation of the flux-linkage estimator is shown in Fig. 6. The currents and voltages are transformed into a 2ph stator co-ordinate system and then the flux-linkage is found by analog integration of the voltage. As expected there was some drift in the integrators, to compensate for the drift the DC-gain of the op-amps was limited to 10x. This causes the gain to be 25% too low @400rpm, resulting in an increased flux-linkage magnitude at low speeds. This increase in flux at low speeds does not in fact influence the control much. The current magnitude stays virtually constant, but the voltage angle is decreased giving a slightly lower fundamental power factor and efficiency.

Positive side effects of the increased flux magnitude is increased torque reserve, and as this increase in flux occurs at low speeds there are no risk of running out of volt. As most of the drift was caused by the DC-drift in the current and voltage transducers there would be no great advantage use digital integration.

The conventional method used to compensate for integrator drift which measures the distance the measured centre of the flux-linkage circle has moved from the origin and compensate for this. This method is fine for PM motors as the flux is constant and produced by magnets and there is a relatively small contribution due to the currents in the machine. However, TVC can not use this approach because the flux-linkage is being produced by the currents, and is controlled so that the measured flux-linkage describe a perfect circle. The actual flux-linkage magnitude will thus under offset conditions vary as it rotating. Compensation for DC-offset under TVC is done by recording the offset values whenever the motor is stopped and subtracting the offset values from the measured values when the motor is running.

Since a high performance processor was already in use, and the calculation of torque and flux-linkage magnitude (squared) are simple to perform digitally and not computational intensive they were computed by the DSP.

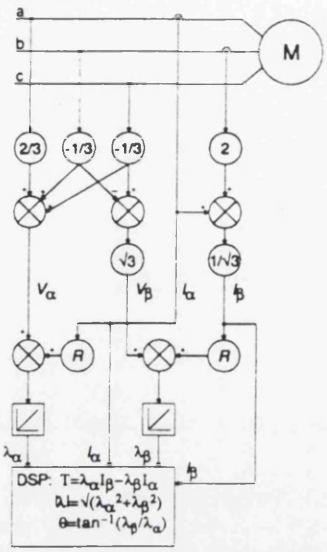

Fig. 6. Stator Flux and Torque Estimator.

As TVC only requires the flux-linkage vector position to be determined to be in one of the six sectors in Fig. 3 the position can be uniquely identified by testing for the sign of λ_α, the sign of λ_β and a magnitude comparison $\sqrt{3}|\lambda_\beta|$ and $|\lambda_\alpha|$. These test are performed by the DSP on the unfiltered flux-linkage values from the analog integrator. Use of the arctan function to determine the position of the flux-linkage vector is thus not necessary for the torque loop and this saves valuable CPU time. The position test could also have been implemented in analog hardware by use of a few comparators and op-amps.

At low speeds the motional voltage component becomes less than or equal to the voltage across the stator resistance. It thus becomes important that the correct value of stator resistance is used in the flux-linkage estimator. A wrong stator resistance value causes an offset in the flux-linkage angle, and cause the TVC algorithm to detect and use the wrong flux-linkage sector.

Speed Estimator

The flux-linkage is used to estimate the rotor speed as this has a relatively clean wave form. In the steady-state the flux-linkage vector is synchronised to the rotor and the flux-linkage vector speed is the true rotor speed. However, transiently when torque demand is changed the speed estimate will be effected, because the flux-linkage vector moves relatively to the rotor to produce the new torque level. A increase in demanded torque will cause the flux-linkage vector to move opposite to the speed of rotation causing the speed estimate to be low until a new steady-state position is reached. Similarly for a reduction in torque demand, but the speed is in this case over estimated.

These effects can be minimised by limiting the rate of change of torque. If it is not desirable to limit the rate of change of torque the speed estimator could be disabled during large torque demand changes.

The speed estimator has been implemented digitally in the DSP. The speed estimator differentiate the position of the flux-linkage vector to obtain an estimate of the speed (13).

$$\omega_e = \frac{d\theta}{dt} \tag{13}$$

The speed estimator determines the position using a four quadrant arctan2 function. The standard arctan function in the DSP C-library was found to be too slow. It was replaced, by a 1024 (90°) entry look-up table and bisection search algorithm. Even tough the flux-linkage wave forms look quite sinusoidal they require filtering before use in the speed-estimator. Unfiltered flux-linkage wave forms result in a speed estimate with high frequency jitter since the flux-linkage vector may move either way during a control interval. The flux-linkage wave form was filtered using a first order filter with f_c=16Hz. The filter introduces a delay of 2-5ms, however as the position is only used in the speed estimator, and not by the torque-loop, this is acceptable.

Another method for speed estimation was also tried, this method used the crossing from one flux-sector to another to estimate the speed. However, the discontinuous nature of the estimator and the code-required to avoid false detection proved to cause more problems, and took just as long to execute as the method using a arctan look-up table method.

Offsets in the flux-linkage estimate that occur during the operation is not compensated for and cause the real flux-linkage vector to be moved off-center. The measured flux linkage is still centred, but the speed of the measured flux-linkage vector is modulated by a sinusoidally shaped function with a frequency equal to the electrical rotor frequency.

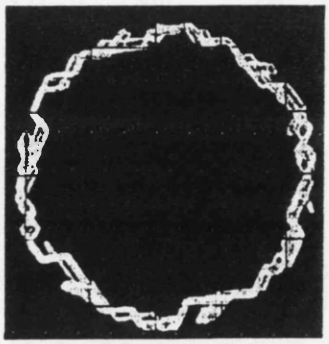

Fig. 7. TVC flux-linkage. ($0.25Vs_{pk}$).

Speed and Torque Controller

The torque controller used is quite simple as the torque vector control algorithm only accepts request for positive or negative torque. The desired torque from the speed controller is compared with the estimated motor torque, if the motor torque is less than the desired torque a request for positive torque is passed to the TVC control algorithm, otherwise a request for negative torque is passed.

The torque vector control algorithm may override any torque request passed to it if the motor torque is larger than the rated torque. If the motor torque is positive larger than the rated torque then a negative torque demand overrides any previous selection, likewise if a negative motor torque of magnitude greater than the rated torque is measured then a positive torque request overrides and is applied.

The speed controller however is more involved and is linked closely to the speed estimator described above. A conventional PI speed controller was used as basis, but required some modification to work well.

The most problematic aspect of the speed controller was the ripple in estimated speed due to offsets in the flux-linkage. The effects of this was most noticeable at higher speeds as the ripple frequency approached the speed controller bandwidth and caused oscillation. There were basically two approaches to solve this problem; to increase the bandwidth of the speed estimator or to filter out the speed variation. To further low-pass filter the speed estimate would result in slow dynamic response which was not desirable. The filtering was reduced and hence the speed estimator bandwidth increased, this increased the ripple present in the speed estimate. However, the PI gain was increased, and this combined with the increased bandwidth gave improved dynamic response while at the same time maintain the steady state accuracy. The resultant speed variation is of an approximately fixed magnitude (25rpm) and is clearly visible at low speeds. This variation in the speed estimate could eliminated at high speeds by averaging over one revolution. However at low speeds this would seriously degrade the dynamic response of the system. It might be possible to use a notch filter with variable center frequency to remove the variation, but this has not been attempted.

Performance Issues

Torque vector control operates with a constant flux-linkage magnitude at all loads. The use of constant flux-linkage means that there will always current to flowing in the motor to maintain the flux, even in no-load situations. The effect this has on the performance will depend on loss mechanisms in the motor. In the 120W test motor the iron-losses were found to be relatively independent of the load, and mostly a function of the flux-linkage ripple.

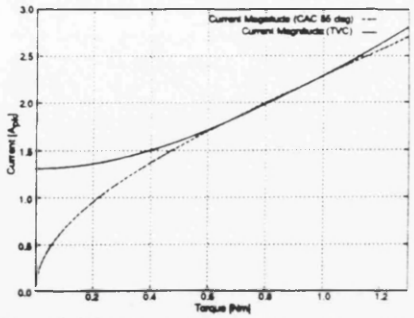

Fig. 8. Theoretical Current magnitude as function of torque in TVC and constant current angle controllers.

To compare the difference in losses of torque vector control and constant angle control it should thus be sufficient to compare the copper losses. Fig. 8. shows the current magnitude for a constant angle control (CAC) of 55° compared with torque vector control. The flux-linkage magnitude is set to achieve the maximum efficiency current angle at a load of 1Nm. As can be seen the copper losses of the two control methods will be almost the same for loads ranging from 60% to 110% of rated load. Outside this range TVC has a larger copper losses than constant angle controllers, especially at low loads.

Torque vector control has fast dynamic torque response compared to constant current angle controllers since the currents in the motor can be changed faster. The torque change is faster under TVC as almost all the current change occurs in the least inductive axis whereas for constant current angle control the change in current is equal in both axis.

The efficiency of torque vector control could be increased at low loads by including a efficiency optimising loop that would lower the flux-linkage magnitude when the motor is operating at light loads. However, some the dynamic response of TVC would have to be sacrificed if efficiency optimising is used because the flux-linkage magnitude would have to be rebuilt before full torque could be produced, this would make TVC dynamic performance on par with constant current angle controllers.

V. Results

To explore the performance and limitations of the sensorless closed-loop speed controller an experimental set-up with a 120W axially laminated synchronous reluctance motor was used. The motor has a standard induction motor stator with a low-voltage winding. The test motor and the load machine was coupled with a Vibrometer torque transducer using flexible rubber couplings. The load machine was a brushless permanent magnet motor powered by an Electrocraft BRU controller.

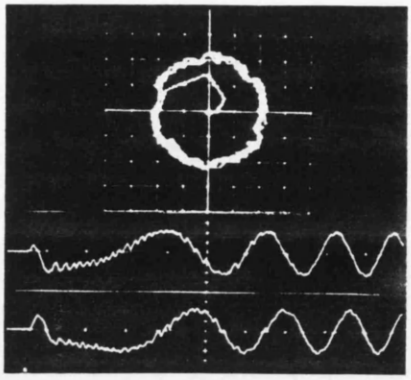

Fig. 9. Flux-linkage (α,β) during start-up.
0.1Vs/div. 10ms/div.

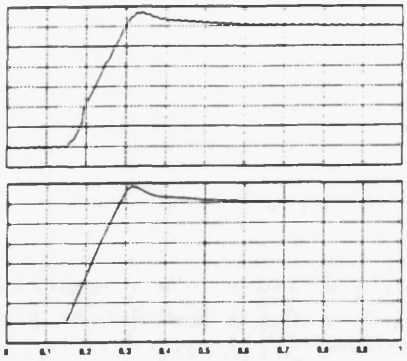

Fig.11. Sensorless: Simulated Speed Reversal -/+1500rpm.
Estimated Speed (top) & True Speed (btm).
500rpm/div, 0.1s/div

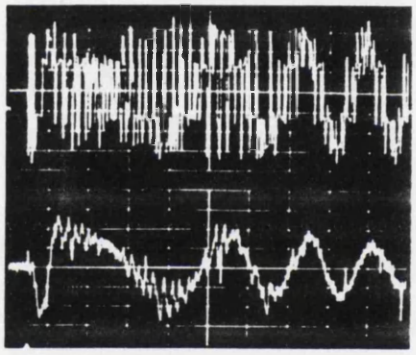

Fig. 10. Phase-Voltage (top) and Current (btm) during start-up.
50V/div, 2A/div, 10ms/div.

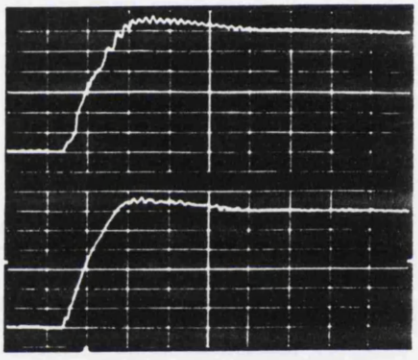

Fig.12. Sensorless: Speed Reversal -/+1500rpm.
Estimated Speed (top) & True Speed (btm).
500rpm/div, 0.1s/div

Startup

When starting the motor any voltage vector may be applied. As can be seen in Fig. 9 the correct flux-linkage position is achieved in less than 4ms, during this time the motor may develop torque in the wrong direction. Fig. 9 illustrates the worst case where the initial applied voltage vector located 180° from the desired position.

Also notice the relatively smooth flux-linkage wave form compared to the current (Fig. 10), making it preferable to use in the speed estimator.

Speed Estimator & Simulation

Simulations of the dynamic behaviour and the actual system has been shown to agree well. Fig. 11 shows a simulation of a speed reversal from -1500rpm to +1500.

In the simulation the flux-linkage was offset by 2.5% in both axis, notice the characteristic ripple on the speed estimate introduced by the offset. This ripple is also present in the experimental wave form Fig. 12.

The characteristic kink in the speed estimate occur due to the rapid change of flux-linkage angle, causing the speed temporarily to be estimated to be much smaller than it actually is (or even of opposite sign). This kink can be found in both the simulation and the experimental wave form and is the response of the digital filter to the impulse speed change present while the flux-linkage angle changes.

Dynamic Performance

The speed range of the drive has been defined to be the range in which the motor could be applied a step-load from no-load to 90% of rated torque without losing

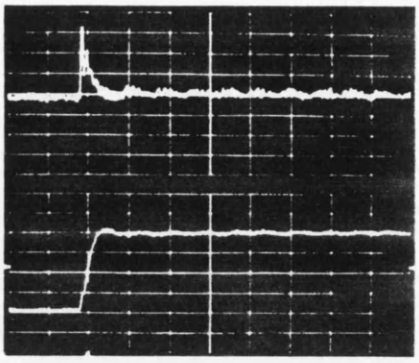

Fig.13. Sensorless: Speed Reversal -/+400rpm,
Torque (top) & Speed (btm).
0.5Nm/div, 200rpm/div, 0.1s/div.

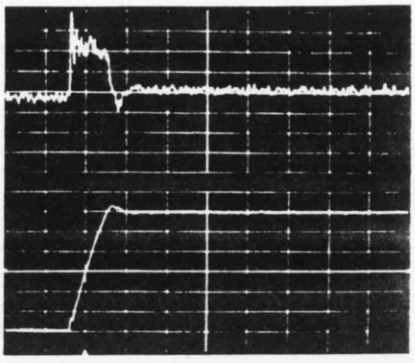

Fig.15. Using Speed-Sensor: Speed Reversal -/+1500rpm,
Torque (top) & Speed (btm).
0.5Nm/div, 500rpm/div, 0.1s/div.

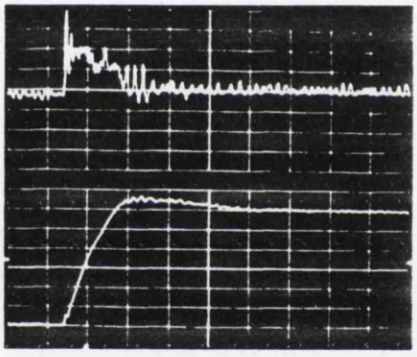

Fig.14. Sensorless: Speed Reversal -/+1500rpm,
Torque (top) & Speed (btm).
0.5Nm/div, 500rpm/div, 0.1s/div

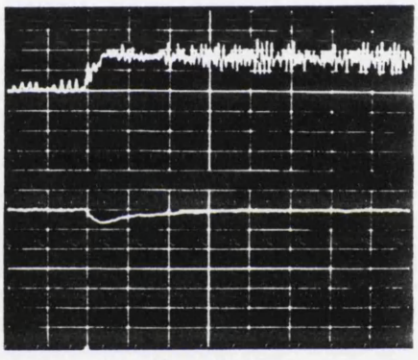

Fig.16. Sensorless: Step-load change 0–0.86Nm @1500rpm
Torque (top) & Speed (btm).
0.5Nm/div, 200rpm/div, 0.1s/div.

synchronisation. The minimum speed achieved that satisfied the above criterion was 400rpm. If the step-load change is limited to 53% of full load the lower speed limit becomes 150rpm.

Fig. 13 shows the a +/-400rpm speed reversal, steady-state speed ripple due to the flux-linkage offset can be seen. A +/-1500rpm speed reversal is shown in Fig.14, the speed reversal takes 150ms which compares well with the 130ms for the constant current angle controller in [1,8]. The settling-time is 325ms compared to 140ms for constant current angle control. This is not a fault of TVC itself, which has excellent response when used with a speed sensor (Fig. 15), but a function of the speed estimator.

The response of the drive to a 90% step-load change is shown in Figs. 16 & 17, notice that the speed drop is constant in magnitude and the recovery time is the same at 400rpm and 1500rpm. The magnitude of the speed drop is a function of the delay in the speed estimator and the recovery time a function of the available acceleration torque. The recovery time for TVC is 400ms compared to a constant current angel controller recovery time of 200ms.

If operated with a speed sensor (Fig. 18) the initial drop is much less due to the shorter delay before the change in speed is sensed. Hence the recovery time is also reduced.

The limit of torque vector control when used with a speed sensor was found to be 50rpm. Below this speed the resistance term in the voltage becomes too dominant to achieve proper synchronisation, inclusion of a stator resistance estimator should improve this.

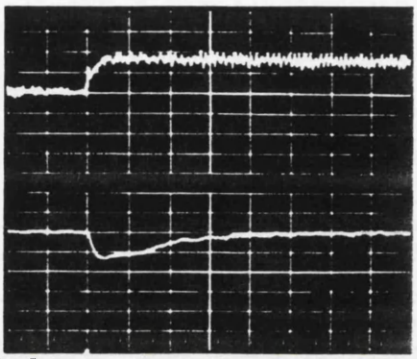

Fig.17. Sensorless: Step-load change 0–0.86Nm @400rpm
Torque (top) & Speed (btm).
0.5Nm/div, 200rpm/div, 0.1s/div.

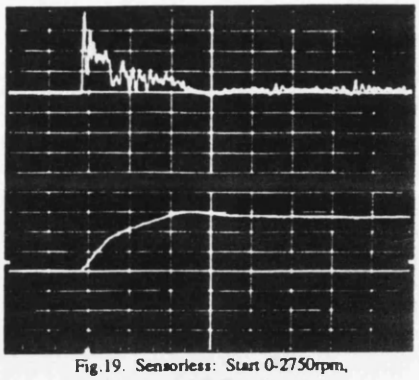

Fig.19. Sensorless: Start 0-2750rpm,
Torque (top) & Speed (btm).
0.5Nm/div, 1000rpm/div, 0.1s/div.

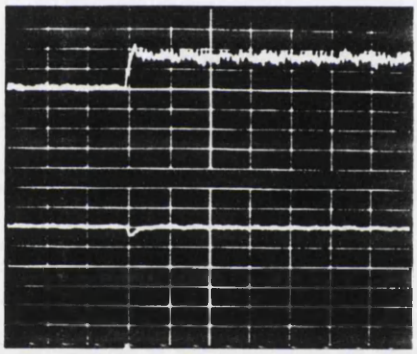

Fig.18. Using Speed-Sensor: Step-load change 0–0.86Nm @400rpm
Torque (top) & Speed (btm).
0.5Nm/div, 200rpm/div, 0.1s/div.

Flux-weakening Operation

The speed range was extended beyond the base speed (1500rpm) using flux-weakening. Above the base speed the motor is operating with constant power. The maximum speed at which the drive could be applied a 90% step-load was 2750rpm, giving a constant power-speed range of 1.83:1. The maximum constant power-speed range for the motor used is 2.13:1 [11]. The limiting factor at this speed is probably a combination of low switching frequency, small flux-linkage magnitude. Fig. 19 shows the motor accelerating from 0rpm to 2750rpm. Notice the characteristic slowdown in acceleration when the flux-weakening region is reached (1500rpm).

Steady-State Performance

The phase current vs. torque is plotted in Fig. 20 this agrees well with the theoretical current (Fig. 8). The measured currents are slightly larger than the theoretical, but this is to be expected as the theoretical does not include iron losses.

The efficiency is shown in Fig. 21 as expected the efficiency of torque vector control is lower than constant current angle control, except at rated torque.

The efficiency could easily be improved by applying a efficiency optimising outer loop to adjust the flux-linkage magnitude. However this would affect the dynamic response.

The steady-state speed regulation (table II) of the drive is generally better than +/-5% for speeds in the range 400-2750rpm. The absolute speed regulation is almost constant at speeds below base speed, and most likely due to offsets in the flux-linkage measurements.

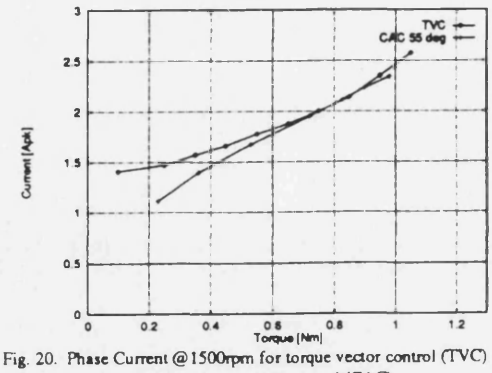

Fig. 20. Phase Current @1500rpm for torque vector control (TVC) and constant current angle control (CAC).

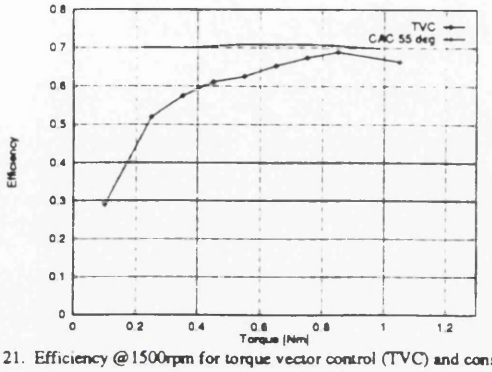

Fig. 21. Efficiency @1500rpm for torque vector control (TVC) and constant current angle control (CAC).

TABLE II
STEADY-STATE SPEED REGULATION

Speed [rpm]	No-load [rpm]	Full-load [rpm]
150	+/-25	+/-25
400	+/-20	+/-30
1000	+/-20	+/-20
1500	+/-40	+/-40
2250	+/-50	+/-50

VI. CONCLUSION

An implementation of sensorless closed-loop sensorless speed control for the synchronous reluctance motor is presented. The drive has been shown to have a base speed range of 400rpm-1500rpm in which a step-load change of 90% full-load torque can be applied. For a step-load of 50% full-load torque the speed range can be extended downwards to 150rpm. Flux-weakening operation has been implemented. The constant power-speed range achieved was 1.81:1. Overall speed range is 6.9:1 for 90% step-load change, and 18:1 if step-load changes of less than 50% are used.

The basic torque vector control is simple and ideally suited for implementation as an ASIC providing closed loop torque control.

For demanding applications (or applications that can tolerate a speed sensor) torque vector control combined with an (inexpensive) tacho-generator should provide excellent performance.

VII. APPENDIX

Motor & System Data:
L_d=180mH(unsat), 152mH(sat); L_q=24.5mH;
R_{phase}=R=8.1Ω; p=2; V_{rated}=110Vrms(Y);
I_{rated}=1.7Arms; $\omega_{m,base}$=1500 rpm; T_{rated}= 0.95 Nm;
Inertia (motor and load)=0.00044 kgm^2;
Friction coefficient=0.00015 Nm/rad/s;
$V_{dc\text{-}link}$=150V; λ_{peak}=0.2Vs; TVC control interval: 96μs;
Maximum Inverter switching frequency: 5.2kHz.

ACKNOWLEDGMENT

The authors thanks: F. Flett & Analog Devices for contribution of linear and data-conversion devices, I.Duthie, A. Hutton & Motorola for the DSP96002 development system, S.E. Wood & Brook Crompton for the motor, D.Staton for designing the axially laminted synchronous reluctance motor rotor and for theoretical and static data for the motor, J. Kelly for making the rotor, P. Miller for designing and building the power electronics.

R.L. thanks: The Committee of Vice-Chancellors and Principals of the Universities of the United Kingdom and the Scottish Power Electronics and Electrical Drives Consortium for financial support. Discussions with W.L. Soong are also gratefully acknowledged by R.L.

REFERENCES

[1] Betz R.E., Lagerquist R., Jovanovic M., Miller T.J.E., Middleton R.H., "Control of synchronous reluctance machines", IEEE Trans. Industry Applications, in press.

[2] Boldea I., Fu Z.X., Nasar S.A., "Digital simulation of a vector controlled axially-laminated anisotropic synchronous motor servo-drive", Electric machines and Power Systems, vol.19, pp415-426, 1991.

[3] Bolognani S., "Torque angle calculator for sensorless reluctance motor drives", EPE Firenze, pp. 4-013 - 4-017, 1991.

[4] Cruickshank A.J.O., Menzies R.W., "Axially laminated anisotropic rotors for reluctance motors", Proc. IEE, Pt.B, vol.113, pp2058-2060, 1966.

[5] El-Antably A., "Proposed control startegy for cageless reluctance motor using terminal voltage and currents", Annual Meeting IEEE-IAS, pp 753-758, 1985.

[6] Eshani M., Husain I., Kulkarni A.B., "Elimiation of direct position sensor and current sensor in switched reluctance motor drives", Annual Meeting IEEE-IAS, pp 518-524, 1990.

[7] Hill R.J., Acamley P.P., Colville W., "Stepping motors and drive circuits therfor", United States Patent 4,520,302, May 28, 1985

[8] Lagerquist R., Betz R.E., Miller T.J.E., "DSP96002 based high performance digital vector controller for synchronous reluctance motors", International Conference on Electrical Machines, Manchester, pp903-907, 1992.

[9] Lipo T.A., Vagati A., Malesani L., Fukao R., "Synchronous reluctance motors and drives - A new alternative", Tutorial held 4 Oct 1992, Annual Meeting IEEE-IAS, 1992.

[10] Panda S.K., Amaratunga F.A.J., "Switched reluctance motor drive without direct rotor positon", Annual Meeting IEEE-IAS, pp 525-530, 1990.

[11] Soong W.L., Miller T.J.E., "Practical field-weakening performance of the five classes of brushless synchronous AC motor drive", EPE 1993, in press.

[12] Wu R., Slemon G.R., "A permanent magnet motor drive without a shaft sensor", Annual Meeting IEEE-IAS, pp 553-558, 1990.

E.2 Control of Synchronous Reluctance Machines

IEEE Transactions on Industry Applications
In press, 1993

Control of Synchronous Reluctance Machines

R.E. Betz[1],
R. Lagerquist[2], M. Jovanovic[1], T.J.E. Miller[2]and R.H. Middleton[1]
Department of Electrical and Computer Engineering
University of Newcastle, Callaghan, NSW, 2308,
Australia.

Abstract

This paper develops a comprehensive approach to the control of inverter-fed synchronous reluctance machines (SYNCREL), based on the machine's ideal model. From the theory a control simulation is designed. Simulation and experimental results are presented. The effects of saturation and iron losses are briefly considered.

Introduction

The Synchronous Reluctance Machine (SYNCRM) is an AC machine with a rotor that has a different permeance on the D and Q axes (P_d and P_q). The simplest rotor that produces this effect is "dumb-bell" shaped. Such primitive rotors however, only produce a relatively small difference in the permeance of the two axes of the rotor. As shall be seen in the following analysis the difference and ratio between these permeances are two of the crucial parameters that determine the performance of the machine (the larger the P_d-P_q difference and P_d/P_q ratio the better the machines properties). Therefore these rotors are of little practical use.

Various other designs have been proposed for the SYNCRM rotor over the years, but the designs that obtain the maximum P_d-P_q and P_d/P_q use an axial lamination principle. Figure 1 is a cross-section of a typical 4 pole machine with axially laminated rotor. The material between the laminations can be any non-magnetic material – slot insulation, aluminium, copper and even injection moulded plastic can be used.

The main motivations for studying the SYNCRM are:–

(i) The control of the SYNCRM appears to be simpler compared to field oriented control of induction machines.

(ii) The SYNCRM is a synchronous machine, and this is advantageous in some applications.

---

[1] Department of Electrical and Computer Engineering, University of Newcastle, Callaghan, NSW, 2308, Australia.
[2] Department of Electronic and Electrical Engineering, University of Glasgow, G12 8QQ, United Kingdom.

(iii) The SYNCRM has a "cold" rotor. This has several implications – the SYNCRM can be used in niche applciations where a cold rotor is required; but more importantly it means that the SYNCRM potentially is more efficient than the induction machine. Therefore for the same total losses the SYNCRM appears to be capable of a higher power density than the induction machine.

(iv) The non-axially laminated SYNCRM is suitable for very high speed applications.

(v) The SYNCRM is robust similar to the induction machine.

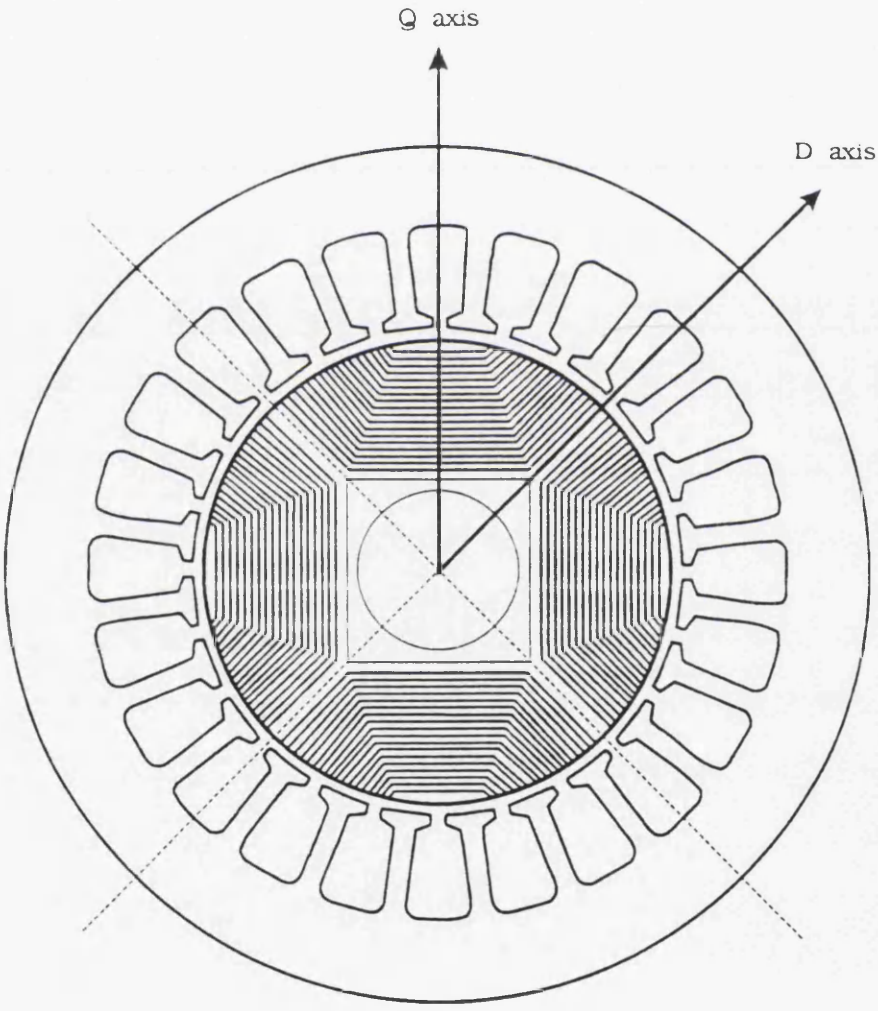

Figure 1 : Cross-section of synchronous reluctance machine with axially laminated rotor

Most of the early work carried out on the SYNCRM has been for dead on-line start applications. Such machines require a squirrel cage to allow the machine to start with mains

frequency input. This constraint compromises performance. The machines which are the subject of this paper have no rotor cage, thereby allowing design for optimal P_d / P_q ratio. The term SYNCREL will be coined for these machines.

In comparison to the induction machine, the control of the SYNCREL has been largely ignored. The main control parameter in the SYNCREL is the angle of the current vector with respect to the high permeance axis of the machine. In this paper this axis is the D axis of the machine (see Figure 1). A significant paper by Chiba and Fukao [1] found that the ideal machine maximum rate of change of torque is obtainable if the current angle with respect to the rotor axis is $\theta_i = \tan^{-1} \xi$, where $\xi = L_d / L_q$. The inherent parameter dependence is not addressed.

Another paper of note is by Fratta, Vagati and Villata [2]. The control for the SYNCREL was derived in a flux oriented reference frame. This allowed the development of a rapid torque response control with a field weakening strategy. Issues of parameter dependence again were not addressed.

The final paper of interest is by Xu, Xu, Lipo and Novotny [3]. This paper tackles the control difficulties associated with saturation and core losses. The key result is that saturation and core losses can make a significant difference to the rotor angles for maximum torque/ampere and maximum efficiency.

This paper consists of two main sections. The first carries out an analysis of the ideal SYNCREL and highlights its basic performance parameters and their inter-relationships for the following control strategies:-

1. Maximum torque control (MTC):- maximum torque/ampere obtained by setting $\theta_i = \pi / 4$.

2. Maximum rate of change of torque control (MRCTC):- control proposed in [1] where $\theta_i = \tan^{-1} \xi$.

3. Maximum power factor control (MPFC):- obtained when $\theta_i = \tan^{-1} \sqrt{\xi}$.

4. Constant current in inductive axis control (CCIAC):- control strategy where constant current is maintained in the D axis, and torque is manipulated by the Q axis current.

The main limitation of the analysis is that it has been done for the ideal machine (i.e. no saturation or losses). By using the ideal machine one is able to develop expressions which allow the theoretical limits of the ideal machine performance to be determined. Despite the

ideal machine limitation, interesting insights into the SYNCREL's properties are gained. Consideration is also given to the effects that saturation and iron losses have on the performance of a "real" machine. More detailed consideration is given to saturation and iron loss aspects of the SYNCREL in [9]. Strategies for estimating the D axis inductance on-line are developed, and simulations of their performance are presented.

The second section of the paper details the design of a digital controller based on the analysis of the previous section. This controller is suitable for implementation on a Digital Signal Processor (DSP). Simulation results for the controller are presented. Experimental results for the controller implemented on a Motorola 96002 Digital Signal Processor are then presented.

Mathematical Modelling

The conventional DQ equations for the ideal SYNCREL using standard notation are:–

$$v_d = L_d \frac{d}{dt} i_d + R i_d - \omega L_q i_q \tag{1}$$

$$v_q = L_q \frac{d}{dt} i_q + R i_q + \omega L_d i_d \tag{2}$$

$$\tau = (L_d - L_q) i_d i_q \tag{3}$$

This form of the machine equations is not suitable for generating machine independent performance information. In order to make this possible the equations are normalised based on the performance of a machine operated at maximum torque per ampere. If ω_o is the angular velocity of the breakpoint in the rated torque-speed characteristic and i_o is the rated current then the other bases for the normalisation are defined as follows:–

$$\tau_o = 1/2 (L_d - L_q) i_o^2 \tag{4}$$

$$\varphi_o = \frac{i_o}{\sqrt{2}} \sqrt{L_d^2 + L_q^2} \tag{5}$$

$$v_o = \omega_o \varphi_o \tag{6}$$

The normalised machine variables therefore become:–

$$\tau_n = \frac{\tau}{\tau_o} \quad \varphi_n = \frac{\varphi}{\varphi_o} \quad \omega_n = \frac{\omega}{\omega_o} \quad i_n = \frac{i}{i_o} \quad v_n = \frac{v}{v_o} \tag{7}$$

Applying the above normalisation's to (1), (2) and (3) and *assuming that the machine resistances can be ignored* the following can be derived:–

$$v_{dn} = \frac{\sqrt{2}\xi}{\sqrt{\xi^2+1}}\left(\frac{1}{\omega_o} p i_{dn} - \frac{\omega_n}{\xi} i_{qn}\right) \tag{8}$$

$$v_{qn} = \frac{\sqrt{2}\xi}{\sqrt{\xi^2+1}}\left(\frac{1}{\xi\omega_o} p i_{qn} + \omega_n i_{qn}\right) \tag{9}$$

$$\tau_n = i_n^2 \sin 2\theta_i \tag{10}$$

where $p \equiv \frac{d}{dt}$.

Utilising the fact that $i_n^2 = i_{dn}^2 + i_{qn}^2$ together with (10) allows the normalised currents to be written as:-

$$i_{dn} = \sqrt{\frac{\tau_n}{2}\cot\theta_i} \tag{11}$$

$$i_{qn} = \sqrt{\frac{\tau_n}{2}\tan\theta_i} \tag{12}$$

Therefore (8) and (9) can be written totally in terms of the torque and the current angle:–

$$v_{dn} = \frac{\xi}{\sqrt{\xi^2+1}}\left(\frac{\sqrt{\cot\theta_i}}{\omega_o} p\sqrt{\tau_n} - \frac{\omega_n}{\xi}\sqrt{\tau_n \tan\theta_i}\right) \tag{13}$$

$$v_{qn} = \frac{\xi}{\sqrt{\xi^2+1}}\left(\frac{\sqrt{\tan\theta_i}}{\xi\omega_o} p\sqrt{\tau_n} + \omega_n\sqrt{\tau_n \cot\theta_i}\right) \tag{14}$$

It should be noted that (13) and (14) assume that θ_i is not a function of time and can therefore be moved outside the "p" operator. In other words this means that the following analysis is constrained to constant angle controllers (CAC's).

Since $v_n^2 = v_{dn}^2 + v_{qn}^2$ then after some manipulation the following expression relating the voltage applied to the machine torque, rate of change of torque and the current angle can be found (note that this is the same as the expression in [1] except that a different normalisation has been used):–

$$v_n^2 = \frac{\tan\theta_i + \xi^2\cot\theta_i}{\xi^2+1}\left(\frac{1}{4\tau_n\omega_o^2}(p\tau_n)^2 + \omega_n^2\tau_n\right) \tag{15}$$

The remaining important expression for the SYNCREL machine is the power factor expression. This can be derived using trigonometry from the vector diagram of the machine:–

$$\cos\varphi = \frac{\xi - 1}{\sqrt{2}} \sqrt{\frac{\sin 2\theta_i}{\tan\theta_i + \xi^2 \cot\theta_i}} \tag{16}$$

Inter-relationships

The relationships between the MTC (i.e. $\theta_i = \pi/4$) and the MRCTC (i.e. $\theta_i = \tan^{-1}\xi$) shall be investigated first. These two control strategies exhibit a duality property with respect to their rated torque and break frequencies.

If the machine is operating at rated current for both control strategies then from (10) the torque for the MTC control is $\tau_n = 1$ and for the MRCTC $\tau_n = 2\xi/(\xi^2+1)$. For large ξ the maximum torque using MRCTC is very low.

If $p\tau_n = 0$ in (15) then the following expression is obtained for the normalised angular velocity of the machine:–

$$\omega_n = \sqrt{\frac{v_n^2(\xi^2+1)}{\tau_n(\tan\theta_i + \xi^2\cot\theta_i)}} \tag{17}$$

Under the condition of rated current if the applied frequency is increased until the feeding inverter runs out of volts then $v_n = 1$ and $\tau_n = \sin 2\theta_i$ in (17). Therefore the general expression for the break frequency in the torque-speed characteristic is:–

$$\omega_{nmax} = \sqrt{\frac{\xi^2+1}{\sin 2\theta_i(\tan\theta_i + \xi^2\cot\theta_i)}} \tag{18}$$

Therefore for MTC, $\omega_{nmax} = 1$, and for MRCTC, $\omega_{nmax} = (\xi^2+1)/2\xi$. Therefore:–

$$(\tau_n\omega_{nmax})_{\pi/4} = (\tau_n\omega_{nmax})_{\tan\theta_i=\xi} = 1 \tag{19}$$

MRCTC control trades off output torque in order to gain a higher break frequency in the torque-speed characteristic. Since the input voltage and current are equal for both the control strategies then the power factors are also equal. Another interesting result is that the above $\tau\omega$ relationship is unique between MTC, MRCTC and the constant power trajectory that can be traversed between them [4].

The other variable of interest is the relationship between the rate of change of torque for the two cases. The MRCTC control was derived in [1] by optimising for rate of change of torque. Substituting for each angle into (15) and taking the ratio we get:–

$$\frac{(p\tau_n)^2_{\tan\theta_i=\xi}}{(p\tau_n)^2_{\pi/4}} = \frac{\frac{\xi^2+1}{2\xi}v_n^2 - \omega_n^2\tau_n}{v_n^2 - \omega_n^2\tau_n} \tag{20}$$

Since $(\xi^2+1)/2\xi > 1$ for $\xi > 1$ then the above ratio is always greater than 1. Note that as the $\omega_n^2\tau_n$ product in the above expression increases then the ratio increases.

A question which arises from the above analysis is whether the $\tau_n\omega_{nmax}$ product obtained for the MTC and MRCTC strategies is optimal, which is the same as asking whether the power factor is optimal. This question is important because power factor of the ideal machine directly affects the kVA required from the inverter supply for a given output shaft power.

The angle of optimal power factor is obtained by differentiating (16) and equating to zero. The result is that the maximum power factor is obtained if the machine is operated with

$$\theta_i = \tan^{-1}\sqrt{\xi} \tag{21}$$

Substituting this into (16) gives the following well known expression for maximum power factor:–

$$\eta_{max} = \frac{\xi - 1}{\xi + 1} \tag{22}$$

Figure 2 plots power factor for the optimal current angle and the $\pi/4$ current angle. Note that as ξ increases operating at optimal power factor angle begins to show a significant difference. The figure also serves to highlight the importance of obtaining a good (≥ 5) ξ value so that the inverter size relative to the shaft output power can be reduced.

The comparative performance of the MPFC strategy relative to the MTC and the MRCTC strategies can be seen in (23) and (24). For both ω_{nmax} and $p\tau_n$ the MPFC is midway between MTC and MRCTC [4].

$$\frac{(p\tau_n)^2_{\tan\theta_i=\sqrt{\xi}}}{(p\tau_n)^2_{\pi/4}} = \frac{\frac{\xi^2+1}{\sqrt{\xi}(\xi+1)}v_n^2 - \omega_n^2\tau_n}{v_n^2 - \omega_n^2\tau_n} \tag{23}$$

$$\omega_{nmax} = \sqrt{\frac{\xi^2+1}{2\xi}} \tag{24}$$

The ξ Parameter

Since both the MRCTC and the MPFC are dependent on knowledge of the ξ parameter then the question arises to how accurately this parameter must be known. In order to assess this a sensitivity analysis was carried out in [4] to determine the effect of inaccurate knowledge of ξ on the control objective of each controller. The sensitivity functions evaluated were $\Delta\eta/\eta^*$ and $\Delta\gamma/\gamma^*$ where η^* is the power factor and γ^* is the rate of change of torque, obtained when there is no error in ξ.

The main conclusions are that MPFC is relatively insensitive to ξ and can tolerate errors of $\pm 30\%$ without much performance lose. MRCTC on the other hand is sensitive to ξ both in terms of rate of change of torque and power factor. However if ξ is known to $\pm 10\%$ the error from optimum performance is not too great. For both MPFC and MRCTC larger values of ξ decrease the parameter sensitivity.

Parameter Estimator for ξ

To implement a controller for the SYNCREL it is clear that the ξ parameter needs to be

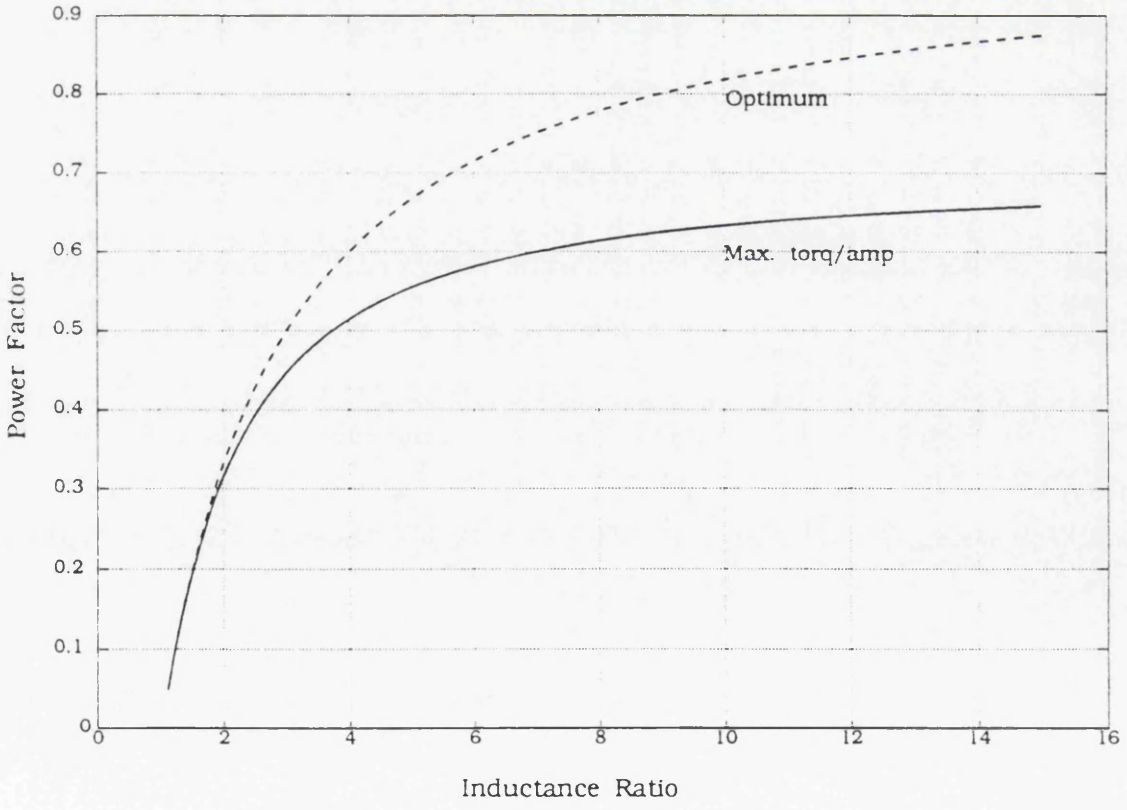

Figure 2: Power Factor versus Inductance Ratio

known. The L_q value is almost constant under all operating conditions since the flux path is dominated by air in the Q axis. However, L_d in reality is a state dependent parameter due to the saturation of the D axis of the machine. One way to obtain ξ under all operating conditions is to measure L_q and the L_d vs i_d relationship for the particular machine being controlled, and then store these in lookup tables.

Alternatively, one can attempt to identify these crucial parameters on-line. This approach has the advantage that to some degree the inverter-controller system has become decoupled from the machine. Therefore for a given power rating, an inverter can support a variety of different machines without having to modify any lookup tables.

There are a number of techniques that can be used to estimate the inductance ratio of a SYNCREL machine. Most estimation schemes used in the adaptive control literature are variants of the basic Recursive Least Squares Estimator (RLSE). Such techniques are applicable to teh estimation of the resistance and inductance values of the SYNCREL machine. For example, if (2) is discretized using an Euler approximation of the derivative the following expression can be written for the Q axis current:-

$$i_q(k+1) = \Theta(k)^T \Phi(k) \tag{25}$$

where

$$\begin{aligned} \Theta(k) &= \left[\left(1 - \frac{\Delta R}{L_q}\right) \quad -\Delta\xi \quad \frac{\Delta}{L_q} \right] \\ \Phi(k) &= \left[i_q(k) \quad \omega(k) i_d(k) \quad v_q(k) \right] \end{aligned} \tag{26}$$

and $\Delta \equiv$sampling interval.

An error $\hat{i}_q(k) - i_q(k)$ can be constructed where $\hat{i}_q(k)$ corresponds to an estimate of $i_q(k)$ generated from (25) using the estimated values for the machine parameters. This error can then be used to drive a RLSE to update the estimates of the parameters. The classical form of the RLSE equations for the scalar case appear in (27).

$$\begin{aligned} \hat{\Theta}(k+1) &= \hat{\Theta}(k) + \mathbf{L}(k+1)[y(k+1) - \Phi(k)^T \hat{\Theta}(k)] \\ \mathbf{P}(k+1) &= \frac{1}{\gamma}(\mathbf{I} - \mathbf{L}(k+1)\Phi(k)^T)\mathbf{P}(k) \\ \mathbf{L}(k+1) &= \frac{\mathbf{P}(k)}{\gamma}\Phi(k)\left(\frac{1}{a} + \frac{\Phi(k)^T \mathbf{P}(k)\Phi(k)}{\gamma}\right)^{-1} \end{aligned} \tag{27}$$

where $a = \gamma = 1$ for ordinary least squares, and $a = 1 - \gamma$, $0 < \gamma < 1$ for exponentially weighted least squares. The memory of the estimator (i.e. the number of previous states which affect the estimate) is approximately $1/(1-\gamma)$. Square root based update techniques for the P matrix are often used because they offer superior numerical properties.

The estimation is based on the Q axis equation for two reasons:–

(a) The equation does not involve incremental values of the D or Q axis inductances.

(b) The Q axis current is the most "active" of the currents for the control strategies considered. This is important in order to supply a persistently exciting input for the estimator.

The traditional technique for using (27) would be to estimate the Θ parameters defined in (26). Once known then the R, L_d, and L_q values can be solved for (since the parameter equations form three independent equations). However this technique does not perform very well in situations where any of the parameters being estimated are state dependent (as is the case for the L_d inductance in the SYNCREL). This is due to the fact that the parameter undergoes very fast changes, and the estimator is always lagging behind the true value of the parameter. What is required is a technique that can estimate the instantaneous values of the state dependent L_d parameter. This can be achieved using a least squares approach by estimating the saturation characteristic of the machine (which is essentially constant and not a state dependent quantity).

The characteristic which must be estimated is the L_d vs i_d curve. This curve can be modelled in a number of different ways – for example, as a polynomial, or perhaps as a sum of exponentials. If the characteristic is modelled as a polynomial then the equation for L_d has the general form:-

$$L_d = c_n i_d(k)^n + c_{n-1} i_d(k)^{n-1} + \cdots\cdots + c_1 i_d(k) + c_0 \qquad (28)$$

If (28) is substituted into (25) then the new Θ can be found consisting of the above 'c' coefficients. Once the 'c' coefficients have been determined by the RLSE then the value of L_d for any i_d can be determined from (28). Improved performance can also be obtained by using *apriori* known information. For example, the value of the L_q inductance is constant under all operating conditions. If this and the resistance are known then the only parameter to be estimated is the D axis inductance. By decreasing the degrees of freedom the estimator performance improves.

An alternative set of basis functions for the L_d inductance are the exponentials. These have been chosen because of their ability to represent the types of curves that are typical of saturation characteristics. Using exponentials it is possible to model the L_d value as:-

$$L_d = c_n e^{(-ai_d^2)} + c_{n-1} e^{(-bi_d^2)} + \cdots\cdots + c_0 \tag{29}$$

Equation (29) can similarly be substituted into (25) and the new Θ determined. It has been found that the use of the exponential basis functions is superior to the polynomial approximation as it often requires a 6th order polynomial to obtain a good fit to the saturation characteristic. This means that even for the case where L_q and R are assumed to be known, 7 parameters (the 'c' coefficients) have to be estimated. On the other hand for the exponential version only 2 or 3 parameters have to be estimated in order to gain acceptable fits. For any choosen set of exponentials one has to choose the power terms 'a, b' etc.

Two other estimation techniques are discussed in [4]. Both these techniques are valid only if the di/dt is small in the machine (i.e. the machine is in steady state).

Field Weakening

Separately excited D.C. machines and vector controlled induction machines can increase their shaft angular velocity above rated speed so that they operate with constant power. This is achieved by weakening the field within the machine. In a SYNCREL machine the concept of the "field" is not easily visualised since the torque production technique does not involve the interaction of a field in the airgap and a current in the rotor. Nevertheless, a constant power characteristic can be obtained from the SYNCREL machine under certain forms of control.

From the steady state version of (15) the following expression for torque is obtained:–

$$\tau_n = \frac{1}{\omega_n^2}\left(\frac{(\xi^2+1)v_n^2}{\tan\theta_i + \xi^2\cot\theta_i}\right) \tag{30}$$

The normal characteristic of the SYNCREL with constant current angle when it runs out of volts is $\tau_n \propto 1/\omega_n^2$.

To implement constant power operation in the region $\omega_n > 1$ then the required characteristic is $\tau_n \propto 1/\omega_n$. For this to hold then from (30):–

$$\frac{\xi^2+1}{\tan\theta_i + \xi^2\cot\theta_i} = K\omega_n \tag{31}$$

If a MTC strategy is employed then $\tau_n = 1$ at $\omega_n = 1$. Therefore $K = 1$. Hence the following equation has to be solved for θ_i with $\omega_n > 1$:–

$$\tan\theta_i + \xi^2 \cot\theta_i - \frac{\xi^2 + 1}{\omega_n} = 0 \tag{32}$$

An explicit solution can be simply obtained for this equation by letting $x = \tan\theta_i$. Therefore

$$\omega_n = \frac{x(\xi^2 + 1)}{x^2 + \xi^2} \tag{33}$$

which is a simple quadratic equation that can be solved for x and consequently for $\tan\theta_i$.

Equation (33) is plotted in Figure 3 for a number of different values of ξ. The following observations can be made from this Figure:–

- As ξ increases there is a corresponding increase in the field weakening range.
- There is a limiting frequency beyond which field weakening cannot occur. At this point there is no θ_i solution to (33) for a particular ω_n and therefore the $1/\omega_n$

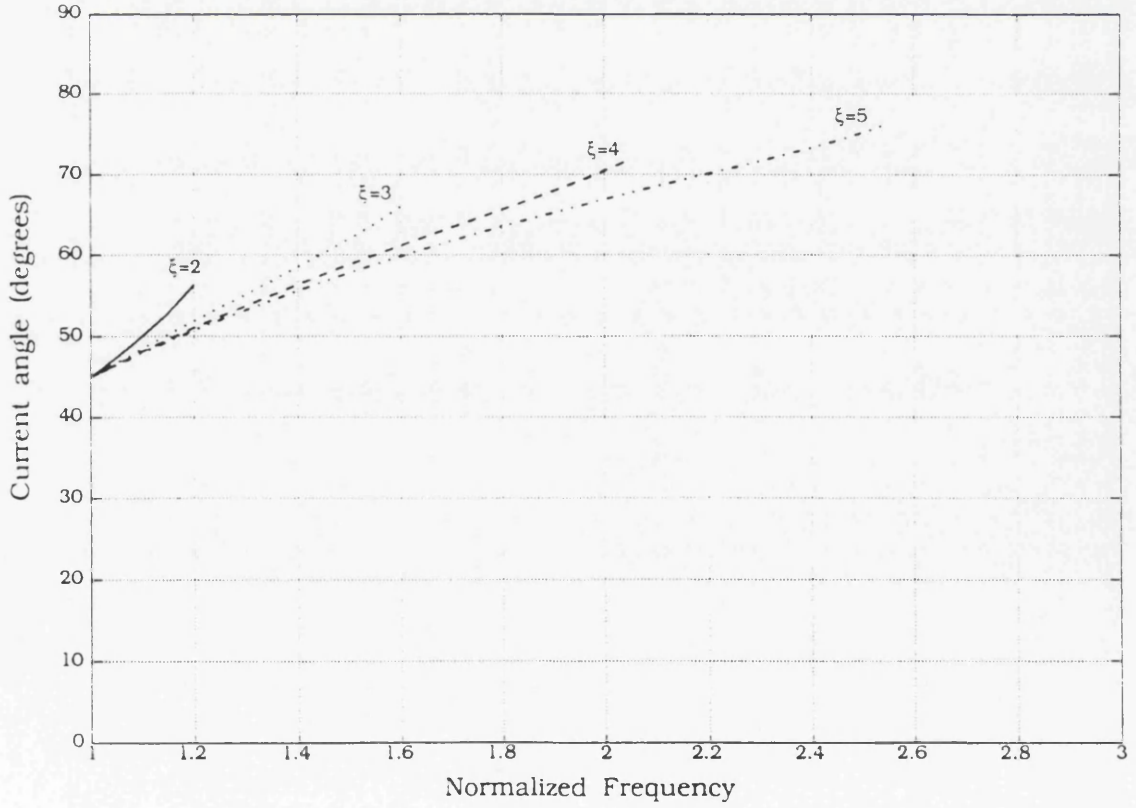

Figure 3 : Current angle required for field weakening

characteristic can no longer be maintained.

- For values of $\xi > 3$ the θ_i versus ω_n curve becomes almost linear up to the field weakening limit.
- For values of $\xi > 3$ the difference between the θ_i versus ω_n curves becomes very small.

The frequencies corresponding to the point where field weakening stops occurring are the ω_{nmax} frequency for the MRCTC. This can be easily proved by differentiating (33). For values of $\xi > 3$ the maximum normalised field weakening frequency is approximately $\xi / 2$ [4].

The current angle for field weakened operation can be found by solving (33) to give

$$x = \frac{(\xi^2 + 1) - \sqrt{(\xi^2 + 1)^2 - 4\omega_n^2 \xi^2}}{2\omega_n} \tag{34}$$

and then use a $\tan^{-1}$ lookup table to find the current angle. Alternative approximate techniques which do not require the $\tan^{-1}$ table appear in [4].

Field weakening using the MPFC strategy has also been investigated. Whilst it is possible to field weaken, the range is not as large as for MTC since it is the difference between the knee of the MPFC characteristic (which is at a higher frequency than the MTC) and the knee of the MRCTC. Furthermore the current required by the machine increases beyond the rated value.

Constant Current in D Axis Control

Thus far the only control strategies which have been considered are constant angle controllers (CAC's) — ie. the current vector angle is maintained constant for all torques and shaft angular velocities ($< \omega_{rated}$). The question which naturally arises is whether this is the best strategy for all circumstances.

This question is answered in [4]. It was found that the $d\tau_n / dt$ for all the CAC strategies was lower than CCIAC (Constant Current in Inductive Axis Control) when the machine output torque and/or shaft angular velocity was somewhat less than rated values.

The relevant equations for the rate of change of torque for the CAC strategies can be simply derived by rearranging (15) under the appropriate angle condition.

For CCIAC the following expression for the $p'\tau_n$ can be derived [4]:–

$$p'\tau_n = \pm\sqrt{2I_{dn}^2(\xi^2+1)v_n^2 - \omega_n^2\tau_n^2} - 2\omega_n\xi I_{dn}^2 \tag{35}$$

where $p' \equiv d/(\omega_o dt)$.

The $p'\tau_n$ equations are complex expressions of ω_n, τ_n and ξ. The CCIAC expression has the added variable of I_{dn}. The following observations can be made:–

- The positive and negative $p'\tau_n$ for the CAC's are symmetric [4].
- The negative $p'\tau_n$ for the CCIAC is always greater than the positive $p'\tau_n$ (see (35)).

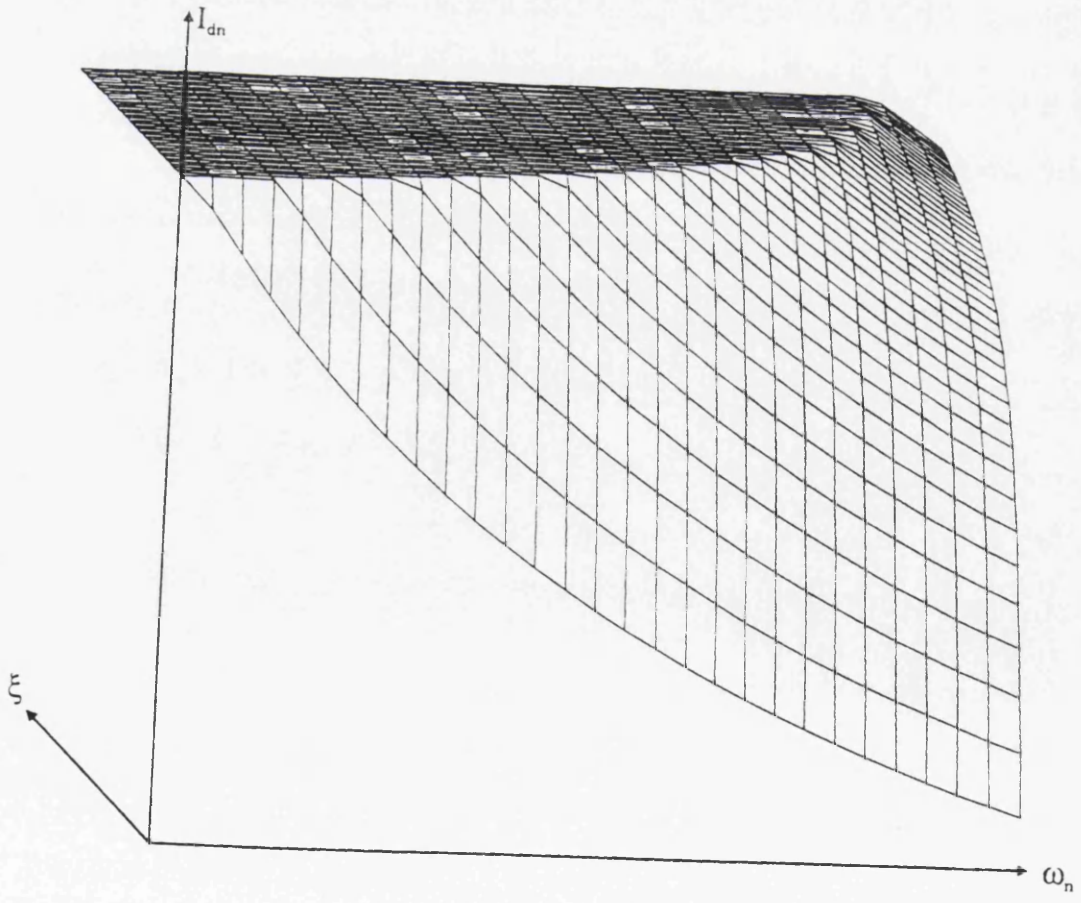

Figure 4 : Three dimensional view of control change over surface.

- The MRCTC has the largest $p'\tau_n$ of all the CAC's as expected [4].
- At high angular velocities the CAC strategies are clearly superior in terms of $p'\tau_n$, the CCAIC being superior at lower angular velocities [4].

An added complication is that as I_{dn} decreases the $p'\tau_n$ performance of the CCIAC improves at higher speeds. Therefore a simple constant I_{dn} control strategy for CCIAC is not optimal. Another difficulty is how to arrange a bumpless transfer between the CCIAC and CAC.

The change over surface between CCIAC and MTC calculated taking into account the difficulties mentioned above is shown in Figure 4. For operating points below the surface CCIAC should be used, and those above MTC. The surface itself gives the value of I_{dn} for CCIAC. For more details see [4].

Saturation and Iron Loss Effects

The analysis of the SYNCREL up to this point has concentrated on the ideal model of the machine. However in a "real" SYNCREL the effects of saturation and iron losses may have a significant effect on the current angles adopted for some of the control strategies being considered.

As mentioned previously, if the rotor of the SYNCREL is axially laminated then the Q axis of the machine has a very low permeance. Consequently this axis usually shows minimal saturation, and in most cases the L_q inductance can be considered to be the unsaturated value. The high permeance D axis on the other hand usually shows significant saturation when the machine is being operated near or at rated conditions. This saturation is the combined effect of saturation in the stator yoke, stator teeth and the rotor laminations, and can reduce the L_d inductance by as much as 50%.

Iron losses in the SYNCREL occur in two parts of the magnetic structure – the stator and the rotor. The losses in the stator are of similar origin to those in a conventional induction machine stator. The rotor would ideally have zero losses (since the spacial flux wave in the machine is rotating at the same angular velocity as the rotor, and therefore the rotor sees a constant flux wave), however in reality the rotor can be subjected to high frequency flux changes as the rotor axial laminations interact with the stator teeth. If the stator is badly designed (ie. with wide teeth openings) these losses may be considerable. In addition considerable eddy current losses can occur in the Q axis if there are no slots in the rotor lamination sheets (these slots should be perpendicular to the axial direction).

The above two losses can be incorporated into the model of the machine resulting the model shown in Figure 5 [3], where R_m is an equivalent resistance to represent the iron losses. As

can be seen R_m allows input current to be diverted away from the torque producing branch of the machine model.

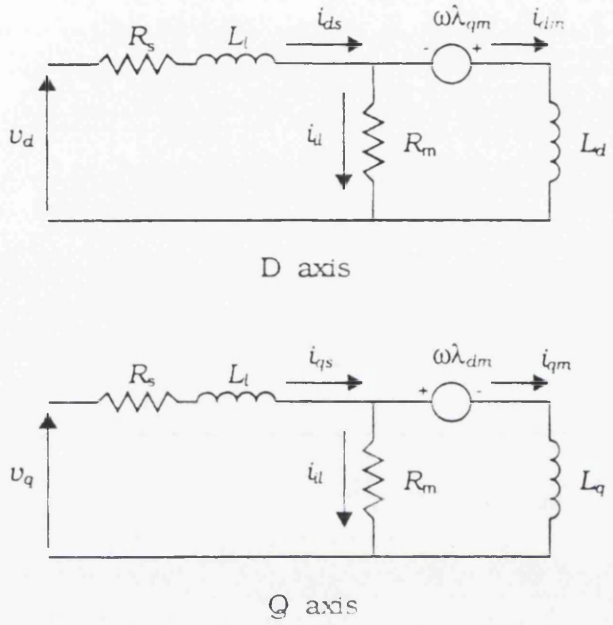

Figure 5 : Saturation and Iron Loss Model

Depending on the particular machine, iron loss or saturation effects may dominate the variations of the optimal current angles from those predicted by the ideal model. In [9] the effects of stator iron loss and saturation were considered for a machine with very high stator iron losses (the machine parameters were reported in [3]). Rotor iron losses were explicitly ignored, however it would appear that they were implicitly included in the stator iron loss, hence the low equivalent resistance value obtained. Although the results in this paper were for a particular set of extreme machine parameters some more general conclusions could be drawn, which are itemised below:–

(i) In a high iron loss machine the saturation effects can be ignored for MTC since the optimal angle of the current vector is so large that the D axis current cannot cause significant saturation.

(ii) The angles for maximum power factor and maximum rate of change of torque are large enough for axially laminated machines that saturation usually does not have to be considered.

(iii) Iron losses serve to improve the value of the power factor above that predicted from the ideal model.

(iv) The presence of the iron loss resistance moves the minimum kVA angle slightly away from the maximum power factor angle.

(v) The ideal angles of operation for maximum power factor and maximum rate of change of torque are reasonably close to those found with saturation and iron losses accounted for.

(vi) Maximum torque per ampere may be effected significantly by saturation and iron losses. The optimal angle is increased above the 45° predicted from the ideal model. The magnitude of this change depends to a large degree on the value of the iron loss resistance. Suffice to say that for iron loss values typical of a standard induction machine the angle difference may not be significant. Maximum efficiency angles are similarly affected.

(vii) Field weakening range is decreased by saturation and iron loss effects.

The general picture to emerge from this study was that the effects of saturation and iron losses vary in significance depending on the machine. In some cases the optimal angles of operation for the control strategies considered in [9] may be very close to those indicated by the ideal model. Studies carried out on machines with iron loss values much closer to those of a similarly rated induction machine indicate that iron loss effects can be ignored and the angle variations for maximum torque per ampere are primarily due to the saturation of the D axis. Furthermore it has been observed that the optimal angles for maximum torque per ampere and maximum efficiency under this condition do not vary much from the ideal model values. The other important point to emerge from [9] was that the general inter-relationships developed in this paper hold for the non-ideal machine.

SYNCREL controller simulator

In order to test the control ideas outlined above a simulation was developed. From the outset one of the main design objectives was to write it in such a manner that the code could be easily ported to a Digital Signal Processor (DSP) system for real-time implementation. Therefore, the simulation includes such things as the PWM generator, a pipelined control evaluation procedure to prevent computational delay from altering the control output times, and a machine model which includes saturation effects.

The machine used for the both the simulation and experimental results had an axially laminated rotor and used a standard 120 Watt 3 phase induction machine stator. It had the following parameters :–

$L_d = 2.6\text{H(unsaturated)}; 1.68\text{H(saturated)}$

$L_q = 0.39\text{H}$

$R_s = 98\Omega$

Poles = 4

$\xi = 6.7\text{(unsaturated)}; 4.3\text{ (saturated)}$

$P_{rated} = 120\text{W}$

$I_{rated} = 0.47$ Amp rms

$V_{rated} = 440$ V rms

and the load had the following parameters:-

Moment of inertia J=0.00044 kgm^2

Friction coefficient f= 0.00005 Nm sec

From Figure 6 it can be seen that the controller supports both position and speed control. The controllers used in the current regulator, speed and position control loops are conventional PI controllers with anti-wind up. In order to eliminate state disturbances in the current loop due to the rotational voltages, state feedback is used [5]. The desired voltages produced by the current loop are fed to a space vector PWM generator [6], and the resultant PWM waveforms drive a model of the machine. Whilst the machine model simulates the saturation effects of the machine, core losses have been neglected in the simulation results presented. The machine model is based on the flux linkage model of the machine. Instantaneous D axis inductance values are determined by using the λ_d vs i_d curves for the particular machine. The model is solved using an automatic step size 4th order Runge-Kutta routine.

An angular velocity observer is used to obtain good estimates of the angular velocity from shaft position measurements [7].

The sampling of the currents occurs a number of times per control interval (20 times in the simulation results presented) and the measurements are averaged to eliminate the effects of

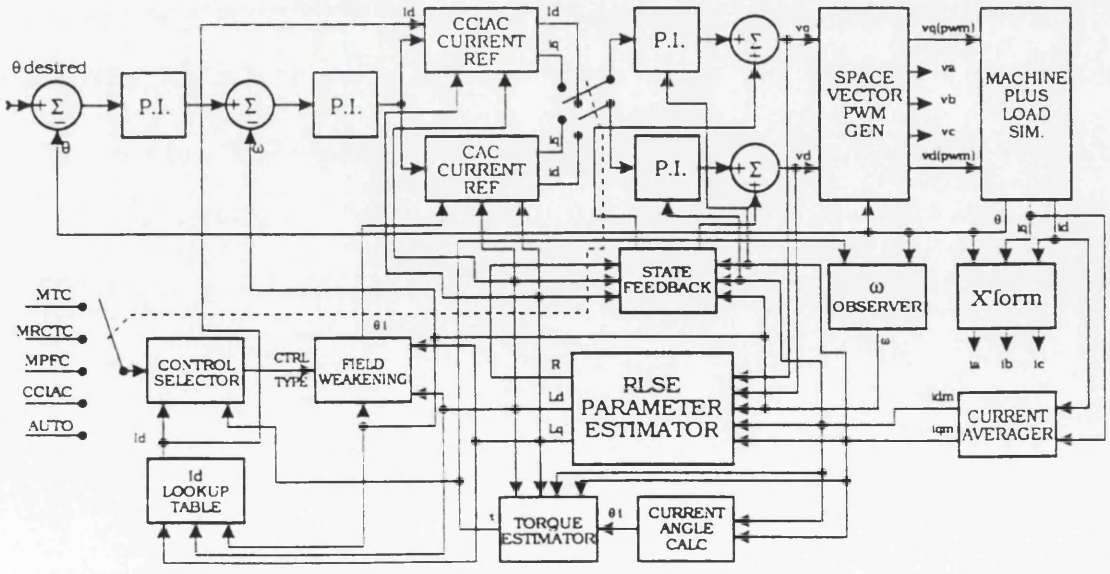

Figure 6 : Block diagram of the SYNCREL simulation program

noise and specific sampling points. The control interval for the results presented in this paper is 500μsec (which is also the frequency of the individual inverter leg firings). Reasonable performance can be obtained for control periods as long as several milliseconds.

The parameter estimator is a RLSE implemented with UD factorisation [10] and exponential forgetting factor as presented in (27). Even though it is possible to estimate all the machine parameters (R, L_d and L_q), the estimator's performance is improved considerably by only estimating L_d using the exponential basis functions as discussed previously. It should be noted that the L_d estimate is the static and not the dynamic inductance of the machine, as it is this value which is relevant to the torque production of the machine and consequently the current reference generators in the control system. As previously mentioned the incremental inductance is not required for the estimation equations since this is based on the Q axis equation of the machine. In this expression the L_d value only features in a rotational voltage term. The incremental inductance however, is required for the current predictions used in the control strategy, and this is easily calculated by taking the derivative of the L_d estimator basis function using the estimated coefficients. This is the same as determining the slope of the L_d vs i_d saturation characteristic.

A control change over surface as per Figure 4 has been stored as a matrix. This is used by the control selector block to decide when to change from CCIAC to CAC when "AUTO" control selection is on. The control type influences the type of current reference generator used (i.e. for CCIAC or CAC) as well as the current angles when in CAC mode.

In order to account for finite computation time, control for the next control interval is computed at the current control interval using predictions of the system variables at the next control interval, and then applied at the next control interval. This means that a whole control interval time is available for computation, and there is no skewing in the application of the control output due to computation time. Simple Euler approximations to the machine's differential equations are used to carry out these predictions. One point to note is that there is a significant effect due to the dL_d / di_d term in the equation that predicts the D axis current. Since the saturation characteristic is being estimated this term is easily found. The ω observer naturally produces ω and θ estimates for the next control time.

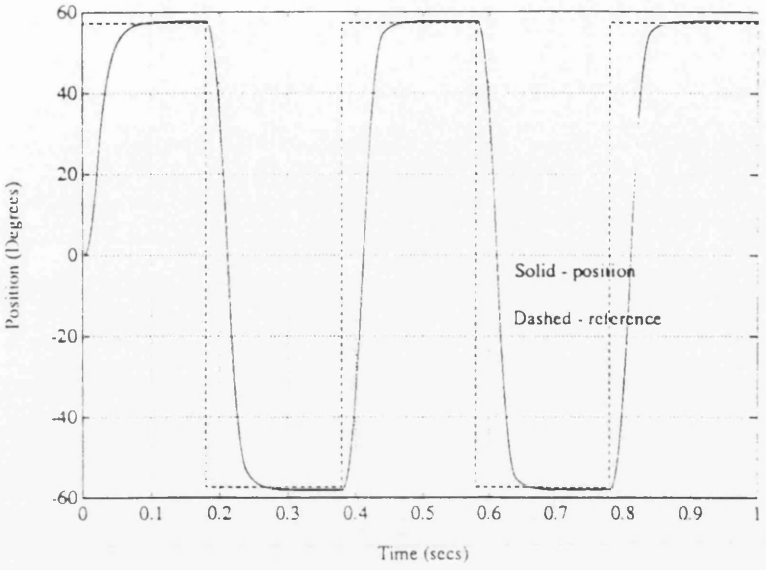

Figure 7a : Position control performance

Some performance results from the simulation are presented in Figures 7a,b, 8a,b,c,d and 9. In all the simulations the estimated value of L_d is used in the controllers. Figures 7a and 7b display the performance of the SYNCREL in position control mode. The control strategy being applied is CCIAC. Note the excellent torque performance. Figures 8a, b, c and d are all plots of various quantities when the objective of the control is to track a speed reference. The control strategy being used is MTC. Figure 8a shows the response of the SYNCREL to a changing speed reference between ±1400 rpm. The machine is able to move between these two speeds in approximately 150 millisecs with very little overshoot.

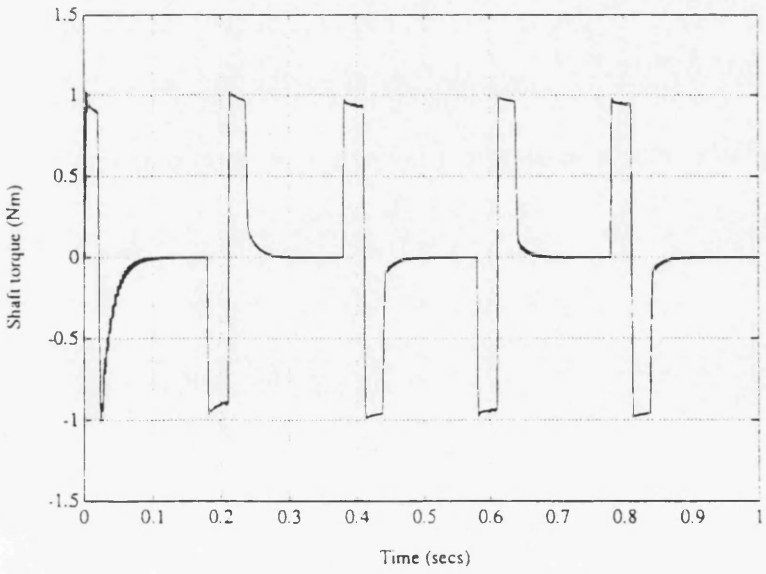

Figure 7b : Machine torque

Figure 8b shows the torque output of the machine during speed control. The actual machine torque accurately follows the reference torque being produced by the speed PI controller. Figures 8c and 8d show the D and Q axis currents for the machine during the test.

Figure 9 plots the estimate of the L_d inductance during the speed control test whose results appear

in Figures 8a–d. The parameter estimation technique is the RLSE outlined in (27), and it is using the following exponential basis function:-

$$L_d = c_2 e^{-25 i_d^2} + c_1 e^{-10 i_d^2} + c_0 \tag{36}$$

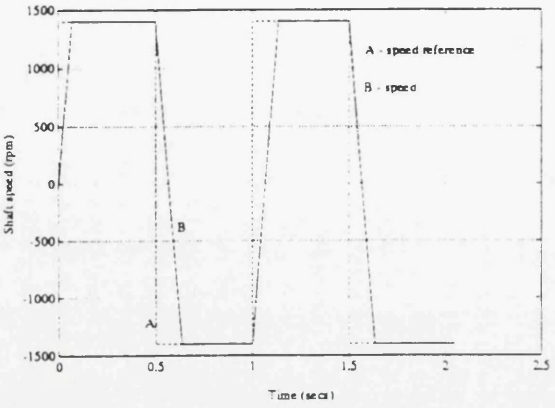

Figure 8a : Speed control performance.

When the simulation begins the initial values of the 'c' coefficients are incorrect. As can be seen from the figure the estimated L_d parameter quicly converges to the correct value. From this point the estimate accurately tracks the true value. Notice that when the true L_d changes with i_d the estimated L_d follows immediately.

In order to obtain good performance from the RLSE the standard UD algorithm as outlined in [10] was modified as follows:–

- limits were set on the diagonal elements of the UD factorization.
- the gain of the estimator was made a function of the inverse of the magnitude of the current.

Without these adjustments the L_d estimates had large overshoots at the transient points and poor accuracy during the constant L_d regions.

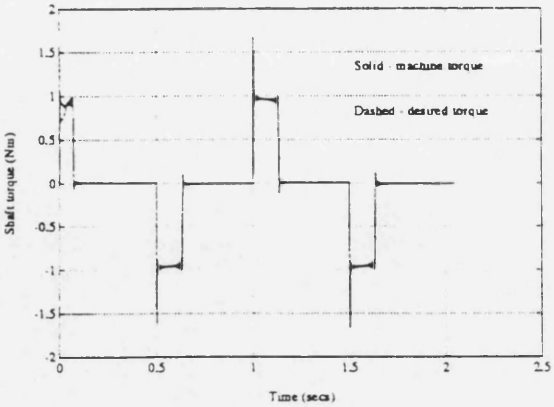

Figure 8b : Torque performance

Figures 10a, b show the performance of the speed control under a transient load torque condition. The control strategy being used in this case is CCIAC. A load torque of 0.8 Nm (which is close to rated torque) is applied to the shaft of the machine at 0.5 seconds and removed at 0.75 seconds. As can be seen from Figure 10a the machine speed dips a little at the point of application of the load torque. Figure 10b shows increase in the shaft torque as a result of the application of the load torque. Note the rapid rise of the torque.

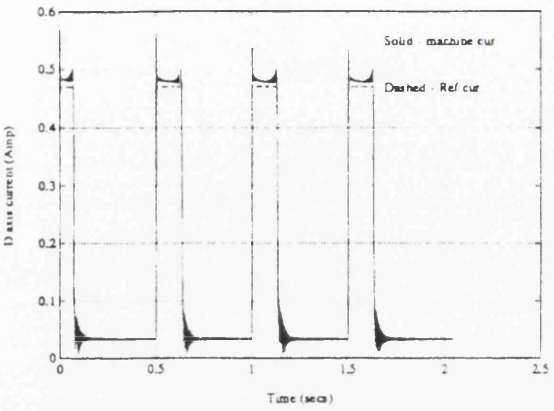

Figure 8c : D axis current

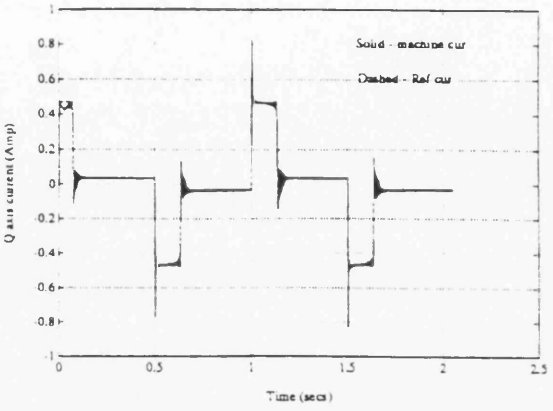

Figure 8d : Q axis current

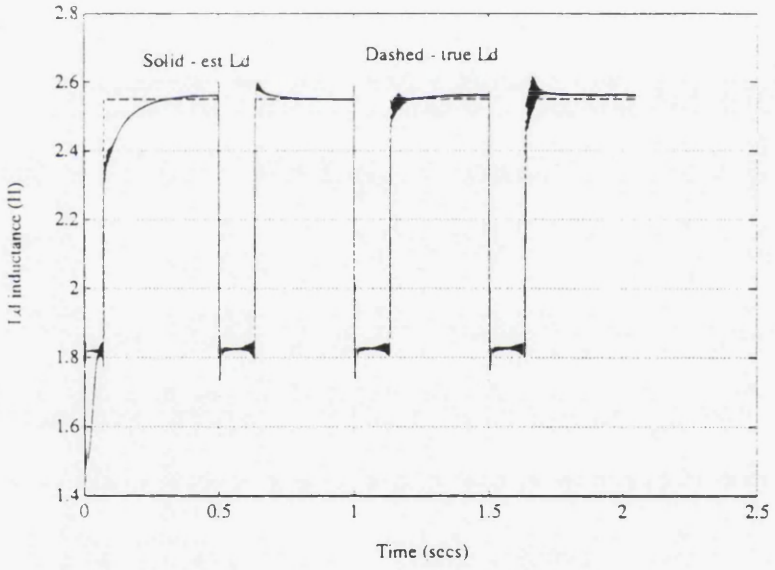

Figure 9 : Estimator performance

Experimental Results

In order to test some of the control strategies outline above an experimental system was developed. This system is based on a Motorola 96002 DSP and custom built power electronic hardware using IGBT's. A totally digital control implementation was chosen in order to maximise the flexibility of the experimental system. The use of the powerful 96002 DSP was deemed necessary in order to allow the majority of the software to be written in high level language and use floating point arithmetic. Figure 11 is a block diagram of the test system. For further details on the hardware refer to [11]. The experimental data was collected on a Nicolet data aquisition system sampling at 1 Mhz using 12 bit A/D converters.

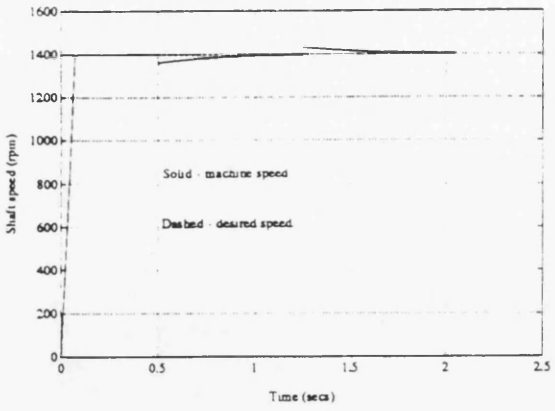

Figure 10a : Transient torque speed response

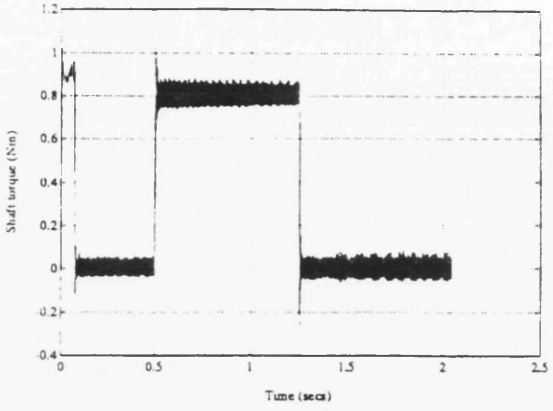

Figure 10b : Shaft torque

The data files produced were processed so that the number of data points could be reduced for plotting. This processing involved averaging each 100 points in the original file and generating a single data point for this value. The resultant files were then plotted.

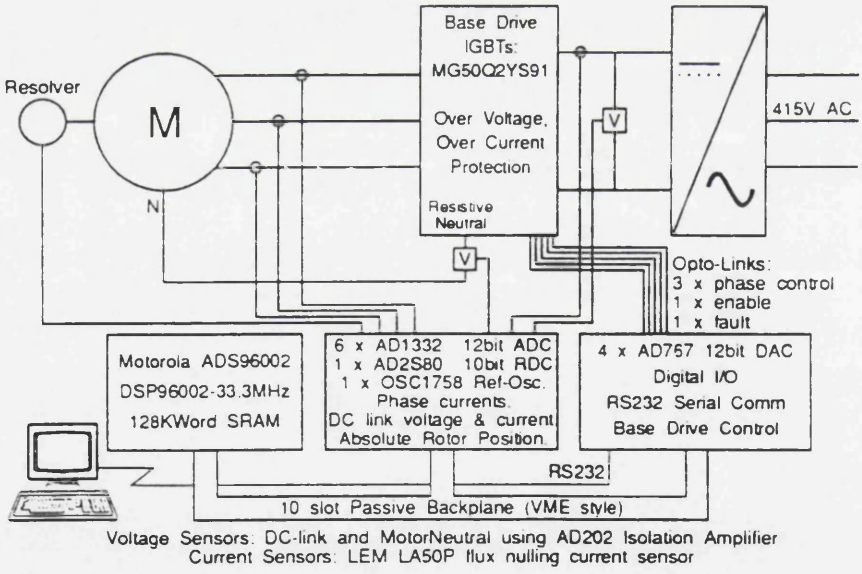

Figure 11 : Experimental system

In order to implement the control, the simulation program (which was 99% ANSI C) was ported over to the DSP hardware implementation. Because the 96002 supports hardware floating point the only changes required in the software were to accommodate interfacing to the various input-output devices and setting up the software to operate in a real-time environment. Unfortunately the compiler technology currently available for the 96002 does

not produce highly optimised code, and consequently the control interval was somewhat compromised. This meant that testing of operation into the field weakening range was not feasible without translating the program into assembly language.

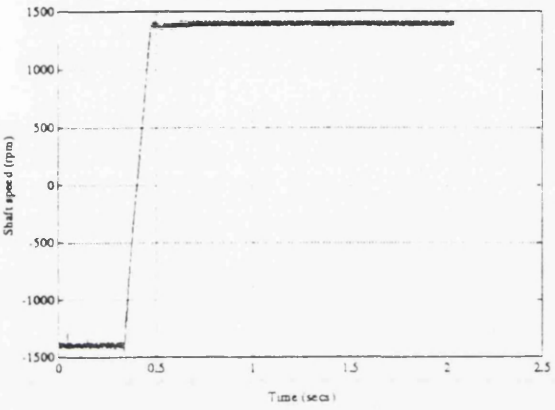

Figure 12a : Experimental speed performance.

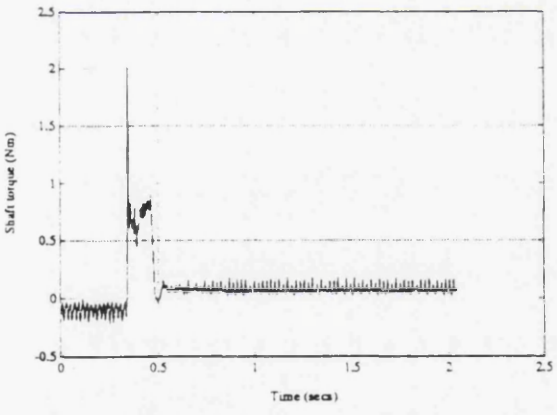

Figure 12b : Torque performance.

The program used for the experimental results presented is a restricted version of that used for the simulation. The restrictions were imposed in order to keep the control interval as short as possible. The main restriction was that the program did not implement parameter estimation. Instead the saturation characteristic for the test machine was measured and the stored in a firmware lookup table. The control algorithms themselves were implemented as outlined earlier.

Figures 12a–d are the experimental results obtained using a maximum torque/ampere (MTC) control strategy for speed reversal from -1400rpm to +1400rpm. The speed reversal has been affected in approximately 100-150 millisecs. These results closely match those obtained in the simulation results presented earlier (see Figures 8a–d). Notice that the lower inductance in the Q axis is evident in the larger rapid variations of the Q axis current around the nominal desired value.

Experiments were also carried out for CCIAC, MRCTC and MPFC. The plots obtained for CCIAC were very similar to those obtained for the MTC, the only differences being that the D axis current remains constant. The actual speed and torque performance was almost the same as the above. The results for MRCTC and MPFC are also similar except that the torque vlaues produced are lower in line with the earlier theoretical predictions. In order to take advantage of the extra SYNCREL torque bandwidth offered by MRCTC a higher bandwidth controller is required for the speed control loop.

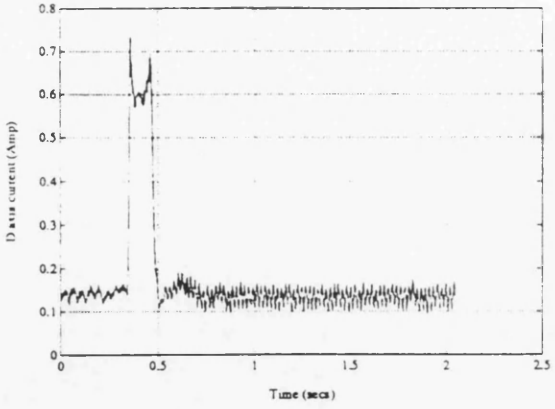

Figure 12c : D axis current

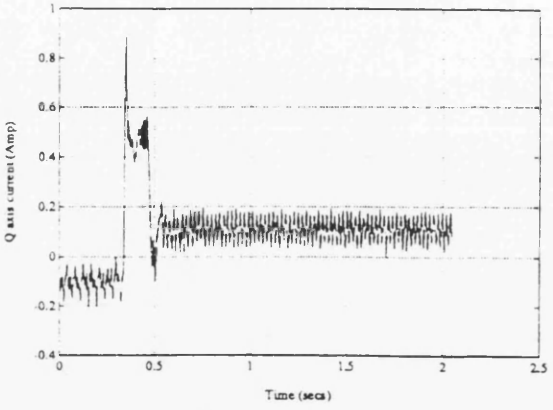

Figure 12d : Q axis current

Figures 13a,b show the performance of the CCIAC control under a transient disturbance torque condition. The disturbance torque applied to the shaft is 80% of rated torque. Note the small speed changes that occur when the torque is applied and removed. These changes are largely a result of the bandwidth of the speed control loop, which is significantly less than the torque bandwidth that the SYNCREL itself can achieve. The experimental results closely match those obtained from the simulation.

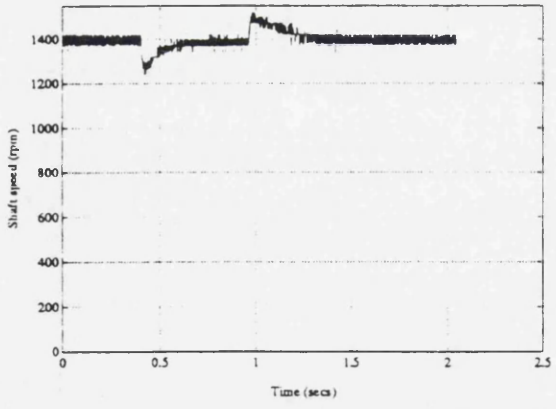

Figure 13a : Experimental speed under transient torque

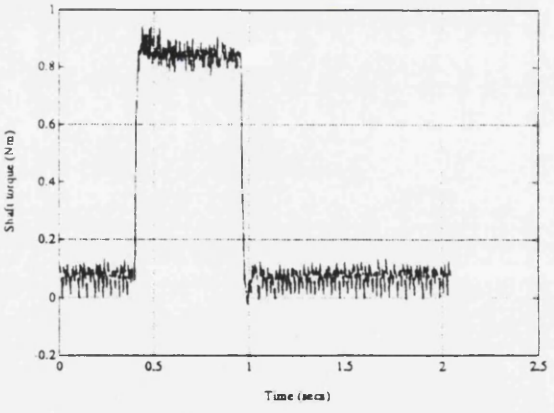

Figure 13b : Shaft torque.

Conclusions

The following conclusions can be drawn from the results presented in this paper:-

- The $\tau_n \omega_n$ product for the MTC and the MRCTC strategies are the same. This relationship is unique for these two control strategies and the constant maximum power curve that exists between them.
- The MRCTC gives the maximum torque-speed curve break frequency.
- Maximum power factor can be obtained from a SYNCREL machine if the current angle is $\tan^{-1}\sqrt{\xi}$.
- The τ_n and $p\tau_n$ performance of MPFC lies between MTC and MRCTC.
- For the same output power MPFC allows significant reductions in inverter size for $\xi > 5$.
- MPFC is insensitive to ξ errors.
- MRCTC is sensitive to knowledge of ξ.
- The MTC strategy can be field weakened to a frequency corresponding to the break frequency of the MRCTC strategy.
- The MRCTC strategy cannot be constant power field weakened.
- The CAC strategies give poor $p\tau_n$ performance at low values of τ_n and/or low values of ω_n.
- CCIAC strategies offer improved $p\tau_n$ performance over CAC's at low speeds and/or torques.
- Virtually all performance parameters for the SYNCREL machine, for all the control strategies are improved by a larger ξ ratio. This serves to highlight the importance of designing the machine to maximise ξ.

It has been observed that if the iron losses in the SYNCREL are of the same order as those of an equivalent sized induction machine, then the effect of the iron losses on the optimal angles of operation calculated using the ideal model can be ignored without significant error. Furthermore, all of the above conclusions hold in general for a non-ideal machine, although there may be some variations in details.

The experimental results were obtained using essentially the same program as the simulation. The control algorithms were those evaluated using the idealized analysis of the machine and were found to perform very well and in reasonable agreement with the simulations.

References

[1] A. Chiba and T. Fukao, "A Closed Loop Control of Super High Speed Reluctance Motor for Quick Torque Response", Conference Record, IEEE-IAS Annual Meeting, Atlanta, Oct. 1987.

[2] A. Fratta, A. Vagati and F. Villata, "Control of a Reluctance Synchronous Motor for Spindle Applications", IPEC, Japan, 1990.

[3] L. Xu, X. Xu, T.A. Lipo and D.W. Novotny, "Vector Control of a Synchronous Reluctance Motor including Saturation and Iron Loss", IEEE Trans. on Industry Applications, Vol. 27, No. 5, Sept/Oct 1991.

[4] R.E. Betz, "Theoretical Aspects of the Control of Synchronous Reluctance Machines", IEE Proceedings-B, Vol. 139, No. 4, July 1992.

[5] R.D. Lorenz and D.B Lawson, "Performance of Feedforward Current Regulators for Field-Oriented Induction Machine Controllers", IEEE Trans. Industry Applications, Vol. IA-23, No. 4, July/August 1987.

[6] H.W. Van der Broeck, H.C. Skudelny and G. Stanke, "Analysis and Realisation of a Pulse Width Modulator based on Voltage Space Vectors", Conference Record, IEEE-IAS Annual Meeting, 1986, pp. 244-251.

[7] R.D. Lorenz, K. Van Patten, "High Resolution Velocity Estimation for All Digital A.C. Servo Drives", Conference Record, IEEE-IAS Annual Meeting, October 1988, pp. 363-368.

[8] D.A. Staton, T.J.E. Miller and S.E. Wood, "Optimisation of the Synchronous Reluctance Motor Geometry", IEE EMD Conference, London, Sept. 1991.

[9] R.E. Betz, M. Jovanovic, R. Lagerquist and T.J.E. Miller, "Control Strategies for the Synchronous Reluctance Machine Including Saturation and Iron Losses", Proceedings of IEEE IAS Annual Meeting, Houston, Texas, Oct, 1992.

[10] Karl J. Astrom and Bjorn Wittenmark, *Computer Controlled Systems*, Prentice-Hall Information and Systems Sciences Series, 1984.

[11] R. Lagerquist, R.E. Betz and T.J.E. Miller, "DSP96002 Based High Performance Digital Vector Controller for Synchronous Reluctance Motors", International Conference on Electric Machines, ICEM92, Manchester, September, 1992.

Acknowledgments

The author wishes to thank the Science and Engineering Research Council (SERC) and Professor T.J.E. Miller and his Scottish Power Electronics and Electric Drives (SPEED) Consortium for making this work possible through their financial support.

The authors would like to acknowledge Mr. Peter Miller who constructed much of the hardware for the experimental system, and Dr. David Staton who designed the 120 Watt SYNCREL rotor.

oOo

E.3 Aspects of the Control of Synchronous Reluctance Machines Including Saturation and Iron Losses

Annual Meeting IEEE–Industry Applications Society

Houston, Texas, October 1992

Aspects of the Control of Synchronous Reluctance Machines Including Saturation and Iron Losses

R.E. Betz[1] M. Jovanovic[1] R. Lagerquist[2] T.J.E. Miller[2]

[1]Department of Electrical and Computer Engineering
University of Newcastle, Callaghan, NSW,
Australia, 2308.

[2]Scottish Power Electronics and Electric Drives Consortium,
Department of Electronics and Electrical Engineering,
University of Glasgow, G12 8QQ,
United Kingdom.

Abstract— **This paper considers aspects of the control of Synchronous Reluctance Machines driven from an inverter when the effects of saturation and iron losses are taken into account. The control strategies considered are:—maximum torque control (ie maximum torque per ampere), maximum power factor control, maximum rate of change of torque control, maximum efficiency control and field weakening control.**

INTRODUCTION

Most of the early work carried out on the synchronous reluctance machine (SynRM) was related to the line start machine. The presence of an induction machine cage for starting together with other factors meant that the SynRM design was a compromise. This compromise manifested itself in terms of poor performance, especially in relation to power factor. However if the machine is controlled via an inverter then the starting cage can be removed from the rotor and it can be designed to give the maximum inductance ratio. The term SYNCREL has been coined for the cageless, electronically controlled SynRM. Interest in this machine has been motivated by the inherently rugged nature of the SynRM, the improved performance of the SYNCREL, and the promise that small to medium size high performance drives may be have simpler control using the SYNCREL as compared to the vector controlled induction machine.

Current research activity into the SYNCREL is concerned with establishing the performance limitations of the system, as well as control techniques which optimise various aspects of the machines operation. Papers [1,2,3] consider the ideal model of the SYNCREL. They establish some interesting relationships between a number of different control objectives for the SYNCREL. The main limitation of this work is that iron losses and saturation were ignored. Papers [5,6] look at more specialised forms of SYNCREL control under similar assumptions. Reference [6] considered the effects that saturation and iron losses have on maximum torque per ampere and maximum efficiency operation. It was found that the optimal current angles of operation were significantly different from those obtained for the ideal model [1]. Finally [7] considered a technique using an observer to identify the current flowing in the magnetising branch of the machine. How the magnetising currents are to be controlled is not considered.

The purpose of the work which is the subject of this paper is to examine in more detail the effects of iron losses and saturation on the performance of the SYNCREL. This involves two steps — the development of expressions for the relevant control objectives accounting for iron losses and saturation, and secondly plot out and comment on curves of these expressions. In the following discussion and analysis the D axis of the machine is considered to lie on the high permeance axis of the machine. The control strategies considered are:—

i) Maximum torque control (MTC) :— This refers to the well known maximum torque per ampere control strategy. For the ideal machine the optimal current angle (with respect to the D axis) is $\pi / 4$ radians.

ii) Maximum rate of change of torque control (MRCTC):— This refers to the control strategy which enables the SYNCREL to maximise the $d\tau / dt$ where τ is the torque of the machine. For the ideal machine the current angle $\theta_i = \tan^{-1} \xi$ where ξ is L_d / L_q [1].

iii) Maximum power factor control (MPFC):— This refers to the control strategy where the machine is operated so that the input power factor is maximised. For the ideal model the current angle is $\theta_i = \tan^{-1} \sqrt{\xi}$ [1]. For the ideal machine this strategy leads to the minimum kVA rating for the inverter.

iv) Maximum efficiency control (MEC):— This refers to the control strategy where the P_{in} / P_o ratio for the

machine is minimised. For the ideal machine the current angle is $\theta_i = \pi / 4$.

v) Field weakening control (FWC):— This refers to the control strategy when the machine is operating above rated speed. The desired torque characteristic is:-

$$\tau \propto \frac{1}{\omega} \tag{1}$$

For the ideal machine it can be shown [1] that the required angle to obtain this characteristic above rated speed is:—

$$\theta_i = \tan^{-1}\left[\frac{(\xi^2+1)-\sqrt{(\xi^2+1)^2-4\omega_n^2\xi^2}}{2\omega_n}\right] \tag{2}$$

where $\omega_n \equiv$ the normalised angular velocity ($\omega_n = \omega / \omega_o$, $\omega_o \equiv$ rated angular velocity).

MATHEMATICAL PRELIMINARIES

A) The SYNCREL Model

The DQ model of the SYNCREL used for the derivation of the following expressions is shown in Fig 1 [6, 7]. The equations for this model are:—

$$\left.\begin{aligned} v_{ds} &= R_s i_{ds} + L_l \frac{di_{ds}}{dt} - \omega\lambda_{qs} + \frac{d\lambda_{dm}}{dt} \\ v_{qs} &= R_s i_{qs} + L_l \frac{di_{qs}}{dt} + \omega\lambda_{ds} + \frac{d\lambda_{qm}}{dt} \\ i_{ds} &= i_{dm} + \frac{1}{R_m}\left[-\omega\lambda_{qm} + \frac{d\lambda_{dm}}{dt}\right] \\ i_{qs} &= i_{qm} + \frac{1}{R_m}\left[\omega\lambda_{dm} + \frac{d\lambda_{qm}}{dt}\right] \\ \tau &= \frac{3}{2} p_p \left(\lambda_{dm} i_{qm} - \lambda_{qm} i_{dm}\right) \end{aligned}\right\} \tag{3}$$

where:—

$$\lambda_{ds} = L_l i_{ds} + \lambda_{dm}$$
$$\lambda_{qs} = L_l i_{qs} + \lambda_{qm}$$
$$\lambda_{dm} = L_{dm} i_{dm}$$
$$\lambda_{qm} = L_{qm} i_{qm}$$

$R_m \equiv$ iron loss resistance

In the case of a machine which has saturation then the L_{dm} value is a function of the current flowing in the d axis of the machine.

In order to simplify the expressions in the remainder of the paper the leakage inductance term (L_l) and stator resistance (R_s) will be assumed to be zero (except for the MEC case). This should result in very little error in the results since L_l is dominated by the other inductances in the model and for most machines R_s is small compared to R_m. The expressions will be developed for a 2 phase single pole pair machine.

B) Maximum Torque Control

After some manipulation it is possible to gain the following expression for the torque produced by the SYNCREL with iron losses:-

$$\tau = (L_{dm} - L_{qm}) R_m^2 \left[\frac{(R_m + \omega L_{qm}\tan\theta_i)(R_m\tan\theta_i - \omega L_{dm})}{(1+\tan^2\theta_i)(R_m^2 + \omega^2 L_{dm} L_{qm})^2}\right] i_{mag}^2 \tag{4}$$

where

$$i_{mag} = \sqrt{i_{ds}^2 + i_{qs}^2} \equiv \text{magnitude of current}$$

$L_{dm} = L_d$; $L_{qm} = L_q$ since $L_l = 0$.

In order to find the precise maximum torque per ampere angle then the non-linear characteristic curves for R_m (R_m vs λ_m) and L_{dm} (L_{dm} vs i_{dm}) have to be included into (4). The resultant equation is transcendental and very complex and has to be solved numerically. This factor also makes it impossible to obtain a closed form expression for the maximum torque per ampere current angle.

In order to simplify the expression if one considers that R_m and L_d are constants (the latter assumption is not unreasonable since the current angle is usually $>> \pi / 4$ and consequently there is little saturation) then (4) can be differentiated with respect to θ_i and equated to zero. The result is the following expression for the optimal maximum torque per ampere current angle:—

$$\theta_i^* = \tan^{-1}\left[\frac{\omega R_m (L_d + L_q)}{R_m^2 - \omega^2 L_d L_q} + \sqrt{\left(\frac{\omega R_m (L_d + L_q)}{R_m^2 - \omega^2 L_d L_q}\right)^2 + 1}\right] \tag{5}$$

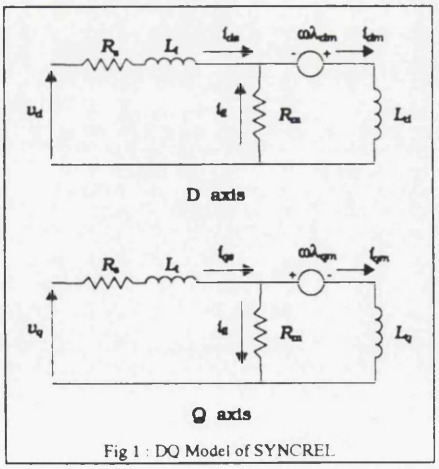

Fig 1 : DQ Model of SYNCREL

If $R_m \to \infty$ then $\theta_i^* \to \pi/4$ as expected.

C) Maximum Power Factor Control

The expression for power factor in the SYNCREL with iron losses is:—

$$\cos\phi = \frac{\frac{1}{2}R_m(L_d - L_q)\sin 2\theta_i + \omega L_d L_q}{\sqrt{L_d^2(R_m\cos\theta_i + \omega L_q \sin\theta_i)^2 + L_q^2(R_m \sin\theta_i - \omega L_d \cos\theta_i)^2}} \tag{6}$$

As with (4) above, the evaluation of this expression is complicated by the dependence of R_m and L_d on the current magnitude and angle (even though this does not explicitly appear in (6)). The fact that current magnitude has an influence on the expression obviously means that the power factor is now a state dependent quantity, as compared to the ideal machine situation where it only depends on the machine parameters [1].

In order to obtain an expression for the maximum power factor a constant R_m and L_d assumption is again used, allowing (6) to be differentiated to give the following equation, which can be solved for the optimal power factor angle.

$$\tan^4\theta_i^* - \frac{2\omega L_d}{R_m}\tan^3\theta_i^* - \frac{2\omega L_d^2}{R_m L_q}\tan\theta_i^* - \frac{L_d^2}{L_q^2} = 0 \tag{7}$$

If $R_m \to \infty$ then $\tan\theta_i^* = \sqrt{\xi}$ as expected from [1]. Substituting for $\tan\theta_i^*$ in (6) one gets the following expression for the maximum power factor:—

$$\cos\phi_{max} = \frac{R_m(L_d - L_q)\tan\theta_i^* + \omega L_d L_q(1+\tan^2\theta_i^*)}{\sqrt{\begin{array}{l} L_q^2(R_m^2 + \omega^2 L_d^2)\tan^4\theta_i^* + 2\omega R_m L_d L_q(L_d - L_q) \\ \tan\theta_i^*(1+\tan^2\theta_i^*) + [R_m^2(L_d^2 + L_q^2) + \\ 2\omega^2 L_d^2 L_q^2]\tan^2\theta_i^* + L_d^2(\omega^2 L_q^2 + R_m^2) \end{array}}} \tag{8}$$

D. Maximum Rate of Change of Torque Control

The determination of the expression for the rate of change of torque in the situation where iron losses and saturation are included is quite messy. Under the condition that leakage and stator resistance are neglected, and R_m and L_d are constant and the machine is being operated with *constant* current angle then the expression for the rate of change of torque is:—

$$p\tau = 2\sqrt{\frac{\tau(L_{dm} - L_{qm})\tan\theta_m}{L_{dm}^2 + L_{qm}^2\tan^2\theta_m}v^2 - \omega^2\tau^2} \tag{9}$$

where $\theta_m \equiv$ the angle of the magnetising current

Differentiating (9) and equating to zero one finds that the optimal angle of operation for maximum rate of change of torque is:—

$$\theta_m^* = \tan^{-1}\frac{L_{dm}}{L_{qm}} = \frac{L_d}{L_q} = \xi \tag{10}$$

Equation (10) is the same expression obtained for the ideal machine model in [1], since the magnetising section of the machine is the same as the ideal machine. If (10) is substituted into (9) then the following expression for the maximum rate of change of torque is obtained:—

$$(p\tau)_{max} = 2\sqrt{\frac{\tau(L_{dm} - L_{qm})}{2L_{dm}L_{qm}}v^2 - \omega^2\tau^2} \tag{11}$$

The input current to the machine can be expressed as—

$$\left.\begin{array}{l} i_{ds} = \dfrac{2\tau(R_m - \omega L_{qm}\tan\theta_m) + L_{dm}p\tau}{2R_m\sqrt{\tau(L_{dm} - L_{qm})\tan\theta_m}} \\ i_{qs} = \dfrac{(2\tau R_m + L_{qm}p\tau)\tan\theta_m + 2\tau\omega L_{dm}}{2R_m\sqrt{\tau(L_{dm} - L_{qm})\tan\theta_m}} \end{array}\right\} \tag{12}$$

Using (12) together with the fact that $\tan\theta_i = i_q/i_d$ and $\tan\theta_m = \tan\theta_m^*$ an expression for the optimal input terminal current angle can be found:—

$$\theta_i^* = \tan^{-1}\left[\sqrt{\frac{L_{dm}}{L_{qm}}}\frac{(R_m + \omega L_{qm})\sqrt{2L_{dm}\tau} + \sqrt{L_{qm}(L_{dm} - L_{qm} - 2L_{dm}L_{qm}\omega^2\tau)}}{(R_m - \omega L_{dm})\sqrt{2L_{qm}\tau} + \sqrt{L_{dm}(L_{dm} - L_{qm} - 2L_{dm}L_{qm}\omega^2\tau)}}\right] \tag{13}$$

The expression for maximum rate of change of torque becomes much more complex if saturation is allowed in the magnetic material. This is due to the fact that the L_{dm} inductance is a function of the current which is a function of time. After considerable manipulation the following expression for $p\tau$ can be found:—

$$p\tau = \frac{B + \sqrt{B^2 - 4AC}}{2A} \tag{14}$$

where:—

$$A = (L_{dm} - L_{qm})^2\left[(L_{dm} - L_{qm})\tan\theta_m(L_{dm}^2 + L_{qm}^2\tan^2\theta_m) + (L_{dm}')^2\tau + 2L_{dm}L_{dm}'\sqrt{(L_{dm} - L_{qm})\tau\tan\theta_m}\right]$$

$$B = 2\omega L_{dm}' L_{qm}(L_{dm} - L_{qm})\tan\theta_m\tau\left[2(L_{dm} - L_{qm})\sqrt{\tau(L_{dm} - L_{qm})\tan\theta_m} + \tau L_{dm}'\right]$$

$$C = \left[2(L_{dm} - L_{qm})\sqrt{\tau(L_{dm} - L_{qm})\tan\theta_m} + \tau L_{dm}'\right]^2 \left[(L_{dm}^2 - L_{qm}^2\tan^2\theta_m)\omega^2\tau - (L_{dm} - L_{qm})v^2\tan\theta_m\right]$$

$$L_{dm}' = \frac{dL_{dm}}{di_{dm}}$$

Note that if $L_{dm}' = 0$ then (14) becomes (9).

E) Maximum Efficiency Control

The maximum efficiency angle can be found by minimising the expression for the power into the machine under the condition of constant power output.

The expression for the power input to the machine (including stator resistance in the model) is:—

$$P_{in} = R_s i^2 + \frac{\omega R_m i_{mag}^{\ 2}}{R_m^{\ 2} + \omega L_d L_q}\left[\frac{L_d\sqrt{R_m^{\ 2}+\omega^2 L_q^{\ 2}}}{2}(\sin(2\theta_i - \delta_1) + \sin\delta_1) - \frac{L_q\sqrt{R_m^{\ 2}+\omega^2 L_d^{\ 2}}}{2}(\sin(2\theta_i + \delta_2) + \sin\delta_2)\right] \quad (15)$$

where:—

$$\delta_1 = \tan^{-1}\frac{\omega L_q}{R_m}; \qquad \delta_2 = \tan^{-1}\frac{-\omega L_d}{R_m}$$

Similarly the output power expression is:—

$$P_o = \frac{\omega(L_d - L_q)R_m^{\ 2} i_{mag}^{\ 2}\sqrt{R_m^{\ 2}+\omega^2 L_q^{\ 2}}\sqrt{R_m^{\ 2}+\omega^2 L_d^{\ 2}}}{2(R_m^{\ 2}+\omega^2 L_d L_q)^2} \cdots \ldots(\sin(2\theta_i + \delta_2 - \delta_1) + \sin(\delta_1 + \delta_2)) \quad (16)$$

Letting the output power be $P_{desired}$ and the angular velocity be $\omega_{desired}$ then using (15) and (16) the following expression for the input power under the constant output power condition can be found:—

$$P_{in} = \left[\frac{P_{desired}E}{A(\sin(2\theta_i + \delta_2 - \delta_1) + \sin(\delta_1 + \delta_2))}\right] \cdots \ldots\left[B + C(\sin(2\theta_i - \delta_1) + \sin\delta_1) - D(\sin(2\theta_i + \delta_2) + \sin\delta_2)\right] \quad (17)$$

where:—

$$A = \omega_{desired}(L_d - L_q)R_m^{\ 2}\sqrt{R_m^{\ 2}+\omega_{desired}^{\ 2}L_q^{\ 2}}\sqrt{R_m^{\ 2}+\omega_{desired}^{\ 2}L_d^{\ 2}}$$

$$B = 2R_s(R_m^{\ 2} + \omega_{desired}L_d L_q)$$

$$C = \omega_{desired}R_m L_d\sqrt{R_m^{\ 2}+\omega_{desired}^{\ 2}L_q^{\ 2}}$$

$$D = \omega_{desired}R_m L_q\sqrt{R_m^{\ 2}+\omega_{desired}^{\ 2}L_d^{\ 2}}$$

$$E = \frac{B}{2R_s}$$

The minimum input power can be found by taking the derivative of (17) with respect to θ_i. Even under the constant R_m and L_d assumption the result is a very messy expression for the optimal θ_i.

F) Field Weakened Control

The concept of field weakening in the SYNCREL is not as straight forward as in the DC machine for example. Field weakening occurs when the machine is to operate over the knee in the torque-speed curve. The normal characteristic for the SYNCREL in this region is $\tau \propto 1/\omega^2$. The objective of field weakening is to make the machine give constant power for a range of frequencies above rated ω_o, ie. the torque characteristic is $\tau \propto 1/\omega$ for $\omega \geq \omega_o$ where $\omega_o \equiv$rated angular velocity. Under these conditions the following equation can be derived which can be solved for the field weakening angle:—

$$\theta_i = \tan^{-1}\left[\frac{-F - \sqrt{F^2 - 4GH}}{2G}\right] \quad (18)$$

where:—

$$F = (L_d - L_q)\left[2R_m L_d L_q \omega^2 P_o - (R_m^2 - \omega^2 L_d L_q)v_o^2\right]$$

$$G = \omega L_q\left[L_q P_o(R_m^{\ 2} + \omega^2 L_d^{\ 2}) - R_m(L_d - L_q)v_o^{\ 2}\right]$$

$$H = \omega L_d\left[(L_d - L_q)R_m v_o^{\ 2} + L_d P_o(R_m^{\ 2} + \omega^2 L_q^{\ 2})\right]$$

If $R_m \to \infty$ then the expression becomes that of (2). Equation (18) can be used to calculate the approximate field weakening angle if the values of R_m and L_d are considered to be constant. A more precise angle can be calculated if the functional relationships for R_m and L_d are used. In this case the solution method is a complex numerical procedure.

OBSERVATIONS

In order to generate the relevant plots for the above equations experimental machine data is required. The following plots all use the data for the machine in [6] which is reproduced below in a slightly altered form for convenience. The test condition for these parameters was:— $\omega = 800$ rpm ($\omega_e = 167.55$rad/sec, pole pairs=2), $P_o = 0$ (ie. zero torque output). The Q axis inductance $L_q = 0.0055$H, and stator resistance $R_s = 0.2\Omega$.

TABLE 1 : MACHINE PARAMETERS

i_{dm}	λ_d	L_d	R_m
2.83	0.1111	0.039	12.65
7.75	0.3114	0.040	17.02
12.18	0.4480	0.037	19.27
20.77	0.5447	0.026	21.04
24.74	0.5603	0.023	21.74
28.05	0.5788	0.021	22.55

A) Maximum Torque Per Ampere

Considering maximum torque control. If (4) is solved for the current magnitude using the precise R_m vs λ and L_{dm} vs i_{dm} curves contained in Table 1 then Fig. 1 results.

This diagram has been generated under the condition that the output power is 508 Watts and ω is as per the Table 1 data. The plots for the higher output powers are very similar. As can be seen from Fig. 1 the maximum torque per ampere operation angle is approximately 57°. This result corresponds very well with that obtained by [6], whose calculated results were obtained by assuming a constant R_m resistance. The insensitivity to the power output (and hence the current output level) can be understood if the L_{dm} and R_m curves are plotted out for the various cases. Because the current angle is $\gg \pi/4$ then the saturation of L_d is virtually zero. For larger power variations the change in the iron loss resistance is more significant, and would result in larger variations in the optimal angle.

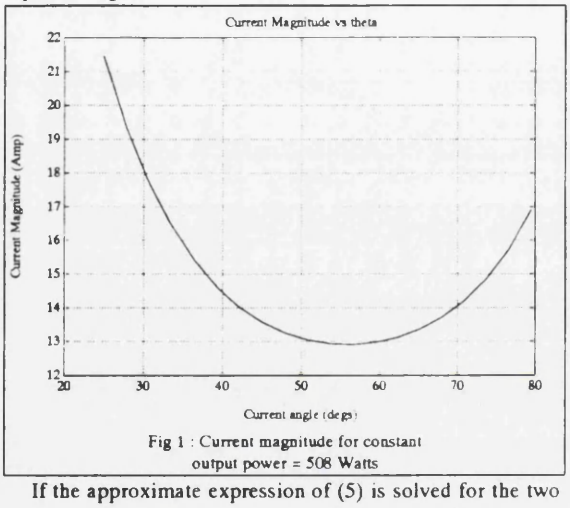

Fig 1 : Current magnitude for constant output power = 508 Watts

If the approximate expression of (5) is solved for the two power output cases then the angle obtained is 57°. It should be noted that this equation is being solved with a good estimate of R_m (18Ω). However if the flux level varies widely from that which corresponds to this value of R_m then the error increases. For the reason explain above L_d does not have a significant effect on the approximate equation.

B) Maximum Power Factor

In the ideal SYNCREL model the maximum power factor point of operation was also the minimum kVA point of operation of the machine. The minimum kVA point of operation is important because of the implications on the size/rating of the inverter.

Fig. 2a shows a plot of (6) for $P_o = 508$ Watts and $P_o = 1130$ Watts. There is virtually no difference between the optimal power factor angle or the optimal power factor value for either case. The optimal power factor angle calculated from the ideal model is 70°, therefore the iron loss has had a minimal effect on the angle. The maximum power factor value from the ideal case is [1] :—

$$\eta_{\max} = \frac{\xi - 1}{\xi + 1} = 0.76 \tag{19}$$

whereas for the real machine model the value is ≈ 0.82. The presence of the resistance in the model results in this improvement. If the approximate equations (7)and (8) are evaluated with $R_m = 18\Omega$ and $L_d = 0.040$H then the optimal power factor angle is 72° and the optimal power factor value is 0.81. The approximation gives reasonable values compared to the exact solution.

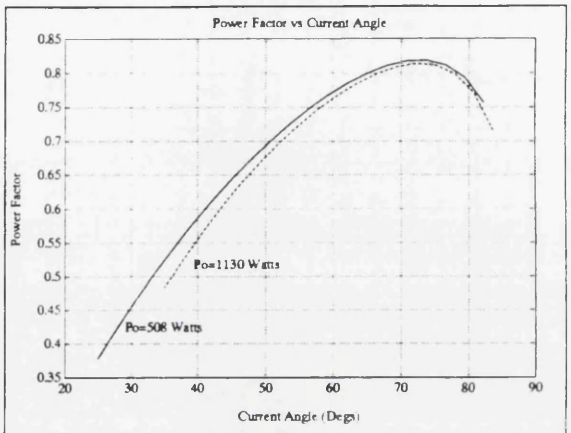

Fig 2a : Power factor

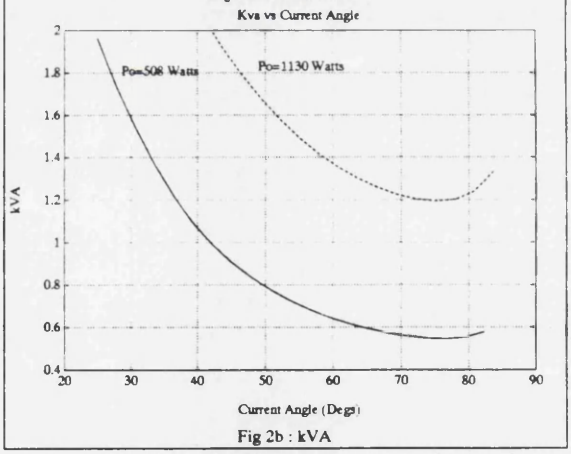

Fig 2b : kVA

Unlike the ideal machine model case, the maximum power factor angle does not guarantee that the machine will be operating at minimum kVA. Fig. 2b shows the kVA for a variety of current angles. Notice that the angle for the minimum kVA from the inverter does not correspond to the maximum power factor angle (although it is still quite

close). In addition the minimum kVA angle does not appear to be very sensitive to the output power of the machine.

C) Maximum Rate of Change of Torque

The maximum rate of change of torque is determined from (9) for the case where there is no saturation , and from (14) when there is saturation. It should be noted that these expressions have been derived with the magnetising current vector angle constant. As can be seen from Figs 3a and 3b the optimal angle of the *magnetising* current does not vary very much for the different power levels. As expected from [1] the higher torque levels lead to higher $d\tau/dt$ values. The other point to note is that saturation has very little effect on the $d\tau/dt$ has shown from the no saturation curve. In fact if expression from [1] for maximum $d\tau/dt$ is used ($\theta_i = \tan^{-1}\xi$) then the angle is 82°, which is very close to that shown in Figs 3a and 3b.

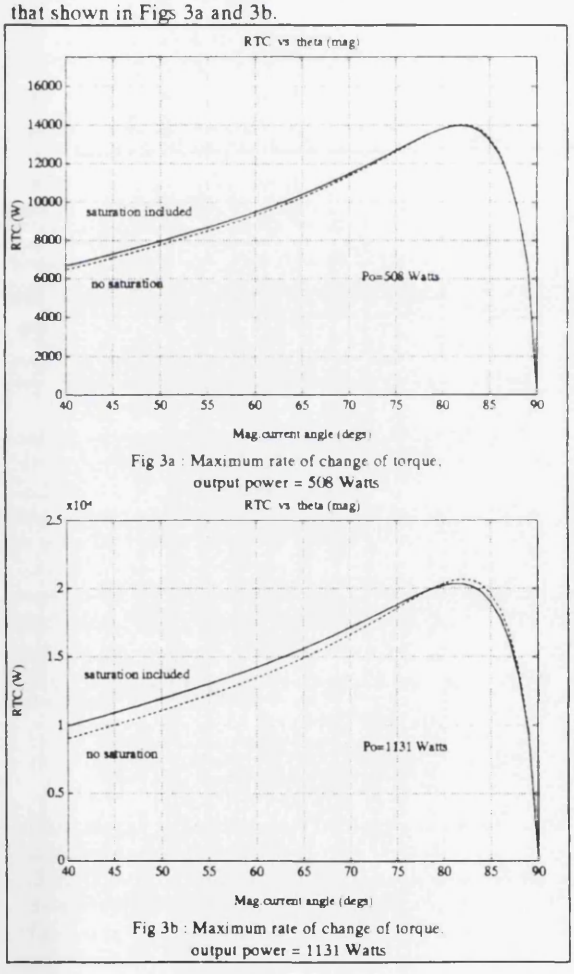

Fig 3a : Maximum rate of change of torque, output power = 508 Watts

Fig 3b : Maximum rate of change of torque. output power = 1131 Watts

D) Maximum Efficiency

One of the most important characteristics of a machine is its efficiency. In order to determine the most efficient current angle for the SYNCREL the power into the machine was plotted for a constant power out. Figs 4a and 4b plot P_{in} vs θ_i for two output powers — 508 Watts and 1131 Watts (corresponding to 6.07 Nm and 13.5 Nm output torque respectively at 800 rpm, as in [6]). The dashed curve on these figures is a plot of (17) with $R_m = 18\Omega$ and $L_d = 0.04\text{H}$. The solid curve is the "exact" curve taking into account the variations in saturation and iron losses.

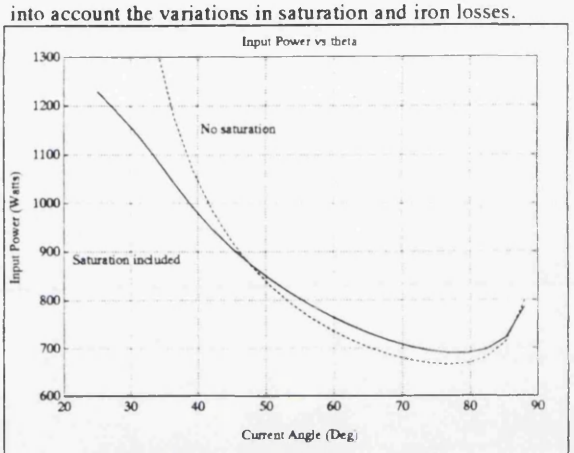

Fig 4a : Input power with output power = 508 Watts, Shaft ang. velocity = 800 rpm

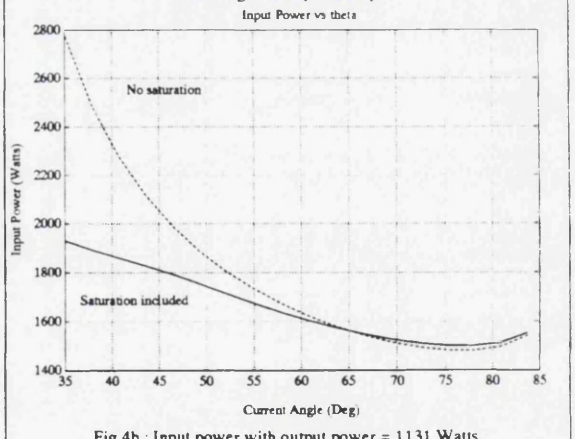

Fig 4b : Input power with output power = 1131 Watts, Shaft ang. velocity = 800 rpm

Three observations are immediately obvious. Firstly the presence of saturation in the machine improves the efficiency of the machine if the optimal current angle is not used. This effect is most predominant for the lower angles of the current since these lead to more saturation in the D axis and consequently lower D axis inductances. This in

turn means that there is less induced voltage to drive current through the iron loss resistor. Secondly, there is very little difference between the optimal efficiency current angle predicted by the approximate solution and that determined from the precise curve. Finally the optimal efficiency angle is much greater than that predicted by the ideal model ($\pi/4$).

The "exact" curves for the efficiency were not found by solving (17) transcendentally, but were computed by using a simpler and more direct set of equations as shown below:—

$$\left(i_{dm} - \frac{\omega L_q i_{qm}}{R_m}\right)\tan\theta_i - \left(i_{qm} + \frac{\omega L_d i_{dm}}{R_m}\right) = 0$$

$$P_d - \tfrac{3\omega}{2}(L_d - L_q) i_{dm} i_{qm} = 0 \qquad (20)$$

where P_d is the constant output power.

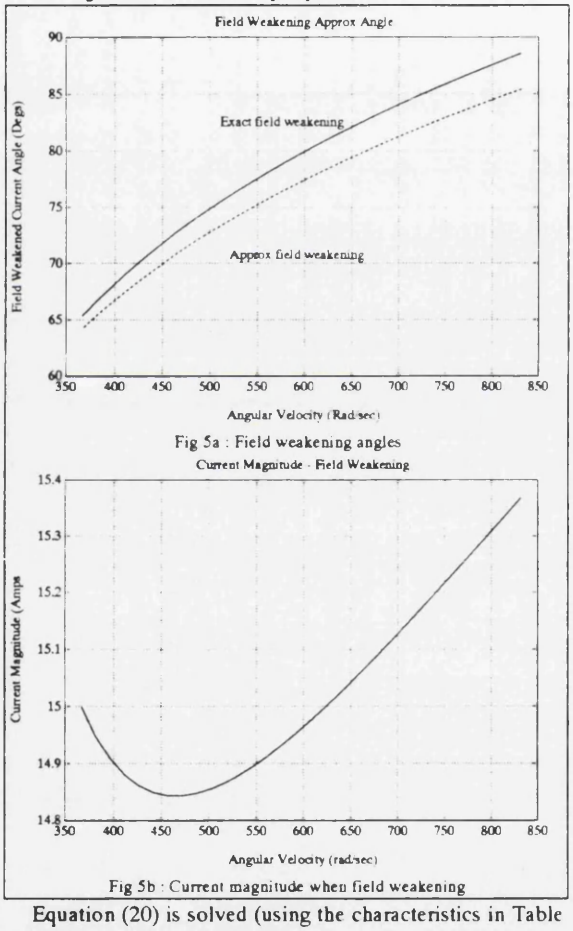

Fig 5a : Field weakening angles

Fig 5b : Current magnitude when field weakening

Equation (20) is solved (using the characteristics in Table 1) for the magnetising currents i_{dm} and i_{qm}. These in turn are substituted into (3) under steady state conditions to give the terminal currents i_{ds} and i_{qs} and the terminal voltages v_{ds} and v_{qs}. The input power is then simply:—

$$P_{in} = v_{ds} i_{ds} + v_{qs} i_{qs} \qquad (21)$$

F) Field Weakening

Figures 5a and 5b show the field weakening angle and current magnitude when field weakening is being attempted. Field weakening is entered into when the angular velocity of a machine is increased to the point where the machine runs out of volts. In the case which is plotted the machine was assumed to be running at 1750 rpm with an input current magnitude of 15 Amps. From this data then the other "rated" conditions were evaluated. Normally this is a straight forward operation, however with the non-linear R_m and L_d characteristics this is not the case. The rated voltage under the above conditions was $v_o = 105$ volts and $\tau_{rated} = 5.4$ Nm. The rated power was therefore $P_o = \tau_{rated}\omega_o / p_p$, which in this case was 990 Watts. This was the constant power value which had to be maintained into the field weakening region.

Fig 5a shows the field weakening angle for angular velocities above the "rated" value. The dashed line is using (18) with both R_m and L_d constant at 18Ω and 0.04H respectively. The solid line denotes the exact field weakening curve, evaluated taking into account the variations in R_m and L_d. One point which is immediately obvious is that both curves are of similar form, and just displaced. The approximate equation underestimates the field angle required.

Fig 5b shows the current magnitude corresponding to the field weakening plot of Fig 5a. The current magnitude decreases as field weakening begins since the machine is approaching the maximum efficiency operating point, and the power output is constant. However as the frequency is raised the current eventually increases above the initial rated value of 15 Amps. The frequency where the current magnitude exceeds 15 Amps is the maximum field weakening frequency (approximately $2\times\omega_o$). This is much less than the field weakening frequency predicted by the ideal model [1] of $3.6\times\omega_o$.

CONCLUSIONS

This paper has developed the expressions for maximum torque per ampere, maximum power factor, maximum rate of change of torque and field weakening for the SYNCREL when the machine is subject to saturation and iron losses.

The derived expressions were then examined graphically using the parameters of the machine in [6]. The following conclusions/observations can be made from this analysis:—

i) When the variations in R_m and L_d are incorporated into the machine model the D axis current angle for the maximum torque per ampere varies very little from that obtained in [6], but dramatically from that predicted by the ideal model [1]. Indeed if the approximate expression (5) is evaluated the optimum obtained is in good agreement with the exact answer.

ii) The maximum power factor angle for the machine is at an angle greater than the maximum torque per ampere. The angle for maximum power factor varies little with the output power of the machine. It was found that the point of maximum power is not necessarily the point of minimum kVA.

iii) The maximum rate of change of torque magnetising current angle varies very little with the output power from the machine. In addition there is little error between the expression which ignores saturation and the more precise expression.

iv) The angle of maximum efficiency is much greater than that predicted by the ideal model, as was observed by [6]. If the non-saturating model is used (but including the iron losses) then the angle obtained for the maximum efficiency is very close to the exact value. The angle of maximum efficiency appears to vary very little with output power. The efficiency of the saturating machine improves compared to the non-saturating machine for lower values of the current angles.

v) The SYNCREL model with saturation and iron losses can be field weakened in the same manner as the ideal model [1]. However the field weakening angle using the non-ideal models are at considerable variance with the ideal model — the field weakening angles are much larger. The approximate expression for the field weakening angle, whilst of the same general form for the field weakening curve as the exact case, is erroneous enough to be of little practical use.

A general observation that can be made about all the strategies considered is that the current angle of operation is usually large so that the saturation in the D axis inductance is minimal, even for the higher output powers. This would indicate that the identification of the saturated values of the L_d inductance may not be required in a practical controller. The iron loss resistance on the other hand plays a crucial role in determining the optimum angles of operation. In some cases a constant value of R_m can be used, but in others greater precision is required.

The above observations are preliminary in nature. Much more work is required to see if the observations for the example machine hold in general. The ultimate objective is to develop control strategies for the machine which will be able to optimise the performance.

ACKNOWLEDGMENTS

R.E. Betz would like to acknowledge the Science and Engineering Research Council, the Scottish Power Electronics and Electric Drives Consortium and Professor T.J.E. Miller for their financial and equipment support during the preliminary phases of this work.

REFERENCES

[1] R.E. Betz, "Theoretical Aspects of the Control of Synchronous Reluctance Machines", to appear *IEE Proceedings, Part B.*

[2] R.E. Betz and T.J.E. Miller, "Aspects of the Control of Synchronous Reluctance Machines", *Proceedings European Power Electronics Conference EPE'91, Florence*, Sept 6-9, 1991.

[3] R.E. Betz, "Control of Synchronous Reluctance Machines", *Annual Meeting IEEE-IAS, Dearborn USA*, pp 456-462, Sept 29-Oct 4, 1991

[4] A. Chiba and T. Fukao, "A Closed Loop Control of Super High Speed Reluctance Motor for Quick Torque Response", *Annual Meeting IEEE-IAS, Atlanta, USA*, Oct 1987.

[5] A. Fratta, A. Vagati and F. Villata, "Control of a Reluctance Synchronous Motor for Spindle Applications", *IPEC, Japan*, 1990.

[6] L. Xu, X. Xu, T.A. Lipo and D.W. Novotny, "Vector Control of a Synchronous Reluctance Motor including Saturation and Iron Losses", *IEEE Trans on Industry Applications*, vol. 27, no. 5, pp 977-985, Sept/Oct 1991

[7] L. Xu and J. Yao, "A Compensated Vector Control Scheme of a Synchronous Reluctance Motor including Saturation and Iron Losses", *Annual Meeting IEEE-IAS, Dearborn, USA*, pp 298-304, Sept 29-Oct 4, 1991.

E.4 DSP96002 Based High Performance Digital Vector Controller for Synchronous Reluctance Motors

International Conference on Electrical Machines
Manchester UK, 15-17 September 1992

DSP96002 Based High Performance Digital Vector Controller for Synchronous Reluctance Motors

R. Lagerquist[1] R.B. Betz[2] T.J.E. Miller[3]

[1,3]Scottish Power Electronics & Electrical Drives Consortium,
Department of Electronics & Electrical Engineering,
University of Glasgow, G12 8QQ,
United Kingdom.

[2]Department of Electrical & Computer Engineering,
University of Newcastle, Callaghan,
Australia. 2308.

Abstract

This paper presents a 7.5kW vector controller for the cageless synchronous reluctance motors (SYNCHREL). The controller features voltage space vector PWM with advanced control algorithms [1,2] implemented entirely in software. The controller employs a high performance DSP96002 digital signal processor.

The controller has shown itself capable of controlling the SYNCHREL with good dynamic performance.

The first section of the paper presents the hardware and software implementation of the controller.

The second section presents dynamic response and performance data. The performance is good compared to an induction motor using the same frame and windings.

Introduction

Commercial controllers often rely on the combination of a micro-controller and an application specific integrated circuit (ASIC) to implement the control. The use of an ASIC often means that the controller is limited to one type of machine. In a research environment or one-off production the development of an ASIC would be costly and counterproductive if the controller were to be used to control other motor types.

The controller presented in this paper uses a high speed digital signal processor (DSP) to implement the entire control in software. The DSP controls the switching of the phases directly and can with an appropriate program control any 3-phase sinusoidally excited motor. By using a DSP and software only approach, we have developed a general test facility for sinusoidally excited motors. By loading appropriate software the controller is easily converted to operate with different motor types.

Vector control of the synchrel is important as the performance characteristics are directly dependent on the placement of the current vector relative to the most inductive axis (d-axis) of rotor. The DSP controller implements the following control strategies identified by Betz in [1,2]:

1. Maximum Torque Control (MTC). This refers to the well-known maximum torque per ampere control strategy. This is obtained with a current angle $\theta = \pi / 4$ radians. The speed at which the inverter runs out of volts using this control method is known as the rated speed, ω_0.

2. Maximum Rate of Change of Torque Control (MRCTC). This refers to the control strategy proposed in [3] where the rate of change of torque is optimised. The required current angle for this is:

   $\theta = \tan^{-1}\xi$, where ξ is the ratio L_d / L_q.

3. Maximum Power Factor Control (MPFC). This control operates the machine at the highest power factor obtainable. This gives the lowest ratio of inverter kVA rating to output torque. The required current angle is [2]: $\theta = \tan^{-1}\sqrt{\xi}$.

4. Constant Current in the Inductive Axis Control (CCIAC). This control method keeps the current in the most inductive axis constant and varies the current in the least inductive (q-axis) to control the torque. Of all the strategies this strategy gives the highest rate of change of torque at low speeds [2].

5. Field Weakening Control (FWC). When the inverter runs out of volts the current angle is increased to maintain constant power at higher speeds. The current angle required for operation above rated speed is [2]:

$$\theta = \tan^{-1}\left[\frac{(\xi^2+1)-\sqrt{(\xi^2+1)-4\omega_n^2\xi^2}}{2\omega_n}\right]$$

$$\omega_n = \omega / \omega_0$$

This paper describes the hardware and software of the DSP controller, and presents experimental results. The performance is compared with a comparable induction motor.

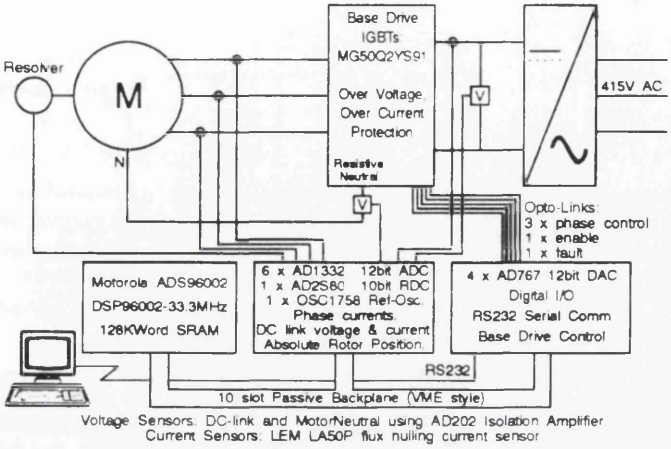

Figure 1. DSP based SYNCHREL vector controller.

DSP based Vector Controller

The philosophy behind this controller was to create a general test facility that would enable tests of almost any sinusoidally excited machine without having to build machine specific hardware for each type of machine. To achieve this full digital control implemented in software is used, and has been taken to the extreme by having the processor control the phase leg switching times using voltage space vector PWM.

The controller is designed to handle loads of 7.5kW with a maximum phase current of 50A. The drive can also be used for regenerative action. At present the maximum regenerated power allowed is 100W.

The user interface to the controller is via a terminal. The user can issue simple commands to control the operation of the motor and receive status information. Several of the control parameters can be changed on-line through the terminal interface. If a computer is connected to the controller it can be used to issue complex command sequences.

Features of the Motorola DSP96002

The Motorola DSP96002 uses a super scalar design allowing more than one instruction per cycle, and has a true IEEE floating point unit. When clocked at 33.3MHz it offers 16.5 MIPS and 49.5M FLOPS peak throughput. This performance is however not attainable using current high level language compilers. The bus interface of the DSP is well suited for interfacing to both fast and slow peripheral-devices as the number of wait states is individually programmable for different parts of the memory. This ensures optimum performance of memory and peripheral devices.

Hardware

The vector controller is split into a digital control-unit and a power-electronics unit. Digital signals between the two units are transmitted over optical fibre. Analog signals are transmitted using 50Ω current loops. The chosen interface methods enhance the system's noise immunity.

Power Electronics

The inverter's DC-link is driven from a 3 phase 415V rectified AC mains supply. The DC-link capacitance is 4500μF. Toshiba MG50Q2YS91 insulated gate bipolar transistor (IGBT) modules with a rating of 1200V 50A are used for the three phase legs. The IGBT gate drive circuits drives the gates with both positive and negative voltage to ensure rapid and precise switching.

By incorporating protection for DC-link over/under-voltage, and DC-link and phase over current, the unit is made self protecting. Self protection in the power electronics unit is important during the commissioning stage of new control programs.

The unit has four high bandwidth flux-nulling LEM LA50P current sensors measuring DC-link and phase currents. DC-link voltage is measured using an AD202 isolation amplifier. The measuring and control electronics are thus totally insulated from the high voltage power electronics.

DSP-control unit

As can be seen from figure 1 the control unit is a bus based system. The processor and peripheral cards plug into a standard VME style passive back plane. The back plane can accommodate a maximum of 10 expansion cards facilitating easy expansion of the system. The design allows for the use of two different bus speeds when accessing devices on the bus. For fast devices the access times used is 91ns, slow devices are accessed with 180ns. On-board memory is accessed at maximum speed, 30ns.

The system consists currently of three double size Eurocards housed in a standard 19" rack enclosure. The boards are:

Processor board

The processor board used is the DSP96002ADS development board from Motorola. It features 128k words of 32bit static RAM and operates with a clock frequency of 33.3MHz. Unfortunately this processor board is not capable of driving the back plane directly, and requires an external bus-buffer board.

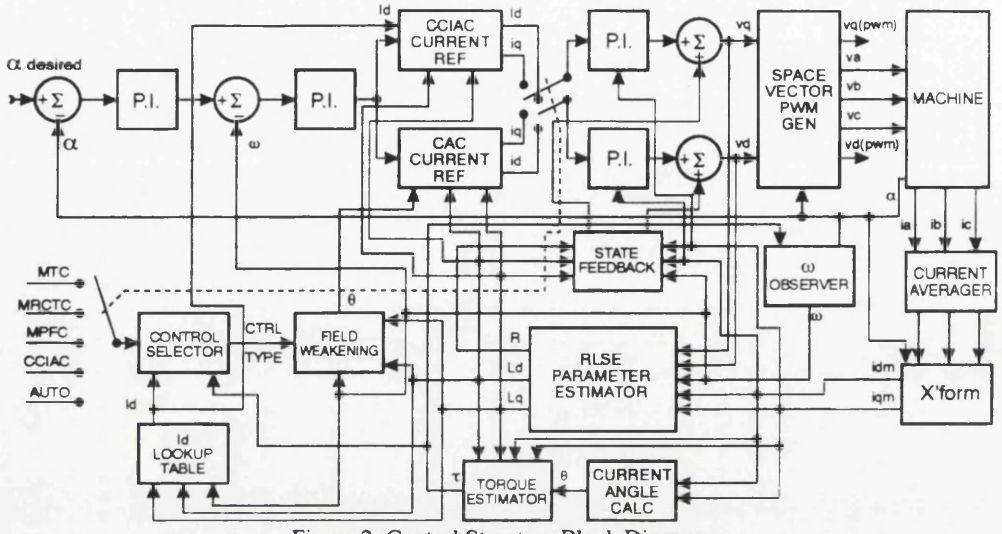

Figure 2. Control Structure Block Diagram

Data acquisition board

The data acquisition is responsible for sampling all analog measurements required, and to drive and decode the shaft position from a resolver. The board was made using SpeedWire as this system is fast and well suited for bus work.

Analog to digital conversion is performed by six AD1332s 12-bit ADCs. These devices suit the application especially well as they incorporate a 32 entry FIFO which buffers the samples and generates an interrupt at either full or half-full buffer. The sample period is controlled by an Intel 8254 16-bit programmable timer driven by a 10MHz oscillator. The system is set up to use the half-full interrupt to initiate a new control interval.

At the start of the control interval each ADC contains 16 data points stored in the FIFOs; these are read with an access time of 91ns for each point. By interrupting the processor only once during the control interval, overhead that would have resulted from 15 additional interrupts has been eliminated.

The rotor position is measured once each control interval using a resolver that gives an absolute position signal. The rotor of the resolver is excited by a harmonic free, high power 5.6kHz sinusoidal oscillator, OSC1758. The resolver produces sin and cos wave forms corresponding to the rotor position. These signals are decoded by an AD2S80 resolver to digital converter (RDC). The RDC is capable of delivering 16-bit accuracy, but it is used at 10-bit accuracy to enable high-speed operation.

Base drive control and analog output board

An i8251 UART and an i8254 timer forms the serial communication interface. Using the i8254 as a baud rate generator a wide range of baud rates can be programmed.

Four AD767 12-bit digital to analog converters (DAC) are used to output real time data that would be impossible to transmit over a low speed serial line.

The base drive control circuit's function is to produce a desired voltage vector. The desired voltage vector is made up of three distinct voltage vectors which during the control interval add up to the desired voltage vector. The base drive control circuit consists of an i8254 16-bit timer, optical fibre transmitters and glue logic. The DSP will at the start of a control interval set the state of the phase legs and program the timer to change the state at particular times during the control interval. The use of a timer saves processor execution time because the processor does not constantly have to poll a timer to determine when to switch the phase legs.

Programming Environment

The DSP programs can be written in C or assembler and are compiled, assembled, linked and relocated to produce an absolute program file on a PC. The program file is downloaded to the DSP's RAM through a special PC-adapter card connected to the debug interface of the DSP. If programs were not downloaded to RAM from the PC four eproms would have to be programmed for each program/debug cycle, thus considerable time is saved during development using this system.

Control program structure

The control program running on the DSP implements the following operating modes; MTC, MRCTC, MPFC, CCIAC and FWC. The control program is based on the SYNCHREL simulation program described

in [1] and consists of 99% ANSI-C code which uses floating point arithmetic throughout. The use of floating point variables and basing the control program on an existing simulation program, written in C, has drastically reduced development time.

The control interval is at present 576μs and with some production engineering could either be reduced or make it possible to use a less expensive processor, e.g. DSP56000. This would involve rewriting in assembler and/or conversion to fixed-point arithmetic.

Control Structure

Figure 2 shows the structure of the vector controller. As can be seen, the controller supports both speed and position control. The control structure may look complex, however the program flow is quite straightforward. The control program consists of a main program which does command interpretation / response, and an interrupt routine which executes the actual control algorithms. The flow of the interrupt program is as follows:

1. Program timers with voltage space vector PWM pattern for current control interval.
2. Read in all sampled data and rotor position. Averages sampled data and convert currents into d-q frame values.
3. Check serial input for characters. Acts on stop command and pass other characters to the main program for interpretation.
4. Estimate machine parameters (L_d, R) using recursive least squares (RLS) estimator.
5. Predict currents and average torque over the current control interval.
6. Predict rotational velocity using ω observer.
7. For position control, calculate desired speed using PI control.
8. Using selected control type perform field weakening calculation to determine required current angle.
9. Calculate the desired torque using PI control from the desired speed and current angle.
12. Calculate d- and q-axis current reference values based on desired torque, speed and current angle values.
13. Calculate desired d-q voltages from the desired d-q currents using PI control. Correct voltage for terms due to resistance and motional emf.
14. Calculate the most efficient switching pattern that achieves the required voltage vector using voltage space vector PWM [5], save the pattern for use at start of next control interval.

Results and Conclusion

Table 1 shows that the performance of the SYNCHREL is better than a comparable induction motor. Figure 3 shows the d-q currents, and phase current and voltage. The voltage shows a characteristic chopped six-step wave form. Figure 4 shows the drive doing a speed reversal in 0.1s, the time for MPFC is 0.094s and CCIAC is 0.17s. Figure 5 shows a step torque change, the torque reaches the required level after 33ms.

A high performance DSP based drive system has been built. The system has shown good dynamic performance. The efficiency of the SYNCHREL proved to be good. The field weakening capability has not been tested fully as the d-q frame movement, with the present control interval, gets too large at high speeds.

Full-Load Parameters	MTC 120W SYNCHREL	120W Induction Motor
Shaft Power [W]	142.5	120
Speed [RPM]	1500	1360
Torque [Nm]	0.90	0.84
Load Current [A]	0.3998	0.46
Supply Voltage [V]	438.0	400
VA Rating	303.29	318.7
Power Factor	0.6678	0.62
Efficiency [%]	70.34	61.2
Total Losses [W]	60.03	76

Table 1. SYNCHREL and Induction Motor Performance Data

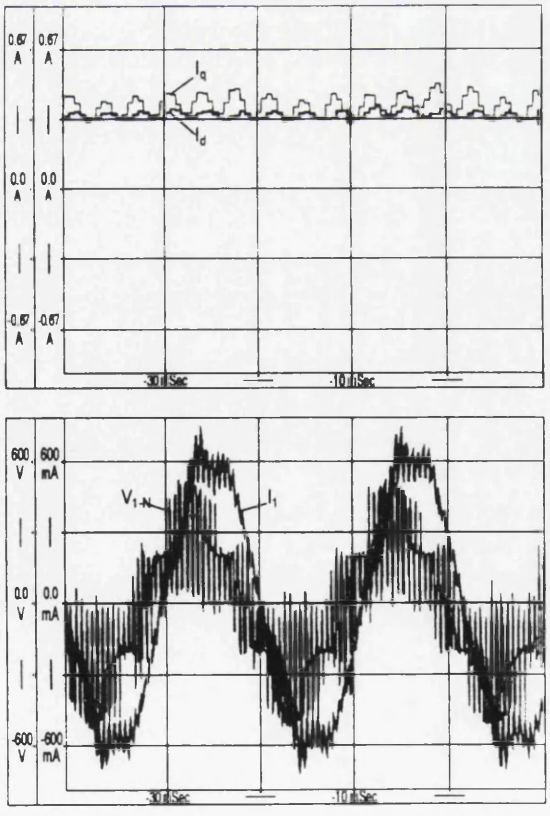

Figure 3. Voltage and Current wave forms for MTC operation. ω=1400rpm, T=0.84Nm.
Top: d-q currents. Bottom: phase current and voltage.

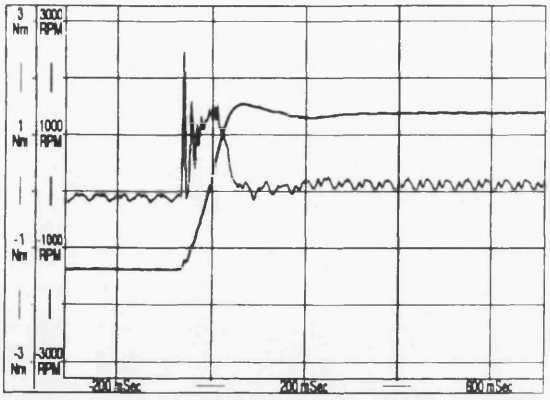

Figure 4. Speed reversal during MTC operation. ω =+/- 1400 rpm.

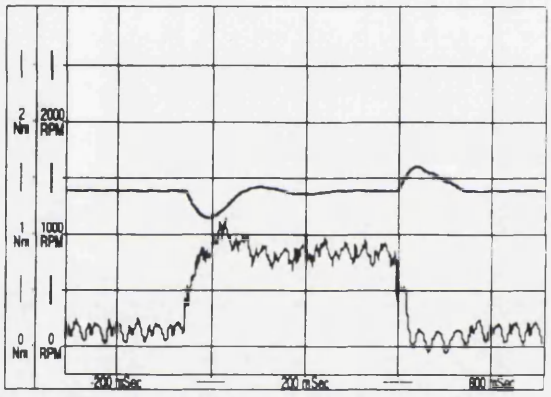

Figure 5. Step load change during MTC operation. ω=1400rpm, T=0.14Nm - 0.84Nm (0.17 p.u.-1.0 p.u.).

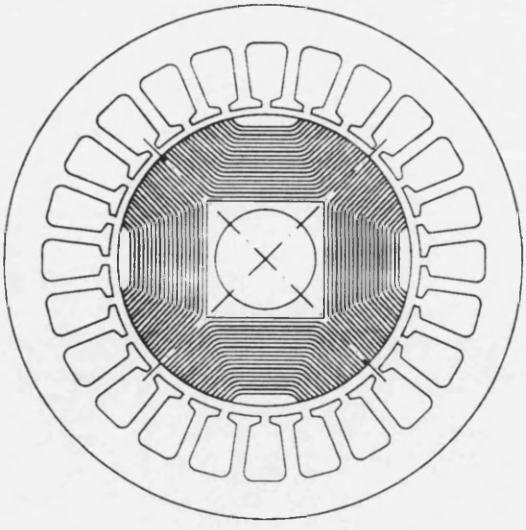

Figure 6. Cross-section of 120W Axially Laminated Synchronous Reluctance Motor.

SYNCHREL Data

The SYNCHREL rotor is an axially laminated design shown in figure 6. It is using the same frame and windings as the induction motor it is compared with.

Ld (unsat)	=	2.60 H
Ld (Id_{pk}=0.61A)	=	1.68 H
Lq	=	0.39 H
R_{phase} @ 20°C	=	98.0 Ω
Rated Phase Current	=	0.47 A

Acknowledgements

The authors would like to thank the following companies and individuals:

The *Committee of Vice-Chancellors and Principals of the Universities of the United Kingdom* (CVCP ORS-award) and the *Scottish Power Electronics and Electrical Drives Consortium* (SPEED) for financial support of R. Lagerquist.
Science and Engineering Research Council (SERC) for financial support of R.E. Betz (visiting Fellowship).
F. Flett & Analog Devices for contribution of linear and data-conversion devices.
I. Duthie, A. Hutton & Motorola for the DSP development system.
S.E. Wood & Brook Crompton for the motor.
D. Staton for designing the SYNCHREL rotor, and for theoretical and static data for the SYNCHREL.
J. Kelly for making the SYNCHREL rotor.
P. Miller for designing and building the power electronics.

References:

[1] Betz R E, "Control of Synchronous Reluctance Machines", Annual Meeting IEEE-IAS, Sept 29-Oct 4, Dearborn, USA, 1991.

[2] Betz R E, Miller T J E, "Aspects of the Control of Synchronous Reluctance Machines", EPE Firenze, pp. 1-380 - 1-385, 1991

[3] Chiba A, Fukao T, "A Closed Loop Control of super High Speed Reluctance Motor for Quick Torque Response", Annual Meeting IEEE-IAS, Atlanta, USA, 1987.

[4] Lorenz R D, Van Patten K, "High Resolution Velocity Estimator for All Digital AC Servo Drives", Annual Meeting IEEE-IAS, pp 363-368, 1988.

[5] van der Broeck H W, Skudelny H C, Stanke G, "Analysis and Realization of a Pulse Width Modulator Based on Voltage Space Vectors", Annual Meeting IEEE-IAS, pp 244-251, 1986.

E.5 The synchronous reluctance motor for motion control applications

21st Annual Symposium on Incremental Motion Control Systems and Devices
San Jose, California, June 15-19, 1992

THE SYNCHRONOUS RELUCTANCE MOTOR FOR MOTION CONTROL APPLICATIONS

JR Hendershot Jr
Magna Physics Corp.
Hillsboro OHIO 45133

TJE Miller, DA Staton, R Lagerquist
SPEED Laboratory, University of Glasgow
Glasgow G12 8LT, UK

Abstract

The synchronous reluctance motor is under renewed development and evaluation for motion-control applications and variable-speed drives. Although it has a long history as a *line-start* motor with a cage winding on the rotor, recent developments have focussed on the *cageless* motor with current-regulated PWM inverter control. Because of the field-orientation of this type of drive, and the enhanced electromagnetics without the starting cage, much higher performance is possible, not only in terms of efficiency and power-factor, but also in terms of control performance. In order to realise these benefits the axially-laminated rotor construction is virtually essential, as this is the only structure that permits a sufficiently high saliency ratio to achieve competitive performance. The stator and the power electronic circuit are similar to those used with induction motors or brushless DC motors. Consequently many of the advantages claimed for the *switched* reluctance motor can be realised using standard components. These advantages include high efficiency at low speed, constant-power operation over a wide speed range, and freedom from permanent magnets. In addition, the synchronous reluctance motor has lower torque ripple and is quieter than the equivalent switched reluctance motor.

1. INTRODUCTION

This paper reviews the synchronous reluctance motor (SYNCHREL motor) in the light of recent developments in its electromagnetic design and its electronic control.

The SYNCHREL motor has many of the advantages of the switched reluctance (SR) motor, yet it uses standard components in common with brushless DC or induction motors, including the stator and the power-electronic circuit. The torque ripple is also less than that of the SR motor.

The main advantages of the SYNCHREL motor are as follows:

1. Freedom from permanent magnets
2. A wide speed range at constant power
3. Synchronous operation, leading to high efficiency and the ability to maintain full torque at zero speed (which is difficult with induction motors)

The main disadvantages are as follows:

1. In small motors the torque/ampere and the torque/volume are lower than in PM motors
2. A sinewave drive is required, with continuous shaft position feedback for orientation of the stator MMF
3. A small airgap is required, comparable to that of induction motors.

The first of these disadvantages will become much less significant in larger motors, say, over 5-10kW in rating, because of the high cost of magnets in large motors, and also because the reluctance motor performance improves rapidly with increasing size.

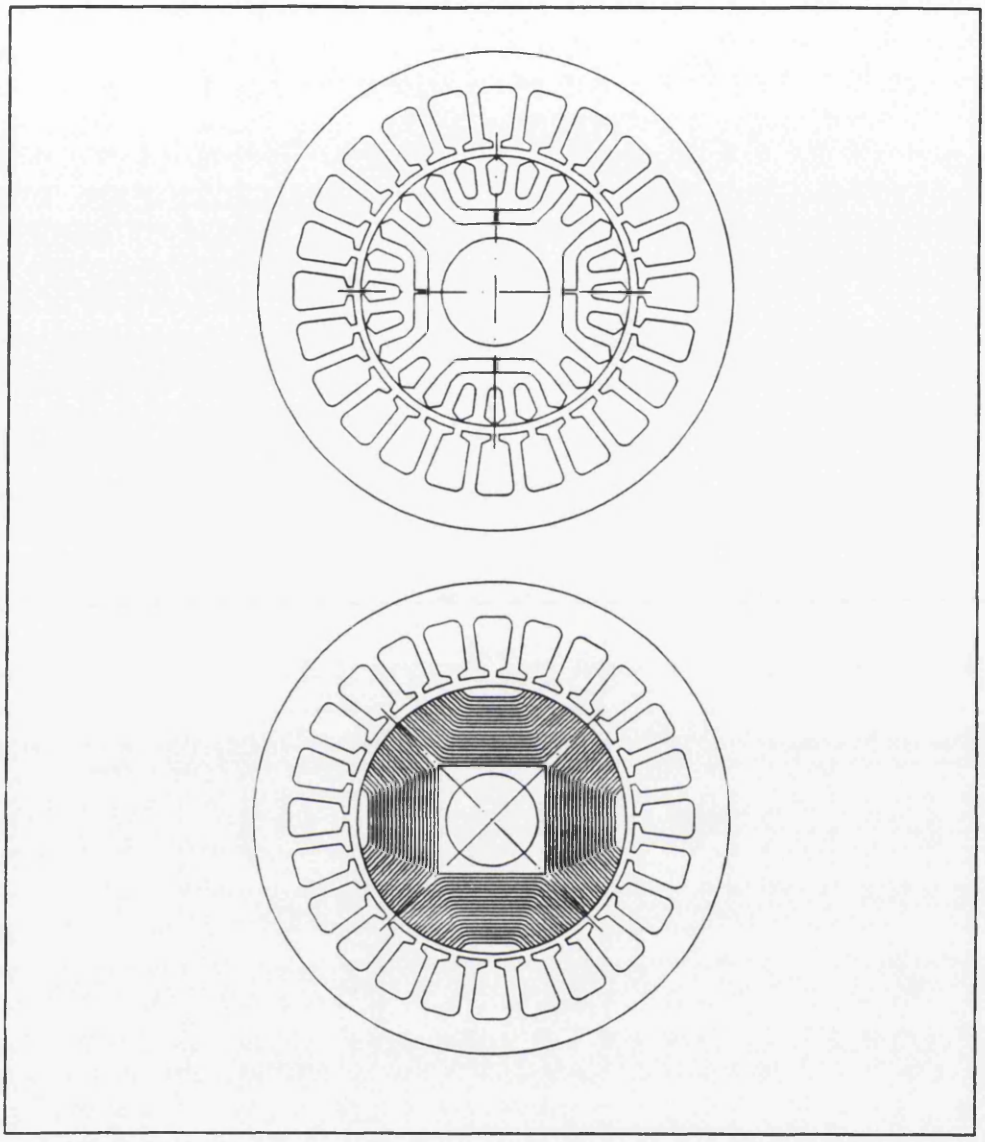

Fig. 1 Segmental (upper) and axially-laminated (lower) synchronous reluctance motors. The segmental type shown here has an amortisseur winding and is self-starting. The axially-laminated type has a higher saliency ratio but requires shaft position feedback and a current-controlled PWM (field-oriented) inverter.

The performance of the SYNCHREL motor depends critically on the X_d/X_q ratio or *saliency ratio*, and in order to achieve a high saliency ratio the axially-laminated construction is virtually essential, Fig. 1. This form of construction was introduced by Cruickshank et al [1], but it has been "re-invented" recently without the cage winding, and coupled with the modern vector-controlled type of PWM inverter. Both of these modifications bring significant performance advantages.

One of the main reasons for the current interest in the SYNCHREL motor is that it is seen as a potential alternative to the *switched* reluctance motor, providing most of the advantages with few of the disadvantages (non-standard components, high noise and torque ripple). Several papers on the SYNCHREL motor and its predecessors are listed in the References.

2. THE SYNCHRONOUS RELUCTANCE MOTOR

The SYNCHREL motor is a true AC motor: this means that it has a rotating MMF produced by polyphase sinewave currents flowing in sine-distributed windings, exactly like the induction motor or the sinewave brushless DC permanent-magnet motor. In fact, the stator can be identical to that of either of these motors. Apart from slotting, and the fact that the windings are not perfectly sine-distributed, it satisfies the necessary conditions for the production of *constant instantaneous torque* (i.e. zero torque ripple). These conditions are the same ones that make possible the use of *dq-axis* theory, and therefore the synchronous reluctance motor can be controlled by a *field-oriented AC controller* in much the same way as any other synchronous machine. This is the preferred form of control for high-performance applications.

The use of standard components in the stator, the winding configuration, and the power electronic circuit means that the characteristics of the reluctance motor can be achieved with minimum re-investment in new tooling and design techniques.

SYNCHREL vs. Induction Motor

First, because there is no slip, the rotor losses are lower than those of the induction motor. This is important at low speed, where the torque is limited by rotor losses. The SYNCHREL motor should have higher power factor and higher continuous torque rating at low speed, when compared to the induction motor. The higher power factor translates into a lower inverter kVA requirement. The differences may typically be of the order of a few percent, which may not seem great, but in specialty applications such as electric vehicle drives a few percent in kVA or efficiency can make a large difference.

The full-load efficiency at rated speed, and the speed range at constant power, should also exceed the values obtainable with induction motors. However, *all* the performance advantages of the synchronous reluctance motor are obtainable only with a sufficiently high *saliency ratio*, that is, the ratio between the d-axis and q-axis synchronous reactances. Tests on a series of D132 motors have shown that in order to outperform the induction motor by a significant margin over the entire speed range, the saliency ratio needs to be at least 8:1. This high value is extremely difficult to achieve with segmental-rotor designs such as the one shown in Fig. 1. Indeed it appears that such a high value is possible *only* with the axially-laminated construction. Note that the axially-laminated rotor cannot be built from the material punched out of the stator lamination, but requires fresh material in the form of cut strip which must be formed, stacked, and bolted to a square or hexagonal shaft.

SYNCHREL vs. Brushless PM Motor

The SYNCHREL motor is free from the attendant problems of permanent magnets, but the price paid for this is a significantly lower torque per ampere in small frame sizes. On the other hand, the SYNCHREL motor has a naturally inverse speed/torque characteristic, and with the correct control

strategy it can maintain constant-power operation over a wide speed range, which is approximately equal to half the saliency ratio. In large sizes (say, over 10kW) the price of magnets is often prohibitive, while the performance of the SYNCHREL motor improves with size. Therefore there is likely to be a size range where the SYNCHREL motor has a clear advantage as a synchronous brushless motor with high efficiency and power factor, especially if operation is required at very low or very high speeds.

SYNCHREL vs. Switched Reluctance Motor

The most striking advantage of the *switched* reluctance motor over induction motors is the ability to maintain full torque down to very low speed without exceeding the thermal limits. As a synchronous machine, the SYNCHREL motor has the same characteristic. Unlike the switched reluctance motor, it does not suffer from high torque ripple because it is a true synchronous AC motor. But its raw power density may be somewhat lower than that of the switched reluctance motor.

3. CONTROL OF THE SYNCHREL MOTOR

The SYNCHREL motor requires correct MMF orientation to be maintained at all load points, necessitating a vector type of current-controlled PWM inverter with precise shaft-position feedback (e.g. a resolver, 1000-line encoder, or equivalent). Such transducers are, of course, also used with field-oriented control in induction motor drives; but whereas the induction-motor has line-start capability as a back-up operating mode, this is not the case with the cageless SYNCHREL motor. Unlike the induction motor, the SYNCHREL motor cannot be operated stably without vector control. Earlier types of self-starting synchronous reluctance motors with amortisseur (cage) windings could run open-loop, but their performance is significantly lower than that of the controlled cageless type discussed here.

The torque angle, i.e. the orientation of the MMF with respect to the rotor position, is not as simple as might be supposed. In the classical theory of the synchronous machine, the electromagnetic torque is given by the equation

$$T = mpI_dI_q(L_d - L_q) = \frac{m}{2} pI^2 \sin 2\gamma \qquad (1)$$

where m is the number of phases, p is the number of pole-pairs, L_d and L_q are the direct- and quadrature-axis synchronous inductances respectively, and γ is the torque angle. This equation is often quoted in isolation and is interpreted to mean that the torque per ampere is maximized if the *inductance difference* is maximized and the torque angle maintained at a constant 45°. However, this ignores the fact that the inverter *voltage* is limited, and in order to minimize the volt-ampere *product* the torque angle should be given by

$$\gamma = \tan^{-1}\left[\frac{L_d}{L_q}\right] \qquad (2)$$

These considerations apply to *steady-state operation only*. In steady-state operation the angle may be chosen to maximize the power-factor or the torque per ampere, but not both at the same time. If dynamics are important, for example operation at high speed with a constant-power characteristic, or maintaining constant speed with a rapidly varying load torque, then the angle must be controlled by a more complex type of algorithm that is comparable in complexity to those used in field-oriented control of induction motors. Several alternative algorithms for this purpose have been developed and analyzed by Betz [10], and an experimental vector controller has been designed and built in the SPEED laboratory [11].

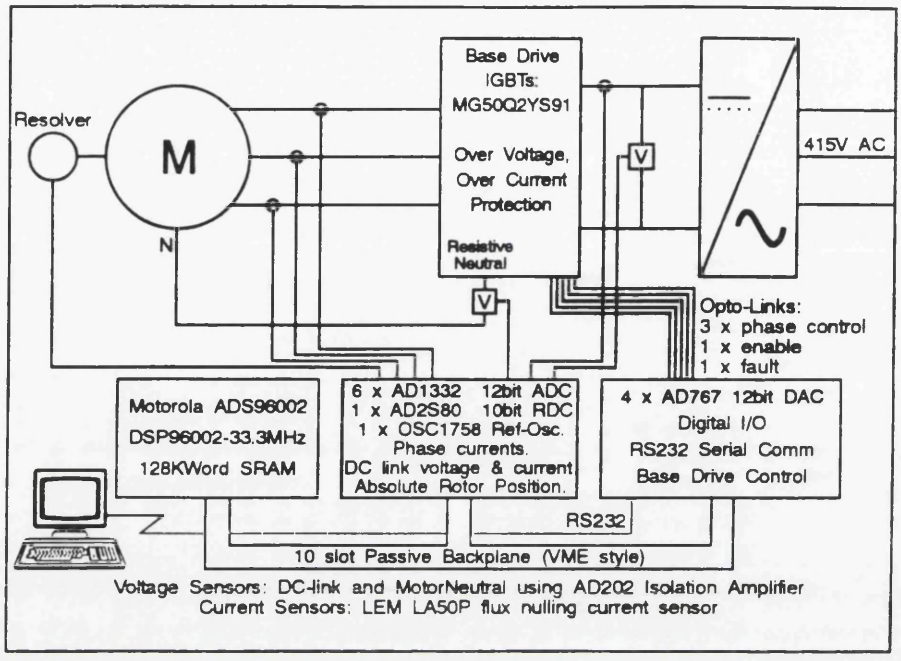

Fig. 2 DSP based SYNCHREL motor controller

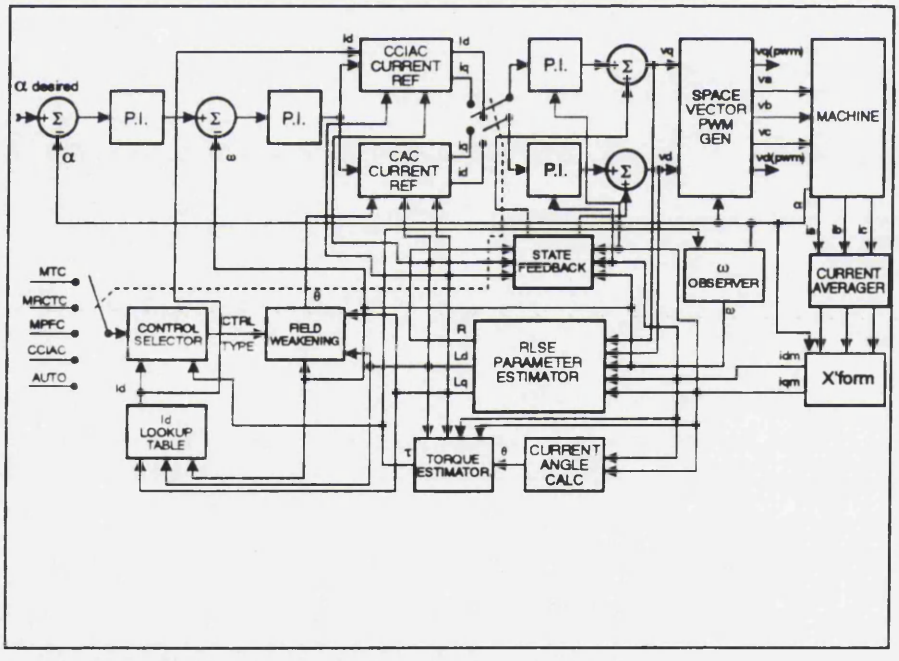

Fig. 3 SYNCHREL motor controller block diagram

This controller is shown in Figs. 2 and 3. The rating is 7.5kW with 415V 3-phase AC input at 50Hz. The power semiconductor devices are IGBT modules, and the main control processor is the Motorola DSP96002 clocked at 33MHz. The control algorithms described in [10,11] are *all* implemented in the block diagram in Fig. 3 as alternatives that can be selected by software switches for experimental evaluation. The complexity of a production version would not be nearly so great as suggested by this diagram. The real-time code for the DSP control was derived from a simulation of the entire drive in 'C' which was ported to the DSP development system and re-compiled for the 96002, a process which drastically cuts the development time required for systems of this complexity.

4. PRELIMINARY PERFORMANCE COMPARISON DATA

The following data provides a comparison between the performance of three motors in D132 totally-enclosed fan-ventilated frames. The data is a highly condensed summary of a series of tests and studies, but it provides an idea of the main differences *at rated load and full speed*. None of the SYNCHREL motor test data was taken with the new controller described in Section 3, since these tests are still incomplete. The test data presented here was obtained with a modified commercial induction motor inverter.

The three motors are as follows :

1. A commercial induction motor designed for sinewave operation at 50Hz, in a D132 aluminium frame.

2. A synchronous reluctance motor built into the induction motor stator, with an axially-laminated rotor.

3. A commercial switched reluctance motor (also described in Ref. 9) designed for variable-speed operation from 300-1500 rpm in a D132 cast-iron frame.

The performance comparison depends very much on how the machines are rated. Two tables of data are given, corresponding to two different ratings for the AC motors. Table 1 has them rated at 11kW, which is the maximum continuous thermal rating of the induction motor running from a sinewave supply at full speed.

When the induction motor is operated from a PWM inverter, its full-speed rating has to be decreased to 6 kW (40 Nm at 1471 rpm) so that the maximum torque can be provided all the way down to zero speed without exceeding the temperature-rise on which the sinewave rating of 11 kW is based. Therefore in Table 2 the motors are compared at the reduced rating.

In order to provide comparison data with the SRM at the same ratings, the SRM data is calculated by PC-SRD, starting with the normal rating (7.5kW) and modifying the winding turns (from 70/pole at 7.5kW to 77 at 6kW and 58 at 11kW) to give approximately the same output power as the two AC motors. The modelling of this particular SRM with PC-SRD is known to be very accurate at the full-load point, and the error introduced by scaling the turns is considered to be negligible for the present purposes.

Comparison at 11 kW rating (Table 1)

At the maximum thermal rating the synchronous reluctance motor has an efficiency nearly 1.5% higher than that of the induction motor (89.6% compared with 88.2%), but its power factor is slightly lower (0.855 compared with 0.867). The efficiency of the switched reluctance motor lies between the figures for the two AC motors at 89.2%, but its inverter kVA requirement is higher: 122.4 kVA compared with 115 kVA (see **Notes**). These differences are not large, and are not likely to be significant for general-purpose adjustable-speed drives. But in applications such as compressor drives or electric vehicle traction, where efficiency at sustained full-load operation is a critical parameter, the synchronous reluctance motor comes out clearly ahead, with the highest efficiency but a lower kVA requirement than the switched

reluctance motor (and with all components standard except the rotor and the inverter control algorithm).

Comparison at 6 kW rating (Table 2)

For full variable-speed operation this is the correct rating figure to use as a basis for comparison. Now the switched reluctance motor has the highest efficiency (89%) but it is only marginally better than the 88.8% of the induction motor. However, the power factor of the induction motor, at what is essentially a part-load rating, is significantly lower than at full-load and its kVA requirement is 80.3 kVA compared with 69.4 for the switched reluctance motor. It is interesting that the kVA per kW for the switched reluctance motor does not change appreciably between the two ratings. The synchronous reluctance motor now has the lowest efficiency, at 88.2%, but it also has the lowest kVA requirement at 63.5kVA.

This basis of comparison does not really bring out the major differences between the SRM and the two AC motors. These differences are likely to be more pronounced at very low speeds. Although we do not have test data to verify this, we know that the synchronous and the switched reluctance motors do not need to be de-rated for PWM inverter operation, and we can assume that any de-rating necessary to permit low-speed operation (with reduced cooling) will be quite small, because these motors have no slip losses and they can maintain their effective power-factor over the entire speed range. The de-rating of the induction motor was from 73 Nm to 40 Nm, a reduction of 45%. If half of this de-rating was required for low-speed operation of the reluctance motors, they would be delivering about 56 Nm at low speed, which is about 40% more torque than the induction motor. A test calculation with PC-SRD shows that at 55 Nm and 300 rpm, the losses in the switched reluctance motor are only about half the full-load value and the winding current-density is only 0.9 of the full-load value.

PARAMETER	Induction	Synchrel	SRM
Full-load shaft power (kW)	11.0	11.0	10.9
Full-load speed (rpm)	1439	1500	1500
Full-load torque (Nm)	73.0	70.0	69.1
Transistor peak kVA requirement	115.0	114.9	122.4
Full-load power-factor	0.867	0.855	NA
Full-load efficiency %	88.2	89.55	89.2
Inductance ratio	NA	11.2	11.6

Table 1 Comparison data at 11 kW

PARAMETER	Induction	Synchrel	SRM
Full-load shaft power (kW)	6.0	6.0	6.1
Full-load speed (rpm)	1471	1500	1500
Full-load torque (Nm)	39.8	38.2	38.9
Transistor peak kVA requirement	80.3	63.5	69.4
Full-load power-factor	0.688	0.856	NA
Full-load efficiency %	88.8	88.2	89.0
Inductance ratio	NA	11.6	11.6

Table 2 Comparison data at 6 kW

Notes The induction-motor data is appropriate to a commercial motor designed for mass production rather than for the ultimate performance. The synchronous reluctance motor uses the same stator and the same airgap length. The figures for the synchronous reluctance motor are estimates and do not include any allowance for end-winding inductance; they are therefore slightly optimistic, but it is calculated that this effect reduces the inductance ratio by 13% and increases the kVA requirement by only 2.5%. The kVA requirement is evaluated as the product of the number of transistors times the peak current times the DC link voltage in the controller, and the surprisingly low kVA requirement of the synchronous reluctance motor should be noted. This is due to the high saliency ratio achievable with the axially-laminated construction. The efficiencies calculated for the switched reluctance motor are based on the use of 3% Silicon steel. The other two motors use low-carbon steel in the stator but the synchronous reluctance rotor has 1.5% Silicon steel laminations.

5. CONCLUSION

The synchronous reluctance motor appears to offer several of the advantages of the switched reluctance motor while retaining many components in common with the induction motor, including the stator and the power electronic controller circuit. At the maximum thermal rating the synchronous reluctance motor has the highest efficiency and lowest kVA requirement. But at the maximum thermal low-speed rating of the induction motor, the switched reluctance motor has the highest efficiency. Indications are that at low speeds both reluctance motors should be capable of more torque than the induction motor, perhaps by as much as 40%, with the synchronous reluctance motor having the advantage of lower kVA than the switched reluctance motor.

ACKNOWLEDGEMENT

The authors would like to thank Stephen E. Wood of Brook Crompton, Huddersfield, for close collaboration on this project and especially for the test data and calculations on the induction and synchronous reluctance motors. The SYNCHREL motor control algorithms mentioned in Section 3 were originated by Dr. Robert Betz of the University of Newcastle, NSW, Australia, during a Visiting Fellowship in the SPEED Laboratory supported by the UK Science and Engineering Research Council. Several colleagues in the SPEED laboratory have contributed to the test programme.

7. REFERENCES

1. Cruickshank AJO, Anderson AF, and Menzies RW : "Theory and performance of reluctance motors with axially laminated anisotropic rotors", IEE Proceedings, **118**, No. 7, July 1971, pp. 887-894

2. Miller TJE, Staton DA, and Wood SE : "Optimization of the synchronous reluctance motor geometry", IEE Conference on Electrical Machines and Drives, London, September 13-15, 1991

3. Xu L, Lipo T, and Rao SC : "Analysis of a new variable-speed singly-salient reluctance motor utilizing only two transistor switches", IEEE Transactions, **IA-26**, No. 2, Mar/Apr 1990

4. Fratta A, Vagati A and Villata F : "Control of a reluctance synchronous motor for spindle applications", International Power Electronics Conference, Tokyo, April 1990, pp. 708-715

5. Fukao T, Chiba A and Matsui M : "Test results on a super high-speed amorphous-iron reluctance motor", IEEE Transactions, **IA-25**, No. 1, pp. 119-125

6. Honsinger V.B. : "The inductances Ld and Lq of reluctance machines", IEEE Transactions, **PAS-90**, No. 1, Jan/Feb 1971, pp. 298-304

7. Lawrenson PJ and Gupta SK : "Developments in the performance and theory of segmental-rotor reluctance machines", IEE Proceedings, **114**

8. Miller, TJE, Staton, DA, and Wood, SE : "Maximizing the Saliency Ratio of the Synchronous Reluctance Motor", paper submitted for publication in Proceedings IEE, 17 January 1992

9. Harris, MR and Miller, TJE : "Comparison of Design and Performance Parameters in Switched Reluctance and Induction Motors", IEE Conference on Electrical Machines and Drives, London, September 1989

10. Betz RE : "Control of synchronous reluctance machines", IEEE IAS Annual Meeting, Dearborn, September 28-October 4, 1991, Conference Record, pp. 456-462

11. Lagerquist R, Betz RE and Miller TJE : "DSP96002 based vector controller for synchronous reluctance motors", to be published in International Conference on Electric Machines (ICEM'92), Manchester, September 13-15, 1992

References

[1] D. Platt, "Reluctance motor with strong rotor anisotropy", in *IEEE Ind. Appl. Society Annual Meeting*, 1990, pp. 225–229.

[2] M. Ehsani, I. Husain, and A. B. Kulkarni, "Elimiation of direct position sensor and current sensor in switched reluctance motor drives", in *IEEE Ind. Appl. Society Annual Meeting*, 1990, pp. 518–524.

[3] R. J. Hill, P. P. Acarnley, and W. Colville, "Stepping motors and drive circuits therfor", in *United States Patent 4,520,302*, May 1985.

[4] S. K. Panda and F. A. J. Amaratunga, "Switched reluctance motor drive without direct rotor positon sensor", in *IEEE Ind. Appl. Society Annual Meeting*, 1990, pp. 525–530.

[5] R. Wu and G. R. Slemon, "A permanent magnet motor drive without a shaft sensor", in *IEEE Ind. Appl. Society Annual Meeting*, 1990, pp. 553–558.

[6] A. El-Antably, "Proposed control startegy for cageless reluctance motor using terminal voltage and currents", in *IEEE Ind. Appl. Society Annual Meeting*, 1985, pp. 753–758.

[7] S. Bolognani, "Torque angle calculator for sensorless reluctance motor drives", in *European Power Electronics Conference*, 1991, pp. 4–013–4–017.

[8] I. Boldea, Z. X. Fu, and S. A. Nasar, "Torque vector control (tvc) of axially-laminated anisotropic (ala) reluctance motors", *Electrical Machines and Power Systems*, vol. 19, pp. 381–398, 1991.

[9] R. E. Betz, "Control of synchronous reluctance machines", in *IEEE Ind. Appl. Society Annual Meeting*, 1991, pp. 456–462.

[10] R. E. Betz and T. J. E. Miller, "Aspects of the control of synchronous reluctance machines", in *European Power Electronics Conference*, 1991, pp. 1–380–1–385.

[11] J. K. Kostko, "Polyphase reaction synchronous motor", *Journal of the AIEE*, vol. 24, 1923.

[12] D. A. Staton, T. J. E. Miller, and S. E. Wood, "Maximizing the saliency ratio of the synchronous reluctance motor", *Proc. IEE*, vol. 140, no. 4, pp. 249–259, 1993.

[13] C. H. Lee, "The theory and design of a very slow-speed reluctance motor", *Journal of the AIEE*, pp. 1638–1689, February 1960.

[14] P. J. Lawrenson and L. A. Agu, "Theory and performance of polyphase reluctance machines", *Proc. IEE*, vol. 111, no. 8, pp. 1435–1445, 1964.

[15] P. J. Lawrenson and L. A. Agu, "Low-inertia reluctance machines", *Proc. IEE*, vol. 111, no. 12, pp. 2017–2025, 1964.

[16] P. J. Lawrenson and S. K. Gupta, "Developments in the performance and theory of segmental-rotor reluctance motors", *Proc. IEE*, vol. 114, no. 5, pp. 645–653, 1967.

[17] W. Fong, "Change-speed reluctance motors", *Proc. IEE*, vol. 114, no. 6, pp. 797–801, 1967.

[18] W. Fong and J. S. C. Htsu, "New type of reluctance motor", *Proc. IEE*, vol. 117, no. 3, pp. 545–551, 1970.

[19] V. B. Honsinger, "The inductances l_d and l_q of reluctance machines", *IEEE Trans. Power App. Syst.*, vol. PAS-90, no. 1, pp. 298–304, 1971.

[20] V. B. Honsinger, "Inherently stable reluctance motoros having impoved performance", *IEEE Trans. Power App. Syst.*, vol. PAS-91, pp. 1544–1554, 1972.

[21] A. J. O. Cruickshank, A. F. Anderson, and R. W. Menzies, "Theory and performance of reluctance motors with axially laminated anisotropic rotors", *Proc. IEE*, vol. 118, pp. 887–894, 1971.

[22] R. W. Menzies, "Theory and operation of reluctance motors with axially laminated anisotropic rotors i – analysis", *IEEE Trans. Power App. Syst.*, vol. PAS-91, no. 1, pp. 35–41, 1972.

[23] R. W. Menzies, R. M. Mathur, and H. W. Lee, "Theory and operation of reluctance motors with axially laminated anisotropic rotors ii – synchronous performance", *IEEE Trans. Power App. Syst.*, vol. PAS-91, no. 1, pp. 41–45, 1972.

[24] S. C. Rao, "Dynamic performance of reluctance motors with magnetically anisotropic rotors", *IEEE Trans. Power App. Syst.*, vol. PAS-95, no. 4, pp. 1369–1376, 1976.

[25] A. El-Antably and T. L. Hudson, "The design and steady-state performance of a high-efficiency reluctance motor", in *IEEE Ind. Appl. Society Annual Meeting*, 1985, pp. 770–777.

[26] A. Fratta and A. Vagati, "Axially laminated reluctance motor: an analytical approach to the magnetic behaviour", in *Proc. Int. Conf. Electrical Machines*, 1988, pp. 1–6.

[27] I. Marongiu and A. Fratta, "Improved modelling if a distributed synchronous reluctance machine", in *IEEE Ind. Appl. Society Annual Meeting*, 1991.

[28] T. J. E. Miller, A. Hutton, C. Cossar, and D. A. Staton, "Design of a synchronous reluctance motor drive", *IEEE Trans. Ind. Appl.*, vol. 27, no. 4, pp. 741–749, 1991.

[29] I. Boldea, Z. X. Fu, and S. A. Nasar, "High-performance reluctance generator", *Proc. IEE*, vol. 140, no. 2, 1993.

[30] T. Fukao, A. Chiba, and M. Matsui, "Test results on a super-high-speed amorphous-iron reluctance motor", *IEEE Trans. Ind. Appl.*, vol. 25, no. 1, pp. 119–125, 1989.

[31] A. Chiba, F. Nakamura, and T. Fukao, "Inductances of cageless reluctance-synchronous machines having nonsonusoidal space distributions", in *IEEE Ind. Appl. Society Annual Meeting*, 1989, pp. 314–319.

[32] A. Chiba, F. Nakamura, T. Fukao, and M. A. Rahman, "Inductances of cageless reluctance-synchronous machines having nonsinusoidal space distributions", *IEEE Trans. Ind. Appl.*, vol. 27, no. 1, pp. 44–51, 1991.

[33] J. W. Finch and P. J. Lawrenson, "Reluctance motors", *Proc. IEE*, vol. 125, no. 12, pp. 1350–1356, 1978.

[34] V. B. Honsinger, "Steady-state performance of reluctance machines", *IEEE Trans. Power App. Syst.*, vol. PAS-90, no. 1, pp. 305–317, 1971.

[35] J. W. Finch and P. J. Lawrenson, "Asynchronous performance of single-phase reluctance motors", *Proc. IEE*, vol. 126, no. 12, pp. 1249–1254, 1979.

[36] R. E. Betz, "Theoretical aspects of the control of synchronous reluctance machines", *Proc. IEE*, vol. 139, no. 4, 1992.

[37] A. Chiba and T. Fukao, "A closed loop control of super high speed reluctance motor for quick torque response", in *IEEE Ind. Appl. Society Annual Meeting*, 1987.

[38] A. Fratta, A. Vagati, and F. Villata, "Control of super high speed reluctance motor for quick torque response", in *IPEC*, 1990.

[39] L. Xu, X. Xu, T. A. Lipo, and D. W. Novotny, "Vector control of a reluctance synchronous motor including saturation and iron losses", *IEEE Trans. Ind. Appl.*, vol. 27, no. 5, pp. 977–985, Sept/Oct 1991.

[40] L. Xu and J. Yao, "A compensated vector control scheme of a synchronous reluctance motor including saturation and iron losses", in *IEEE Ind. Appl. Society Annual Meeting*, 1991, pp. 298–304.

[41] R. E. Betz, M. Jovanovic, R. Lagerquist, and T. J. E. Miller, "Aspects of synchronous reluctance machines including saturation and iron losses", in *IEEE Ind. Appl. Society Annual Meeting*, 1992, pp. 456–463.

[42] R. E. Betz, R. Lagerquist, M. Jovanovic, T. J. E. Miller, and R. H. Middleton, "Control of synchronous reluctance machines", *IEEE Trans. Ind. Appl.*, 1993, in press.

[43] A. E. Fitzgerald and C. K. Kingsley, *Electric Machinery*, McGraw Hill, second edition, 1961.

[44] Motorola Inc., *DSP96002 IEEE Floating-Point Dual-Port Processor User's Manual*, 1989.

[45] H. W. van der Broeck, H. C. Skudelny, and G. Stanke, "Analysis and realization of a pulse width modulator based on voltage space vectors", in *IEEE Ind. Appl. Society Annual Meeting*, 1986, pp. 244–251.

[46] R. D. Lorenz and K. van Patten, "High resolution velocity estimator for all digital ac servo drives", in *IEEE Ind. Appl. Society Annual Meeting*, 1988, pp. 363–368.

[47] J. R. Frus and B. C. Kuo, "Closed-loop control of step motors without feedback encoders", in *Fifth Annual Symposium on Incremental Motion Control Systems and Devices*, 1976, pp. CC–1–CC–11.

[48] B. C. Kuo and A. Cassat, "On current detection in variable-reluctance step motors", in *Sixth Annual Symposium on Incremental Motion Control Systems and Devices*, 1977, pp. 205–220.

[49] A. J. C. Bakhuizen, "On self-synchronisation of stepping motors", in *International conference in stepping motors and systems*, 1979.

[50] S. R. MacMinn, C. M. Stephens, and P. M. Szezesny, "Switching reluctance motor drive system and laundering apparatus employing same", in *United States Patent 4,959,596*, Sep 1990.

[51] W. D. Harris and J. H. Lang, "A simple motion estimator for variable-reluctance motors", *IEEE Trans. Ind. Appl.*, vol. 26, no. 2, pp. 237–243, 1990.

[52] G. Hedlund and H. Lundberg, "A motor energizing circuit", in *United States Patent 4,868,478*, Sept 1989.

[53] J. T. Bass, M. Ehsani, and T. J. E. Miller, "Robust torque control of switched-reluctance motors without a shaft position sensor", *IEEE Transactions on IE*, vol. 33, no. 3, pp. 212–216, 1986.

[54] M. Jufer and R. Osseni, "Back emf indirect detection for self commutation of synchronous motors", in *European Power Electronics Conference*, 1987, pp. 1125–1129.

[55] P. P. Acarnley and N. Ertugrul, "Rotor position estimation in pm motors", in *IEEE Ind. Appl. Society Annual Meeting*, 1992, pp. 622–626.

[56] P. P. Acarnley and N. Ertugrul, "A new algorithm for sensorless operation of permanent magnet motors", in *Proc. Int. Conf. Electrical Machines*, 1992, pp. 414–421.

[57] H. Katsushima, S. Miyazaki, H. Watnabe, and T. Fujii, "A measuring method of rotor position of the direct drive servo motor", in *IPEC*, 1990.

[58] I. Boldea, Z. X. Fu, and S. A. Nasar, "Digital simulation of a vector controlled axially-laminated anisotropic synchronous motor servo-drive", *Electrical Machines and Power Systems*, vol. 19, pp. 415–426, 1991.

[59] T. A. Lipo, A. Vagati, L. Malesani, and R. Fukao, "Synchronous reluctance motors and drives - a new alternative", IEEE Ind. Appl. Society Annual Meeting Tutorial, Oct. 1992.

[60] W. L. Soong and T. J. E. Miller, "Practical field-weakening performance of the five classes of brushless synchronous ac motor drive", in *European Power Electronics Conference*, 1993, in press.

[61] R. Lagerquist, R. E. Betz, and T. J. E. Miller, "Dsp96002 based high performance digital vector controller for synchronous reluctance motors", in *Proc. Int. Conf. Electrical Machines*, 1992, pp. 903–907.